Dynamics of Semi-Flexible Fibres in Viscous Flow

Samantha Mary Harris

Submitted in accordance with the requirements for the degree of Doctor of Philosophy

The University of Leeds

Department of Applied Mathematics

July 2007

Abstract

The dynamics of semi-flexible fibres in shear flow and the effect of flexibility on the swimming speed of helical flagella are investigated. High aspect ratio particles such as carbon and glass fibres are often added as fillers to processed polymers. Although these materials have high rigidity, the large aspect ratio makes the fibres liable to bending during flow. Other high aspect ratio fibres that behave as semi-flexible fibres include carbon nano-tubes, paper fibres and semi-flexible polymers such as the muscle protein f-actin. Most theoretical studies assume that fibres are either rigid or completely flexible, but in this thesis fibres with a finite bending modulus are considered.

A semi-flexible fibre is modelled as a chain of shorter rods linked together. A bending torque is included at the joints between the rods to account for the rigidity. In shear flow the simulation reproduces the C and S turns observed in experiments on semi-flexible fibres. The results for finite aspect ratio fibres predict changes to the period of rotation and drift between Jeffery orbits. The direction of drift for a flexible fibre depends on both the intial orientation and the fibre's flexiblity.

We also present a linear analysis of how small distortions to a straight semi-flexible fibre grow when the flow places the fibre under compression. These results are in agreement with our full simulations and the growth rates of the distortions to a straight fibre allow us to predict the most unstable mode at a particular flow rate.

To allow for intrinsically bent or helical equilibrium shapes a second simulation method is developed that includes a twisting torque at the joints between the rods as well as a bending torque. Using this simulation we measure the period of rotation and orbit drift of permanently deformed fibres in shear flow and show that due to the asymmetry of a helix, shear induced rotation results in translation and orbit drift for both rigid and semi-flexible fibres.

Bacteria such as *Vibrio alginolyticus* and *Escherichia coli* swim by rotating one or more

helical flagella. *Vibrio alginolyticus* has only one flagella and changes direction by altering its sense of rotation. Experimental observations of *Vibrio alginolyticus* have found that backwards swimming is 50% faster than forwards swimming speed however, previous numerical simulation results have shown only a 4% difference for flagella of the same dimensions. We use our simulation to consider how flexiblity affects the swimming speed of helical flagella and show that for a constant angular velocity, difference between forwards and backwards swimming speed ranges between $0-23\%$ depending on the exact stiffness chosen. We explain the differences in swimming speeds of semi-flexible fibres by investigating the shape changes which occur and comparing them to the results for swimming speeds of rigid flagella of varying dimensions.

Acknowledgements

Samantha Harris would like to thank her superivisors Dr Oliver Harlen and Dr Tanniemola Liverpool for all their help and support. Samantha would like to acknowledge the EPSRC and the University of Leeds (Research Scholarship) for their financial support. She would also like to thank Dr Helen Wilson for her help with the Shooting Technique.

Contents

List of figures

List of tables

Chapter 1

Introduction

1.1 Fibres

This thesis is concerned with the motion of semi-flexible fibres in viscous fluids. We define a fibre as a slender object of circular cross-section with a length that is large compared to its diameter. The ratio of length to diameter is called aspect ratio and is denoted by $a_r = \frac{l}{2b}$ (where l is the length and b is the radius).

We regard a fibre as semi-flexible if it has a bending stiffness that is comparible in magnitude to the hydrodynamic torques being applied to the fibre. A fibre may be

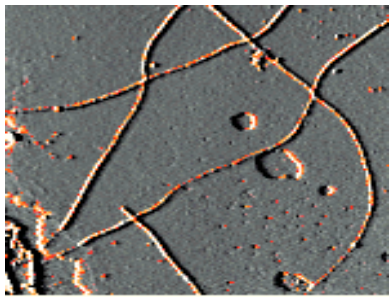

Figure 1.1: F-actin viewed on a Discover AFM microscope. Picture taken from reference [41].

regarded as rigid if its bending stiffness is sufficiently high that it does not change shape, while a fibre is flexible if the bending stiffness is negligible so that there is effectively no resistance to bending. The bending stiffness of an homogeneous fibre is dependent upon its Young's modulus and its size and shape. The exact form of the bending stiffness for an elastic fibre of circular cross section is derived in section 1.3.1.

The motion and deformation of semi-flexible fibres in viscous flows is important both in industry and in nature. Understanding the translational and rotational motion of fibres helps to explain the orientation of fibres in suspensions and the formation of fibre aggregates. Both are very important to the paper industry as they affect the sheet strength and optical properties of paper. Fibres are also used in reinforced composite materials. By including glass or carbon fibres in a thermosetting polymer the strength and heat conduction of the polymer is improved. The shear flow applied to the polymer during molding cause the fibres to align in the same direction producing a product with an anisotropic structure. Although fibres such as glass and carbon are commonly thought of as being rigid their large aspect ratio reduces their effective bending stiffness allowing them to be classed as semi-flexible. Other examples of fibres used in industry include polystyrene, polyethylene fibres and carbon nanotubes.

In biology protein filaments, such as F-actin (see figure 1.1) that make up the cytoskeleton, can be modelled as semi-flexible fibres. Determining how fibres bend and twist allows the mechanical properties of the cell to be established and in turn allows the modelling of tissues and organs. Other biological structures such as D.N.A can also be modelled as fibres, as can cilia and flagella. Cilia and flagella are projections from a cell. They are actively motile and convert energy in the form of the fuel adenosine triphosphate (A.T.P.) into mechanical work. They are designed either to move the cell itself or to move substances over or around the cell. The primary purpose of cilia in mammalian cells is to move fluid, mucous, or cells over their surface.

Bacteria are propelled by the rotation of one or more helical flagella. The flagella are

stiff and are driven at their base by a rotary motor [25]. Direction change is achieved by either changing the rotation direction (to swim backwards) as is the case of the bacterium *Vibrio alginolyticus*, or in the case of some bacteria with more than one flagella, direction change is achieved by one or more of the flagella ceasing to rotate or changing their sense of rotation. The mechanical principles behind flagella propulsion are beginning to be used in biomedical applications. Synthetic propulsion mechanisms are being used to direct artificial viruses through cells and nanodevices through the bloodstream [25].

As well as flexibility another important property of a fibre is its intrinsic shape or ground state. Whereas the flagella of bacteria have an intrinsic helical shape [9], the cilia or flagella of spermatazoa are intrinsically straight [25, 9]. They are driven by internal motors and undulate to provide forward thrust [6]. Instrinsic shape is also important for industrial fibres. Most theoretical work on industrial fibres assumes that they are intrinscially straight, however, this is rarely the case in practice. Small changes in the intrinsic shape of a fibre, particularly from being perfectly straight, can have significant effects on the fibre's dynamics.

1.2 Fluid Flow

1.2.1 Stokes Flow

An incompressible viscous fluid can be described by a velocity field, $\mathbf{u}$, which satisfies the Navier-Stokes equations

$$\rho\frac{D\mathbf{u}}{Dt} = -\nabla p + \mu\nabla^2\mathbf{u}, \tag{1.2.1}$$

together with the condition of incompressibility

$$\nabla\cdot\mathbf{u} = 0, \tag{1.2.2}$$

where ρ is the fluid density, p is the pressure and μ is the dynamic viscosity. $\frac{D\mathbf{u}}{Dt}$ is the material derivative given by

$$\frac{D\mathbf{u}}{Dt} = \frac{\partial \mathbf{u}}{\partial t} + \mathbf{u} \cdot \nabla \mathbf{u}.$$

For steady flow around a particle of length l with velocity U we can introduce the following non-dimensional variables

$$\nabla^* = l\nabla,$$

$$\mathbf{u}^* = \frac{\mathbf{u}}{U},$$

$$p^* = \frac{l}{\mu U} p,$$

and

$$t^* = t\frac{U}{l}.$$

Dropping the stars, the non-dimensional form of equations (1.2.1) and (1.2.2) become

$$R_e \frac{D\mathbf{u}}{Dt} = -\nabla p + \nabla^2 \mathbf{u},$$

and

$$\nabla \cdot \mathbf{u} = 0,$$

where

$$Re = \frac{\rho U L}{\mu},$$

is the Reynolds number, which measures the relative magnitudes of the inertial and viscous forces. The Reynolds number will be small if the fluid is sufficiently viscous, the particle is small and the velocity is slow (or a suitable combination of the three). In the limit of vanishing Reynolds number, the Navier-Stokes equations reduce to the Stokes equations

$$\mu\nabla^2\mathbf{u} - \nabla p = 0$$

$$\nabla \cdot \mathbf{u} = 0.$$

The viscosity and density of water are of order $10^{-3}\ Pa\ s$ and 10^3 kgm^{-3} respectively so that a particle of length 100μm moving at 100μms^{-1} has a Reynolds number of 10^{-2}.

The Navier-Stokes equations also assume that the fluid may be treated as a continuum, however, non-continuum Brownian forces become important for very small particles.

The Brownian diffusivity of a particle is given by the Stokes-Einstein relation

$$D = \frac{kT}{\xi},$$

where k is the Boltzman constant, T is the absolute temperature and ξ is the hydrodynamic resistivity of the particle which is proportional to μl.

The dimensionless measure of the importance of Brownian diffusion is the Peclet number

$$Pe = \frac{Ul}{D} = \frac{Ul\xi}{kT}.$$

Provided $Pe >> 1$ we may neglect the effects of Brownian motion.

For a 100μm particle moving at 100μms^{-1} in water, $Pe \approx 10^6$, while a 1μm particle moving at 1μms^{-1} has a Peclet number of $Pe \approx 1$. Thus there is a range of particle sizes from approximately 10μm to 100μm in water for which the Reynolds number is small but the Peclet number is large. Furthermore since Reynolds number decreases with increasing viscosity and the Peclet number increases with increasing viscosity this range of particle sizes is wider for more viscous fluids.

The dimensions of typical biological and artificial flagella allow low Reynolds number, high Peclet number approximations to be used. Using the values suggested by Takano

and Goto [35, 12] for the bacterium *Vibrio alginolyticus* of flagella length 7.3μm and swimming speed 136μms^{-1}, gives a Reynolds number of order 10^{-4} and Peclet number of order 10^3. As the flagella diameter is only 0.02μm [35, 12] the aspect ratio is 365 and hence the flagella may be classed as a high aspect ratio fibre.

1.2.2 Free Space Green's Function for Stokes Flow

Since the Stokes equations are linear there exists a Green's function representation corresponding to the solution of the singularly forced Stokes equations

$$\mu\nabla^2\mathbf{u} - \nabla p = -\mathbf{g}\delta(\bar{\mathbf{x}}), \tag{1.2.3}$$

$$\nabla \cdot \mathbf{u} = 0,$$

where $\bar{\mathbf{x}} = \mathbf{x} - \mathbf{x}'$ and $\mathbf{g}\delta(\bar{\mathbf{x}})$ is a point force of strength $\mathbf{g}$ at $\mathbf{x}'$. The solution satisfying the boundary condition $|\mathbf{u}| \to 0$ as $|\mathbf{x} - \mathbf{x}'| \to \infty$ is given by

$$u_i = \frac{1}{8\pi\mu} G_{ij} g_j,$$

where G is the free space Green's function given by

$$G_{ij}(\bar{\mathbf{x}}) = \frac{\delta_{ij}}{|\bar{\mathbf{x}}|} + \frac{\bar{x}_i \bar{x}_j}{|\bar{\mathbf{x}}|^3}.$$

The solution to any linear boundary value problem for the Stokes equation may be written in the form of boundary integrals of velocity $\mathbf{u}$ and surface force density $\mathbf{f}$ over the surface bounding the fluid volume [28] such that

$$u_j(\mathbf{x}') = \frac{1}{8\pi\mu}\int_S f_i(\mathbf{x}) G_{ij}(\mathbf{x}, \mathbf{x}') dS(\mathbf{x}) + \frac{1}{8\pi}\int_S u_i(\mathbf{x}) T_{ijk}(\mathbf{x}, \mathbf{x}') n_k(\mathbf{x}) dS(\mathbf{x}),$$

where T_{ijk} is given by

$$T_{ijk} = -6\frac{\bar{x}_i\bar{x}_j\bar{x}_k}{|\bar{\mathbf{x}}|^5}.$$

It can be shown that for the flow produced by the translation and rotation of a rigid body the second integral can be eliminated so that

$$u_j(\mathbf{x}') = \frac{1}{8\pi\mu}\int_{S_B} f_i(\mathbf{x})G_{ij}(\mathbf{x},\mathbf{x}')dS(\mathbf{x}), \tag{1.2.4}$$

where S_B is the surface of the body [28].

1.2.3 Linear Flow

In many applications the typical size of the suspended particle, l, will be small compared to the lengthscale of the external flow L_{ext}. In these situations, the external flow may be expanded in a Taylor Series about the particle centre $\mathbf{x}_c$ as

$$\mathbf{u}^\infty(\mathbf{x}) = \mathbf{U}_0 + \mathbf{K}\cdot\mathbf{x}_c + \mathbf{K}\cdot(\mathbf{x}-\mathbf{x}_c) + O(\frac{\dot{\gamma}l^2}{L_{ext}})$$

where $\mathbf{U}_0 = \mathbf{u}^\infty(0)$, $\mathbf{K}$ is the velocity gradient $K_{ij} = \frac{\partial u_i^\infty}{\partial x_j}$, $\dot{\gamma} = \sqrt{K_{ij}K_{ij}}$ and $\mathbf{x}$ is a general point in the fluid.

The velocity gradient tensor $\mathbf{K}$ may be expressed as the sum of its symmetric and anti-symmetric parts, namely the rate of strain tensor $\mathbf{E}$ and the vorticity tensor $\mathbf{\Omega}$ where $E_{ij} = \frac{1}{2}(K_{ij}+K_{ji})$ and $\Omega_{ij} = \frac{1}{2}(K_{ij}-K_{ji})$. We can therefore write the flow as

$$\mathbf{u}^\infty(\mathbf{x}) = \mathbf{U}_0 + \mathbf{K}\cdot\mathbf{x}_c + \mathbf{\Omega}\cdot(\mathbf{x}-\mathbf{x}_c) + \mathbf{E}\cdot(\mathbf{x}-\mathbf{x}_c) + O(\frac{\dot{\gamma}l^2}{L_{ext}})$$

or

$$\mathbf{u}^\infty(\mathbf{x}) = \mathbf{U}_0 + \mathbf{K}\cdot\mathbf{x}_c + \frac{1}{2}\boldsymbol{\omega}^\infty\times(\mathbf{x}-\mathbf{x}_c) + \mathbf{E}\cdot(\mathbf{x}-\mathbf{x}_c) + O(\frac{\dot{\gamma}l^2}{L_{ext}})$$

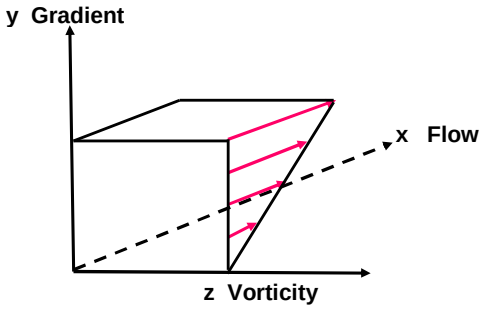

Figure 1.2: 3-Dimensional diagram of shear flow.

where $\boldsymbol{\omega}^{\infty} = \nabla \times \mathbf{u}^{\infty}$ is the vorticity of the fluid. The vorticity vector $\boldsymbol{\omega}^{\infty}$ is related to the vorticity tensor Ω by $\frac{1}{2}\omega_i^{\infty} = \epsilon_{ijk}\Omega_{jk}$. The first two terms in the expression for fluid velocity represent a translational flow, the third term a rotational flow and the fourth a strain field.

The most common linear flow is simple shear flow and is the one we shall consider most often in this thesis. The fluid velocity is given by $\mathbf{u}^{\infty} = (\dot{\gamma}y, 0, 0)$ so that the x axis is along the flow direction, the y axis is along the gradient direction and the z axis is along the vorticity direction as shown in figure 1.2.

The velocity gradient tensor is given by

$$\mathbf{K} = \begin{pmatrix} 0 & \dot{\gamma} & 0 \\ 0 & 0 & 0 \\ 0 & 0 & 0 \end{pmatrix},$$

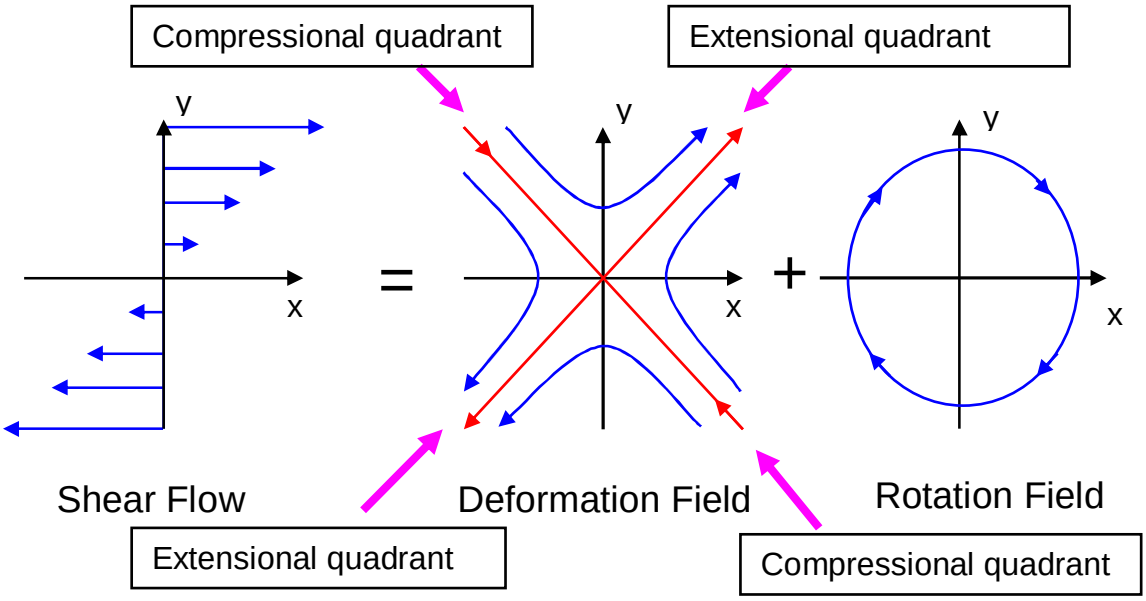

Figure 1.3: Diagram showing shear flow in the $x - y$ plane. The flow can be decomposed into a deformation and rotation fields. The plane can be divided into compressional and extensional quadrants determined by the deformation field.

so that the strain-rate or deformation field tensor is given by

$$\mathbf{E} = \begin{pmatrix} 0 & \frac{\dot{\gamma}}{2} & 0 \\ \frac{\dot{\gamma}}{2} & 0 & 0 \\ 0 & 0 & 0 \end{pmatrix},$$

the vorticity tensor by

$$\mathbf{\Omega} = \begin{pmatrix} 0 & \frac{\dot{\gamma}}{2} & 0 \\ -\frac{\dot{\gamma}}{2} & 0 & 0 \\ 0 & 0 & 0 \end{pmatrix}$$

which is related to the vorticity vector $\boldsymbol{\omega}^{\infty} = (0, 0, -\dot{\gamma})$, by $\Omega_{ij} = \frac{1}{2}\epsilon_{ijk}\omega_k^{\infty}$.

The symmetric strain rate tensor represents an extensional flow or deformation field and the anti-symmetric vorticity tensor, a rotational field as shown in figure 1.3.

1.2.4 Grand Resistance Tensor

In Stokes flow the velocity and angular velocity of any rigid particle in a linear flow are linearly related to the force and torque applied to the particle. This linear relationship can be summarised by a set of resistivity tensors that make up the grand resistance tensor for that particle. Consider a particle performing rigid body motion described by

$$\mathbf{u}^r = \mathbf{U} + \boldsymbol{\omega} \times (\mathbf{x} - \mathbf{x}_c), \tag{1.2.5}$$

where $\mathbf{U}$ is the velocity of the particle centre and $\boldsymbol{\omega}$ is the angular velocity of the particle, in a linear flow field given by

$$\mathbf{u}^{\infty} = \mathbf{U}_0 + \mathbf{K} \cdot \mathbf{x}_c + \frac{1}{2}\boldsymbol{\omega}^{\infty} \times (\mathbf{x} - \mathbf{x}_c) + \mathbf{E} \cdot (\mathbf{x} - \mathbf{x}_c). \tag{1.2.6}$$

The hydrodynamic force $\mathbf{F}$ on the particle is given by

$$\mathbf{F} = \int_S \mathbf{f} dS,$$

where $\mathbf{f}$ is the surface force density and the torque $\mathbf{T}$ given by

$$\mathbf{T} = \int_S (\mathbf{x} \times \mathbf{f}) dS.$$

The contribution of the particle to the stress in the suspension is given by the stresslet $\mathbf{S}$ [2] given by

$$\mathbf{S} = \frac{1}{2} \int_S (\mathbf{xf} + \mathbf{fx}) dS.$$

The hydrodynamic force, torque and stress on the particle are given in terms of the grand resistance matrix and, fluid and rod velocity by

$$\begin{pmatrix} \mathbf{F} \\ \mathbf{T} \\ \mathbf{S} \end{pmatrix} = \begin{pmatrix} \mathbf{A} & \tilde{\mathbf{B}} & \tilde{\mathbf{G}} \\ \mathbf{B} & \mathbf{C} & \tilde{\mathbf{H}} \\ \mathbf{G} & \mathbf{H} & \mathbf{M} \end{pmatrix} \begin{pmatrix} \mathbf{U}_0 - \mathbf{U} + \mathbf{K} \cdot \mathbf{x}_c \\ \frac{1}{2}\boldsymbol{\omega}^{\infty} - \boldsymbol{\omega} \\ \mathbf{E} \end{pmatrix}.$$

The elements $\mathbf{A}$ and $\mathbf{C}$ are 2nd rank, symmetric tensors relating force to translation and torque to rotation respectively. $\mathbf{B}$ and $\tilde{\mathbf{B}}$ relate torque to translation and force to rotation respectively. It can be shown that $\mathbf{B}$ is the transpose of $\tilde{\mathbf{B}}$ *i.e.* $B_{ij} = \tilde{B}_{ji}$ [20]. $\tilde{\mathbf{G}}$ and $\tilde{\mathbf{H}}$ are 3rd rank tensors relating force to strain and torque to strain respectively, while $\mathbf{G}$ and

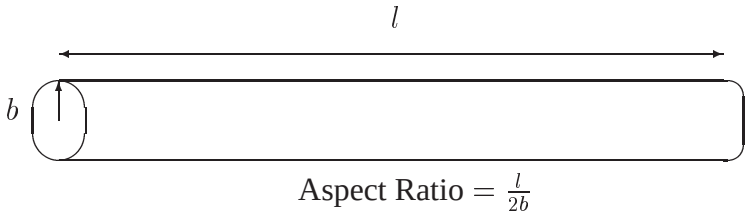

Figure 1.4: Sketch of a cylindrical fibre of aspect ratio $a_r = \frac{l}{2b}$.

$\mathbf{H}$ relate stress to translation and stress to rotation respectively. Again it can be shown that $\mathbf{G}$ and $\mathbf{H}$ are related to $\tilde{\mathbf{G}}$ and $\tilde{\mathbf{H}}$ by $G_{ijk} = \tilde{G}_{kij}$ and $H_{ijk} = \tilde{H}_{kij}$ [20]. The fourth rank tensor $\mathbf{M}$ relates stress to strain and satisfies $M_{ijkl} = M_{klij}$.

We can calculate the elements in the Grand Resistance matrix for a large aspect ratio fibre by using slender-body theory.

1.2.5 Slender-body Theory

Slender-body theory is an asymptotic technique that can be used to obtain analytic approximations to the solutions for Stokes flow around a particle such as a slender rod for which the length is large compared to its thickness.

Slender-body theory was originally developed by Burgers [5], who modelled the fibre as a line of point forces (called Stokeslets) on the particle axis. Later Tillett [39], made use of matched asymptotic expansion to give an improved result. This was developed further by Batchelor [1] who considered particles of non-circular cross section and Cox [8] who considered non-straight particles of circular cross section in a general ambient field. The basic method for a straight particle of circular cross section is described here.

We consider a straight cylindrical particle of length l and radius b where the aspect ratio $a_r = \frac{l}{2b}$. The velocity field $\mathbf{u}$ surrounding this particle must satisfy Stokes' equations

$$\mu\nabla^2\mathbf{u} - \nabla p = 0,$$

$$\nabla \cdot \mathbf{u} = 0,$$

together with the boundary conditions

$$\mathbf{u} \to \mathbf{u}^\infty \text{ as } |\mathbf{x}| \to \infty,$$

and

$$\mathbf{u} = \mathbf{u}^r \text{ on } S,$$

where S is the surface of the fibre.

In slender-body theory the solution is found by matching an inner solution for radial distances much less than the fibre length to an outer solution value at radial distances much greater than the fibre radius, with the inner solution satisfying the no-slip boundary condition on the particle surface and the outer solution satisfying the condition at infinity.

Inner Solution

For the cylindrical fibre of length l and radius b we define Cartesian co-ordinates centred on the particle centre with 3-axis along the fibre axis so that the surface S is given by $x_1^2 + x_2^2 = b^2$ for $-\frac{l}{2} \leq x_3 \leq \frac{l}{2}$.

To simplify the calculation we can subtract the external flow by replacing $\mathbf{u}$ with $\mathbf{u}^* = \mathbf{u} - \mathbf{u}^\infty$ so that the boundary conditions on $\mathbf{u}^*$ are

$$\mathbf{u}^* \to 0 \text{ as } |\mathbf{x}| \to \infty$$

and

$$\mathbf{u}^* = \mathbf{U}^* = \mathbf{u}^r - \mathbf{u}^\infty \text{ on } S.$$

For the inner solution we define inner variables in cylindrical polar co-ordinates (ρ, θ, z)

by scaling x_1 and x_2 with the radius b and x_3 with respect to the fibre half length length $\frac{l}{2}$ so that

$$x_1 = b\rho\cos\theta,$$

$$x_2 = b\rho\sin\theta,$$

$$x_3 = \frac{l}{2}z.$$

Substituting into the Stokes equations we have at leading order in a_r^{-1}

$$\begin{aligned} \mu\tilde{\nabla}^2\mathbf{u}^* - \tilde{\nabla}p &= 0, \\ \tilde{\nabla}\cdot\mathbf{u}^* &= 0, \end{aligned} \tag{1.2.7}$$

where $\tilde{\nabla}$ and $\tilde{\nabla}^2$ are respectively the two-dimensional del and Laplace operators in the (ρ,θ) plane together with the leading order boundary condition

$$\mathbf{u}^* = \mathbf{U}^*(z) \text{ on } \rho = 1,$$

where

$$\mathbf{U}^*(z) = \mathbf{U} - \mathbf{U}_0 + l((\boldsymbol{\omega} - \frac{1}{2}\boldsymbol{\omega}^\infty)\times(0,0,z)) - l\mathbf{E}\cdot(0,0,z),$$

so that

$$\left.\begin{aligned} u_\rho^* &= U_1^*\cos\theta + U_2^*\sin\theta, \\ u_\theta^* &= U_2^*\cos\theta - U_1^*\sin\theta, \\ u_z^* &= U_3^* \end{aligned}\right\} \text{ on } \rho = 1.$$

Solving Stokes equations (1.2.7) subject to the new boundary conditions gives

$$\begin{aligned} u_\rho^* &= A(\frac{1}{\rho^2} - 1 + 2\log\rho)\cos\theta + U_1^*\cos\theta + B(\frac{1}{\rho^2} - 1 + 2\log\rho)\sin\theta + U_2^*\sin\theta, \\ u_\theta^* &= A(\frac{1}{\rho^2} - 1 - 2\log\rho)\sin\theta - U_1^*\sin\theta + B(-\frac{1}{\rho^2} + 1 + 2\log\rho)\cos\theta + U_2^*\cos\theta, \\ u_z^* &= C\log\rho + U_3^*. \end{aligned} \tag{1.2.8}$$

Taking the outer limit of the inner solution we obtain

$$\begin{aligned} u_\rho^* &\to (2A\log\rho + U_1^*)\cos\theta + (2B\log\rho + U_2^*)\sin\theta, \\ u_\theta^* &\to -(2A\log\rho + U_1^*)\sin\theta + (2B\log\rho + U_2^*)\cos\theta, \\ u_z^* &\to C\log\rho + U_3^*, \end{aligned} \tag{1.2.9}$$

as $\rho \to \infty$.

Outer Solution

Since $|\mathbf{u}^*| \to 0$ as $|\mathbf{x}| \to \infty$ the flow outside the fibre can be written using the boundary integral formulation given in equation (1.2.4). At leading order in $\frac{1}{a_r}$, in the outer approximation we can replace the surface integral by a line integral along the axis of the cylinder so that

$$u_i^* = \frac{1}{8\pi\mu}\int_{-\frac{l}{2}}^{\frac{l}{2}} \frac{\delta_{ij} f_j(x_3')}{|\mathbf{x}-\mathbf{x}'|} dx_3' + \frac{1}{8\pi\mu}\int_{-\frac{l}{2}}^{\frac{l}{2}} \frac{(x_i - x_i')f_j(x_3')(x_j - x_j')}{|\mathbf{x}-\mathbf{x}'|^3} dx_3', \tag{1.2.10}$$

where $|\mathbf{x}-\mathbf{x}'| = \sqrt{(x_3 - x_3')^2 + r^2}$ and $r^2 = x_1^2 + x_2^2$.

To find the limiting behaviour as $r \to 0$ we write the first integral in the form

$$I_1 = f_i(x_3)\int_{-1}^{1} \frac{1}{\sqrt{(x_3 - x_3')^2 + r^2}} dx_3' + \int_{-1}^{1} \frac{f_i(x_3') - f_i(x_3)}{\sqrt{(x_3 - x_3')^2 + r^2}} dx_3',$$

where all variables are scaled with respect to the half length of the fibre $\frac{l}{2}$. In this limit as $r \to 0$ the second integral only contributes to u_3^* and is written in the form

$$I_2 = f_3(x_3)\int_{-1}^{1} \frac{(x_3 - x_3')^2}{(\sqrt{(x_3 - x_3')^2 + r^2})^3} dx_3' + \int_{-1}^{1} \frac{(x_3 - x_3')^2 (f_3(x_3') - f_3(x_3))}{(\sqrt{(x_3 - x_3')^2 + r^2})^3} dx_3'.$$

The first integrals in I_1 and I_2 are singular at $x_3 = x_3'$ as $r \to 0$ however, the second integrals are non-singular, provided $f(x_3)$ is a continuously differentiable function and $f'(x_3)$ is bounded since we can expand $f(x_3)$ in a Taylor expansion about x_3', such that

$$f(x_3) = f(x_3') + (x_3 - x_3')f'(x_3') + ...$$

This means that the second integrals in I_1 and I_2 provide only $O(1)$ contribution to the solution. Therefore the expressions for both I_1 and I_2 are dominated by the first integrals as $r \to 0$ [22].

The first integral in I_1 is given by

$$I_1 = 2f_i(\log(\frac{1}{r}) + \log 2 + \log\sqrt{1 - z^2}) = 2f_i \log\frac{2}{r} + O(1))$$

as $r \to 0$. The first integral in I_2 is given by

$$I_2 = 2f_3(\log(\frac{1}{r}) + \log 2 + \log\sqrt{1 - z^2} - 1) + O(a_r^{-2}) = 2f_3 \log\frac{2}{r} + O(1)$$

as $r \to 0$. Therefore from equation (1.2.10) we can write the inner limit of the outer solution as

$$u_i^* \to \frac{1}{4\pi\mu} \log\frac{2}{r}(f_i(x_3) + \delta_{i3} f_3(x_3))$$

as $r \to 0$.

To compare with the inner solution we change to the inner scaling so that $r = a_r^{-1}\rho$ and we write in polar co-ordinates so that $\mathbf{u}^*$ is given by

$$\begin{aligned} u_\rho^* &\rightarrow \frac{1}{4\pi\mu}\log\frac{2a_r}{\rho}(f_1\cos\theta + f_2\sin\theta) \\ u_\theta^* &\rightarrow \frac{1}{4\pi\mu}\log\frac{2a_r}{\rho}(f_2\cos\theta - f_1\sin\theta) \\ u_z^* &\rightarrow \frac{1}{2\pi\mu}\log\frac{2a_r}{\rho}f_3 \end{aligned} \tag{1.2.11}$$

as $\rho \rightarrow 0$.

Matching

We can now obtain the values of the unknown constants by matching similar terms in the inner and outer solutions. Matching the $\log(\rho)\cos\theta$ term in u_ρ^* gives

$$2A = -\frac{1}{4\pi\mu}f_1,$$

matching the $\cos\theta$ term gives

$$U_1^* = \frac{1}{4\pi\mu}f_1\log 2a_r.$$

Matching the $\log(\rho)\sin\theta$ term in u_θ^* gives

$$2B = -\frac{1}{4\pi\mu}f_2,$$

matching the $\sin\theta$ term gives

$$U_2^* = \frac{1}{4\pi\mu}f_2\log 2a_r.$$

Finally matching the $\log(\rho)$ term in u_z^* gives

$$C = -\frac{1}{2\pi\mu} f_3,$$

and matching the $O(1)$ term gives

$$U_3^* = \frac{1}{2\pi\mu} f_3 \log 2a_r.$$

Substituting in the value of $\mathbf{U}^*$ we can then write the force density along a slender body as

$$\mathbf{f} = \frac{2\pi\mu}{\log 2a_r}(2\mathbf{I} - \mathbf{pp}) \cdot (\mathbf{u}^r - \mathbf{u}^\infty),$$

where $\mathbf{p}$ is a unit vector indicating the orientation of the fibre.

1.2.6 Grand Resistance Matrix for a Slender Body

We can now use this result to find leading order contributions to the grand resistance matrix for a fibre of aspect ratio $a_r \gg 1$ by substituting $\mathbf{u}^r = \mathbf{U} + \boldsymbol{\omega} \times (\mathbf{x} - \mathbf{x}_c)$ and $\mathbf{u}^\infty = \mathbf{U}_0 + \mathbf{K} \cdot \mathbf{x}_c + \frac{1}{2}\boldsymbol{\omega}^\infty \times (\mathbf{x} - \mathbf{x}_c) + \mathbf{E} \cdot (\mathbf{x} - \mathbf{x}_c)$, giving a force distribution

$$\mathbf{f} = \frac{2\pi\mu}{\log 2a_r}(2\mathbf{I} - \mathbf{pp}) \cdot (\mathbf{U}_0 + \mathbf{K} \cdot \mathbf{x}_c - \mathbf{U} + (\frac{1}{2}\boldsymbol{\omega}^\infty - \boldsymbol{\omega}) \times (\mathbf{x} - \mathbf{x}_c) + \mathbf{E} \cdot (\mathbf{x} - \mathbf{x}_c)).$$

The total force $\mathbf{F}$ acting on a fibre of length l is given by

$$\mathbf{F} = \int_{-\frac{l}{2}}^{\frac{l}{2}} \mathbf{f} ds = \frac{2\pi\mu l}{\log 2a_r}(2\mathbf{I} - \mathbf{pp}) \cdot (\mathbf{U}_0 + \mathbf{K} \cdot \mathbf{x}_c - \mathbf{U}).$$

Thus the leading order approximation to the sub-matrix $\mathbf{A}$ in the grand resistance matrix

is given by

$$A_{ij} = \frac{2\pi\mu l}{\log 2a_r}(2\delta_{ij} - p_i p_j) = \xi_f(2\delta_{ij} - p_i p_j),$$

where

$$\xi_f = \frac{2\pi\mu l}{\log 2a_r}$$

is the resistance co-efficient for force. It should be noted that resistance to perpendicular motion is twice that of motion tangential to the fibre axis. The matrices $\tilde{B_{ij}}$ and $\tilde{G_{ijk}}$ are both zero as the symmetry of the particle means there is no coupling between rotation, strain-rate and force.

The total torque $\mathbf{T}$ acting on the fibre is given by

$$\mathbf{T} = \int_{-\frac{l}{2}}^{\frac{l}{2}} (\mathbf{x} - \mathbf{x}_c) \times \mathbf{f} ds = \frac{\pi\mu l^3}{3\log 2a_r}(\mathbf{I} - \mathbf{pp}) \cdot (\frac{1}{2}\boldsymbol{\omega}^\infty - \boldsymbol{\omega}) + \frac{\pi\mu l^3}{3\log 2a_r}\mathbf{p} \times \mathbf{E} \cdot \mathbf{p}.$$

The sub-matrix C_{ij} is therefore given by

$$C_{ij} = \frac{\pi\mu l^3}{3\log 2a_r}(\delta_{ij} - p_i p_j) = \xi_t(\delta_{ij} - p_i p_j),$$

and sub matrix $\tilde{H}_{ijk}$ by

$$\tilde{H}_{ijk} = \frac{\pi\mu l^3}{3\log 2a_r}\epsilon_{ilj} p_l p_k = \xi_t \epsilon_{ilj} p_l p_k,$$

where

$$\xi_t = \frac{\pi\mu l^3}{3\log 2a_r}$$

is the resistance co-efficient for torque. As expected matrix B_{ij} is zero.

The total stresslet $\mathbf{S}$ exerted by the fibre on the flow is given by

$$\mathbf{S} = \frac{1}{2}\int_{-\frac{l}{2}}^{\frac{l}{2}} ((\mathbf{x}-\mathbf{x}_c)\mathbf{f} + \mathbf{f}(\mathbf{x}-\mathbf{x}_c))\, ds = \frac{\pi\mu l^3}{6\log 2a_r}(\mathbf{p}(\frac{1}{2}\boldsymbol{\omega}^\infty - \boldsymbol{\omega})\times\mathbf{p} + (\frac{1}{2}\boldsymbol{\omega}^\infty - \boldsymbol{\omega})\times\mathbf{pp})$$

$$+\frac{\pi\mu l^3}{6\log 2a_r}(\mathbf{pE}\cdot\mathbf{p} + \mathbf{E}\cdot\mathbf{pp} - \mathbf{p}\cdot\mathbf{E}\cdot\mathbf{ppp}).$$

Matrix H_{ijk} is therefore given by

$$H_{ijk} = \frac{\pi\mu l^3}{6\log 2a_r}(p_i\epsilon_{jkl}p_l + \epsilon_{ikl}p_lp_j) = \xi_s(p_i\epsilon_{jkl}p_l + \epsilon_{ikl}p_lp_j)$$

and matrix M_{ijkl} by

$$M_{ijkl} = \frac{\pi\mu l^3}{12\log 2a_r}(p_i\delta_{jl}p_k + p_j\delta_{il}p_k + p_i\delta_{jk}p_l + p_j\delta_{ik}p_l - 2p_ip_jp_kp_l)$$

$$= \frac{\xi_s}{2}(p_i\delta_{jl}p_k + p_j\delta_{il}p_k + p_i\delta_{jk}p_l + p_j\delta_{ik}p_l - 2p_ip_jp_kp_l)$$

where

$$\xi_s = \frac{\pi\mu l^3}{6\log 2a_r} \tag{1.2.12}$$

is the resistance co-efficient for stress. Matrix G_{ijk} is zero as expected.

1.2.7 Stress Contribution of a Rigid Fibre

Here we consider the stress contribution of a rigid fibre in shear flow. For a rigid fibre of length l and velocity $\mathbf{U}+\boldsymbol{\omega}\times(\mathbf{x}-\mathbf{x}_c)$ in a linear flow described by
$\mathbf{u}^\infty = \mathbf{U}_0 + \mathbf{K}\cdot\mathbf{x}_c + \frac{1}{2}\boldsymbol{\omega}^\infty\times(\mathbf{x}-\mathbf{x}_c) + \mathbf{E}\cdot(\mathbf{x}-\mathbf{x}_c)$ the stress contribution is given by

$$S_{ij} = H_{ijk}(\frac{1}{2}\omega_k^\infty - \omega_k) + M_{ijkl}E_{kl} \tag{1.2.13}$$

where $\mathbf{H}$ and $\mathbf{M}$ are entries in the grand resistance matrix for a slender body calculated in subsection 1.2.6. Substituting in these values and the rotation rate $\boldsymbol{\omega}\times\mathbf{p} = \mathbf{K}\cdot\mathbf{p}-\mathbf{p}\cdot\mathbf{K}\cdot\mathbf{pp}$ [20] for a rigid, torque free fibre we obtain the stress contribution

$$\mathbf{S} = \xi_s \mathbf{p}\cdot\mathbf{E}\cdot\mathbf{ppp}$$

where ξ_s is the resistance co-efficient for stress given in equation 1.2.12. Non-dimensionalising with respect to the resistance co-efficient ξ_s and shear rate $\dot{\gamma}$ we get

$$\mathbf{S} = \mathbf{p}\cdot\mathbf{E}\cdot\mathbf{ppp}. \tag{1.2.14}$$

Let us now consider the fibre rotating in the the $x-y$ plane in a shear flow such that the non-dimensional strain rate tensor is given by

$$\mathbf{E} = \begin{pmatrix} 0 & \frac{1}{2} & 0 \\ \frac{1}{2} & 0 & 0 \\ 0 & 0 & 0 \end{pmatrix}$$

and the orientation vector is given by

$$\mathbf{p} = \begin{pmatrix} \cos\theta \\ \sin\theta \\ 0 \end{pmatrix}$$

where θ is the angle with the x axis.

Substituting these into equation (1.2.14) gives a shear stress contribution of

$$\sigma_{xy} = \cos^2\theta\sin^2\theta = \frac{1}{4}\sin^2 2\theta,$$

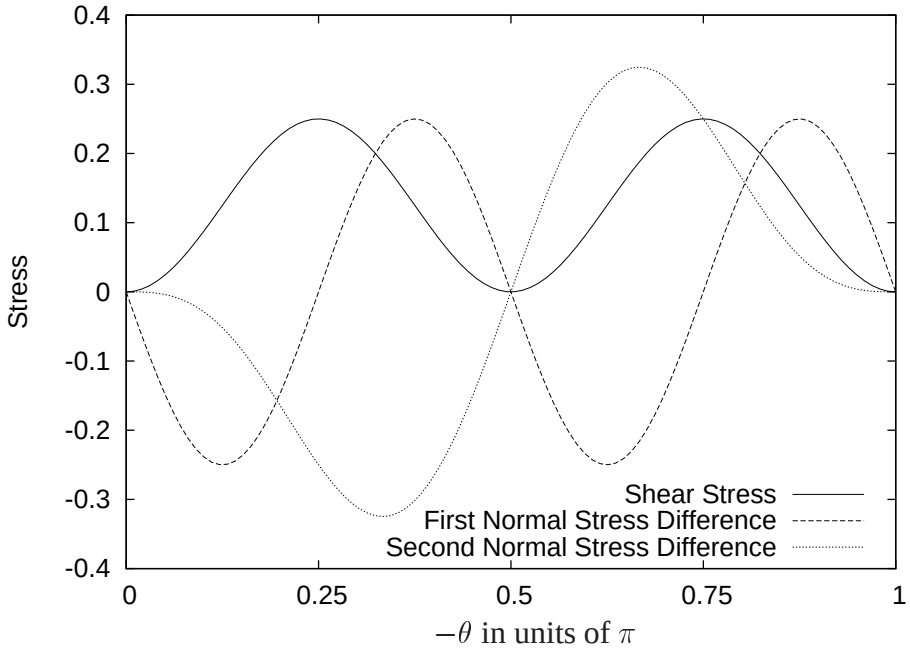

Figure 1.5: Stress vs $-\theta$ for a rigid fibre rotating in the $x-y$ plane.

a first normal stress difference of

$$N_1 = \sigma_{xx} - \sigma_{yy} = \cos^3\theta \sin\theta - \sin^3\theta \cos\theta = \frac{1}{4}\sin 4\theta$$

and a second normal stress difference of

$$N_2 = \sigma_{yy} - \sigma_{zz} = \sin^3\theta \cos\theta.$$

Figure 1.5 shows σ_{xy}, N_1 and N_2 against $-\theta$ for half an orbit.

The shear stress is zero when the fibre is aligned with either the x or the y axis as the compressional and extensional forces are negligible at these orientations for a high aspect ratio fibre. Maximum shear stress occurs at an angle of $\theta = -\frac{\pi}{4}$ or $\theta = -\frac{3\pi}{4}$ with the x axis when the fibre is under maximum compressive or extensional force respectively. First normal stress difference is zero when the fibre is aligned with either the x or y axis, or

when the the fibre is at an angle of $-\frac{\pi}{4}$ or $-\frac{3\pi}{4}$ with the x axis. The latter cases occur as the compressive and extensive forces cancel each other out. N_1 has maximums at $\theta = -\frac{3\pi}{8}$ and $\theta = -\frac{7\pi}{8}$ and minimums at $\theta = -\frac{\pi}{8}$ and $\theta = -\frac{5\pi}{8}$.

Integrating σ_{xy}, N_1 and N_2 over a complete orbit gives a contribution of $\frac{\pi}{4}$ to the shear stress and zero contributions to the first and second normal stress difference.

1.3 Elasticity Theory

1.3.1 Bending Stiffness

The results in section 1.2.3 are valid for a rigid particle. However, long slender particles are prone to bending due to hydrodynamic forces. To quantify the degree of bending we must first derive the stiffness of a fibre in terms of its material properties. To define the bending stiffness we consider an intrinsically straight fibre made of an isotropic, homogenous material, bent into a circular arc as shown in figure 1.6. In any section of this arc the material on the inside of the arc will compress while the material on the outside of the arc will be stretched.

We consider a thin strip of the arc at a distance y from the centre line. Provided the angle of bending is small, the strain in that section, $\frac{\Delta L}{L}$, is equal to $\frac{y}{R}$, where R is the radius of curvature.

In a linear elastic material the extensional stress σ is related to the extensional strain ϵ by $\sigma = E\epsilon$ where E is the Young's modulus. Therefore the extensional stress acting on a section of arc is given by

$$\sigma(y) = E\frac{y}{R}.$$

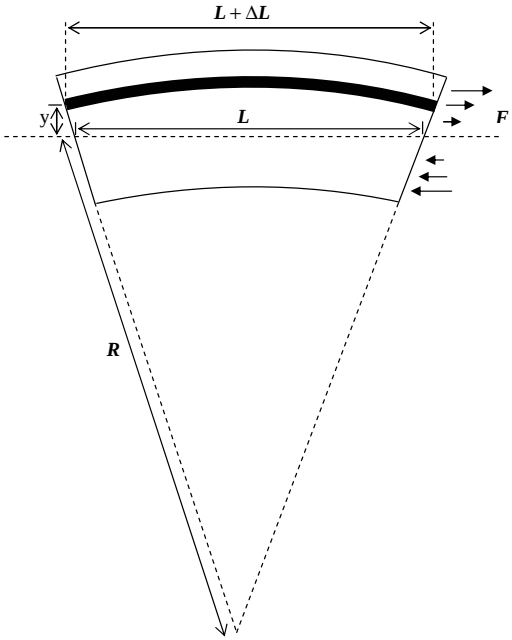

Figure 1.6: Fibre bent into circular arc with radius of curvature R. The section of the fibre highlighted is at a distance y from the centre line and has extension ΔL. Picture taken from Howard [18].

Integrating over the surface area of the cross section we obtain the total torque acting on the fibre

$$T = \int \sigma y dA = \int E \frac{y^2}{R} dA$$

so that

$$T = \frac{EI}{R} \tag{1.3.15}$$

where $I = \int y^2 dA$ is the second moment of inertia of the cross section. This equation is known as the beam equation and the constant of proportionality, EI, is known as flexural or bending rigidity.

For a fibre of circular cross-section, $\int y^2 dA = \frac{1}{2} \int r^2 dA$, where r is distance in a radial direction, so that $I = \frac{\pi b^4}{4}$ for a fibre of radius b.

Although the beam equation was derived for a circular arc it can be generalised to any deformation by replacing the arc radius by the radius of curvature so that $\frac{1}{R} = \frac{d\theta}{ds}$ where θ is the tangent angle measured in an anti-clockwise direction from the x axis and the tangent of the fibre. Non-dimensionalising arc length with respect to the length of the fibre l, so that $s = s^* l$ gives

$$T = \frac{EI}{l} \frac{d\theta}{ds^*} = k^{(B)} \frac{d\theta}{ds^*}$$

where $k^{(B)} = \frac{EI}{l}$ is the bending stiffness.

1.3.2 Twisting Stiffness

The material property that determines bending stiffness is the Young's modulus, however, the property determining twisting stiffness is shear modulus. The shear modulus is related

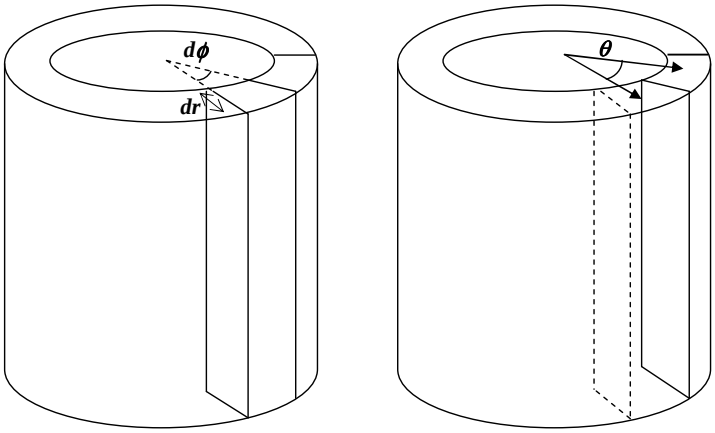

Figure 1.7: A section of cylinder of radial width dr and angle $d\phi$ twisted through an angle of θ.

to Young's modulus via the Poisson ratio by

$$G = \frac{E}{2(1+\nu)}.$$

The Poisson ratio is the ratio of sideways contraction to lengthwise strain for a material of length L and width w is given by

$$\nu = \frac{\Delta w}{w} / \frac{\Delta L}{L}$$

and is equal to $\frac{1}{2}$ for an incompressible material. Most materials have a Poisson ratio in the range 0.2-0.5 [18].

We now consider a small section of a cylindrical fibre of length l and radius b that is subject to a twist through an angle of θ as shown in figure 1.7. The shear stress acting on this section is given by the shear modulus G multiplied by the shear strain γ, so that

$$\sigma = G\gamma.$$

The shear strain γ is given by

$$\gamma = \frac{r\theta}{l}$$

where θ is the angle of twist.

The force acting on a section of the fibre is therefore given by

$$\Delta F = G\frac{r\theta}{l} r dr d\phi$$

and the torque acting about the fibre axis is given by

$$T = \int G\frac{r^2\theta}{l} r dr d\phi.$$

Integrating over the cross section of a fibre with radius b we obtain an expression for the total torque acting on the fibre as

$$T = \frac{\pi b^4}{2}\frac{G\theta}{l}$$

or

$$T = \frac{2GI\theta}{l}.$$

Again we can write the twisting torque as

$$T = k^{(T)}\theta$$

where $k^{(T)} = \frac{2GI}{l}$ is the twisting stiffness and θ is the angle of twist.

1.3.3 Scale Analysis

From section 1.3.1 the bending torque on a fibre of length l is given by

$$T = k^{(B)} \frac{d\theta}{ds^*}$$

where bending stiffness $k^{(B)} = \frac{EI}{l}$. To assess the degree to which a fibre will bend due to hydrodynamic torques we define a non-dimensional bending stiffness with respect to the shear rate $\dot{\gamma}$ and the rotational resistance co-efficient of the fluid $\xi_t = \frac{\pi\mu l^3}{3\log 2a_r}$ as

$$k^{*(B)} = \frac{EI}{\dot{\gamma} l \xi_t} = \frac{3\log 2a_r}{\dot{\gamma}\pi\mu l^4} EI = \frac{3E}{64\mu\dot{\gamma}} \left[\frac{\log 2a_r}{a_r^4}\right].$$

The effective stiffness of a material is affected by its material properties (ie. its Young's modulus), its shape, and the viscosity and shear rate of the surrounding fluid. In particular we note that since $I = \frac{\pi b^4}{4}$ the effective stiffness scales with the inverse 4th power of the aspect ratio. We now consider the effective stiffness of some industrial and biological fibres from their Young's modulus, length and radius, and shear rate and viscosity of the surrounding fluid.

In the experiments of Trevelyan and Mason [40], rigid glass fibres are observed in high viscosity corn syrup. The fibres have aspect ratios of $20 - 120$, the shear rate of the fluid is between 0.2 and $1.4s^{-1}$ and the viscosity of the corn syrup is 9.12 Pa.s [11]. The Young's modulus of glass is $73\ GPa$ [18]. These values give us a bending stiffness of between 3.08 and 18784.43. As a rough guide we shall therefore classify rigid fibres as those with bending stiffness of order unity or higher.

In the experiments of Forgacs and Mason [10], dacron and rayon fibres are used. The table below (1.3.3), lists the data for some of the fibres used and whether the fibre behaved as a rigid or semi-flexible fibre. The final column gives the non-dimensional bending and twisting stiffness calculated using the definition given in this section. As we can see, in

Material	a_r	$\mu\dot{\gamma}$ ($kgm^{-1}s^{-2}$)	*E (GPa)*	Turn	$k^{*(B)}$
Rayon	43	31.9	26.4	Rigid	22
	100	24.9		Rigid	1.14
	173	33.8		Rigid	0.104
	241	31.1		Semi-flexible	3.16×10^{-02}
	357	30.8		Semi-flexible	7.06×10^{-03}
Dacron	102	54.1	7.26	Rigid	0.134
	139	54.2		Rigid	4.11×10^{-02}
	180	46.9		Rigid	1.77×10^{-02}
	228	54.4		Semi-flexible	6.16×10^{-03}
	310	45.5		Semi-flexible	2.31×10^{-03}
	414	44.0		Semi-flexible	7.68×10^{-04}
	228	4.47		Rigid	7.49×10^{-02}
	310	5.43		Rigid	1.89×10^{-02}
	414	5.43		Semi-flexible	6.23×10^{-03}

Table 1.1: Table showing the values of aspect ratio a_r, viscosity and shear rate product $\mu\dot{\gamma}$, Young's modulus, E and bending stiffness, $k^{*(B)}$, for the rigid and semi-flexible fibres used in the experiments of Forgacs and Mason [10]. The fibres used were 3.5μm diameter Rayon fibres and 7.8μm diameter Dacron fibres.

general fibres that behave as semi-flexible fibres have bending stiffness values of the order of 10^{-3} to 10^{-4}.

Carbon nanotubes have a very high Young's modulus of 1000 GPa [18], however, a single walled carbon nanotube has a typical diameter of $1.2 - 1.4nm$ and can be up to $2mm$ in length. Under the conditions used in the experiments of Forgacs and Mason [10] ($\mu = 9.12Pa.s$ and $\dot{\gamma} = 5.5s^{-1}$) carbon nanotubes would have a bending stiffness as low as 7.9×10^{-16} which is far more flexible than the fibres listed above. A carbon nanotube of $1\mu m$ in length has a bending stiffness of order 10^{-3} which is in the range of semi-flexible fibres.

Actin filaments have a Young's modulus of 2.3 GPa, a diameter of approximately $6nm$ and lengths of up to several tens of microns [18]. Thus actin fibres in water, which has a viscosity of $0.001Pa.s$ [20], at shear rates as low as $0.01 - 0.1s^{-1}$ have a bending stiffness

in the 10^{-3} to 10^{-4} range of the semi-flexible fibres in the experiments of Forgacs and Mason [10]. Shorter filaments would be semi-flexible at higher shear rates.

For all of the industrial fibres listed above the Reynolds number is of order 10^{-2} or smaller and the Peclet number is of order 10^{9} or greater therefore easily satisfying the low Reynolds number, high Peclet number criteria discussed in section 1.2.1. For actin in an aqueous suspension at a shear rate of $0.01s^{-1}$ the Reynolds number is of order 10^{-6} and the Peclet number is of order 10^{7} and therefore also satisfies our criteria. At higher shear rates the Peclet and Reynolds number would increase but the Reynolds number still remains very small for all reasonable shear-rates.

The twisting torque on a fibre of length l is given by

$$T^{(T)} = k^{(T)}\theta$$

where twisting stiffness $k^{(T)} = \frac{2GI}{l}$. To assess the degree to which a fibre will twist due to the hydrodynamic torque we define a non-dimensional twisting stiffness with respect to the shear rate $\dot{\gamma}$ and the resistance co-efficient of the fluid for axial rotation of a cylinder $\xi_a = 4\pi\mu b^2 l$ as

$$k^{*(T)} = \frac{2GI}{\dot{\gamma} l \xi_a} = \frac{GI}{2\dot{\gamma}\pi\mu l^2 b^2} = \frac{G}{32\mu\dot{\gamma}}\left[\frac{1}{a_r^2}\right].$$

The scaling analysis shows that for a high aspect ratio semi-flexible fibre with $k^{*(B)}$ of order unity $k^{*(T)}$ will be large so that twisting will be negligible. It might be assumed therefore that twist can be ignored in modelling such fibres. However, bending and twisting are coupled through a process called writhe, because it is possible to produce an effective net twist by a series of bends alone.

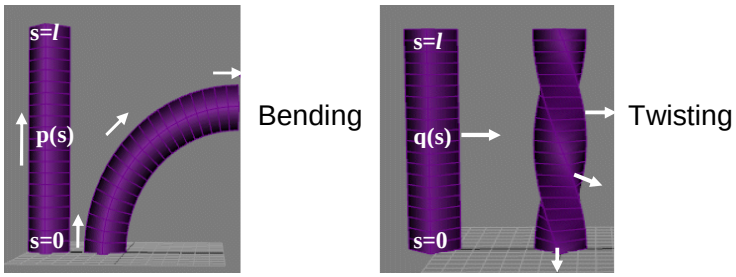

Figure 1.8: Illustration of bending (left) and twisting (right). Picture taken from [26].

1.3.4 Bending, Twisting and Writhe

In order to define bending and twisting for a general fibre configuration let us consider a point at a distance s along a fibre. We denote the tangent vector at this point as $\mathbf{p}(s)$ and a vector normal to the fibre as $\mathbf{q}(s)$. We define bending as rotation of the tangent vector $\mathbf{p}$ and twisting as rotation of a normal vector $\mathbf{q}$ about the tangent vector $\mathbf{p}$ as shown in figure 1.8 (left) and figure 1.8 (right) respectively.

To illustrate writhe, consider the slender fibre shown in figure 1.9 taken from Maggs [24]. The fibre is bent through an angle of $\frac{\pi}{2}$ in 3 places and the normal vector $\mathbf{q}$ is parallel transported at each bend so that there is no twist at each joint. The fibre is bent such that there is no net change in the direction of the tangent vector between the two ends of the fibre. The normal vector has, however, rotated by $\frac{\pi}{2}$ about the tangent vector despite the fibre being bent but not twisted. This fibre has a non-zero writhe which is by convention measured in units of 2π. In this case the fibre has writhe of $\frac{1}{4}$.

The rotation about the tangent vector can be explained if we consider the tangent vector $\mathbf{p}$ to exist on a unit sphere as shown in figure 1.10. The normal vector $\mathbf{q}$ always remains tangential to the sphere.

The tangent vector $\mathbf{p}_1$ shown in figure 1.9 lies along the line joining the centre of the

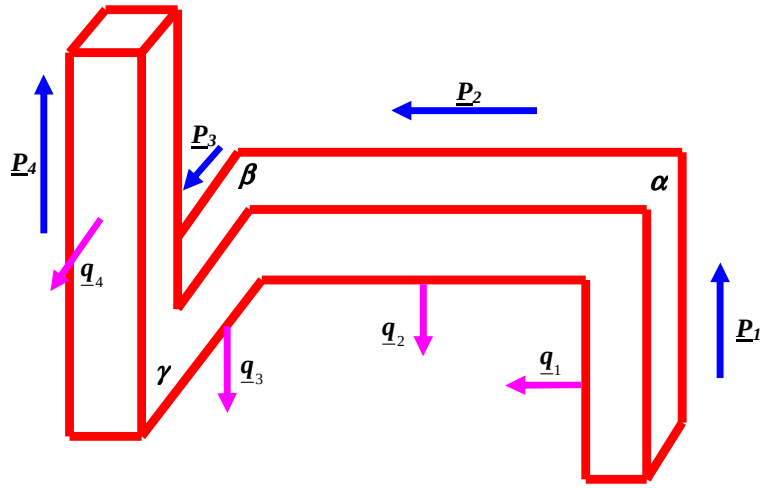

Figure 1.9: Diagram of a fibre bent in three places, each by an angle of $\frac{\pi}{2}$, so that there is no net change in the tangent vector between the two ends of the fibre. The normal vector is parallel transported at each bend so that there is no net twist at each joint. There is however a net change of $\frac{\pi}{2}$ in the normal vector between the two ends of the fibre. Diagram taken from Maggs [24].

sphere and the point p_1 shown in figure 1.10, similarly vectors $\mathbf{p}_2$,..,$\mathbf{p}_4$ in figure 1.9 lie along the lines joining the centre of the sphere and the points p_2,..,p_4 respectively in figure 1.10. The arcs α, β, γ in figure 1.10 represent the bends α, β, γ in figure 1.9 and the vectors $\mathbf{q}_1$, .., $\mathbf{q}_4$ in figure 1.10 represent the corresponding normal vectors in figure 1.9.

The vector $\mathbf{q}$ is parallel transported in a loop on the sphere from position 1, through positions 2 and 3 to position 4. The rotation of $\mathbf{q}$ about the tangent vector $\mathbf{p}$ in figure 1.9 is a manifestation of the curvature of the sphere on which $\mathbf{p}$ lies.

The total rotation of a fibre about its axis is given by the sum of the rotation due to twisting and the rotation due to writhe. This is known as White's Theorem [24].

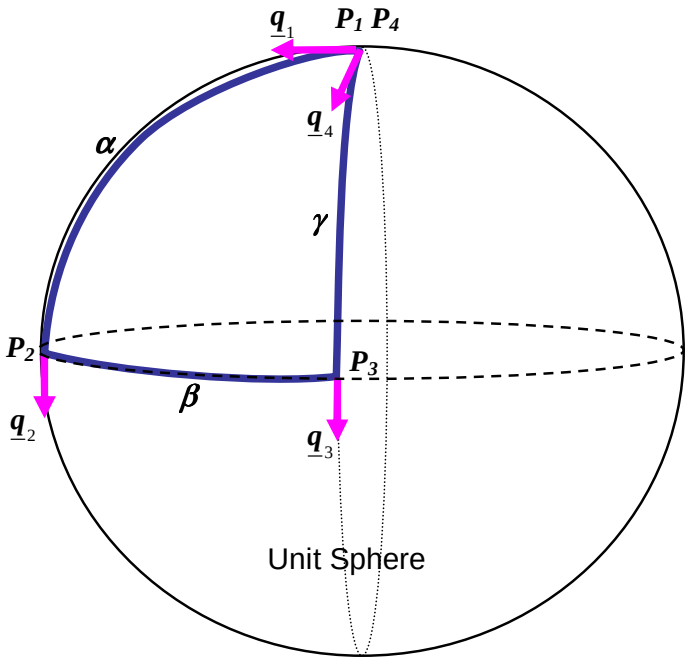

Figure 1.10: Illustration of writhe by showing the tangent vector on a unit sphere. The tangent vectors corresponding to figure 1.9 join the centre of the sphere to points p_1 to p_4, the arcs correspond to the bends in the fibre and the vectors $\mathbf{q}_1$ to $\mathbf{q}_4$ show the normal vectors.

1.4 Fibre Dynamics

We shall divide the dynamics of fibres into three categories, motion of rigid fibres, motion of semi-flexible and flexible fibres, and active propulsion of fibres.

1.4.1 Rigid Fibres

The motion of prolate spheroids in shear flow of a viscous fluid was first considered theoretically in 1922 by Jeffery [19]. He showed that such particles rotate in closed periodic orbits, which are now known as Jeffery orbits. Later Bretherton [4] showed by way of the "mirror-symmetry time reversal theorem" that any axisymmetric body in shear flow will rotate in a closed periodic orbit provided that the aspect ratio in Jeffery's equations is replaced by an equivalent aspect ratio a_{r_e} based on the whole body shape. Trevelyan and Mason [40] performed experiments on cylindrical fibres in shear flow and found good agreement with the orbits predicted by Jeffery when effective aspect ratio a_{r_e} was calculated using orbit period. Effective aspect ratio $a_{r_e}$was found to be significantly less that the actual aspect ratio in agreement with the theoretical analysis by Burgers [5] which showed that the disturbance caused by a cylinder of aspect ratio a_r was equal to an ellipsoid of aspect ratio $0.74a_r$.

The orientation of a fibre can be described by two angles, θ the angle with the z axis and ϕ the angle between the y-axis and the $x-y$ projection as shown in figure 1.11. In these co-ordinates, Jeffery orbits are described by

$$\tan\theta = \frac{Ca_r}{\sqrt{a_r^2\cos^2\phi + \sin^2\phi}}, \tag{1.4.16}$$

$$\tan\phi = a_r\tan(2\pi\frac{t}{T}), \tag{1.4.17}$$

where a_r is the aspect ratio [20]. The constant C is called the orbit constant and is

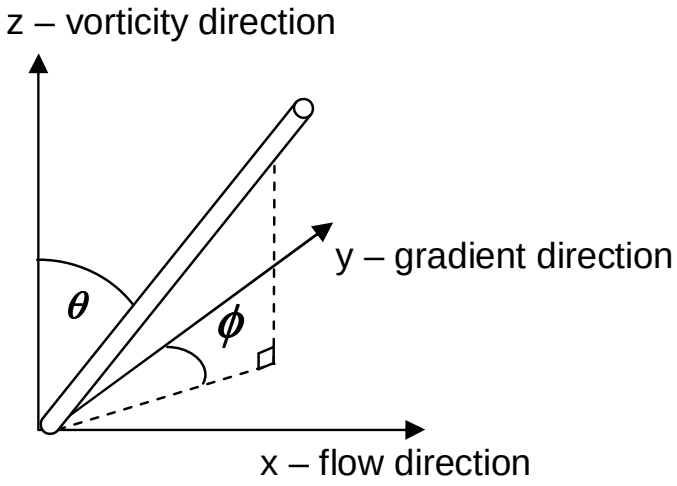

Figure 1.11: Fibre orientation described in spherical polar co-ordinates. Angle θ is the angle between with the vorticity axis z and angle ϕ is the angle between the $x - y$ projection of the fibre and the gradient direction y.

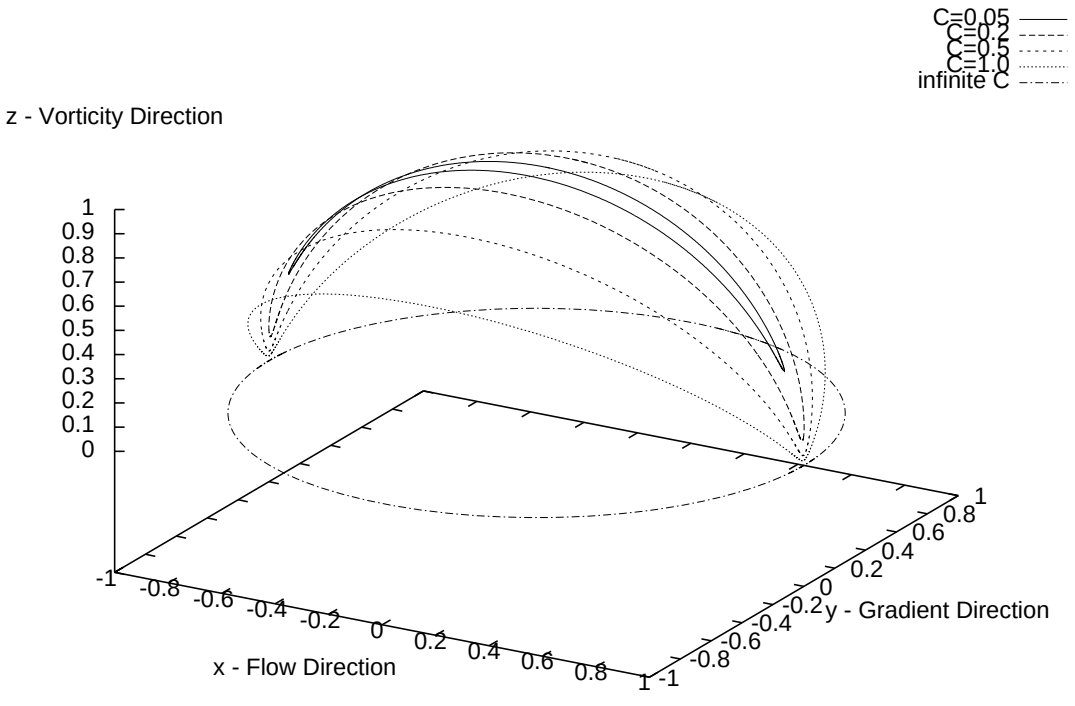

Figure 1.12: Plots of Jeffery orbits for a fibre with orbit constants of $C = 0.05$,$C = 0.2$, $C = 0.5$, $C = 1.0$ and $C = \infty$.

determined by the initial orientation of the fibre,

$$C = \tan\theta_0 \sqrt{\cos^2\phi_0 + \frac{1}{a_r^2}\sin^2\phi_0}. \tag{1.4.18}$$

A fibre placed in the $x-y$ plane will have an infinite orbit constant and will rotate solely in the $x-y$ plane. High aspect ratio fibres with large orbit constants remain close to the $x-y$ plane and flip quickly in the $x-y$ plane in a time of order $\frac{1}{\dot{\gamma}}$ but spend a time of order $\frac{1}{\dot{\gamma}}a_r$ passing through the $x-z$ plane. A fibre placed along the z axis will have an orbit constant of zero and will spin about the z axis. Fibres with small orbit constants so that they are close to the z axis appear to wobble about the axis.

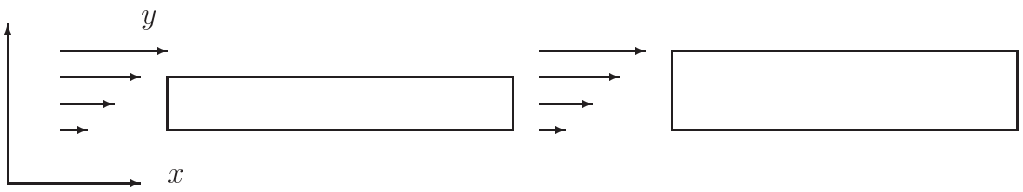

Figure 1.13: The fibre on the right has a smaller aspect ratio and therefore experiences a greater velocity difference across the end of the fibre.

The orbit period, T for any orbit constant C is the same and is equal to

$$T = \frac{2\pi}{\dot{\gamma}}(a_r + \frac{1}{a_r}) \tag{1.4.19}$$

where $\dot{\gamma}$ is the shear rate. Thus for large aspect ratios the period is proportional to the aspect ratio [20].

The shorter period of small aspect ratio fibres is due to the larger velocity difference across the ends of the fibre as it passes through the $x-z$ plane. This creates a larger couple acting on the fibre and hence leads to faster rotation (figure 1.13). A large aspect ratio particle spends almost all of its time in the $x-z$ plane.

Period of rotation

For a single fibre of finite aspect ratio, the rotation of the fibre is described by [20]

$$\dot{\mathbf{p}} = \mathbf{\Omega} \cdot \mathbf{p} + \frac{a_r^2 - 1}{a_r^2 + 1}(\mathbf{E} \cdot \mathbf{p} - \mathbf{p} \cdot \mathbf{E} \cdot \mathbf{pp})$$

where $\mathbf{p}$ is the tangent vector and dots denote derivatives with respect to time.

Written in component form this is

$$\dot{p_x} = \frac{\dot{\gamma}}{2}p_y + \frac{a_r^2 - 1}{a_r^2 + 1}(\frac{\dot{\gamma}}{2}p_y - \dot{\gamma}p_x^2 p_y),$$

$$\dot{p_y} = -\frac{\dot{\gamma}}{2}p_x + \frac{a_r^2 - 1}{a_r^2 + 1}(\frac{\dot{\gamma}}{2}p_x - \dot{\gamma}p_x p_y^2), \tag{1.4.20}$$

For a fibre rotating in the $x - y$ plane close to the flow direction so that $p_y \sim O(\frac{1}{a_r})$ we may rescale equation (1.4.20) such that

$$p_y = \epsilon P_y$$

and

$$p_x = \sqrt{1 - p_y^2} = \sqrt{1 - \epsilon P_y^2}$$

where $\epsilon = \frac{1}{a_r}$ and $P_y \sim O(1)$. As $\epsilon << 1$ we can use the following approximation for p_x

$$p_x = 1 - \frac{1}{2}\epsilon^2 P_y^2.$$

Equation (1.4.20) now becomes

$$\epsilon \dot{P_y} = \frac{\dot{\gamma}}{2}\left(-(1 - \frac{1}{2}\epsilon^2 P_y^2) + \frac{a_r^2 - 1}{a_r^2 + 1}(1 - \frac{1}{2}\epsilon^2 P_y^2)(1 - 2\epsilon^2 P_y^2)\right),$$

$$\epsilon \dot{P_y} = \frac{\dot{\gamma}}{a_r^2 + 1}\left(\frac{\epsilon^2 P_y^2}{2}(3 - 2a_r^2) - 1\right) + O(\epsilon^4).$$

Solving the differential equation we get

$$p_y = \epsilon P_y = -\frac{1}{\sqrt{a_r^2 - \frac{3}{2}}}\tan\left(\frac{\sqrt{a_r^2 - \frac{3}{2}}}{a_r^2 + 1}\dot{\gamma}t + C\right).$$

Applying the initial condition $P_y(0) = 0$ we get

$$\epsilon P_y = -\frac{1}{\sqrt{a_r^2 - \frac{3}{2}}}\tan\left(\frac{\sqrt{a_r^2 - \frac{3}{2}}}{a_r^2 + 1}\dot{\gamma}t\right). \tag{1.4.21}$$

Using equation (1.4.21) we find that the time taken for p_y to become large compared to ϵ is

$$t = \frac{\pi(a_r^2 + 1)}{2\dot{\gamma}\sqrt{a_r^2 - \frac{3}{2}}}$$

and that for large a_r the time taken for p_y to get out of the $O(\frac{1}{a_r})$ range is approximately $t \approx \frac{a_r \pi}{2\dot{\gamma}}$. As there are four such regions in one complete orbit then time spent within $O(\frac{1}{a_r})$ of the $x-z$ plane is $t \approx \frac{2\pi a_r}{\dot{\gamma}}$. From equation (1.4.19) we can see that this accounts for nearly all of the total orbit time.

1.4.2 Flexible and Semi-flexible Fibres

The motion of semi-flexible fibres in shear flow was studied in the experiments of Forgacs, Mason and co-workers [10, 11] using dacron, rayon and nylon fibres in a Couette apparatus. They observed that semi-flexible fibres deform in shear flow and as a consequence do not follow Jeffery's predictions for orbit patterns and periods of rotation.

They found that the observed fibres deformations could be divided into 3 categories

i) 'Springy turns' as shown in figure 1.14. These were observed for stiff fibres where the shear-rate only just exceeds the critical condition for bending to occur, given by

$$(\dot{\gamma}\mu)_{crit} = \frac{E(\log 2a_r - 1.75)}{2a_r^4}.$$

ii) 'Snake Turns', or what we shall call 'C turns', as shown in figure 1.15. These were observed for more flexible fibres.

iii) 'S-turns' as shown in figure 1.16. These were only observed in flexible, symmetrical particles that were "entirely free of any permanent deformations".

It is important to note that most of the fibres in their study were not intrinsically straight.

A fibre rotating in the $x-y$ plane will bend whilst it is in the compressional quadrant and straighten in the extensional quadrant (see figure 1.3). The fibre experiences maximum compressive forces at an angle of -45° with the x axis.

All fibres exceeding the critical condition for bending were observed to exhibit orbit drift either towards the $x-y$ plane or towards the z axis. Fibres that performed snake turns *i.e* the more flexible fibres, showed an increased tendancy to drift towards the $x-y$ plane.

Figure 1.14: Fibre performing a Springy Turn in the $x-y$ plane.

Figure 1.15: Fibre performing a Snake Turn in the $x-y$ plane.

Figure 1.16: Fibre performing an S Turn in the $x-y$ plane.

Flexible Fibre Simulations

Klingenberg and collaborators have developed a number of different numerical simulations of semi-flexible fibres. In these models the fibres are modelled as; chains of prolate spheriods connected by ball and socket joints with three rotational degrees of freedom [31]; rigid spheres connected by hinges [34] and rigid rods connected by hinges [33]. All three models incorportated bending and twisting stiffness so that the flexibility of the fibre could be altered.

Simulations using spheres [34] and spheroids [31] both showed that type of shape deformation was determined by flexibility. Stiffer fibres performed springy turns or C turns and more flexible fibres performed S turns. Simulations using chains of rigid rods [33] showed that only S turns were obtained by intrinsically straight fibres with flexibility only effecting the sharpness of the turn. Only fibres with permanent deformations produced C turns.

Skjetne, Ross and Klingenberg [34, 31] concluded that the main determining factor in drift direction was the initial orbit constant. Fibres starting close to the z axis, so that initial orbit constant is small, drift towards a zero orbit constant while fibres starting closer to the $x-y$ plane, so that the orbit constant is large, drift towards an infinite orbit constant.

The other two determining factors for drift direction are flexibility and aspect ratio [34]. High flexibility and small aspect ratio both allow greater bending. This allows fibres with smaller initial orbit constants to drift towards the $x-y$ plane rather than the vorticity axis. These three parameters (flexibility, aspect ratio and initial orbit constant) also affect drift rate [34].

A fibre that does not bend will not drift, hence it follows that a flexible fibre will drift faster the more flexible it is. Similarly, the smaller the aspect ratio, the more a fibre will deform and the faster it will drift. Fibres drifting towards the $x-y$ plane drift faster than those moving towards the vorticity axis. This is due to the larger compressional forces

experienced close to the $x-y$ plane.

Whereas the orbit period of rigid rods is independent of orbit constant the same is not true of flexible fibres. In studying the dimensionless orbit period of flexible fibres Skjetne [34] concluded that fibres at large C have periods that are shorter than that of rigid rods of the same aspect ratio and decrease with decreasing stiffness, whereas fibres at small C have periods that are longer than rigid rods and increase with decreasing stiffness.

Linear Stability Analysis of Flexible Fibres

Hinch [17] examines the shape distortions of an inextensible thread with zero bending stiffness. The thread is assumed to be very thin so that only the leading order terms from slender body theory are retained. This means the thread will not cross the $x-z$ plane but will become aligned with the x-axis. A finite aspect ratio thread would eventually cross due to a small couple from the velocity difference across the fibre width. Evolution equations for the change in shape of a thread are derived and then linearised for small perturbations from a straight thread. The linear equations are solved by the method of normal modes. The first distortion mode is symmetric about the centre (a C mode) and the second is the antisymmetric S mode. Hinch notes that the neglected couples exerted on the thread by the shear flow might be expected to produce odd modes.

For fibres in shear flow the distortions decay algebraically in time for an infinite aspect ratio fibre and decay completely by the time the fibre reaches the x axis. He concludes that the changes in shape of a flexible fibre do not enable a high aspect ratio fibre to cross the x axis.

Becker and Shelley [3] carried out a similar perturbation analysis to that of Hinch but include the finite bending stiffness, for fibres in a compressional flow. They found that the C mode was the first to become unstable with increasing flexibility.

1.4.3 Active Propulsion of Fibres

Two of the main biological examples of active propulsion by fibres are the rotation of helical flagella in prokaryotic cells and the beating motion of elastic rods in eukaryotic organisms [25, 9]. In this thesis, we consider the first case and investigate the effect of flexibility upon the speed of propulsion.

Research into the swimming motion of flagella-propelled micro-organisms includes observations and physical models of bacteria, and analytical studies and numerical simulations collectively known as flagella hydrodynamics.

Observations and Physical Models

Organisms that swim by the rotational or wave motion of flagella range from mono-flagellate bacteria such as *Vibrio alginolyticus* to petriciously flagellated bacteria such as *S.meliloti* which has between 4 and 6 flagella. Forward swimming motion is often achieved through the rotation of helical flagella. In bacteria which possess more than one flagella, the flagella form a bundle and rotate together [32].

There are several mechanisms by which organisms can change direction. The photosynthetic bacterium *R.sphaeroides*, possess a single flagella which rotates only in a clockwise direction. Directional change occurs by the stopping and restarting of this motion. Enterobacteria, such as *Escherichia coli* and *Salmonella*, change direction when one or more of their flagella switches from counterclockwise to clockwise rotation, this induces a helical transition from left-handed to right-handed and causes the cell to tumble.

S.meliloti possess several flagella that rotate in a bundle. By varying the speeds of individual flagella the bacterium changes direction as a result of the speed differential. *R.lupini* also possess several flagella which rotate together in a bundle. Tumbles or directional changes are induced by one or more flagella slowing down or stopping. This causes the bundle to fall apart. The bundle reforms as the rotary speed increases once again. The size of directional change is dependant on the number and length of the

filaments. The more flagella per cell the smaller the directional change as the effect of a single filament stopping becomes less significant. Cells with long filaments also exhibit small directional changes as bundles of long filaments take longer to seperate [32].

Flagella Hydrodynamics

Early flagella models include those of Taylor [37, 38], Hancock [14] and Gray and Hancock [13]. The latter developed the Resistive Force Theory technique that has been used in much of the subsequent research. The work of Gray and Hancock considered only sinusoidal waves.

Resistive Force Theory uses the fact that propulsive components of force acting normally to the surface of the body can overcome the drag forces acting tangentially along the body provided the orientation of the surface of the body to the axis of translation of the whole cell is such that the normal force has a forward propulsive component. By balancing the total propulsive thrust by the drag on the cell body, the swimming speed of the organsim can be calculated.

Chwang and Wu [7] applied resistive force theory to helical waves. To consider helical waves both linear and angular motion must be taken into account. For a creature composed of a spherical head and a helical tail, lying along the x-axis each section of the tail rotates about the x-axis with angular velocity ω with respect to the cell body, in a counter-clockwise direction and moves parallel to the x-axis with speed U_o. While the motion of the tail generates a forward propulsive thrust, it also generates a torque, T, causing the entire creature to rotate clockwise about the x-axis with angular velocity, Ω. This means the flagellum has an 'apparent' angular velocity with respect to the surrounding fluid, $\omega_{app} = \omega - \Omega$, as defined by Chwang and Wu [7], resulting in a reduced propulsive force.

In the model considered by Chwang and Wu [7] the tail does not rotate as a whole relative to the head, only the 'waveform' progresses with angular velocity ω relative to the head.

The alternative, is the model used by Goto, Inaoka and Takano [12] in which a rigid helical flagellum is driven by a rotary motor at its junction with the cell body.

Propulsive velocity is small if the head is small as the head is not large enough to resist the whole body rotation induced by the viscous torque created by the motion of the flagellum. Hence Ω is large and therefore ω_{app} is small. Forward propulsion is also limited if the head is too large as the tail cannot generate enough forward thrust to overcome the drag on the head. There is therefore an optimum head to tail ratio where the head is large enough to resist rotation and hence reduce Ω and increase ω_{app} but is not too large that the tail can still propel it forwards.

Chwang and Wu [7] considered the presence of a cell body but did not consider the interaction between the cell body and the flagellum. Higdon [15] developed an improved approximation by introducing higher order corrections to slender-body theory due to long range hydrodynamic interactions which not only take into account the interaction between the cell body and the flagellum but also interactions between different sections of flagellum. He represented the flagellum as a distribution of Stokeslets and dipoles along its centre line and the cell body (a sphere) by two sets of singularities. The first is an image system which cancels the velocity on the sphere which was induced by singularities along the flagellum and the second comprises Stokeslets, dipoles and rotlets which match the velocity on the sphere due to translation and rotation.

Higdon [16] found that for flagella of constant length $2L$ and pitch angle $\beta = \tan^{-1}\frac{a}{b}$, where a is the helix radius and b is the pitch parameter such that $2\pi b$ is the pitch, as shown in figure 1.17, an increase in the number of turns n_t of the helix resulted in an increase in swimming speed up to a maximum at an optimum number of turns determined by the ratio of the flagella length $2L$ to the cell body radius. Further increases in n_t resulted in a decrease in swimming speed. For fixed L and pitch angle increasing the number of turns reduces the helix radius resulting in a smaller torque acting on the cell body. The reduction in Ω gives a larger ω_{app} and hence a larger propulsive thrust. However for large

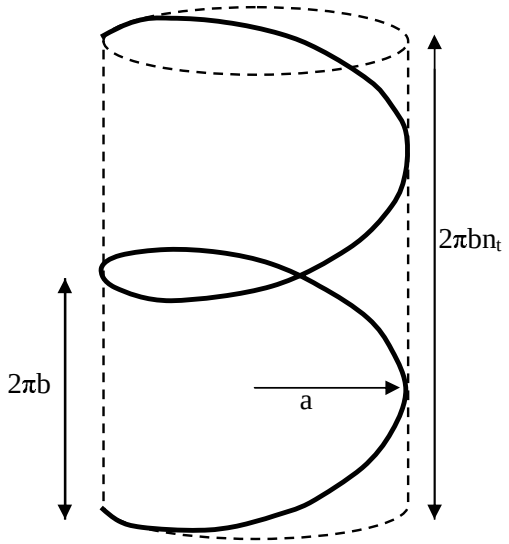

Figure 1.17: Diagram of a helix showing the radius a, pitch $2\pi b$ and axial length $2\pi b n_t$ where n_t is the number of turns.

n_t this is off-set by the reduction in propulsive thrust due to a decrease in pitch. This reduces the propulsive thrust of the flagellum by reducing the ratio of pitch to flagella diameter (slenderness ratio [16]).

For a flagellum of constant length and number of turns, Higdon found that an increase in pitch angle resulted in an increase in swimming speed up to a maximum at a pitch angle of $63.4°$. This is because the closer a section of flagellum is to being perpendicular to the direction of motion the larger the thrust it provides. For pitch angles greater than 63.4 there are no changes in swimming speed except for the case of a small cell body in which the swimming speed decreases. The decrease is due to two effects; the reduction in pitch reduces the slenderness ratio and hence reduces propulsion, and the increase in helix radius increases the torque on the cell body and hence reduces ω_{app}. The flagellum with the smaller cell body attached has a greater reduction in swimming speed as the cell body is unable to resist the torque imposed upon it.

Goto, Inaoka and Takano [12] confirmed Higdon's findings using the same slender-body

method, although Goto *et al*. obtained a maximum swimming speed at a pitch angle of 44° due to the different non-dimensionalisation of swimming speed used. Phan-Thien [27] also produced similar results using a boundary-element method, the advantages of which are that any geometry of cell body and flagella may be used, although results were only presented for a spherical cell body.

Flexible Flagella

Takano and Goto [35], used a numerical algorithm for the Kirchoff rod model to examine the motion of the semi-flexible flagellum of Vibrio alginolyticus and establish whether the difference between forward and backward swimming speeds observed by Magariyama [23] was due to deformation of the flagellum. The model used an ellipsoidal cell body and flagellum whose radius increased exponentially as distance from the cell body increased, until reaching a constant radius for the remainder of its length.

They found that during forward swimming (generated by an anti-clockwise rotation of the flagellum) the radius of the helix became smaller and the number of turns increased. The forward swimming speed of the flexible flagellum was slower (134 $\mu m s^{-1}$) compared to the speed of the rigid flagellum. In backwards swimming (generated by clockwise rotation) the radius of the helix became slightly larger and the number of turns decreased. The backwards swimming speed was found to be faster (139 $\mu m s^{-1}$) than that of the rigid flagellum, however the differences were not as large as the factor of 1.5 observed by Magariyama [23].

Takano *et al.* [36] found that for forwards swimming of Vibrio alginolyticus the axial length and pitch angle remained constant but the number of turns increased. The radius and pitch of the helix both showed a small decrease. For backwards swimming they found that axial length and pitch angle remained constant but number of turns decreased and radius and pitch increased.

In summary forwards swimming caused the helical flagellum to wind-up and swim slower,

backwards swimming caused the helix to wind-off and swim faster.

1.5 Outline of Thesis

This thesis considers three main areas

- The motion of instrinsically straight fibres in shear flow and what determines the occurrence of C and S turns.
- The motion of intrinsically bent and helical fibres in shear flow.
- The effect of flexibility on the swimming speed of helical flagella.

We develop two different simulation models for flexible fibres. In both simulations the fibre is modelled as a chain of rigid rods, rather than chains of spheres or spheroids linked together by ball and socket joints (the Kirkwood model [21]), as has been used in the research of Skjetne, Ross and Klingenberg [34, 31]. The rigid rod model has the advantage of allowing fibres of larger aspect ratios to be studied. Skjetne, Ross and Klingenberg studied fibres with aspect ratios in the range of 25 to 100, which required up to 20 spheres or spheroids to be linked together. In our simulation we study fibres with aspect ratios of up to 1000 whilst only requiring 10 to 20 rods to be linked together. To obtain such large aspect ratios using the sphere or spheroid model would greatly increase the computation time due to the large stiffnesses that would be required at each joint. In chapter two we describe the first of our simulation models, which is appropriate for intrinsically straight fibres. The simulation results from this model together with perturbation analysis for the onset of bending are described in chapter three. In this chapter we explain the occurence of C and S turns observed for semi-flexible fibres in shear flow and also establish a determining parameter for the deformation and rotation rate of an intrinsically straight fibre. For non-intrinsically straight fibres we require a

second model that takes account of both bending and twist, which is described in chapter four. In chapter five we present the results from this model for fibres with permanent shape deformations in shear flow. In chapter 6 we use this model to discuss the effects of flexibility on swimming of a helical flagella. Finally we give our conclusions in chapter 7.

Chapter 2

Fibre Model for an Intrinsically Straight Fibre.

In this chapter we describe our model for an intrinsically straight fibre. As we remarked in chapter 1 the dimensionless twisting stiffness $k^{(T)}$ of a high aspect ratio fibre is much larger than the bending stiffness $k^{(B)}$, so that any twist in the fibre will relax instantaneously. Furthermore, for an intrinsically straight fibre the bending energy is proportional to $(\frac{\partial \mathbf{p}}{\partial s})^2$ so that we need only calculate the tangential vector, $\mathbf{p}$ along the fibre.

We will first describe the model and simulation method for an infinite aspect ratio fibre, and then describe the modification to the rotation equation to account for finite aspect ratio.

2.1 Infinite Aspect Ratio Model

We model a fibre of length $2L$ and radius b such that $L >> b$. This assumption together with those of low Reynolds number and low Peclet number as detailed in section 1.2.3

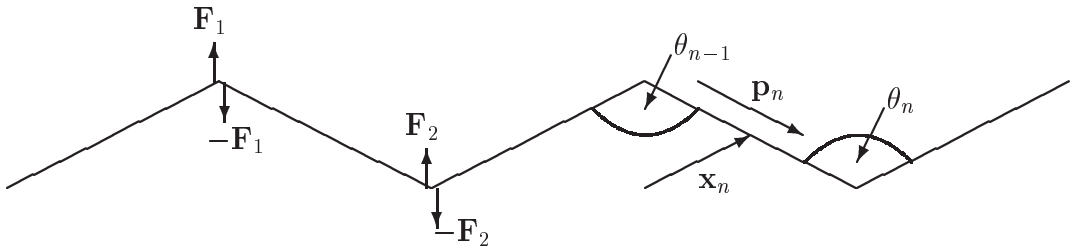

Figure 2.1: Fibre model consisting of a chain of rigid rods joined together by constraint forces $\mathbf{F}_n$. The bending stiffness at the joints is proportional to the angle θ_n between the joints. The orientation vector $\mathbf{p}_n$ and position vector $\mathbf{x}_n$ of rod n is also illustrated.

allows us to use the slender body approximations for Stokes flow described in section 1.2.5. The fibre is modelled as a chain of N rigid rods of length $\frac{2L}{N}$, see figure 2.1. In this figure the rods are numbered from left to right, and the joints are numbered from 1 to N-1, again from left to right. Connectivity is maintained via constraint forces $\mathbf{F}_n$ acting at the joints. The constraint forces act such that there is no net force at the joints and therefore no net force on the fibre. Resistance to bending is imposed by torques at the joints that are proportional to the angle θ_n between the rods. As the fibre is intrinsically straight then the equilibrium values of θ_n are given by $\theta_n^{eq} = \pi$ for all values of n.

Each rod is specified by the position $\mathbf{x}_n$ of its centre and orientation vector $\mathbf{p}_n$, as shown in figure 2.1. The position of a point on the rod at a distance s from its centre is given by $\mathbf{x}_n^r(s) = \mathbf{x}_n + s\mathbf{p}_n$ and the velocity of that point on the rod is given by $\mathbf{u}_n^r = \dot{\mathbf{x}}_n + s\dot{\mathbf{p}}_n$ which can be written in the form $\mathbf{U}+\boldsymbol{\omega}\times(\mathbf{x}-\mathbf{x}_c)$ by taking $\mathbf{U} = \dot{\mathbf{x}}_n$ and $\boldsymbol{\omega}\times(\mathbf{x}-\mathbf{x}_c) = \boldsymbol{\omega}_n \times s\mathbf{p}_n = s\dot{\mathbf{p}}_n$.

As detailed in section 1.2.3 we shall consider only linear flows of the form $\mathbf{u}^\infty = \mathbf{U}_0 + \mathbf{K}\cdot\mathbf{x}_c + \frac{1}{2}\boldsymbol{\omega}^\infty \times (\mathbf{x}-\mathbf{x}_c) + \mathbf{E}\cdot(\mathbf{x}-\mathbf{x}_c)$. Therefore by taking $\mathbf{x}_c = \mathbf{x}_n$ and $(\mathbf{x}-\mathbf{x}_c) = s\mathbf{p}_n$ we get $\mathbf{u}^\infty = \mathbf{U}_0 + \mathbf{K}\cdot\mathbf{x}_n + \frac{1}{2}\boldsymbol{\omega}^\infty \times s\mathbf{p}_n + \mathbf{E}\cdot s\mathbf{p}_n$ for the fluid flow on

the surface of the rod.

Using the values of the tensors $\mathbf{A}(\mathbf{p}_n)$, $\mathbf{C}(\mathbf{p}_n)$ and $\tilde{\mathbf{H}}(\mathbf{p}_n)$ of the grand resistance matrix calculated in secton 1.2.6 we can write the force and torque balance on each rod as

$$\mathbf{A}(\mathbf{p}_n) \cdot (\mathbf{U}_0 + \mathbf{K} \cdot \mathbf{x}_n - \dot{\mathbf{x}}_n) = -\mathbf{F}_n^c \tag{2.1.1}$$

and

$$\mathbf{C}(\mathbf{p}_n) \cdot (\frac{1}{2}\boldsymbol{\omega}^\infty - \boldsymbol{\omega}_n) + \tilde{\mathbf{H}}(\mathbf{p}_n) \cdot \mathbf{E} = -(\mathbf{T}_n^c + \mathbf{T}_n^b). \tag{2.1.2}$$

where the only forces acting on each rod are the constraint forces $\mathbf{F}_n^c$ given by

$$\mathbf{F}_n^c = \mathbf{F}_n - \mathbf{F}_{n-1}$$

and the total torque acting on each rod is comprised of the torques arising from the constraint forces $\mathbf{T}_n^c$;

$$\mathbf{T}_n^c = \frac{L}{N}\mathbf{p}_n \times (\mathbf{I} - \mathbf{p}_n\mathbf{p}_n) \cdot (\mathbf{F}_n + \mathbf{F}_{n-1})$$

and the torques arising from the resistance to bending $\mathbf{T}_n^b$. We assume that bending resistance is given by linear elasticity so that bending torque is given by

$$\mathbf{T}_n^b = -k\theta_n \frac{\mathbf{p}_n \times \mathbf{p}_{n+1}}{|\mathbf{p}_n \times \mathbf{p}_{n+1}|} + k\theta_{n-1} \frac{\mathbf{p}_{n-1} \times \mathbf{p}_n}{|\mathbf{p}_{n-1} \times \mathbf{p}_n|}$$

where the angle θ_n between rods n and $n+1$ is given by

$$\cos\theta_n = \frac{-\mathbf{p}_n \cdot \mathbf{p}_{n+1}}{|\mathbf{p}_n||\mathbf{p}_{n+1}|}$$

and k is the bending stiffness at the joints and is given by $k = \frac{EIN}{2L}$ where E is the Young's modulus and I is the second moment of inertia of the cross section. The bending stiffness

of the whole fibre is given by $k^{(B)} = \frac{EI}{2L}$ which can be written in terms of the joint stiffness by $k^{(B)} = \frac{1}{N}k$.

Rearranging equation 2.1.1 and substituting in the values of $\mathbf{A}_n$ and $\mathbf{F}_n^c$ we obtain an equation for the translational velocity of the centre of each rod

$$\dot{\mathbf{x}}_n = \mathbf{U}_0 + \mathbf{K}\cdot\mathbf{x}_n + \frac{1}{2}\xi_f^{-1}(\mathbf{I}+\mathbf{p}_n\mathbf{p}_n)\cdot(\mathbf{F}_n - \mathbf{F}_{n-1}) \tag{2.1.3}$$

where ξ_f is the resistance coefficient for force as derived in section 1.2.6.

To obtain an equation for the rotation rate of each rod $\dot{\mathbf{p}} = \boldsymbol{\omega}_n \times \mathbf{p}_n$ we take the cross product of equation 2.1.2 and substitute in the values of $\mathbf{C}_n$ and $\tilde{\mathbf{H}}_n$ to give

$$\xi_t((\mathbf{I}-\mathbf{p}_n\mathbf{p}_n)\cdot(\frac{1}{2}\boldsymbol{\omega}^\infty\times\mathbf{p}_n - \boldsymbol{\omega}_n\times\mathbf{p}_n) + \mathbf{p}_n\times\mathbf{E}\cdot\mathbf{p}_n\times\mathbf{p}_n = -(\mathbf{T}_n^c+\mathbf{T}_n^b)\times\mathbf{p}_n$$

where ξ_t is the resistance co-efficient for torque as derived in section 1.2.6.

Using $\frac{1}{2}\boldsymbol{\omega}^\infty\times\mathbf{p}_n = \boldsymbol{\Omega}\cdot\mathbf{p}_n$, where $\boldsymbol{\Omega}$ is the vorticity given in section 1.2.3, $\mathbf{p}_n\cdot\dot{\mathbf{p}}_n = 0$ and the identity $\mathbf{p}\times\mathbf{A}\times\mathbf{p} = (\mathbf{I}-\mathbf{pp})\cdot\mathbf{A}$ we get

$$\xi_t((\mathbf{I}-\mathbf{p}_n\mathbf{p}_n)\cdot\mathbf{K}\cdot\mathbf{p}_n - \dot{\mathbf{p}}_n) = -(\mathbf{T}_n^c+\mathbf{T}_n^b)\times\mathbf{p}_n \tag{2.1.4}$$

so that the difference between the rotation rate of the rod and the rotation rate of a free rod in a linear flow is proportional to the cross product of the torque acting on the rod and $\mathbf{p}_n$. Rearranging 2.1.4 and substituting in the values of $\mathbf{T}_n^c$ and $\mathbf{T}_\mathbf{n}^\mathbf{b}$ gives

$$\begin{aligned}\dot{\mathbf{p}}_n &= (\mathbf{I}-\mathbf{p}_n\mathbf{p}_n)\cdot\mathbf{K}\cdot\mathbf{p}_n + \xi_t^{-1}\frac{L}{N}(\mathbf{I}-\mathbf{p}_n\mathbf{p}_n)\cdot(\mathbf{F}_n+\mathbf{F}_{n-1}) \\ &\quad -\xi_t^{-1}k(\theta_n-\theta_n^{eq})\frac{\mathbf{p}_n\times\mathbf{p}_{n+1}}{|\mathbf{p}_n\times\mathbf{p}_{n+1}|}\times\mathbf{p}_n + \xi_t^{-1}k(\theta_{n-1}-\theta_{n-1}^{eq})\frac{\mathbf{p}_{n-1}\times\mathbf{p}_n}{|\mathbf{p}_{n-1}\times\mathbf{p}_n|}\times\mathbf{p}_n.\end{aligned} \tag{2.1.5}$$

To solve equations 2.1.3 and 2.1.6 we need to calculate the constraint forces. We do this by enforcing the connectivity constraint

$$\mathbf{x}_{n+1} - \mathbf{x}_n = \frac{L}{N}(\mathbf{p}_{n+1} + \mathbf{p}_n). \tag{2.1.6}$$

We non-dimensionalise equations (2.1.3), (2.15) and (2.1.6) expressing time in units of $\dot{\gamma}^{-1}$, such that $t^* = \dot{\gamma}t$ and $\mathbf{K}^* = \frac{1}{\dot{\gamma}}\mathbf{K}$, $\mathbf{x}$ in units of L, $\mathbf{x}^* = \frac{1}{L}\mathbf{x}$ and force in units of $2L\dot{\gamma}\xi_f$, $\mathbf{F}^* = \frac{1}{2L\dot{\gamma}}\xi_f^{-1}\mathbf{F}$ giving a non-dimensional stiffness of $k^* = \frac{1}{\dot{\gamma}}\xi_t^{-1}k$ so that our new equations are

$$\dot{\mathbf{x}}_n = \mathbf{K}\cdot\mathbf{x}_n + (\mathbf{I} + \mathbf{p}_n\mathbf{p}_n)\cdot(\mathbf{F}_n - \mathbf{F}_{n-1}), \tag{2.1.7}$$

$$\begin{aligned}\dot{\mathbf{p}}_n \;=\; & \mathbf{K}\cdot\mathbf{p}_n - \mathbf{p}_n\cdot\mathbf{K}\cdot\mathbf{p}_n\mathbf{p}_n + 3N(\mathbf{I} - \mathbf{p}_n\mathbf{p}_n)\cdot(\mathbf{F}_n + \mathbf{F}_{n-1}) \\ & -k(\theta_n - \theta_n^{eq})\frac{\mathbf{p}_n\times\mathbf{p}_{n+1}}{|\mathbf{p}_n\times\mathbf{p}_{n+1}|}\times\mathbf{p}_n + k(\theta_{n-1} - \theta_{n-1}^{eq})\frac{\mathbf{p}_{n-1}\times\mathbf{p}_n}{|\mathbf{p}_{n-1}\times\mathbf{p}_n|}\times\mathbf{p}_n,\end{aligned} \tag{2.1.8}$$

$$\mathbf{x}_{n+1} - \mathbf{x}_n = \frac{1}{N}(\mathbf{p}_{n+1} + \mathbf{p}_n), \tag{2.1.9}$$

where the *s have been dropped for convenience. Non-dimensional bending stiffness is given by $\frac{3\log 2a_r EI}{\dot{\gamma}\pi\mu l^4}$ (as derived in section 1.3.1), where l is the fibre length given by $l = 2L$ and hence the rod length is given by $l = \frac{2L}{N}$. We can therefore write the non-dimensional bending stiffness of the whole fibre in terms of the non-dimensional joint stiffness as $k^{(B)} = \frac{1}{N^4}k$.

Differentiating equation (2.1.9) and substituting in equations (2.1.7) and (2.18) yields a tridiagonal system of equations

$$\boldsymbol{\alpha}_{n+1}\cdot\mathbf{F}_{n+1} + \boldsymbol{\beta}_n\cdot\mathbf{F}_n + \boldsymbol{\alpha}_n\cdot\mathbf{F}_{n-1} = \boldsymbol{\Gamma}_n, \tag{2.1.10}$$

where

$$\boldsymbol{\alpha}_n = 2(\mathbf{I} - 2\mathbf{p}_n\mathbf{p}_n),$$

$$\boldsymbol{\beta}_n = 2(4\mathbf{I} - \mathbf{p}_{n+1}\mathbf{p}_{n+1} - \mathbf{p}_n\mathbf{p}_n),$$

$$\begin{aligned}\boldsymbol{\Gamma}_n &= \mathbf{K}\cdot(\mathbf{x}_{n+1}-\mathbf{x}_n) - \frac{1}{N}(\mathbf{I}-\mathbf{p}_{n+1}\mathbf{p}_{n+1})\cdot\mathbf{K}\cdot\mathbf{p}_{n+1} - \frac{1}{N}(\mathbf{I}-\mathbf{p}_n\mathbf{p}_n)\cdot\mathbf{K}\cdot\mathbf{p}_n \\ &+\frac{k}{N}(\theta_n-\theta_n^{eq})\frac{\mathbf{p}_n\times\mathbf{p}_{n+1}}{|\mathbf{p}_n\times\mathbf{p}_{n+1}|}\times\mathbf{p}_n - \frac{k}{N}(\theta_{n-1}-\theta_{n-1}^{eq})\frac{\mathbf{p}_{n-1}\times\mathbf{p}_n}{|\mathbf{p}_{n-1}\times\mathbf{p}_n|}\times\mathbf{p}_n \\ &+\frac{k}{N}(\theta_{n+1}-\theta_{n+1}^{eq})\frac{\mathbf{p}_{n+1}\times\mathbf{p}_{n+2}}{|\mathbf{p}_{n+1}\times\mathbf{p}_{n+2}|}\times\mathbf{p}_{n+1} - \frac{k}{N}(\theta_n-\theta_n^{eq})\frac{\mathbf{p}_n\times\mathbf{p}_{n+1}}{|\mathbf{p}_n\times\mathbf{p}_{n+1}|}\times\mathbf{p}_{n+1}\end{aligned} \quad (2.1.11)$$

Solving this system of equations using LU decomposition with forward and backward substitution yields the values of the constraint forces $\mathbf{F}_n$ [29]. The motion of the fibre can then be obtained by integrating equations 2.1.7 and 2.1.9 using 4th order Runge Kutta [29].

2.2 Modification for Finite Aspect Ratio

To model a semi-flexible fibre with finite aspect ratio, a_r, it is necessary to replace the term $\mathbf{K}\cdot\mathbf{p}_n - \mathbf{p}_n\cdot\mathbf{K}\cdot\mathbf{p}_n\mathbf{p}_n$ in equation (2.1.9), which describes the rotation rate of a torque free slender body, with

$$\boldsymbol{\Omega}\cdot\mathbf{p}_n + \frac{\tilde{a}_r^2-1}{\tilde{a}_r^2+1}(\mathbf{E}\cdot\mathbf{p}_n - \mathbf{p}_n\cdot\mathbf{E}\cdot\mathbf{p}_n\mathbf{p}_n) \quad (2.2.12)$$

which describes the rotation rate of a torque free prolate spheroid of aspect ratio $\tilde{a}_r$ as derived in reference [20]. In our simulation we use $\tilde{a}_r = \frac{1}{N}a_r$ where $\frac{1}{N}a_r$ is the aspect ratio of the individual rods.

2.3 Stress Contribution of a Semi-Flexible Fibre

In subsection 1.2.7 we considered the stress contribution of a rigid fibre in shear flow. We now obtain the stress contribution for a semi-flexible fibre composed of N rigid rods of length $\frac{2L}{N}$. The force density along each rod is given by

$$\mathbf{f}_n = \frac{\xi_f N}{2L}(2\mathbf{I} - \mathbf{p}_n\mathbf{p}_n) \cdot (\mathbf{u}_n^r - \mathbf{u}_n^\infty). \tag{2.3.13}$$

The fluid velocity at a point s along the rod is given by $\mathbf{u}_n^\infty = \mathbf{K} \cdot \mathbf{x}(s) = \mathbf{K} \cdot (\mathbf{x}_n + s\mathbf{p}_n)$ where $\mathbf{x}_n$ is the position vector of the centre of rod n and $\mathbf{p}_n$ is the orientation vector of rod n. The velocity of each rod is given by $\mathbf{u}_n^r = \dot{\mathbf{x}}_n + s\dot{\mathbf{p}}_n$ where $\dot{\mathbf{x}}_n$ and $\dot{\mathbf{p}}_n$ are given by the equations

$$\dot{\mathbf{x}}_n = \mathbf{K} \cdot \mathbf{x}_n + \frac{1}{2}\xi_f^{-1}(\mathbf{I} + \mathbf{p}_n\mathbf{p}_n) \cdot (\mathbf{F}_n - \mathbf{F}_{n-1}) \tag{2.3.14}$$

and

$$\dot{\mathbf{p}}_n = \mathbf{K} \cdot \mathbf{p}_n - \mathbf{p}_n \cdot \mathbf{K} \cdot \mathbf{p}_n\mathbf{p}_n + \frac{\xi_t^{-1}L}{N}(\mathbf{I} - \mathbf{p}_n\mathbf{p}_n) \cdot (\mathbf{F}_n + \mathbf{F}_{n-1}) + \xi_t^{-1}\mathbf{T}_n^b \times \mathbf{p}_n \tag{2.3.15}$$

respectively (see section 2.1). Here $\mathbf{T}_n^b$ is the bending torque given by

$$\mathbf{T}_n^b = -k(\theta_n - \theta_n^{eq})\frac{\mathbf{p}_n \times \mathbf{p}_{n+1}}{|\mathbf{p}_n \times \mathbf{p}_{n+1}|} + k(\theta_{n-1} - \theta_{n-1}^{eq})\frac{\mathbf{p}_{n-1} \times \mathbf{p}_n}{|\mathbf{p}_{n-1} \times \mathbf{p}_n|}.$$

Substituting the fluid and rod velocity into equation 2.3.13 gives,

$$\begin{aligned} \mathbf{f}_n &= s\frac{\xi_f N}{2L}\mathbf{p}_n\mathbf{p}_n \cdot \mathbf{K} \cdot \mathbf{p}_n - \frac{N}{2L}(\mathbf{F}_n - \mathbf{F}_{n-1}) \\ &\quad -s\frac{3N^2}{2L^2}\left[(\mathbf{I} - \mathbf{p}_n\mathbf{p}_n) \cdot (\mathbf{F}_n + \mathbf{F}_{n-1}) + \frac{N}{L}\mathbf{T}_n^b \times \mathbf{p}_n\right] \end{aligned} \tag{2.3.16}$$

for the force density along the boundary of rod n.

The stresslet [2] for each rod is then calculated using

$$\mathbf{S}_n = \frac{1}{2}\int_{-\frac{L}{N}}^{\frac{L}{N}} (\mathbf{x}_n + s\mathbf{p}_n)\mathbf{f}_n + \mathbf{f}_n(\mathbf{x}_n + s\mathbf{p}_n)ds. \tag{2.3.17}$$

Substituting equation 2.3.17 into equation 2.3.17 gives

$$\begin{aligned}\mathbf{S}_n &= \xi_s(\mathbf{p}_n\cdot\mathbf{K}\cdot\mathbf{p}_n)\mathbf{p}_n\mathbf{p}_n - \frac{1}{2}\left(\mathbf{x}_n(\mathbf{F}_n-\mathbf{F}_{n-1}) + (\mathbf{F}_n-\mathbf{F}_{n-1})\mathbf{x}_n\right)\\ &\quad -\frac{L}{2N}\left(\mathbf{p}_n(\mathbf{I}-\mathbf{p}_n\mathbf{p}_n)\cdot(\mathbf{F}_n+\mathbf{F}_{n-1}) + (\mathbf{I}-\mathbf{p}_n\mathbf{p}_n)\cdot(\mathbf{F}_n+\mathbf{F}_{n-1})\mathbf{p}_n\right)\\ &\quad -\frac{1}{2}\left(\mathbf{p}_n\mathbf{T}_n^b\times\mathbf{p}_n + \mathbf{T}_n^b\times\mathbf{p}_n\mathbf{p}_n\right).\end{aligned} \tag{2.3.18}$$

The stress along the whole fibre is given by $\mathbf{S} = \sum_{n=1}^{N}\mathbf{S}_n$.

Using the non-dimensionalisation $\mathbf{S}^* = \frac{1}{\dot\gamma N^3}\xi_s^{-1}\mathbf{S}$, $\mathbf{x}^* = \frac{\mathbf{x}}{L}$, $\mathbf{F}^* = \frac{N}{2L\dot\gamma}\xi_f^{-1}\mathbf{F}$ and $k^* = \frac{1}{\dot\gamma}\xi_t^{-1}k$ where the resistance co-efficients are calculated using the rod length $\frac{2L}{N}$, we obtain the following non-dimensionalised form of the stress tensor for a semi-flexible fibre,

$$\begin{aligned}\mathbf{S}^* &= \frac{1}{N^3}\sum_{n=1}^{N}(\mathbf{p}_n\cdot\mathbf{K}\cdot\mathbf{p}_n)\mathbf{p}_n\mathbf{p}_n - 3N^2\left(\mathbf{x}_n(\mathbf{F}_n-\mathbf{F}_{n-1}) + (\mathbf{F}_n-\mathbf{F}_{n-1})\mathbf{x}_n\right)\\ &\quad -3N\left(\mathbf{p}_n(\mathbf{I}-\mathbf{p}_n\mathbf{p}_n)\cdot(\mathbf{F}_n+\mathbf{F}_{n-1}) + (\mathbf{I}-\mathbf{p}_n\mathbf{p}_n)\cdot(\mathbf{F}_n+\mathbf{F}_{n-1})\mathbf{p}_n\right)\\ &\quad -\left(\mathbf{p}_n\mathbf{T}_n^b\times\mathbf{p}_n + \mathbf{T}_n^b\times\mathbf{p}_n\mathbf{p}_n\right).\end{aligned} \tag{2.3.19}$$

2.4 Numerical Simulation - Accuracy Checks

2.4.1 Time Step

Our numerical method is essentially a forward time, centered space scheme for solving a diffusion equation and so a stability criterion of

$$\frac{kh}{(\Delta s)^2} < \frac{1}{2}$$

would be expected [29], where h is the time-step and Δs is the space discretisation. Given our space step is $\Delta s = 1$ we can simplify this to

$$kh < \frac{1}{2}. \tag{2.4.20}$$

By calculating the orbit period of fibres with rod numbers of $N = 10,\ 12,\ 15$,and 20 and rod stiffnesses of $k = 10,\ 50,\ 100$ and 500 at various time-steps and determining at which time-step the simulation becomes unstable in each case we confirm equation (2.4.20) is a suitable stability criterion for this simulation method.

Time steps which are too large lead to the system becoming unstable very quickly, however, once a time-step satisfies the criterion then further reductions in size result in only minor improvements in accuracy. In our simulation we have used $h = 0.01$ for rod stiffnesses of $k \leq 50$ and $h = 0.001$ for $50 \leq k \leq 500$.

2.4.2 Individual Rod Stiffness

In section 2.1 we find that the whole fibre stiffness as derived in subsection 1.3.1 is linked to the stiffness of each individual rod in the fibre model by

$$k = N^4 k^{(B)} \tag{2.4.21}$$

where k is the individual rod stiffness. By measuring the orbit period for a fibre of aspect ratio $a_r = 200$ and whole fibre stiffness $k^{(B)} = 5 \times 10^{-4}$ for various values of rod number N we tested the accuracy of this relationship. The individual rod stiffness was calculated using equation (2.4.21) and the rod aspect ratio was given by $\frac{a_r}{N}$. It was found that there was a 0.5% increase in the orbit period of the fibres when the rod number was increased from 10 to 20 rods.

The values of N that can be used are limited as values below 6 give highly inaccurate results as there are too few locations in which bending can occur and hence the model is unrealistic. High values of N, in this case values above 20, result in the aspect ratio of the individual rods being too small and hence no longer satisfying the slender body criteria.

2.4.3 Replication of Rigid Fibre Results

We check that the simulation reproduces known results for rigid fibres. Simulations were run for rigid fibres in shear flow, $\mathbf{u} = (\dot{\gamma}y, 0, 0)$ non-dimensionalised with respect to $\dot{\gamma}$. Fibres were composed of 10 rods, each of aspect ratio 10, so that the fibre had aspect ratio 100. Bending stiffness was set so that the fibre had overall stiffness $k^{(B)} = 0.1$ and the change in end to end length of the fibre was $< 1 \times 10^{-9}\%$. The orbit period was measured for a variety of initial orbit constants, C, and was found to be independant of C. For large aspect ratios, we can define the effective aspect ratio from the period of oscillation by $a_{r_{eff}} = \frac{\dot{\gamma}T}{2\pi}$. This gives an effective aspect ratio of 100.46 compared to the actual aspect

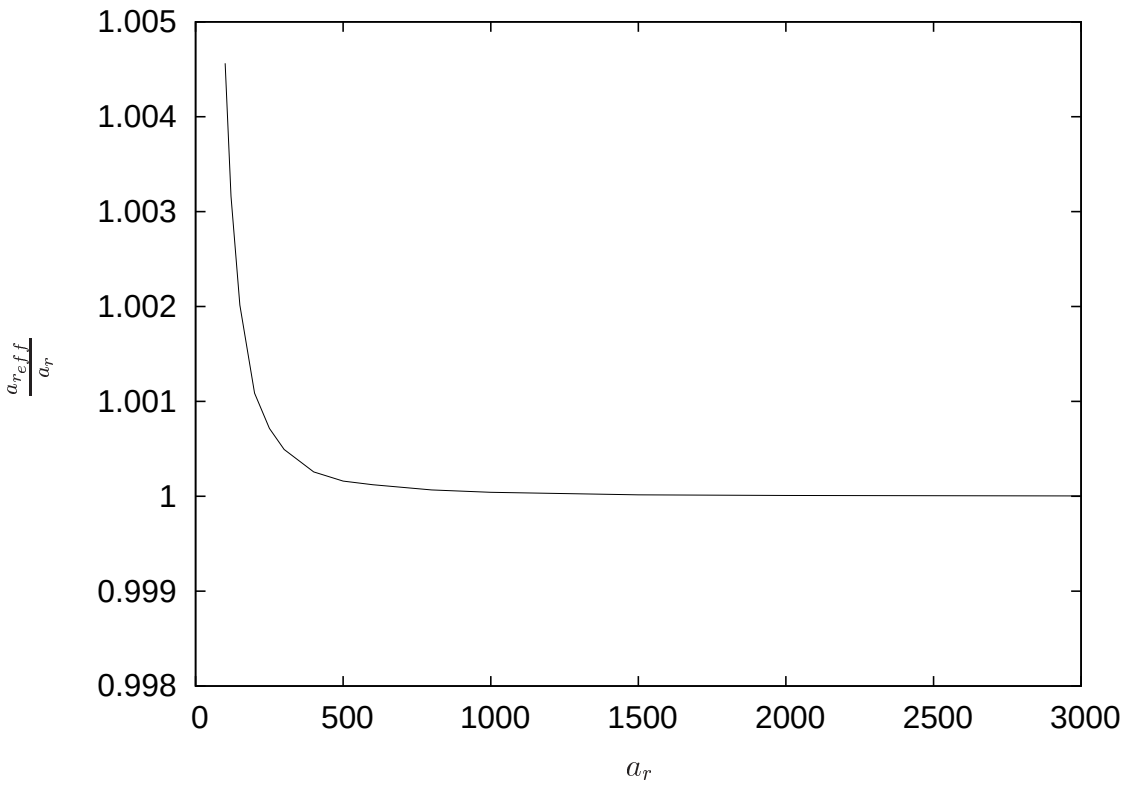

Figure 2.2: Ratio of effective to actual aspect ratio as a function of aspect ratio.

ratio of 100. Figure 2.2 shows the ratio of effective to actual aspect ratio against aspect ratio. All fibres had a stiffness of $k^{(B)} = 0.1$ and further increases in stiffness resulted in no change in orbit period. The trend of decreasing ratio with increasing aspect ratio is consistent with the simulation results obtained by Skjetne, Ross and Klingenberg [34] and the experimental results obtained by Trevelyan and Mason [40]. However, the actual values of $\frac{a_{r_{eff}}}{a_r}$ are higher than those obtained by Skjetne *et. al.* [34] due to the differing fibre geometries and treatment of hydrodynamic interactions. For very high aspect ratios the ratio tends to one as the shape of the fibre is no longer significant.

Plots of Jeffery orbits for varying initial orbit constants and aspect ratio plotted along side Jeffery orbits for an ellipsoid with aspect ratio equal to the fibre's effective aspect ratio show good agreement (figure 2.3). Simulations were run for 10+ consecutive periods and

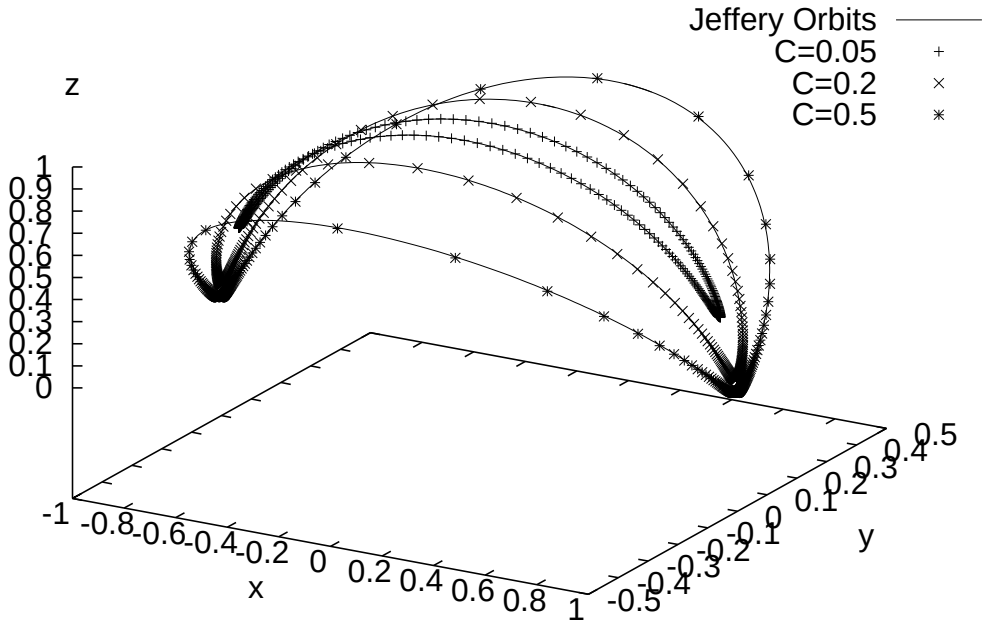

Figure 2.3: Jeffery orbits of fibre compared to predicted Jeffery orbits for an ellipsoid of equivalent aspect ratio. Orbits are shown for orbit constants of $C = 0.05$,$C = 0.2$ and $C = 0.5$.

no orbit drift was observed.

Chapter 3

Results for Instrinsically Straight Fibres

In chapter 2 we described the numerical simulation method for intrinsically straight fibres. Experimental observations of Forgacs and Mason [10] report that dacron and elastomer fibres perform C turns except in the case of perfectly straight fibres which perform S turns. Simulation results of Ross and Klingenberg [31] and Skjetne, Ross and Klingenberg [34] find that the shape the fibre forms whilst rotating is dependent upon the fibre stiffness. In his stability analysis Becker also concluded that stiffness was the determining factor and that mode 1 (the C mode) was the most unstable in compressional flow. For smaller stiffnesses mode 2 (the S mode) became the most unstable, followed by mode 3 and then mode 4 at even smaller stiffnesses. The mode number describes the number of turning points in the fibre shape so that mode 4 has 4 turning points and hence is an odd mode.

In this chapter we begin by investigating the types of turns performed by instrinsically straight fibres in the $x - y$ plane (section 3.1.1). We also consider how fibre stiffness and aspect ratio effects bending energy (section 3.1.2) and orbit period (section 3.1.3). To explain our findings we consider the fibre dynamics in the two regions of the orbit in which bending can occur, the compressional quadrant and the $x - z$ plane. For bending in the compressional quadrant we perform a linear stability analysis (section 3.2.1) similar to that of Becker [3] and for bending in the $x - z$ plane we use a torque balance argument

to determine the shape of the fibre at this point in the orbit (section 3.2.3).

In section 3.4 we go on to consider a fibre with an initial orientation out of the $x-y$ plane and explain why, unlike rigid fibres which rotate in closed Jeffery orbits, semi-flexible fibres exhibit orbit drift. We also consider the effect of fibre stiffness and aspect ratio on the rate and direction of drift.

3.1 Semi-Flexible Fibres in the Flow-Gradient Plane

We shall first consider fibres that rotate in the flow-gradient ($x - y$) plane. Fibres start with initial alignment along the x-axis. We shall consider the shape of the fibres during rotation and the period of rotation.

3.1.1 Fibre Shape

A perfectly straight fibre aligned along the x-axis will rotate and deform into an S-like shape providing it is sufficiently flexible. This is in agreement with the experimental results of Forgacs and Mason [11] and the simulation of Schmid, Switzer and Klingenberg [33] which observed that perfectly straight fibres performed S turns. Figure 3.1 shows a fibre of aspect ratio $a_r = 100$ performing an S turn with time t given in strain units, $\dot{\gamma}t$. A very flexible, high aspect ratio fibre will perform a mode 4 turn (perturbation has two maxima and two minima) when rotating as shown in figure 3.2. A fibre of aspect ratio 1000 will perform a mode 4 turn if the stiffness is less than $k^{(B)} = 0.0013$, for stiffness greater than this it will remain straight whilst rotating. A fibre of aspect ratio 400 will perform an S turn for $k^{(B)} > 0.0013$ and a mode 4 turn for $k^{(B)} < 0.0013$. We may therefore expect fibres with smaller stiffnesses to produce higher mode turns such as mode 6 and mode 8 turns although we have not observed these in our simulation results.

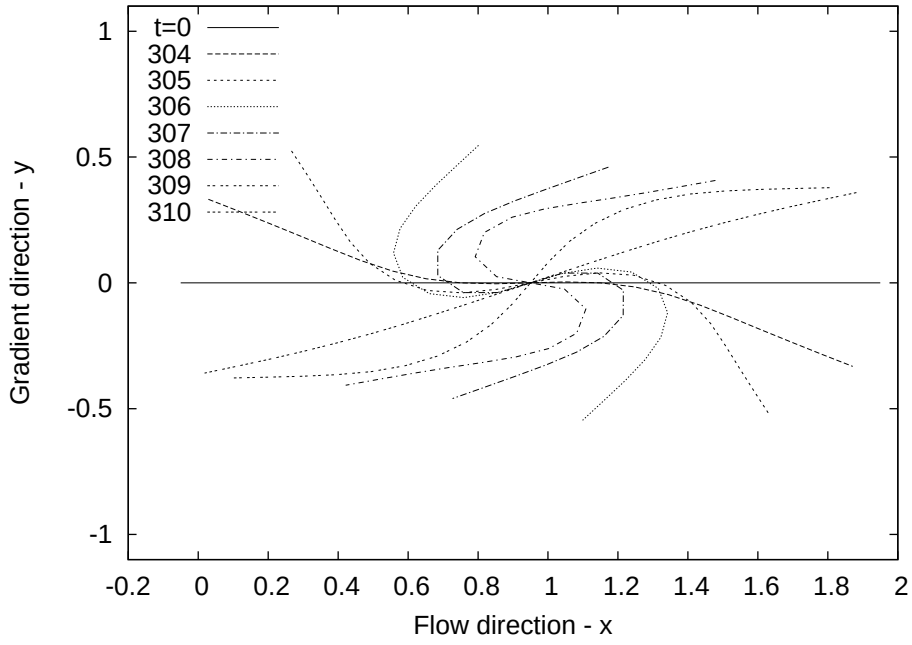

Figure 3.1: Fibre of aspect ratio, $a_r = 200$ and non-dimensional bending stiffness (as derived in section 1.3.3) $k^{(B)} = 6.25 \times 10^{-4}$ performing an S turn in the x-y plane.

We will however investigate the presence of higher order modes in the linear stability analysis described in section 3.2.1.

A fibre that is not sufficiently flexible to perform an S turn does not perform a C turn but remains straight while rotating. Whether or not a fibre will bend is dependent both upon the fibre stiffness, $k^{(B)}$ and the aspect ratio a_r. We shall investigate this dependence further in subsection 3.1.2.

To obtain a C turn (see figure 3.3) the fibre must either be intrinsically bent (as we shall demonstrate in chapter 5) or have an initial deformation that is not antisymmetric. In the latter case only the initial rotation will be a C turn. As the fibre realigns with the x-axis it will straighten completely and therefore all subsequent rotations will be S turns. The size of the initial deformation must be at least of the order of the fibre diameter.

As we discuss further in subsection 3.2.3 the initial buckling of a perfectly straight fibre

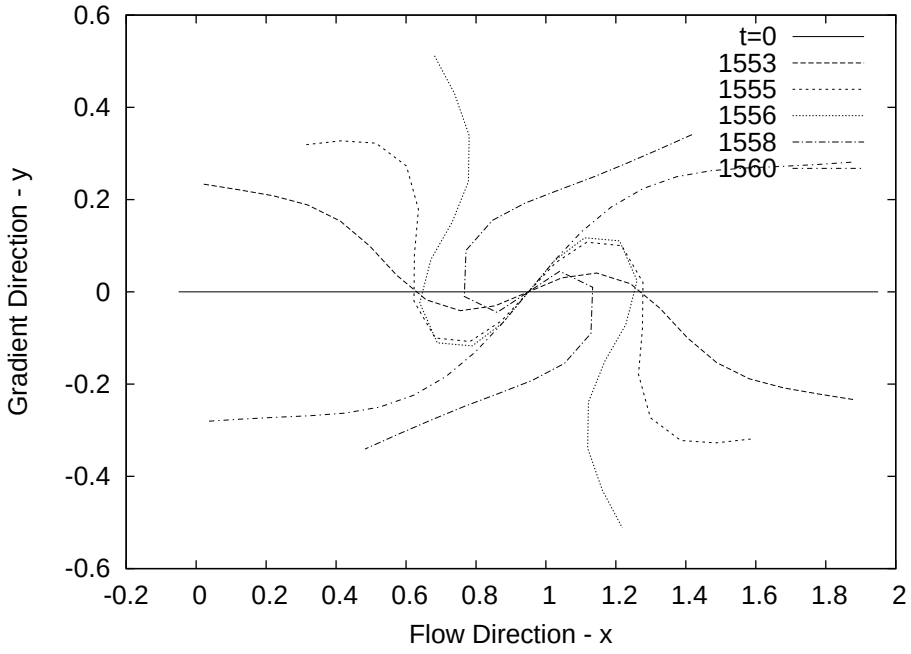

Figure 3.2: A fibre of aspect ratio $a_r = 1000$ and stiffness $k^{(B)} = 3.125 \times 10^{-4}$ rotating in the $x - y$ plane. The fibre shows a mode 4 shape in the compressional quadrant.

of finite aspect ratio aligned along the x-axis is anti-symmetric and therefore produces an S turn no matter what the flexibility of the fibre. To obtain a C turn requires a perturbation that breaks this anti-symmetry. This suggests that the propensity for C turns in the experiments of Forgacs and Mason [11] was due to the fact that most of the fibres used were not intrinsically straight.

3.1.2 Fibre Flexibility

To determine the bending stiffness required for the fibre to no longer bend we plot the bending energy per half orbit against stiffness for fibres of different aspect ratios (figure 3.4). We define the bending energy per half orbit by

$$E = \frac{1}{2} \int_0^{\frac{T}{2}} \sum_{n=1}^{N-1} (\theta_n - \theta_{eq})^2 dt, \tag{3.1.1}$$

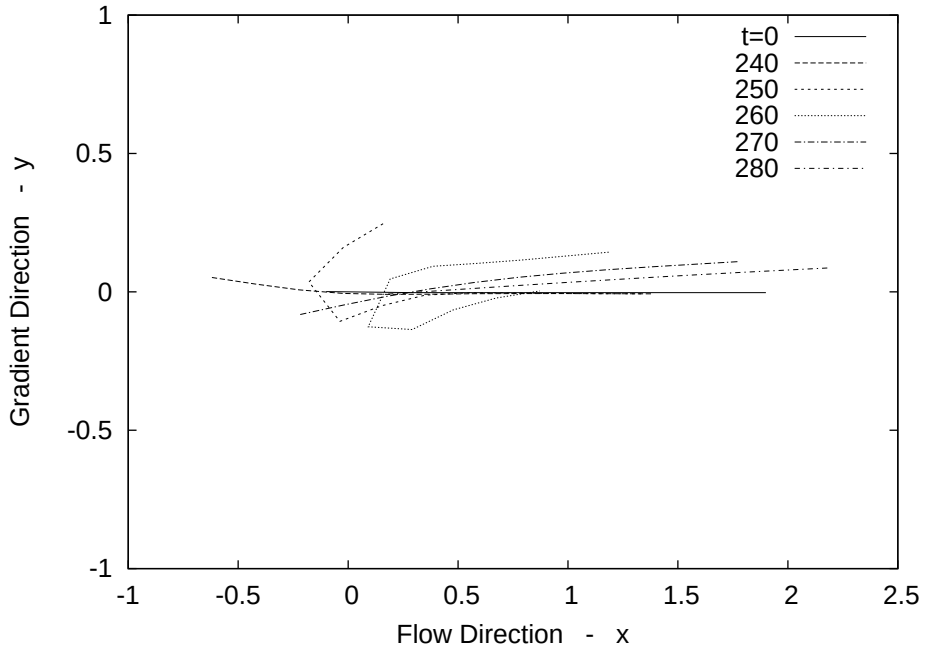

Figure 3.3: Fibre of stiffness $k^{(B)} = 7.5 \times 10^{-5}$ and aspect ratio $a_r = 300$ performing a C turn in the x-y plane.

where T is the orbit period, θ_n is the angle at the joint and $N - 1$ is the number of joints. For low stiffnesses where there is considerable bending in the compressional quadrant the bending energy is independent of aspect ratio and is proportional to $k^{(B)^{-\frac{1}{2}}}$. For larger stiffnesses aspect ratio becomes important. This can be seen more clearly on the log-log plot of energy against stiffness shown in figure 3.5. At a stiffness of approximately 0.0008 the gradient changes and there is a sharp decrease in bending energy marking the boundary between a low stiffness regime in which there is no significant aspect ratio dependence and a high stiffness regime $(k^{(B)} \geq 0.005)$ in which bending energy can be multiplied by aspect ratio cubed to give a universal plot (figure 3.6). In this high stiffness regime Ea_r^3 is proportional to $k^{(B)^{-2}}$. The reasons for this change in regime from low to high stiffness will be discussed later in section 3.3.

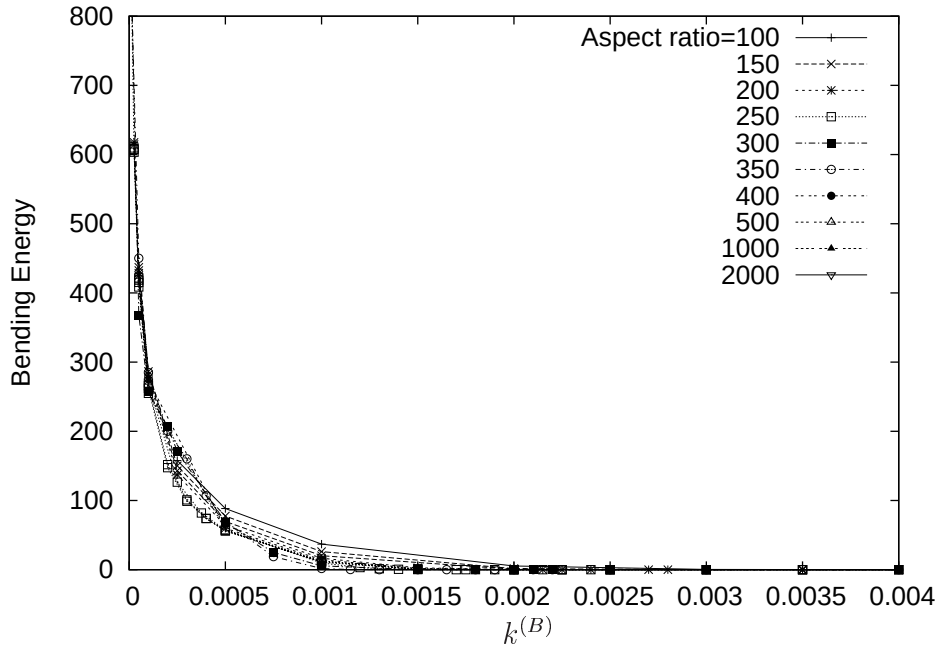

Figure 3.4: Bending energy per half orbit plotted against fibre stiffness $k^{(B)}$ for fibres of aspect ratio $a_r = 100$ to $a_r = 2000$. The vertical dotted lines show fibre stiffnesses of $k^{(B)} = 0.001$ and $k^{(B)} = 0.005$.

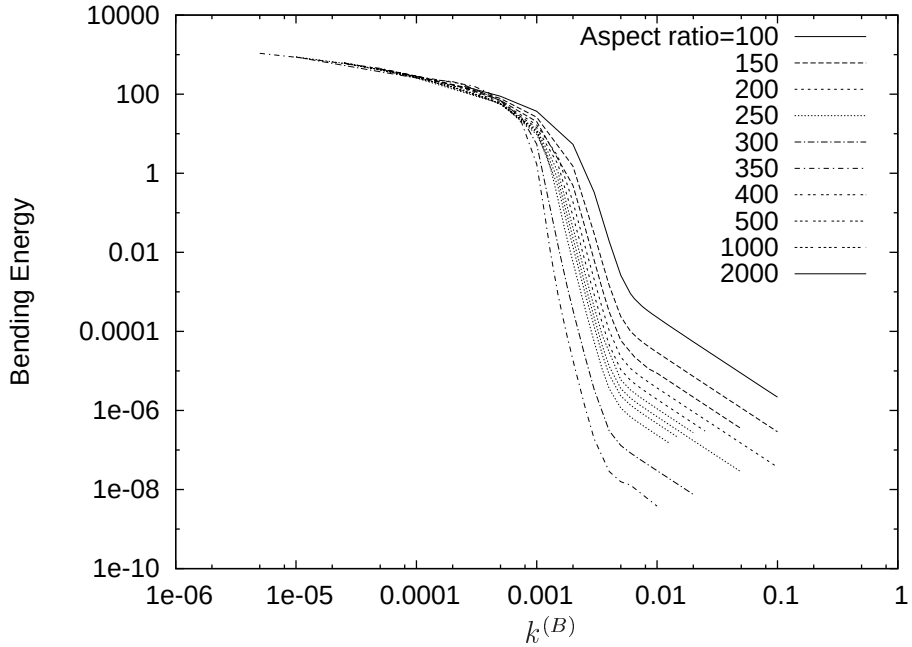

Figure 3.5: Log-log plot of bending energy per half orbit against stiffness for fibres of aspect ratio $a_r = 100$ to $a_r = 2000$.

3.1.3 Period of Rotation

As discussed in the introduction decreasing the aspect ratio of the fibre causes it to rotate faster, as the larger cross-section gives a greater velocity difference across the ends of the fibre, producing a larger couple to rotate the fibre. Bending due to flexibility leads to faster rotation as the bend in the fibre decreases its effective aspect ratio, as illustrated in figure 3.8.

In figure 3.9 we show the orbit period as a function of aspect ratio for fibres of various stiffnesses. Figure 3.10 shows the orbit period as a function of fibre stiffness for fibres of various aspect ratios. The period of rotation of a high aspect ratio rigid fibre is given by

$$T = \frac{2\pi}{\dot{\gamma}} a_r \tag{3.1.2}$$

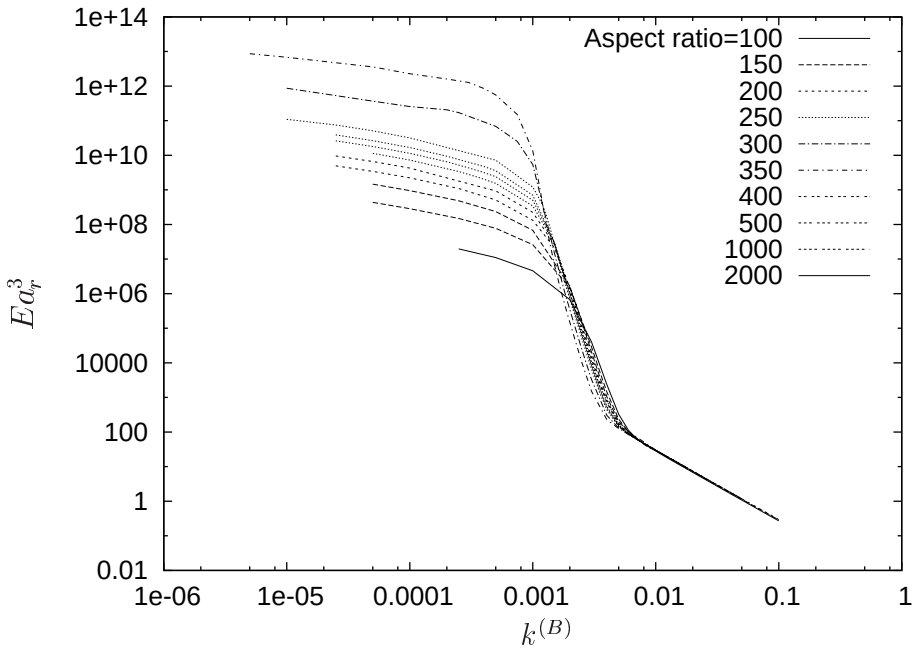

Figure 3.6: Log-log plot of bending energy per half orbit multiplied by a_r^3 against stiffness for fibres of aspect ratio $a_r = 100$ to $a_r = 2000$.

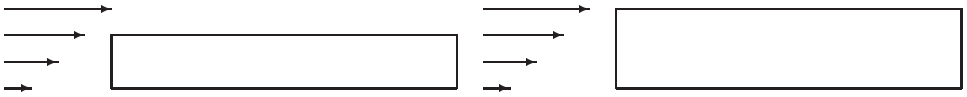

Figure 3.7: The fibre on the right has a smaller aspect ratio and therefore experiences a greater velocity difference across the ends of the fibre.

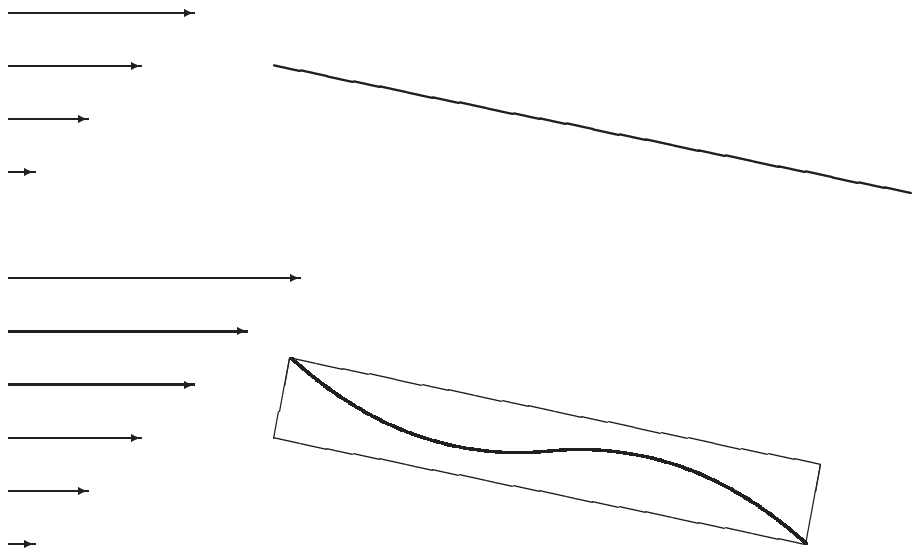

Figure 3.8: A bent fibre has a smaller effective aspect ratio and therefore rotates faster.

so the gradient in figure 3.9 for a rigid fibre is $\frac{2\pi}{\dot{\gamma}}$. For semi-flexible fibres the period of rotation decreases with increasing flexiblity and only increases linearly with aspect ratio at high aspect ratios.

One method for interpreting figure 3.9 is to define an effective aspect ratio based on the period of rotation. For the limit when bending is small we expect this effective aspect ratio to have the form

$$a_{r_{eff}} = \frac{2L}{d(1 + f(\frac{2L}{d}, k^{(B)}))}, \tag{3.1.3}$$

where d is the diameter of the fibre and $df(\frac{2L}{d}, k^{(B)})$ is the effective increase in diameter due to bending where f is a function of both stiffness and aspect ratio defined by

$$f = \frac{T_r}{T} - 1$$

where T is the orbit period and T_r is the orbit period of a rigid fibre. Our scaling analysis

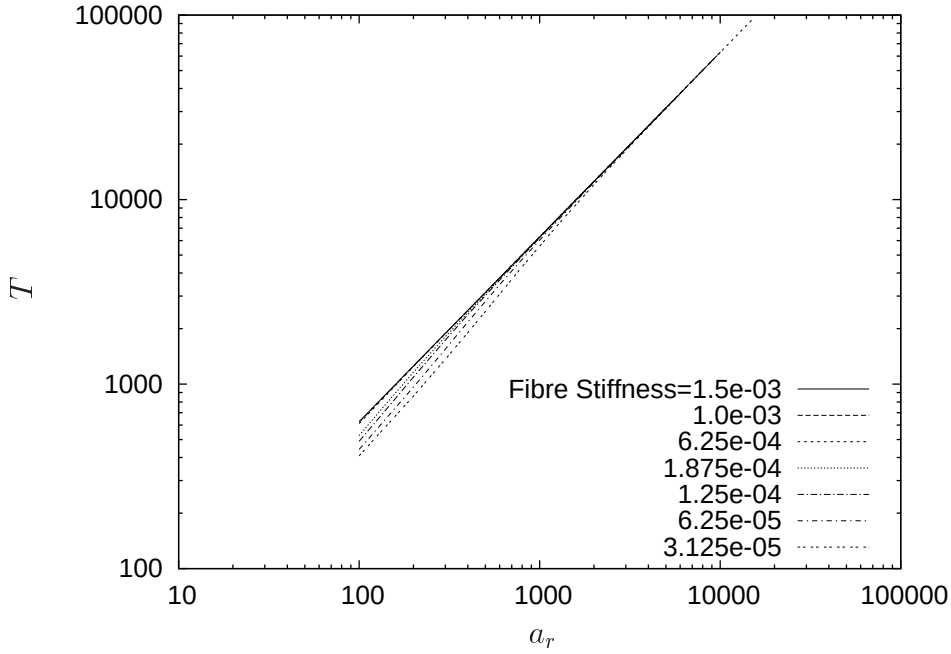

Figure 3.9: Period of rotation vs aspect ratio a_r for fibres of stiffnesses $k^{(B)} = 3.125 \times 10^{-5}$ to $k^{(B)} = 1.5 \times 10^{-3}$.

in chapter one shows that the bending torque on the fibre is proportional to the change in the angle of bend $\frac{d\theta}{ds}$, where the constant of proportionality is $k^{(B)}$. This would suggest that f should be a function of $k^{(B)}$ alone, however, if this were the case the period of rotation of a semi-flexible fibre would be linear in aspect ratio but with a gradient that depends upon flexibility. Instead we find that gradient increases with aspect ratio approaching $\frac{2\pi}{\dot{\gamma}}$ in the limit $a_r \to \infty$. Consequently $f \to 0$ as $a_r \to \infty$.

In figure 3.11 we plot the function $f(\frac{2L}{d}, k^{(B)})$ against $k^{(B)}a_r$ for fibres of different aspect ratios. The collapse of the plots shows that at leading order f is function of $k^{(B)}a_r$. This means that for intrinscially straight fibres in shear flow the dimensionless measure of the effect of bending stiffness on the period is $k^{(B)}a_r$ and not $k^{(B)}$. Recalling that $k^{(B)}$ is inversely proportional to fourth power of aspect ratio, this means that the effective stiffness of intrinsically straight fibres in shear flow actually scales with the inverse cube of aspect ratio.

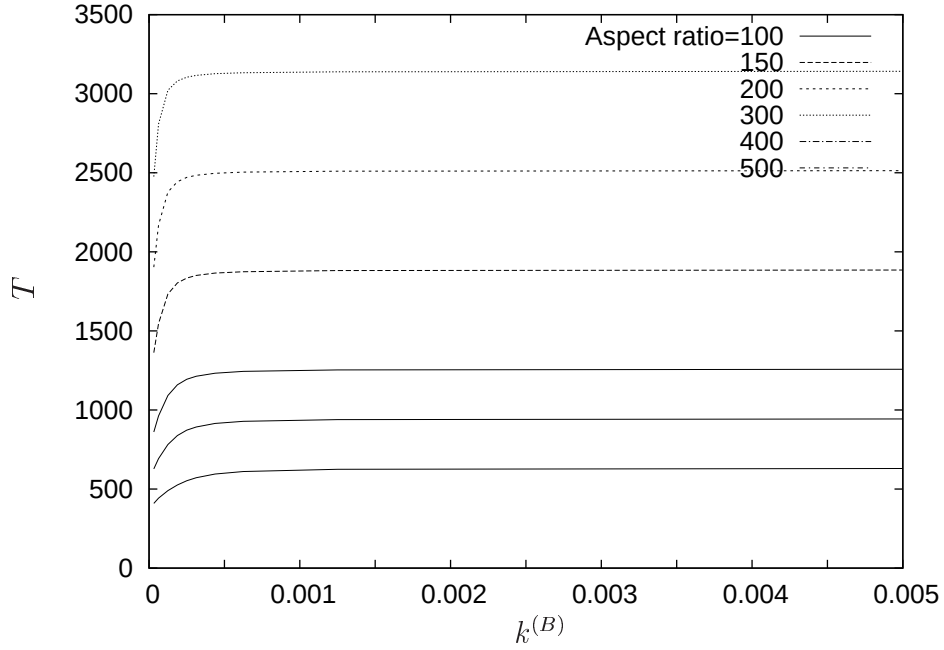

Figure 3.10: Period of rotation vs whole fibre stiffness $k^{(B)}$ for fibres of aspect ratios $a_r = 100$ to $a_r = 500$.

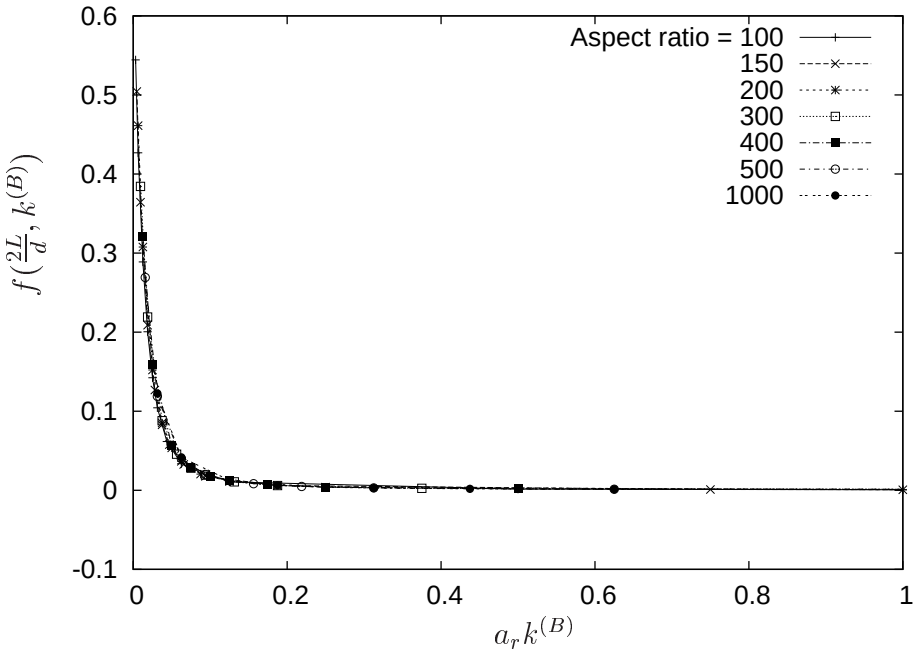

Figure 3.11: Plot of $f(k^{(B)}, a_r)$ against $k^{(B)} a_r$ for aspect ratios of 100 to 1000.

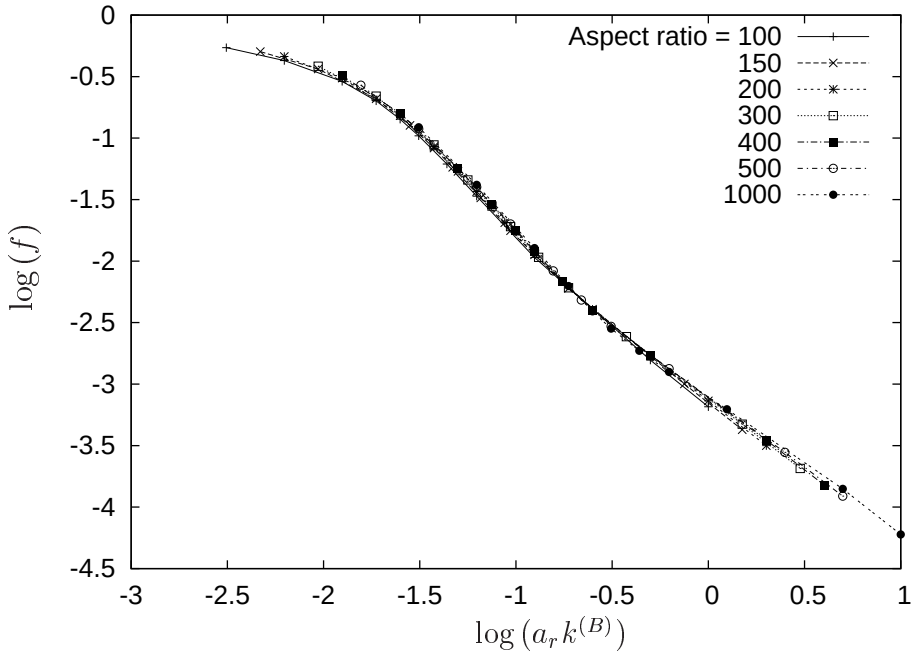

Figure 3.12: Log plot of $f(k^{(B)}, a_r)$ against $k^{(B)}a_r$ for aspect ratios of 100 to 1000.

Figure 3.12 is a log plot of figure 3.11 and shows that for large values of $k^{(B)}a_r$, f is approximately proportional to $\frac{1}{k^{(B)}a_r}$. In order to examine the departure from this behaviour in figure 3.13 we plot $k^{(B)}a_r f(\frac{2L}{d}, k^{(B)})$ against $k^{(B)}a_r$. From this we can see that for smaller $k^{(B)}a_r$ there are higher order contributions, in $(k^{(B)}a_r)^{-1}$, which are also dependent on $k^{(B)}a_r$ and also that for large values of $k^{(B)}a_r$ the plots do not superimpose, suggesting there are higher order contributions dependent on $k^{(B)}$ only. This is confirmed by figure 3.14 which shows $k^{(B)}a_r f(\frac{2L}{d}, k^{(B)})$ against stiffness only, and confirms that after a stiffness of approximately 0.007 the plots superimpose, and show a higher order contribution dependent on $k^{(B)}$ only.

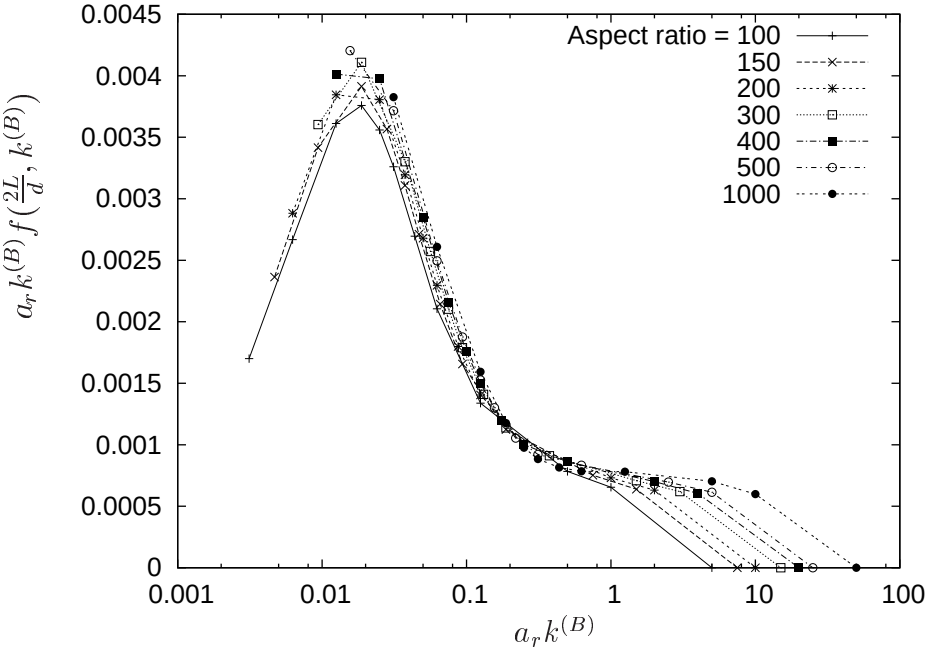

Figure 3.13: Plot of $k^{(B)} a_r f(k^{(B)}, a_r)$ against $k^{(B)} a_r$ for aspect ratios of 100 to 1000.

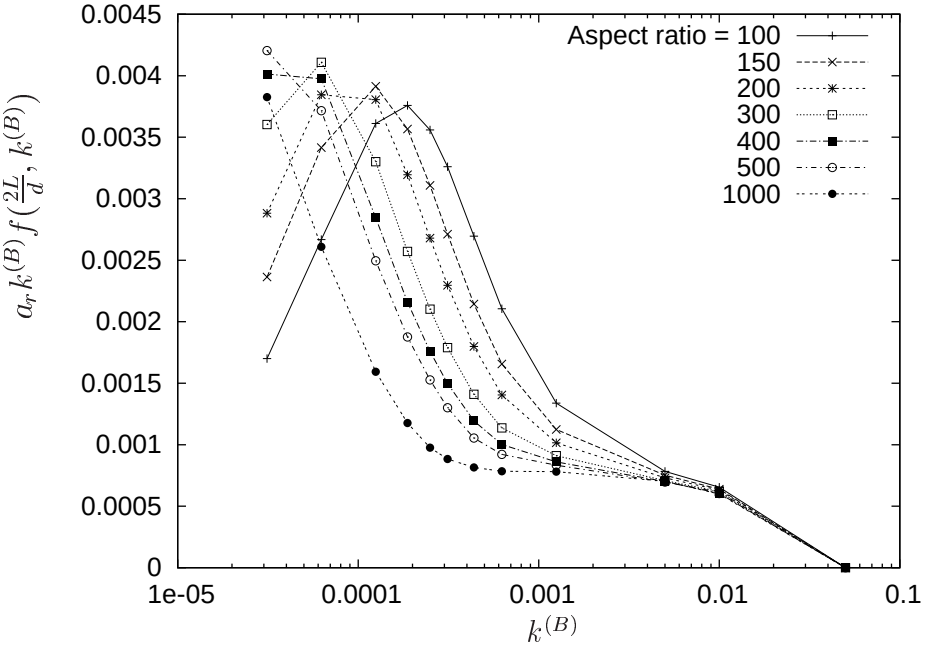

Figure 3.14: Plot of $k^{(B)} a_r f(k^{(B)}, a_r)$ against $k^{(B)}$ for aspect ratios of 100 to 1000.

3.2 Onset of Bending

In order to explain the above results and to gain a greater understanding of the factors governing the dynamics of a semi-flexible fibre in the flow-gradient plane we consider the two most important regions of the orbit. Firstly when the fibre is under maximum compressive force, i.e. when the fibre is at an angle of -45° with the x-axis and secondly when the fibre is within order $\frac{1}{a_r}$ of the flow-vorticity plane.

In both regions the effect of bending on the fibre is important. In the first region the fibre compressive forces are large leading to a significant amount of bending. In the second region the compressive forces are smaller, by a factor of $\frac{1}{a_r}$, however, the time spent in the region is larger by a factor of a_r.

We examine the influence of bending in the compressive quadrant on the fibre dynamics by performing a perturbation analysis similar to that of Hinch [17], who considered a fibre of zero bending stiffness; and Becker and Shelley [3] who incorporated a finite bending stiffness. We develop equations for the evolution of the changes of shape of a fibre in a compressional flow and then linearise the equations for small perturbations to a straight fibre. The linear equations are then solved numerically due to the presence of the fourth order bending term. We then consider the stability of the solutions for various values of the non-dimensional bending parameter.

To examine the influence of bending in the flow vorticity plane we calculate the bending torque distribution along a fibre aligned with the flow axis.

3.2.1 Linear Stability Analysis

Governing equations

We first derive the evolution equations for the changes in shape of a fibre. We consider an intrinsically straight fibre of length $2L$ described by orientation vector $\mathbf{p}(s,t)$ and position

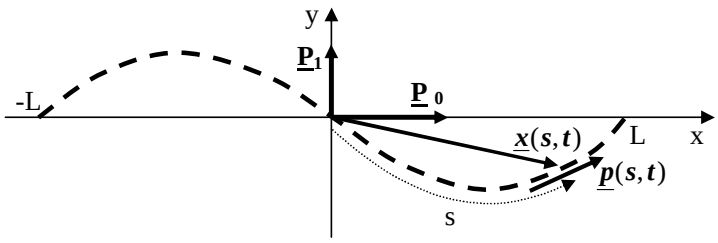

Figure 3.15: Diagram of a fibre showing the arc length s and the position and orientation vectors $\mathbf{x}(s,t)$ and $\mathbf{p}(s,t)$.

vector $\mathbf{x}(s,t)$, as shown in figure 3.15, where s is arc length and t time. The fibre is centred at $s = 0$. Here we shall consider only infinite aspect ratio fibres.

The inextensibility constraint on the fibre is given by

$$\mathbf{p} \cdot \mathbf{p} = 1. \tag{3.2.4}$$

which therefore implies

$$\dot{\mathbf{p}} \cdot \mathbf{p} = 0 \tag{3.2.5}$$

and

$$\mathbf{p}.\mathbf{p}' = 0 \tag{3.2.6}$$

where $\dot{\mathbf{p}} = \frac{\partial \mathbf{p}}{\partial t}$ and $\mathbf{p}' = \frac{\partial \mathbf{p}}{\partial s}$.

For a fibre with velocity $\dot{\mathbf{x}}(s)$ at a position s along the fibre in a linear flow given by $\mathbf{U}^{\infty} = \mathbf{K} \cdot \mathbf{x}$, the viscous force density acting on the fibre, as derived in subsection 1.2.5, is given by

$$\mathbf{f}_v = \frac{2\pi\mu}{\log 2a_r}(2\mathbf{I} - \mathbf{pp})(\mathbf{K} \cdot \mathbf{x} - \dot{\mathbf{x}}).$$

For an semi-flexible fibre the viscous forces $\mathbf{f}_v$, are balanced by the tension in the fibre

and the fibre stiffness such that $-\mathbf{f}_v = \mathbf{f}_f$, where $\mathbf{f}_f$ is given by,

$$\mathbf{f}_f = \frac{\partial}{\partial s}(\tau \mathbf{p}) - EI\frac{\partial^3 \mathbf{p}}{\partial s^3} \tag{3.2.7}$$

where EI is the flexural rigidity. The tension is the net force transmitted over a cross-section of the fibre. It preserves the arc length of the fibre so that it may satisfy the inextensibility constraint 3.2.4.

Equating the two forces and non-dimensionalising time with respect to the inverse shear rate $\frac{1}{\dot{\gamma}}$, length with respect to L and tension with respect to $\frac{2\pi\mu\dot{\gamma}L^2}{\log 2a_r}$, we get

$$\dot{\mathbf{x}} - \mathbf{K}\cdot\mathbf{x} = \frac{1}{2}(\mathbf{I}+\mathbf{pp})\left(\frac{\partial}{\partial s}(\tau\mathbf{p}) - \frac{8}{3}k^{(B)}\frac{\partial^3\mathbf{p}}{\partial s^3}\right)$$

where $k^{(B)} = \frac{3EI\log 2a_r}{16\pi\mu L^4\dot{\gamma}}$ is the non-dimensional bending stiffness derived in section 1.3.3.

Differentiating this with respect to s, gives

$$\dot{\mathbf{p}} - \mathbf{K}\cdot\mathbf{p} = \frac{1}{2}(\mathbf{I}+\mathbf{pp})\left(\frac{\partial^2\tau}{\partial s^2} + \frac{\partial^2\mathbf{p}}{\partial s^2} + \frac{\partial\tau}{\partial s}\frac{\partial\mathbf{p}}{\partial s} - \frac{8}{3}k^{(B)}\frac{\partial^4\mathbf{p}}{\partial s^4}\right)$$

$$+\frac{1}{2}(\mathbf{p}\frac{\partial\mathbf{p}}{\partial s} + \frac{\partial\mathbf{p}}{\partial s}\mathbf{p})\left(\frac{\partial\tau}{\partial s}\mathbf{p} + \tau\frac{\partial\mathbf{p}}{\partial s} - \frac{8}{3}k^{(B)}\frac{\partial^3\mathbf{p}}{\partial s^3}\right),$$

and using constraint equations (3.2.4) and (3.2.6) the main evolution equation for the fibre becomes

$$\dot{\mathbf{p}} = \mathbf{K}\cdot\mathbf{p} + \tau''\mathbf{p} + \frac{1}{2}\tau\mathbf{p}'' + \frac{3}{2}\tau'\mathbf{p}' - \frac{4}{3}k^{(B)}\left(\mathbf{p}^{iv} + (\mathbf{p}(\mathbf{p}.\mathbf{p}'''))'\right). \tag{3.2.8}$$

Here p^{iv} is $\frac{\partial^4\mathbf{p}}{\partial s^4}$.

To obtain an equation for the tension we substitute equation (3.2.8) into the inextensibility

constraint equation (3.2.5). This yields a second order differential equation for the tension

$$\tau'' + \frac{1}{2}(\mathbf{p}')^2\tau = -\mathbf{p}\cdot\mathbf{E}\cdot\mathbf{p} + \frac{8}{3}k^{(B)}(\mathbf{p}^{iv}.\mathbf{p} + \frac{1}{2}\mathbf{p}'.\mathbf{p}''') \tag{3.2.9}$$

with boundary conditions $\tau = 0$ at $s = \pm L$.

Small perturbations to a straight fibre

We shall now consider small perturbations to a straight fibre such that

$$\mathbf{p}(s,t) = \mathbf{p}_0(t) + \epsilon\mathbf{p}_1(s,t) \tag{3.2.10}$$

where $\epsilon << 1$, $\mathbf{p}_0(t)$ is the orientation of the straight fibre and $\mathbf{p}_1(s,t)$ are the first order distortions to the fibre, such that

$$\mathbf{p}_0.\mathbf{p}_1 = 0$$

and

$$\mathbf{p}.\mathbf{p} = \mathbf{p}_0.\mathbf{p}_0 + \epsilon^2\mathbf{p}_1.\mathbf{p}_1 = 1 + O(\epsilon^2).$$

An illustration of vectors $\mathbf{p}_0$ and $\mathbf{p}_1$ are shown in figure 3.15.

We assume that the variation in the tension along the length of the fibre is small and hence write the tension τ as

$$\tau(s,t) = \tau_0(t) + \epsilon\tau_1(s,t).$$

Substituting this into equation (3.2.9) yields

$$\tau'' = -\mathbf{p}_0\cdot\mathbf{E}\cdot\mathbf{p}_0 - 2\epsilon\mathbf{p}_0\cdot\mathbf{E}\cdot\mathbf{p}_1 + \epsilon\frac{8}{3}k^{(B)}\mathbf{p}_1^{iv}.\mathbf{p}_0$$

to order ϵ.

Solving the second order differential equation for tension with the boundary conditions

on τ and $\mathbf{p}' = 0$ at $s = \pm L$ gives

$$\tau = \mathbf{p}_0 \cdot \mathbf{E} \cdot \mathbf{p}_0 \frac{1}{2}(1 - s^2) - 2\epsilon \mathbf{p}_0 \cdot \mathbf{E} \cdot \left(\int_{-1}^{s} \int_{-1}^{s} \mathbf{p}_1 - \frac{1+s}{2L} \int_{-1}^{1} \int_{-1}^{1} \mathbf{p}_1 \right) + \epsilon \frac{8}{3} k^{(B)} \mathbf{p}_1''.\mathbf{p}_0. \tag{3.2.11}$$

Substituting the tension equation (3.2.11) and shape equation (3.2.10) into the evolution equation (3.2.8) and then subtracting the rotation of the straight thread
$\dot{\mathbf{p}}_0 = \mathbf{K} \cdot \mathbf{p}_0 - \mathbf{p}_0 \mathbf{p}_0 . \mathbf{E} \cdot \mathbf{p}_0$, we get an equation for the evolution of the distortions $\mathbf{p}_1$,

$$\dot{\mathbf{p}}_1 = \mathbf{K} \cdot \mathbf{p}_1 + \mathbf{p}_0 \cdot \mathbf{E} \cdot \mathbf{p}_0 \left(-\mathbf{p}_1 + \frac{1}{4}(1 - s^2)\mathbf{p}_1'' - \frac{3}{2} s \mathbf{p}_1' \right) - 2\mathbf{p}_0 \mathbf{p}_0 \cdot \mathbf{E} \cdot \mathbf{p}_1 - \frac{4}{3} k^{(B)} \mathbf{p}^{iv}. \tag{3.2.12}$$

The change in $\mathbf{p}_1$ in time in equation (3.2.12) arise both from the changes in shape and from the rotation of $\mathbf{p}_1$ with $\mathbf{p}_0$. To remove the rotations we introduce the orthonormal triad $\mathbf{p}_0, \mathbf{q}_0$ and $\mathbf{r}_0$ in the frame of the unperturbed fibre. The rotation of vectors $\mathbf{q}_0$ and $\mathbf{r}_0$ result only from the rotation of $\mathbf{p}_0$ so that

$$\dot{\mathbf{q}}_\mathbf{0} = -\mathbf{p}_0 (\mathbf{q}_0 . \dot{\mathbf{p}}_0) = \mathbf{p}_0 (\mathbf{q}_0 \cdot \mathbf{K} \cdot \mathbf{p}_0),$$

$$\dot{\mathbf{r}}_\mathbf{0} = -\mathbf{p}_0 (\mathbf{r}_0 . \dot{\mathbf{p}}_0) = \mathbf{p}_0 (\mathbf{r}_0 \cdot \mathbf{K} \cdot \mathbf{p}_0).$$

Let the distortions from the straight fibre $\mathbf{p}_1$ be written as
$\mathbf{p}_1(s,t) = \mathbf{q}_0(t) q(s,t) + \mathbf{r}_0(t) r(s,t)$. Substituting this into equation (3.2.12) and taking the dot product with $\mathbf{q}_0$ and $\mathbf{r}_0$ gives equations for $\dot{q}$ and $\dot{r}$ respectively.

$$\dot{q} = (\mathbf{q}_0 \cdot \mathbf{K} \cdot \mathbf{q}_0) q + (\mathbf{q}_0 \cdot \mathbf{K} \cdot \mathbf{r}_0) r + \mathbf{p}_0 \cdot \mathbf{E} \cdot \mathbf{p}_0 \left(-q + \frac{1}{4}(1 - s^2) q'' - \frac{3}{2} s q' \right) - \frac{4}{3} k^{(B)} q^{iv} \tag{3.2.13}$$

$$\dot{r} = (\mathbf{r}_0 \cdot \mathbf{K} \cdot \mathbf{q}_0)q + (\mathbf{r}_0 \cdot \mathbf{K} \cdot \mathbf{r}_0)r + \mathbf{p}_0 \cdot \mathbf{E} \cdot \mathbf{p}_0 \left(-r + \frac{1}{4}(1-s^2)r'' - \frac{3}{2}sr'\right) - \frac{4}{3}k^{(B)}r^{iv} \tag{3.2.14}$$

For a bending stiffness of zero the second order differential equation can be solved analytically as described by Hinch [17]. Where $k^{(B)}$ is non-zero, an analytic solution does not exist and so a shooting technique has been employed.

Shooting Technique

Let us consider a fibre located in the $x-y$ plane so that $r = 0$ and $\mathbf{r}_0 \cdot \mathbf{K} \cdot \mathbf{r}_0 = 0$. We therefore have $\mathbf{q}_0 \cdot \mathbf{K} \cdot \mathbf{q}_0 = -\mathbf{p_0} \cdot \mathbf{E} \cdot \mathbf{p_0}$ for a symmetric flow and so equation (3.2.13) becomes

$$\dot{q} = \mathbf{p}_0 \cdot \mathbf{E} \cdot \mathbf{p}_0 \left(-2q + \frac{1}{4}(1-s^2)q'' - \frac{3}{2}sq'\right) - \frac{4}{3}k^{(B)}q^{iv}. \tag{3.2.15}$$

Provided that $\mathbf{p}_0 \cdot \mathbf{E} \cdot \mathbf{p}_0$ remains approximately constant we seek a solution of the form $q = Q(s)e^{\sigma t}$. Substituting this into equation (3.2.15) gives

$$\frac{\sigma}{k^{(B)}}Q = \frac{\mathbf{p}_0 \cdot \mathbf{E} \cdot \mathbf{p}_0}{k^{(B)}} \left(-2Q + \frac{1}{4}(1-s^2)Q'' - \frac{3}{2}sQ'\right) - \frac{4}{3}Q^{iv}. \tag{3.2.16}$$

Before attempting to solve the full equation we shall first consider the simplest case of a fibre in quiescent fluid where $\mathbf{p}_0 \cdot \mathbf{E} \cdot \mathbf{p}_0 = 0$. Equation (3.2.16) then reduces to

$$Q^{iv} - k^4 Q = 0 \tag{3.2.17}$$

where $k^4 = -\frac{3\sigma}{4k^{(B)}}$. This equation has even solutions of the form

$$Q(s) = A(\cos ks + \alpha \cosh ks)$$

and odd solutions of the form

$$Q(s) = B(\sin ks + \beta \sinh ks).$$

Imposing the boundary conditions $q' = q'' = 0$ and hence $Q' = Q'' = 0$ at $s = \pm 1$ we can deduce that the even modes will occur at values of k such that

$$\tan k = \tanh k$$

and the odd modes will occur at values of k such that

$$\tan k = -\tanh k.$$

Substituting our value of k into the corresponding solutions and using the boundary conditions once again we can then obtain the values of α or β for each mode. Figure 3.16 shows the plots of $q(s)$ for the first 6 modes. It should be noted that an even solutions for $Q(s)$ give odd shape solutions and vice-versa as shown in figure 3.17. Mode 1 is the even C shape and mode 2 the odd S shape. As expected at $\frac{p_0 \cdot \underline{\underline{E}} \cdot p_0}{k^{(B)}} = 0$ all values of $\frac{\sigma}{k^{(B)}}$ are negative and hence all modes decay.

To solve equation (3.2.16) when $\frac{p_0 \cdot \underline{\underline{E}} \cdot p_0}{k^{(B)}} \neq 0$ we employ a shooting technique. Putting $Q_0 = Q$, $Q_1 = Q'$, $Q_2 = Q''$ and $Q_3 = Q'''$, equation (3.2.15) can be written as four first order differential equations.

$$\left.\begin{aligned} Q_3' &= -\tfrac{3}{4k^{(B)}}\left(\sigma Q_0 - \mathbf{p}_0 \cdot \mathbf{E} \cdot \mathbf{p}_0 \left(-2Q_0 + \tfrac{1}{4}(1-s^2)Q_2 - \tfrac{3}{2}sQ_1\right)\right) \\ Q_2' &= Q_3 \\ Q_1' &= Q_2 \\ Q_0' &= Q_1 \end{aligned}\right\} \qquad (3.2.18)$$

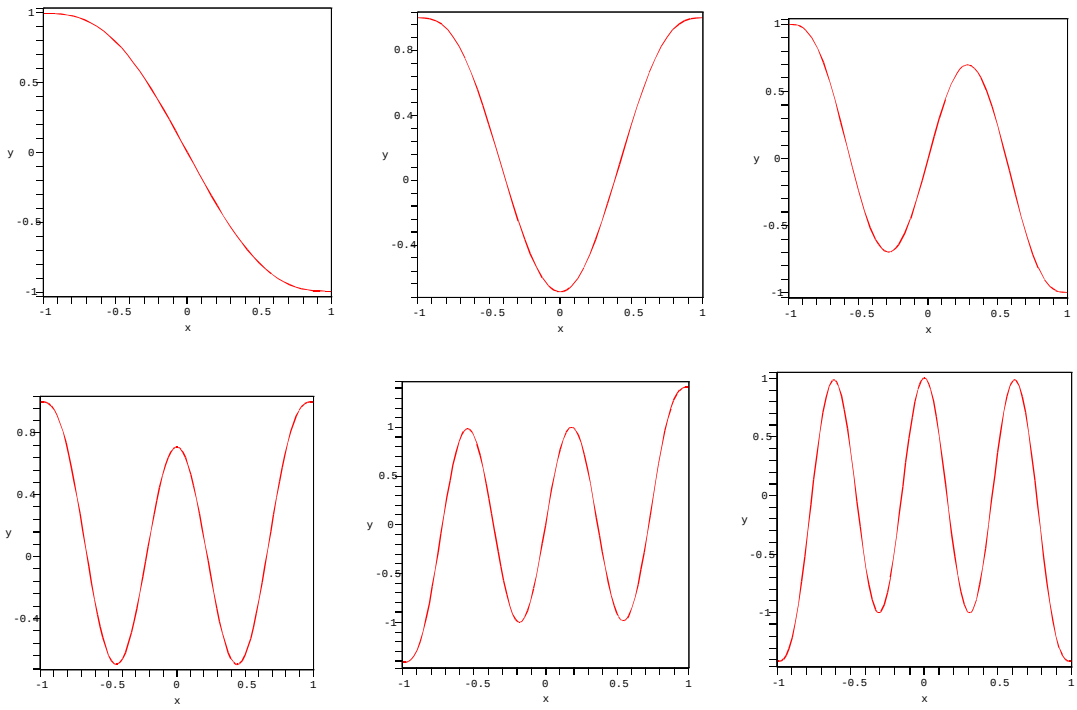

Figure 3.16: Plots of Q(s) for modes 1 to 6 with $A = B = \pm\frac{1}{\sqrt{2}}$

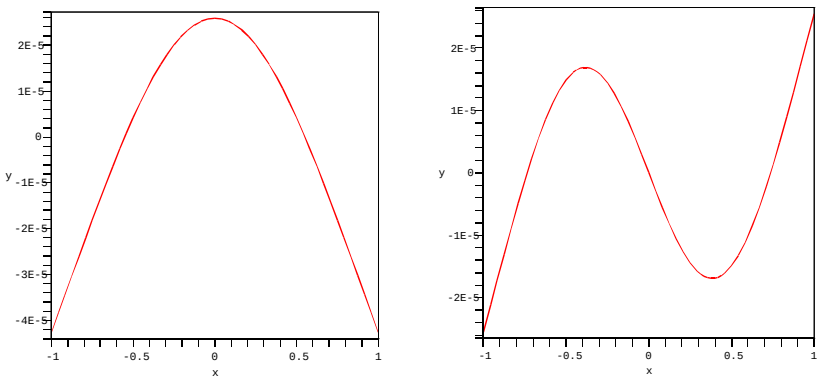

Figure 3.17: Plots of the shape distortions $\mathbf{p}_1$ with $\epsilon = 10^{-4}$ and $A = B = -\frac{1}{\sqrt{2}}$ corresponding to mode 1, C-mode and mode 2, S-mode.

It follows from the boundary condition $\mathbf{p}' = 0$ at $s = \pm 1$ that $Q_1 = 0$ at $s = \pm 1$. The other boundary conditions, $\mathbf{p}'' = 0$ and hence $Q_2 = 0$ at $s = \pm 1$ follow from the net force and net torque on the fibre being zero. The growth rates $\frac{\sigma}{k^{(B)}}$ are the eigenvalues corresponding to eigenfunctions $Q_s(s)$. To find the eigenvalues and eigenfunctions we exploit the linearity and symmetry of the solutions.

Suppose we have a solution for $\mathbf{Q}_s(s)$ where

$$\mathbf{Q}_s(s) = (Q_0(s), Q_1(s), Q_2(s), Q_3(s))$$

of the form

$$\mathbf{Q}_s(s) = D(\mathbf{Q}^a(s) + \lambda \mathbf{Q}^b(s))$$

where

$$\mathbf{Q}^a = (Q_0^a, Q_1^a, Q_2^a, Q_3^a)\,,$$

$$\mathbf{Q}^b = \left(Q_0^b, Q_1^b, Q_2^b, Q_3^b\right).$$

To satisfy the boundary conditions we choose $\mathbf{Q}^a$ and $\mathbf{Q}^b$ to be

$$\mathbf{Q}^a = (1, 0, 0, 0)\,,$$

$$\mathbf{Q}^b = (0, 0, 0, 1)$$

at $s = -1$.

For an even solution we require in addition that $Q_1 = Q_3 = 0$ at $s = 0$ so that

$$\begin{aligned} Q_1^a(0) + \lambda Q_1^b(0) &= 0, \\ Q_3^a(0) + \lambda Q_3^b(0) &= 0. \end{aligned} \tag{3.2.19}$$

To satisfy both conditions simultaneously requires the determinant of the matrix

$$\begin{pmatrix} Q_1^a & Q_1^b \\ \\ Q_3^a & Q_3^b \end{pmatrix}$$

to be zero, which provides our condition at $\frac{\sigma}{k^{(B)}}$.

Similarly an odd solution requires $Q_0 = Q_2 = 0$ on $s = 0$ so that

$$\begin{aligned} Q_0^a(0) + \lambda Q_0^b(0) &= 0, \\ Q_2^a(0) + \lambda Q_2^b(0) &= 0. \end{aligned} \tag{3.2.20}$$

Again to satisfy both conditions simultaneously requires the determinant of the matrix

$$\begin{pmatrix} Q_0^a & Q_0^b \\ \\ Q_2^a & Q_2^b \end{pmatrix}$$

to be zero.

We obtain the values of $\mathbf{Q}^a$ and $\mathbf{Q}^b$ at $s = 0$ by integrating equation (3.2.18) from $s = -1$ to $s = 0$ using fourth order Runge Kutta and starting with the proposed initial values of each solution at $s = -1$. We obtain the correct value of $\frac{\sigma}{k^{(B)}}$ by using either bisection or Newton Raphson to find a zero determinant. Once the value of $\frac{\sigma}{k^{(B)}}$ is found we can obtain λ using equations (3.2.19) or (3.2.20).

Starting from the analytic solutions for $\frac{\mathbf{p}_0 \cdot \mathbf{E} \cdot \mathbf{p}_0}{k^{(B)}} = 0$ we can find the solutions of $\frac{\sigma}{k^{(B)}}$ by decreasing $\frac{\mathbf{p}_0 \cdot \mathbf{E} \cdot \mathbf{p}_0}{k^{(B)}}$ in small increments and using the previous answer of $\frac{\sigma}{k^{(B)}}$ as our initial estimate. At certain values of $\frac{\mathbf{p}_0 \cdot \mathbf{E} \cdot \mathbf{p}_0}{k^{(B)}}$ two different branches of real eigenvalues coalesce, and are replaced by a complex eigenvalue pair. These were found using a Newton Raphson scheme.

3.2.2 Stability Analysis Results

The values of the growth rate $\frac{\sigma}{k^{(B)}}$ obtained for different values of $\frac{\mathbf{p}_0 \cdot \mathbf{E} \cdot \mathbf{p}_0}{k^{(B)}}$ are shown in figure 3.18. For positive values of $\frac{\mathbf{p}_0 \cdot \mathbf{E} \cdot \mathbf{p}_0}{k^{(B)}}$ all modes are stable. At small, negative values of $\frac{\mathbf{p}_0 \cdot \mathbf{E} \cdot \mathbf{p}_0}{k^{(B)}}$ the most unstable mode is mode 1, the C shaped mode. This mode goes unstable at a dimensionless flow strength of -12.77. Mode 2, the S shaped mode goes unstable at a $\frac{\mathbf{p}_0 \cdot \mathbf{E} \cdot \mathbf{p}_0}{k^{(B)}}$ value of -64.5 however at this flow strength the C mode is still the most unstable mode. The S mode does not become the most unstable mode until a flow strength of approximately -146.67. We found no unstable real modes in the region $-378.67 < \frac{\mathbf{p}_0 \cdot \mathbf{E} \cdot \mathbf{p}_0}{k^{(B)}} < -429.33$, however, we did find odd and even complex modes in this region, the even mode being the most unstable.

These results are in good agreement with those of Becker and Shelley [3]. The non-dimensional parameters used in the two studies differ by a factor of 12 in the flow strengths. Multiplying our results for the values at which the C and the S mode become the most unstable by 12 gives flow strengths of -153.24 and -1760 respectively. These compare favourably with the approximate flow strengths of -153.2 and -1880 found by Becker [3] who uses pseudospectral collocation to find the most unstable modes. Our results benefit from showing the growth rates of more than just the most unstable mode at each flow strength.

Figures 3.19 to 3.22 show the shapes of the modes at the positions marked on figure 3.18.

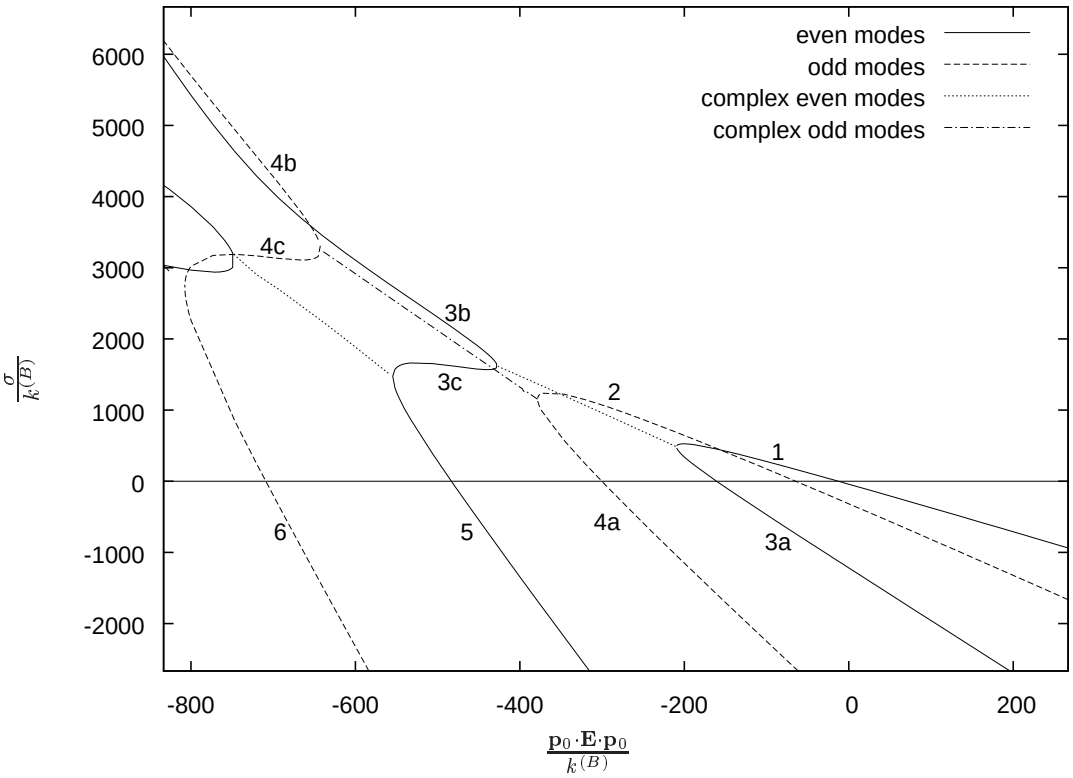

Figure 3.18: Plot of growth rate ($\frac{\sigma}{k^{(B)}}$) vs flow strength ($\frac{\mathbf{p}_0 \cdot \mathbf{E} \cdot \mathbf{p}_0}{k^{(B)}}$) from linear stability analysis of semi-flexible fibre under compressional flow.

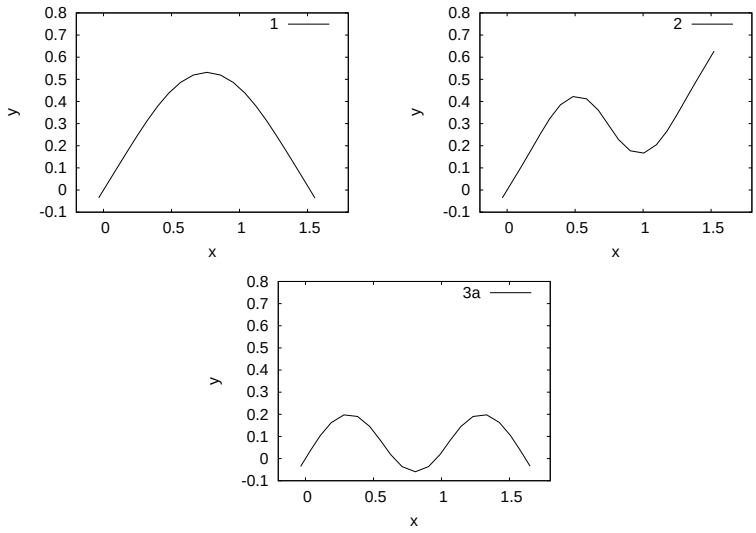

Figure 3.19: From left to right - plots of mode shapes for points marked 1, 2 and 3a in figure 3.18

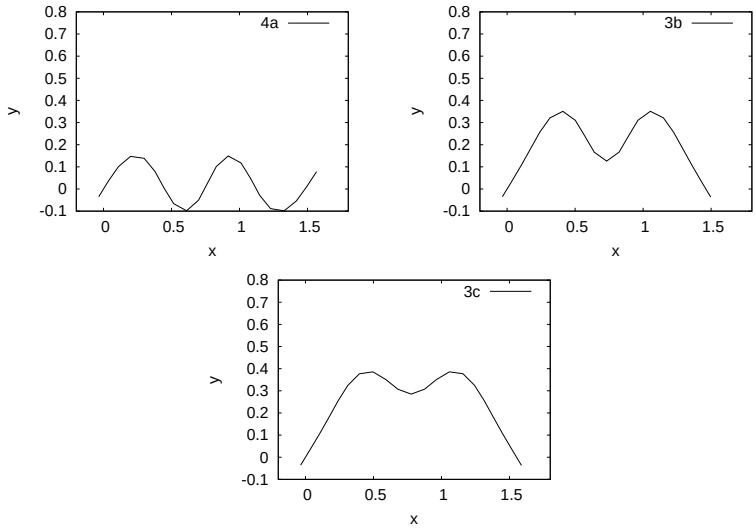

Figure 3.20: From left to right - plots of mode shapes for points marked 4a, 3b and 3c in figure 3.18

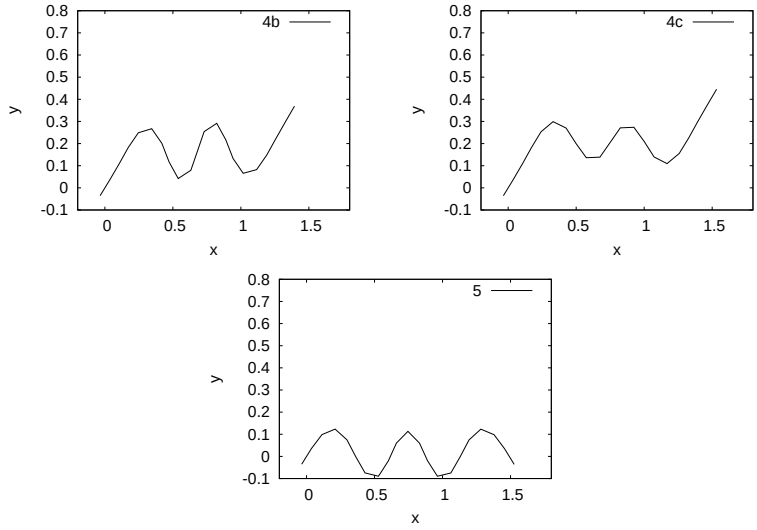

Figure 3.21: From left to right - plots of mode shapes for points marked 4b, 4c and 5 in figure 3.18

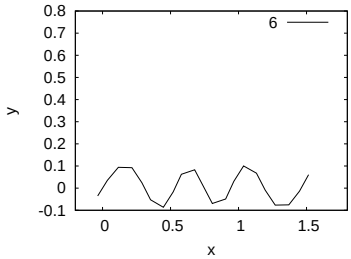

Figure 3.22: Plot of mode shape for point marked 6 in figure 3.18

Simulation Results for Compressional Flow

In shear flow the rotation of the fibre changes the value of $\mathbf{p}_0 \cdot \mathbf{E} \cdot \mathbf{p}_0$. To compare the results of the linear stability analysis with our simulations we consider a fibre aligned along the x axis in the compressional flow, $\mathbf{u} = (-Ex, Ey, 0)$ as shown in figure 3.23. We consider only small order distortions allowing us to make the approximation $\mathbf{p}_0 \cdot \mathbf{E} \cdot \mathbf{p}_0 \approx -E$.

Let us first consider mode 1, the C-shaped mode. At $\frac{E}{k^{(B)}} < 12.77$ it is stable and should therefore decay. At $12.77 < \frac{E}{k^{(B)}} < 209.33$ it is unstable and should therefore grow. Although mode 1 is unstable, mode 2 is the most unstable mode in the range $146.67 < \frac{E}{k^{(B)}} < 209.33$. For $209.33 < \frac{E}{k^{(B)}} < 346.67$ mode 2 is still the most unstable mode however, complex mode 3 has replaced mode 1. We choose an initial orientation such that $\mathbf{p}_0 = (1, 0, 0)$ and perturbation such that $\epsilon = 10^{-4}$ and $A = -\frac{1}{\sqrt{2}}$. Plots of the fibre at flow strengths of $\frac{E}{k^{(B)}} = 0$, $\frac{E}{k^{(B)}} = 53.33$ and $\frac{E}{k^{(B)}} = 240$ are shown in figures 3.24, 3.25 and 3.26 respectively. Figures 3.24 and 3.25 confirm that the mode 1 shape perturbation does decay as expected at $\frac{E}{k^{(B)}} = 0$ and grow as expected at $\frac{E}{k^{(B)}} = 53.33$. At $\frac{E}{k^{(B)}} = 240$ the mode grows initially but is superceded by the complex mode 3. Note that although the odd mode 2 is the most unstable it is completely decoupled from the even modes and so does not appear.

Let us now consider mode 2, the S-shaped mode. At $\frac{E}{k^{(B)}} < 64.5$ mode 2 should decay and for $64.5 < \frac{E}{k^{(B)}} > 378.4$ mode 2 should grow. For $146.67 < \frac{E}{k^{(B)}} < 346.67$ it is the most unstable mode. We choose a fibre with an initial orientation such that $\mathbf{p}_0 = (1, 0, 0)$ and perturbation such that $\epsilon = 10^{-4}$ and $B = -\frac{1}{\sqrt{2}}$. Figures 3.27, 3.28 and 3.29 show plots of the fibre at flow strengths of $\frac{E}{k^{(B)}} = 53.33$, $\frac{E}{k^{(B)}} = 133.33$ and $\frac{E}{k^{(B)}} = 400$ respectively. At $E = 53.33$ the S mode decays as expected, again the mode 1 does not grow despite being unstable at this flow strength because it has the opposite symmetry. At $E = 133.33$ mode 2 grows as expected. At $\frac{E}{k^{(B)}} = 400$ mode 2 grows and is eventually superceded by complex mode 4.

We look at some higher modes to confirm our findings. We consider a fibre with an

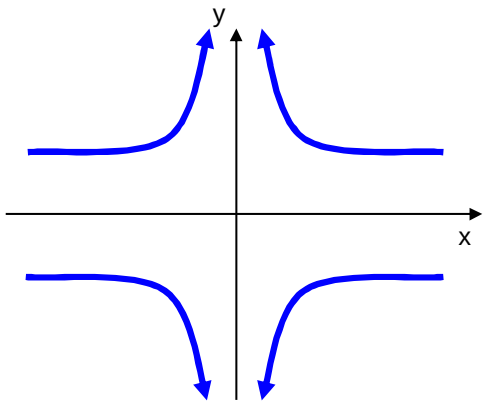

Figure 3.23: Diagram showing the compressional flow $\mathbf{u} = (-Ex, Ey, 0)$.

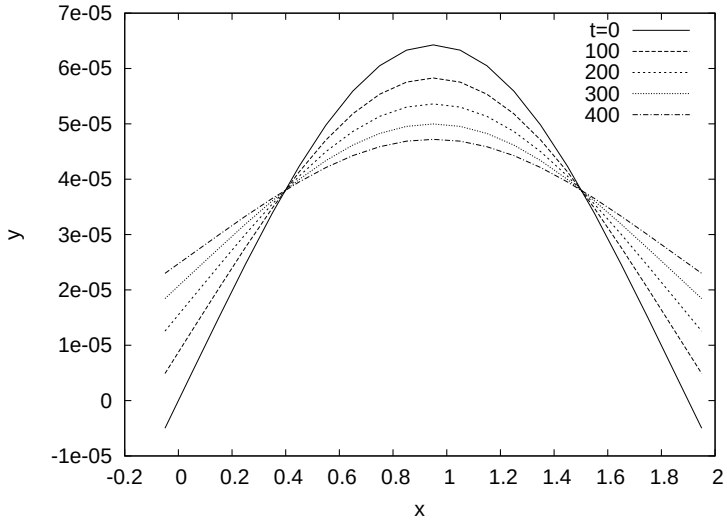

Figure 3.24: Fibre with small initial mode 1 perturbation in a flow of strength $\frac{E}{k^{(B)}} = 0$. The perturbation decays.

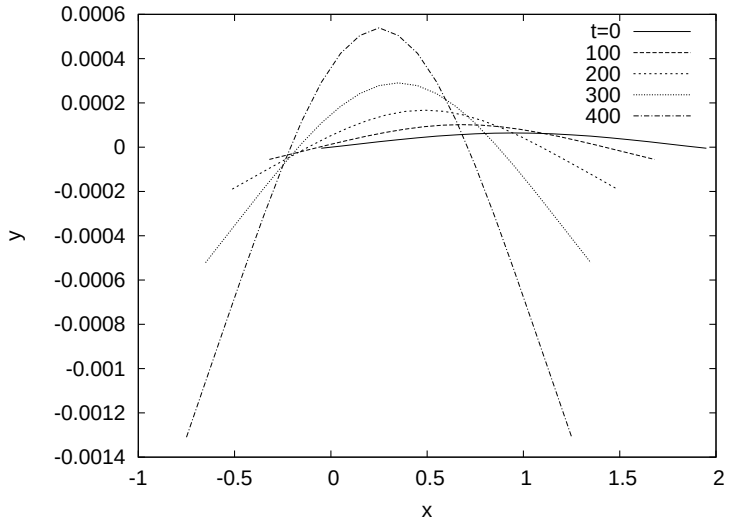

Figure 3.25: Fibre with small initial mode 1 perturbation in a flow of strength $\frac{E}{k^{(B)}} = 53.33$. The perturbation grows.

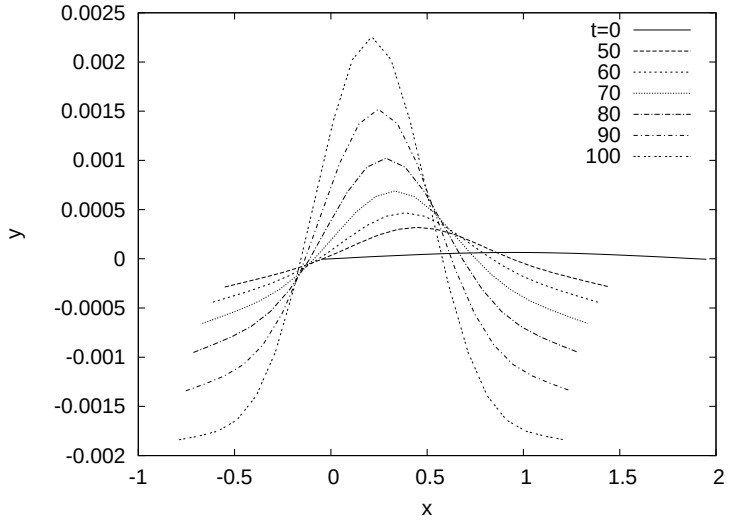

Figure 3.26: Fibre with small initial mode 1 perturbation in a flow of strength $\frac{E}{k^{(B)}} = 240$. The perturbation grows but is eventually superceded by mode 3 as can be seen by the curling upwards of the fibre ends at time $t = 100$.

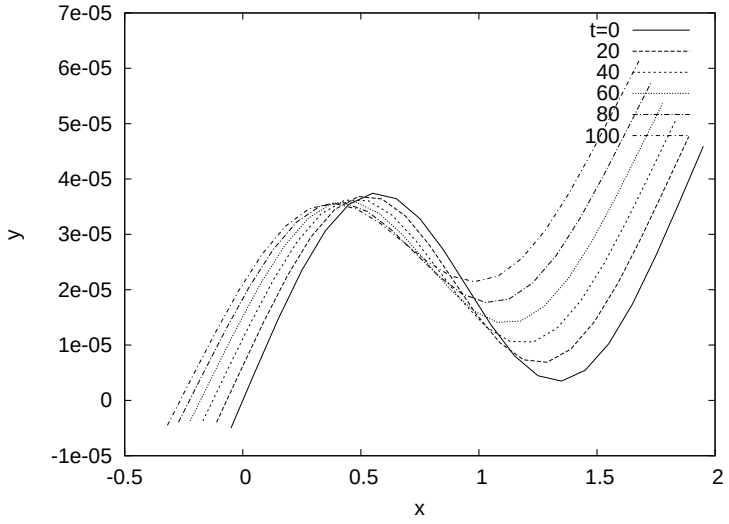

Figure 3.27: Fibre with small initial mode 2 perturbation in a flow of strength $\frac{E}{k^{(B)}} = 53.33$. The perturbation decays.

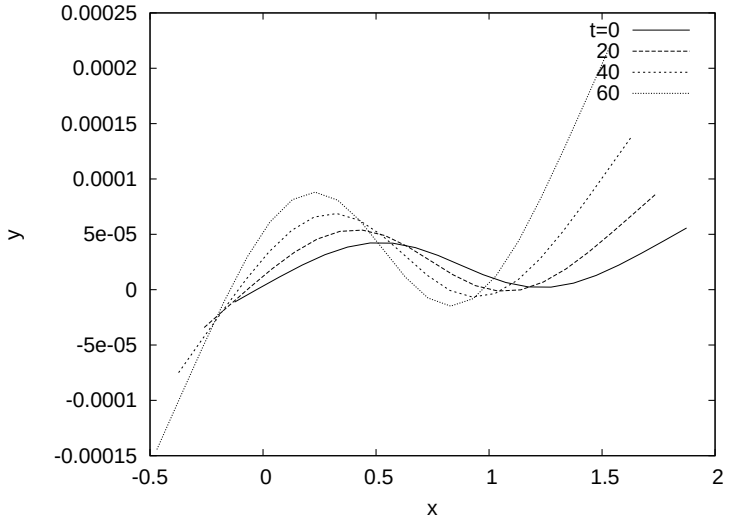

Figure 3.28: Fibre with small initial mode 2 perturbation in a flow of strength $\frac{E}{k^{(B)}} = 133.33$. The perturbation grows.

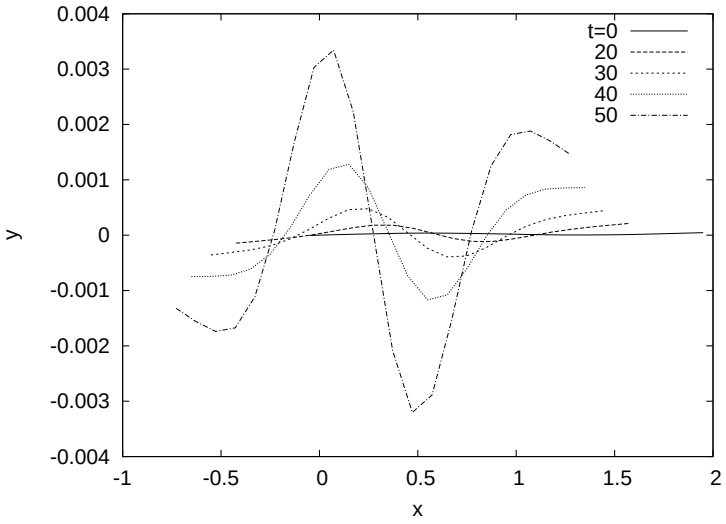

Figure 3.29: Fibre with small initial mode 2 perturbation in a flow of strength $\frac{E}{k^{(B)}} = 400$. The perturbation grows and is eventually superceded by mode 4.

initial orientation $\mathbf{p}_0 = (1, 0, 0)$ and perturbation such that $\epsilon = 10^{-4}$ and $A = \frac{1}{\sqrt{2}}$. At $\frac{E}{k^{(B)}} = 133.33$, mode 3 is not unstable at this flow strength and so does not grow however, mode 1 is unstable and does grow (figure 3.30). At $\frac{E}{k^{(B)}} = 200$ (figure 3.31 and 3.32) mode 3 does grow, however, mode 1 is still more unstable at this flow strength and so mode 3 is superceded by mode 1. At $\frac{E}{k^{(B)}} = 400$ (figure 3.33) mode 3 is the most unstable mode and hence grows.

A fibre with an initial mode 4 deformation (with $\epsilon = 10^{-4}$ and $B = \frac{1}{\sqrt{2}}$) at $\frac{E}{k^{(B)}} = 200$ decays completely (figure 3.34). At $\frac{E}{k^{(B)}} = 373.33$ (figure 3.35 and 3.36) mode 4 grows and is then superceded by the more unstable mode 2.

The results of the linear stability analysis suggest that fibres of low flexibility are more likely to perform C turns and fibres of high flexibility are more likely to perform S turns, however, this is not what we observe in our simulation suggesting that bending in the compressional quadrant is not what determines whether a C turn or an S turn is seen.

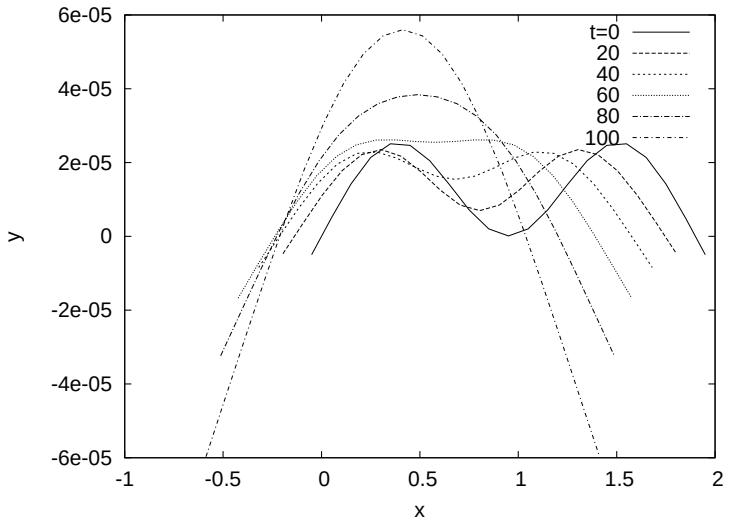

Figure 3.30: Fibre with small initial mode 3 perturbation in a flow of strength $\frac{E}{k^{(B)}} = 133.33$. Mode 1 grows.

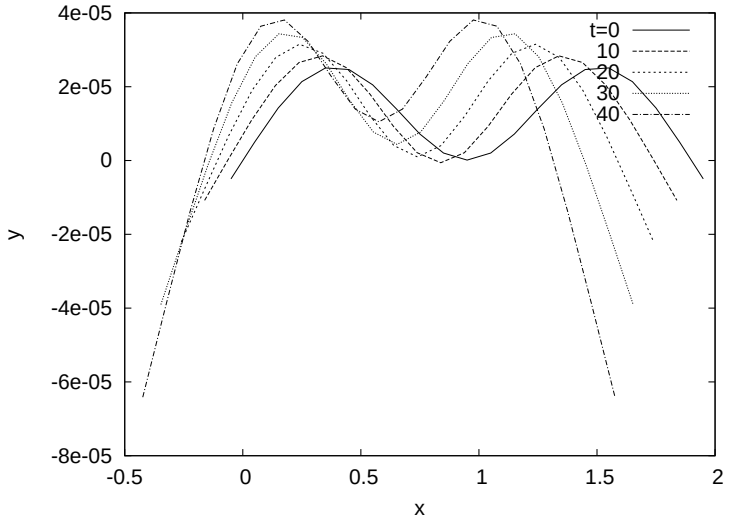

Figure 3.31: Fibre with small initial mode 3 perturbation in a flow of strength $\frac{E}{k^{(B)}} = 200$. The perturbation grows.

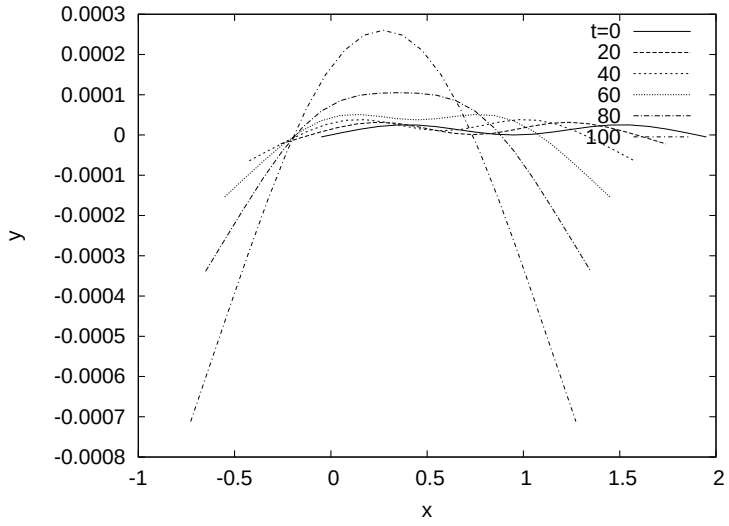

Figure 3.32: Continuation of figure 3.31. The perturbation has continued to grow and is now being replaced by mode 1.

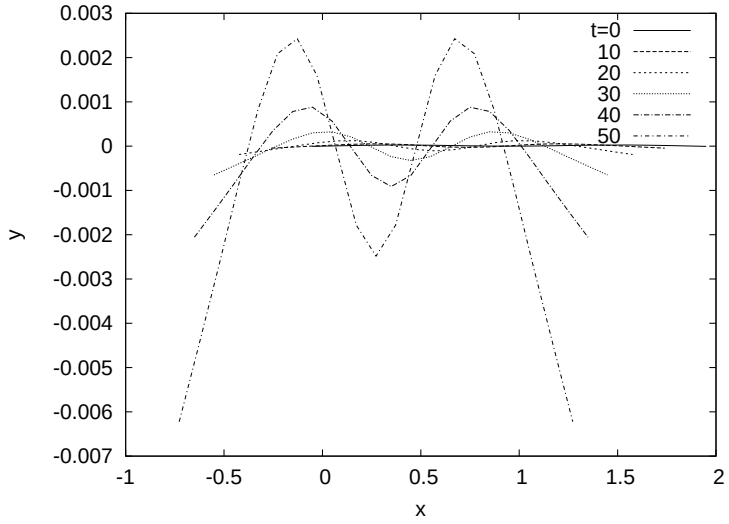

Figure 3.33: Fibre with small initial mode 3 perturbation in a flow of strength $\frac{E}{k^{(B)}} = 400$. The perturbation grows.

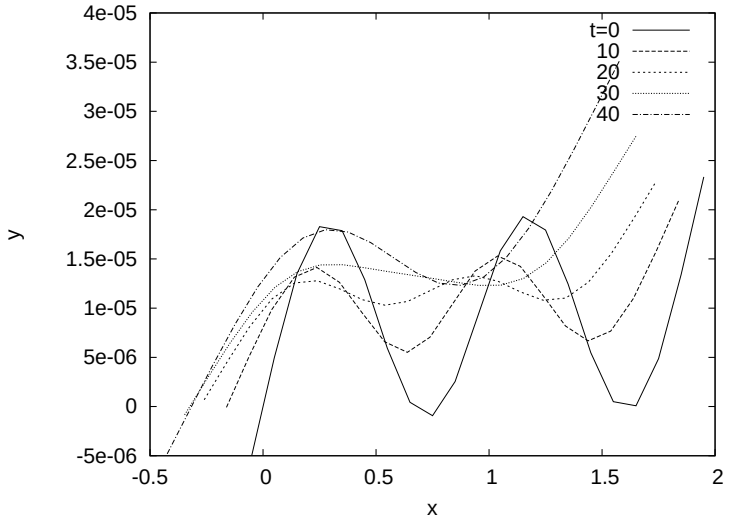

Figure 3.34: Fibre with small initial mode 4 perturbation in a flow of strength $\frac{E}{k^{(B)}} = 200$. The perturbation decays.

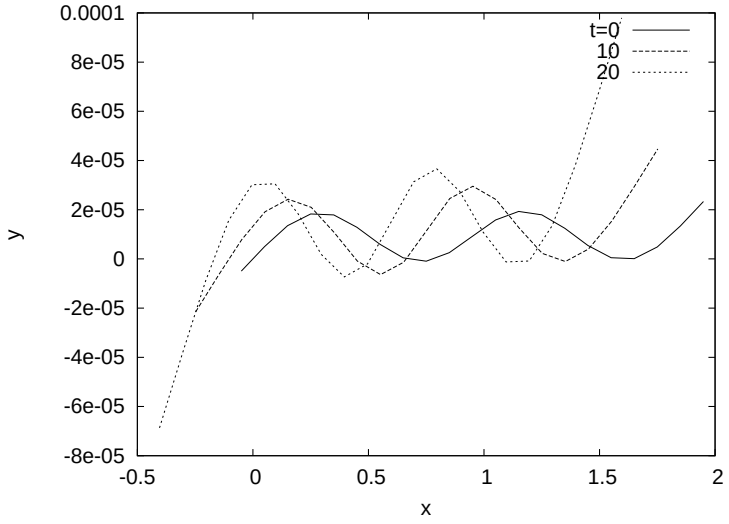

Figure 3.35: Fibre with small initial mode 4 perturbation in a flow of strength $\frac{E}{k^{(B)}} = 373.33$. The perturbation grows.

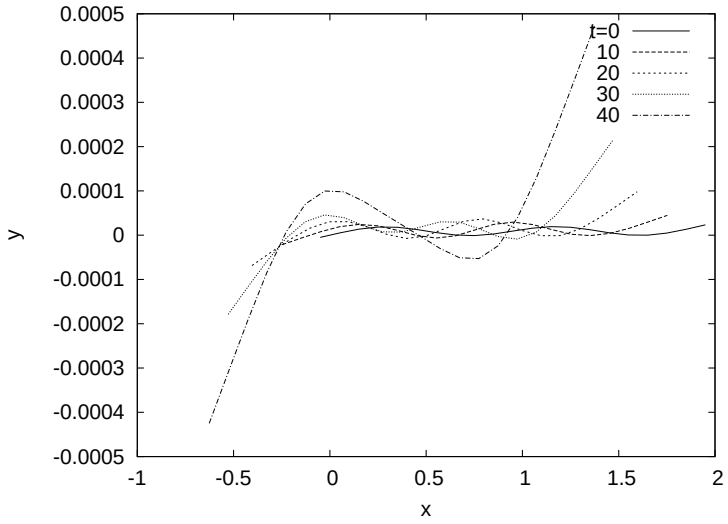

Figure 3.36: Continuation of figure 3.35. The perturbation continues to grow and then change to mode 2.

3.2.3 Bending in the flow-vorticity plane.

We now look at bending of a fibre near the flow vorticity plane. As noted by Hinch [17] an infinite aspect ratio fibre will straighten completely as it approaches the flow-vorticity plane. To establish the shape formed by a finite aspect ratio fibre as it bends due to the velocity difference across the fibre ends we calculate the torque distribution along a straight fibre that is required to keep it straight.

We consider a fibre composed of N rigid rods. We calculate the torque distribution by comparing the rotation rate of a rod in a straight composite fibre with the rotation rate of a freely rotating rod of the same aspect ratio. The difference in the rotation rates is proportional to the total torque acting on that rod so that

$$[\mathbf{T}_n^c + (\mathbf{B}_n - \mathbf{B}_{n-1})] \times \mathbf{p} = \xi_t^*(\dot{\mathbf{p}} - \dot{\mathbf{p}}^f) \tag{3.2.21}$$

where $\mathbf{T}_n^c$ are the constraint torques on rod n arising due to the forces maintaining

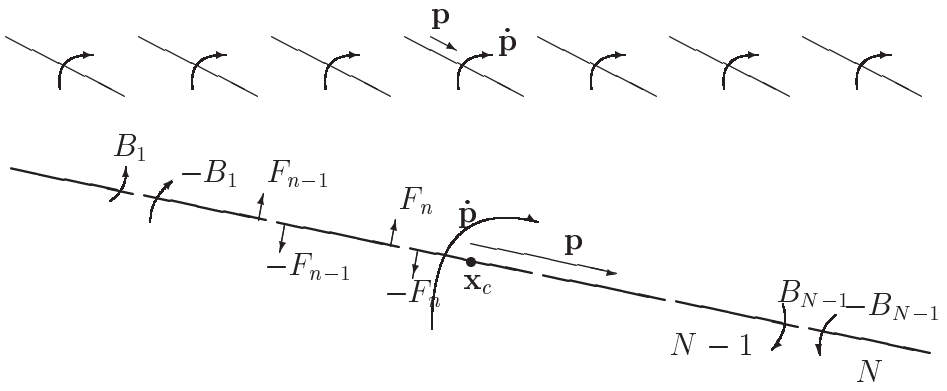

Figure 3.37: Rotation of free rods and composite fibre.

connectivity of the fibre and $(\mathbf{B}_n - \mathbf{B}_{n-1})$ is the sum of the bending torques (shown in figure 3.37). ξ_t^* is resistance co-efficient for torque for a rod of length $l = \frac{2L}{N}$, as derived in section 1.2.6. Here $\dot{\mathbf{p}}$ is the rotation rate of the whole fibre and $\dot{\mathbf{p}}^f$ is the rotation rate of a freely rotating rod. Both can be calculated from equation (2.2.12) in Chapter 2. For $\mathbf{p} = (1, 0, 0)$ these are given by

$$\dot{p}_y = -\frac{\dot{\gamma}}{a_r^2} \tag{3.2.22}$$

and

$$\dot{p}_y^f = -\frac{N^2\dot{\gamma}}{a_r^2}. \tag{3.2.23}$$

where $\dot{\gamma}$ is the shear rate, a_r is the aspect ratio of the whole fibre and $\frac{a_r}{N}$ is the aspect ratio of an individual rod. The x and z components of rotation rate are both zero.

To calculate the torques on rod n we first calculate the constraint forces $\mathbf{F}_n^c = \mathbf{F}_n - \mathbf{F}_{n-1}$ (shown in figure 3.37). The velocity of the centre of each rod in the connected fibre is

given by

$$\dot{x}_{n_y} = s(n)\dot{p}_y = -s(n)\frac{\dot{\gamma}}{a_r^2}$$

where s is the distance from the centre of the fibre to the centre of rod n. For rods numbered from left to right s is given by

$$s = \frac{(2n-1)L}{N} - L = \frac{(2n-N-1)L}{N}$$

regardless of whether the number of rods is even or odd. The rod centre velocities $\dot{x}_{n_y}$ can be calculated in terms of the constraint forces from equation (2.1.3) so that

$$\dot{x}_{n_y} = \frac{1}{2}\xi_f^{*-1}(F_{n_y} - F_{n-1_y})$$

where ξ_f^* is the resistance co-efficient for force for a rod of length $l = \frac{2L}{N}$. Equating the two forms of $\dot{x}_y^n$ gives the following expression for the constraint forces on rod n

$$F_{n_y} - F_{n-1_y} = -\zeta(2n - N - 1)$$

where $\zeta = \frac{2\xi_f^*\dot{\gamma}L}{a_r^2 N}$. The no net force condition,

$$-\zeta\sum_{k=1}^{N}(2k - N - 1) = 0,$$

means that this system of N equations in $N-1$ unknowns can be solved to give

$$F_y^n = -\zeta\sum_{k=1}^{n}(2k - N - 1) = n\zeta(N - n). \tag{3.2.24}$$

The constraint torque on each rod is given by $T_{n_z}^c = (F_{n_y} + F_{n-1_y})\frac{L}{N}$. Substituting

equation (3.2.24) we get

$$T^c_{n_z} = 3\chi(2(n-1)(N-n)+N-1) \tag{3.2.25}$$

where $\chi = \frac{L}{3N}\zeta = \frac{\dot{\gamma}\xi^*_t}{a_r^2}$.

Substituting equations (3.2.25), (3.2.22) and (3.2.23) into equation (3.2.21) we obtain

$$B_{n_z} - B_{n-1_z} = \chi(6n^2 - 6(N+1)n + (N+1)(N+2)).$$

The no net torque condition,

$$\chi\sum_{k=1}^{N}(6n^2 - 6(N+1)n + (N+1)(N+2)) = 0,$$

again means that this system of N equations in $N-1$ unknowns can be solved, giving a bending torque of

$$B_{n_z} = \chi\sum_{k=1}^{n}(6n^2 - 6(N+1)n + (N+1)(N+2)) = n\chi(N-n)(N-2n). \tag{3.2.26}$$

As the bending torque B_{n_z} acts at the joint between rods n and rod $n+1$ then the equivalent value of s at this point would be $s = \frac{2L}{N}n - L$, rearranging we obtain an expression for n in terms of s

$$n = \frac{(s+L)N}{2L}.$$

Substituting this into equation (3.2.26) we obtain the continuous limit of equation (3.2.26)

$$B_z(s) = -\frac{2\pi\mu\dot{\gamma}}{3a_r^2\log 2a_r}s(L^2 - s^2).$$

The beam equation was derived in subsection (1.3.1) and is given by

$$\frac{d\theta(s)}{ds} = \frac{1}{EI}B_z(s)$$

where $\theta(s)$ is the angle between the x axis and the tangent at a point s along the fibre. Substituting in our expression for $B_z(s)$ we get

$$\frac{d\theta(s)}{ds} = \frac{1}{EI}B_z = -\frac{2\pi\mu\dot{\gamma}}{3\log 2a_r EIa_r^2}s(L^2 - s^2).$$

Non-dimensionalising s with respect to L we can write this in terms of the non-dimensional bending stiffness derived in section 1.3.3,

$$\frac{d\theta}{ds} = -\frac{1}{8k^{(B)}a_r^2}s(1 - s^2). \tag{3.2.27}$$

For small angles $\theta \approx \frac{dy}{ds}$ and hence $\frac{d\theta}{ds} \approx \frac{d^2y}{ds^2}$. Substituting into equation (3.2.27), integrating twice and imposing the condition $y = 0$ at $s = \pm 1$ we get

$$y = \frac{1}{32k^{(B)}a_r^2}s(\frac{2}{3}s^2 - \frac{s^4}{5} - \frac{7}{15}).$$

Hence the perturbation is an even mode and produces an S shape as shown in figure 3.38. Note that the magnitude of the projection into the y direction is of order $\frac{1}{k^{(B)}a_r^2}$, whereas the actual width of the fibre is $d = \frac{2}{a_r}$. Hence the the function $f(k^{(B)}, a_r)$ described in section 3.1.3, in which $df(k^{(B)}, a_r)$ describes the effective aspect ratio, is proportional to $\frac{1}{k^{(B)}a_r}$.

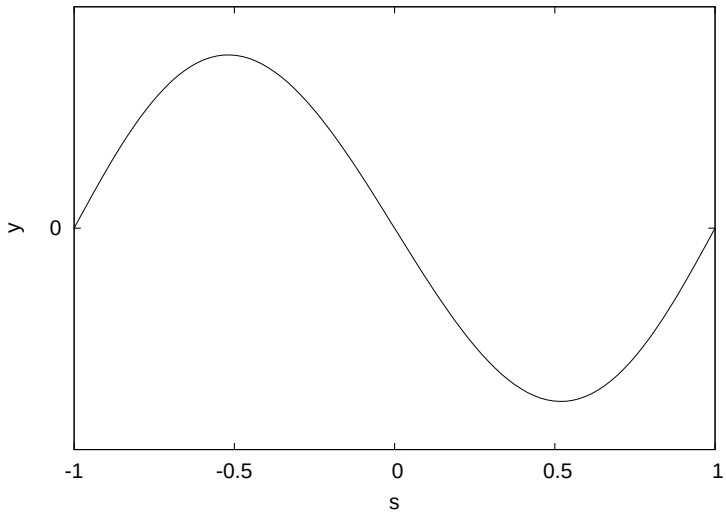

Figure 3.38: The projection into the y direction of a bent fibre in the flow vorticity plane against arc length s.

3.3 Discussion

In section 3.1 we found that the fibre always performs even mode turns and the dimensionless measure of the effect of bending on the period of rotation was $k^{(B)}a_r$ rather than $k^{(B)}$. This would appear to be at odds with the results of the stability analysis for a fibre under compression which show that C-mode is the first to become unstable and that the effects of bending should depend only upon $k^{(B)}$. However, fibres in shear flow rotate through the compressional quadrant in a time of order $\frac{1}{\dot{\gamma}}$. Consequently disturbances do not have time to grow during this section of the orbit where these modes are unstable, before they decay again in the extensional quadrant. Thus it is bending when the fibres are near the flow-vorticity plane that is most significant. In the previous section we showed that this gives rise to an S mode. Furthermore the deformation produces an additional effective cross-section proportional to $\frac{d}{k^{(B)}a_r}$ suggesting that f in subsection 3.1.3 is inversely proportional to $\frac{1}{k^{(B)}a_r}$, which is consistant with the simulation results. Fibres of very high aspect ratio eg. $a_r = 1000$ will only perform mode 4 turns. This is

because for $k^{(B)}a_r$ to be low enough for the fibre to bend in the $x-z$ plane the stiffness must be very low, making mode 4 the most unstable mode.

In section 3.1.2 we encountered two regimes for bending energy; a low stiffness regime in which E is proportional to $\frac{1}{k^{(B)\frac{1}{2}}}$; and a high stiffness regime in which Ea_r^3 is proportional to $\frac{1}{k^{(B)2}}$. In the low stiffness regime, most bending occurs in the compressional quadrant, away from the $x-z$ plane and hence aspect ratio is relatively unimportant. The stiffness values at which the transistion between the two regimes occurs is between 0.0008 and 0.005. Referring back to our stability analysis, S modes are stable for flow strengths, $\frac{\mathbf{p}_0\cdot\mathbf{E}\cdot\mathbf{p}_0}{k^{(B)}}$, less than 64.5, this corresponds to stiffnesses greater than 0.00775 for a fibre under maximum compression at an angle of $-45°$. A fibre of stiffness 0.005 will be unstable to S mode growth within the range $-20°$ to $-69.92°$, a section of the orbit where the fibre rotates quickly and hence the S mode does not have time to grow. Thus fibres of stiffness greater than 0.005 remain effectively straight during their rotation. The high stiffness regime therefore describes stiffnesses that are sufficiently large that only bending in the $x-z$ region of the orbit is important as distortions decay in the compressional quadrant. It is for this reason that at high stiffnesses bending energy is also dependent on aspect ratio.

From equation (3.2.27) the bending of the fibre when it is aligned in the flow direction is given by

$$\frac{d\theta}{ds} = -\frac{1}{8k^{(B)}a_r^2}s(1-s^2).$$

This gives a bending energy of

$$\frac{1}{32k^{(B)^2}a_r^4}\int_{-1}^{1} s^2(1-s^2)^2 ds = \frac{1}{210k^{(B)^2}a_r^4}.$$

For large $k^{(B)}a_r$ the period of the orbit will be approximately that of a rigid fibre of the

same aspect ratio. Hence the energy over half an orbit, E is proportional to $\frac{a_r}{k^{(B)^2} a_r^4}$ and hence we obtain our result from section 3.1.2 that $E a_r^3 \propto k^{(B)^{-2}}$.

3.4 Fibre Orbits

The previous section considered the special case of fibres with an initial orientation in the flow-gradient plane. In this section we consider general initial orientations and examine the effect of flexiblity on Jeffery orbits.

3.4.1 Orbit Drift

Unlike rigid fibres, semi-flexible fibres do not rotate in closed orbits but drift across orbits. Fibres drift either towards $C = 0$ so that they spin about the vorticity axis or $C = \infty$ so that they rotate in the $x - y$ plane. Figure 3.39 shows the trajectory of the right-hand end of the fibre when drifting towards the vorticity axis (left) and towards the $x - y$ plane (right).

The direction of drift depends upon the initial orbit constant of the fibre, the fibre stiffness and the fibre's aspect ratio. For a given stiffness and aspect ratio there exists a critical orbit constant C^* such that for $C > C^*$ fibres drift towards $C = \infty$ and fibres with $C < C^*$ drift towards $C = 0$. The value of C^* is a function of the stiffness and aspect ratio of the fibre. Figures 3.40(a) and (b) show how C^* varies with increasing stiffness and increasing aspect ratio respectively. For a fixed fibre stiffness the value of C^* is found to be proportional to the inverse aspect ratio squared of the fibre. However, as there is a factor of aspect ratio between the orbit constant and the angle of alignment in the $x - z$ plane, the critical angle corresponding to C^* is inversely proportional to aspect ratio. For a fibre of fixed aspect ratio the value of C^* and hence the critical angle in the $x - z$ plane is proportional to the inverse stiffness of the fibre. As the aspect ratio is constant then the

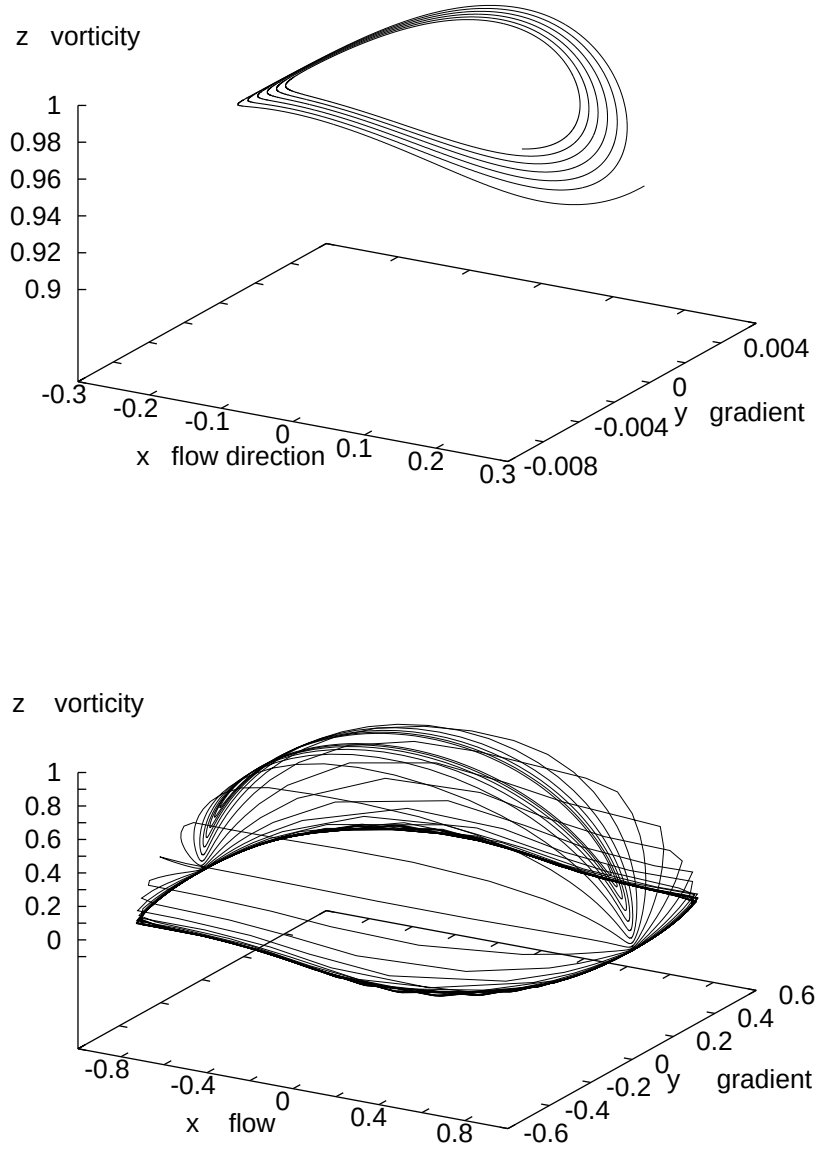

Figure 3.39: Trajectory of right-hand end of fibre drifting towards the vorticity axis, $C_0 = 0.006$, $k^{(B)} = 2 \times 10^{-4}$(top). The trajectory of right-hand end of fibre drifting towards the flow plane, $C_0 = 0.01$, $k^{(B)} = 3 \times 10^{-3}$ (bottom).

critical angle of the fibre is also inversely proportional to stiffness. Again this shows that the dimensionless parameter controlling orbit drift is $k^{(B)}a_r$.

3.4.2 Drift Rate

The rate of drift across orbits is affected by aspect ratio, stiffness and orbit constant. For fibres of differing aspect ratios (figure 3.41) and stiffnesses (figure 3.42) we have plotted the angle λ_{xz} between the fibre and the z axis as the fibre passes through the $x-z$ plane vs the number of orbits. The figures on the top are for the case of drift towards the flow-gradient plane and the figures on the bottom are for drift towards the vorticity axis. In all cases drift towards the flow-gradient plane is faster than drift towards the vorticity axis. In figures 3.43 and 3.44 the number of orbit periods has been scaled with aspect ratio and stiffness respectively for drift towards the flow plane. We see that drift rate per orbit towards the flow-gradient plane is approximately inversely proportional to aspect ratio and inversely proportional to stiffness. However, the drift rate towards the vorticity axis is both slower and more sensitive to aspect ratio and stiffness. The scaling for drift towards the vorticity axis is between $\frac{1}{k^{(B)2}}$ and $\frac{1}{k^{(B)3}}$ for stiffness and $\frac{1}{a_r^2}$ and $\frac{1}{a_r^3}$ for aspect ratio.

3.4.3 Drift Mechanism

This scaling behaviour suggests that it is again bending in the flow-vorticity plane that is the dominant mechanism for drift. To confirm this we consider a fibre of initial orbit constant $C = 0.2$ and stiffness $k^{(B)} = 2 \times 10^{-3}$ drifting towards the $x-y$ plane. Figure 3.45 shows the trajectory of the right-hand end of the fibre as viewed in the $x-y$ plane. The dotted lines show the Jeffery orbits. The fibre orbit follows the Jeffery orbit during the flipping section of the orbit, drifting away only slightly (towards $C = \infty$) from the Jeffery orbit in the compressive quadrant but then drifting back again in the extensional quadrant. Significant drifting occurs only when the fibre is passing through the $x-z$

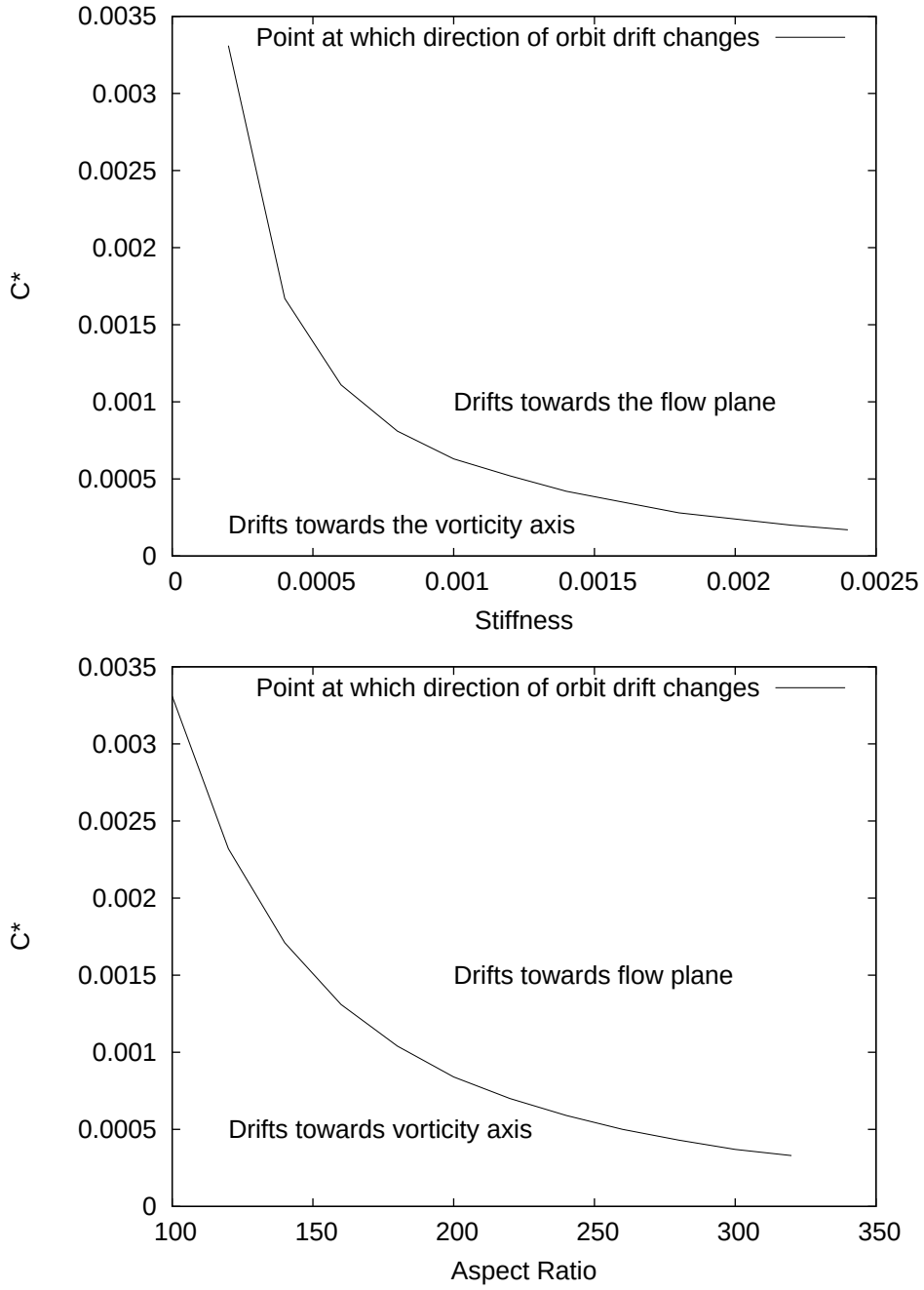

Figure 3.40: Relationship between direction of orbit drift and stiffness $k^{(B)}$ for $a_r = 100$. (top) Relationship between direction of orbit drift and aspect ratio a_r for $k^{(B)} = 2 \times 10^{-4}$.(bottom)

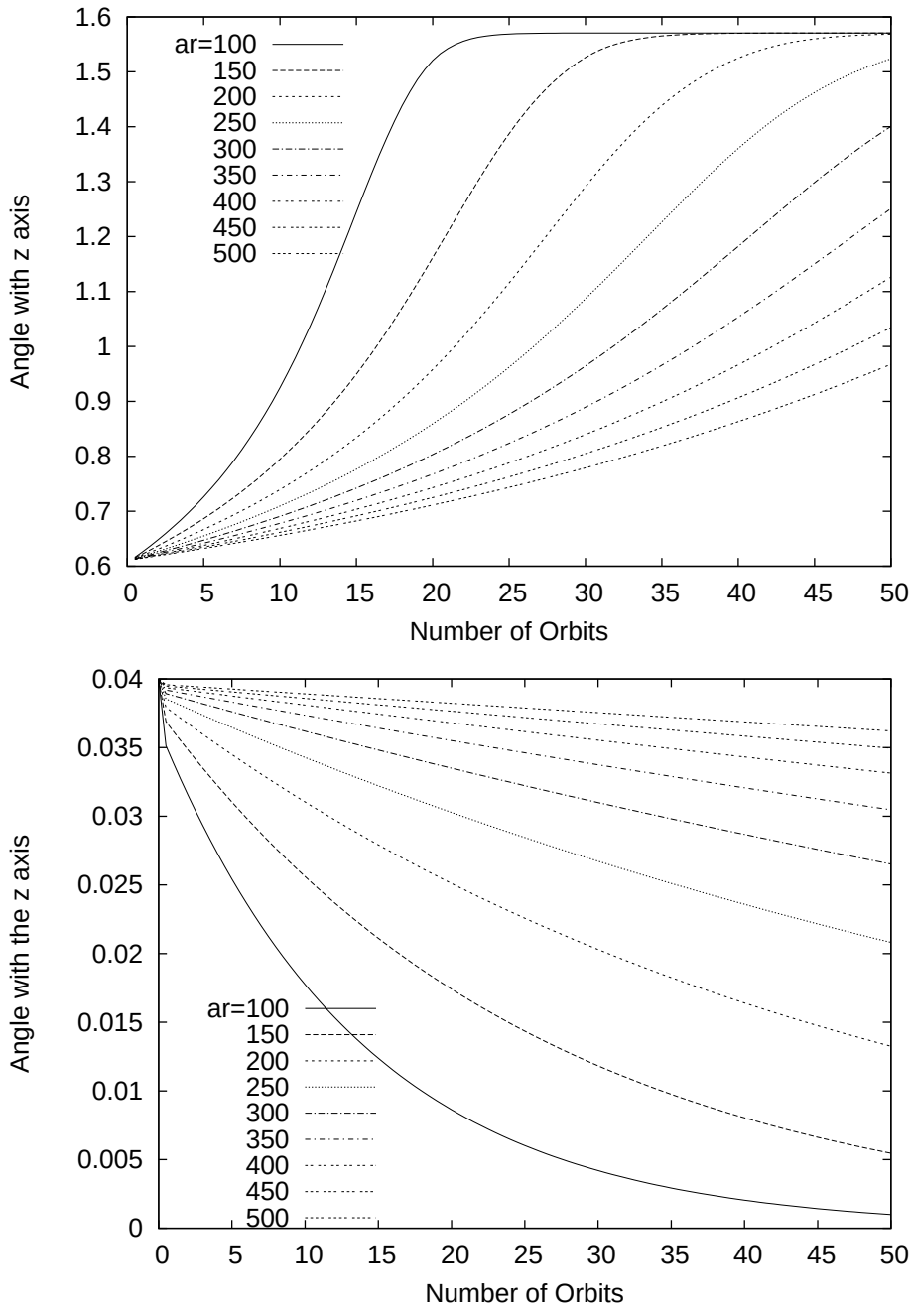

Figure 3.41: λ_{xz} vs number of orbits for fibres of aspect ratio 100 to 500 and stiffness 0.0005 drifting towards the flow-gradient plane (top) and fibres of aspect ratio 100 to 500 and stiffness 0.0001 drifting towards the vorticity axis (bottom).

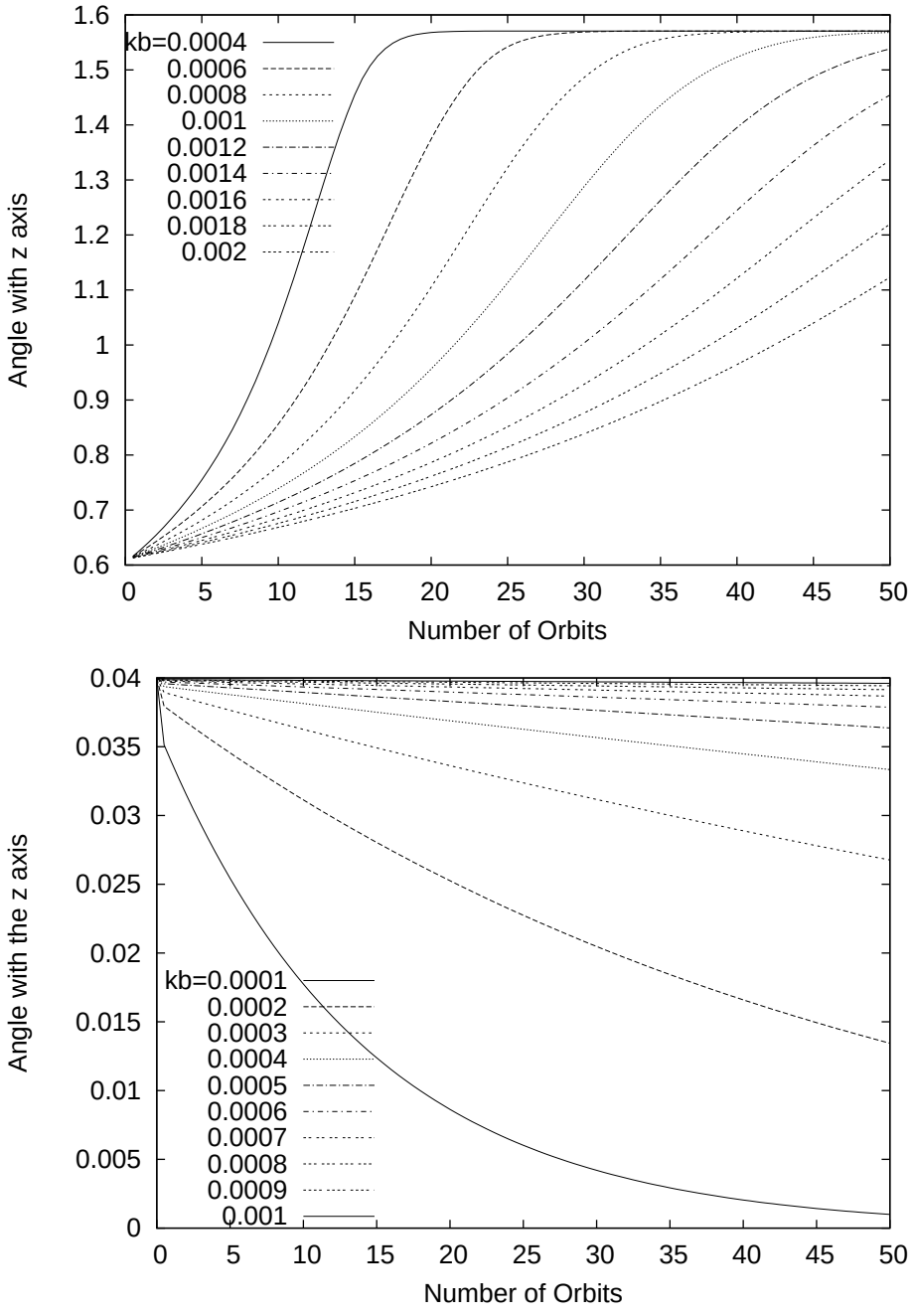

Figure 3.42: λ_{xz} vs number of orbits for fibres of stiffness 0.0004 to 0.002 drifting towards the flow-gradient plane (top) and fibres of stiffness 0.0001 to 0.001 drifting towards the vorticity axis (bottom). All fibres have an aspect ratio of 100.

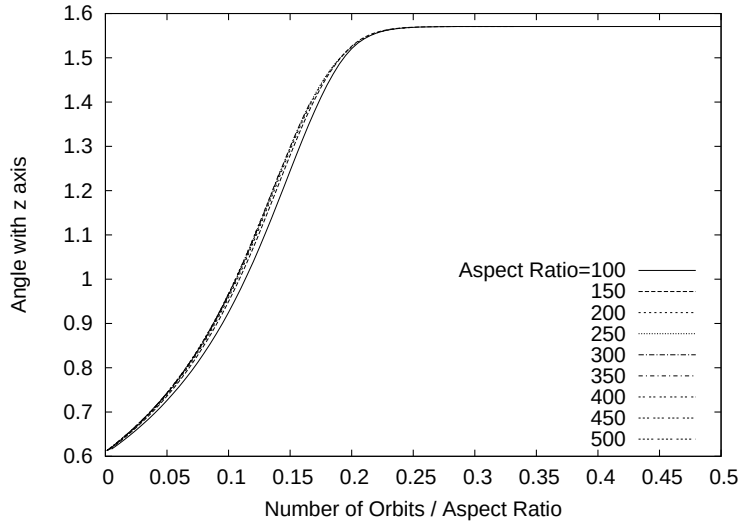

Figure 3.43: λ_{xz} vs number of orbits scaled with aspect ratio for fibres of aspect ratio 100 to 500 and stiffness 0.0005 drifting towards the flow-gradient plane

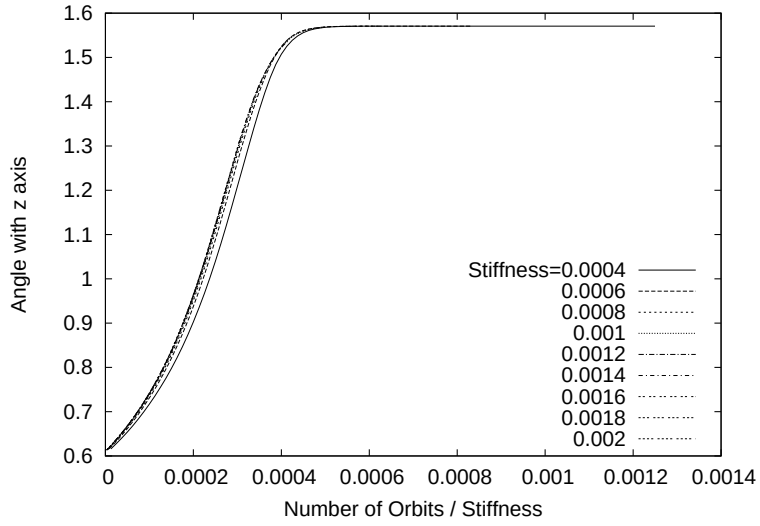

Figure 3.44: λ_{xz} vs number of orbits scaled with stiffness for fibres of stiffness 0.0004 to 0.002 and aspect ratio 100 drifting towards the flow-gradient plane (top)

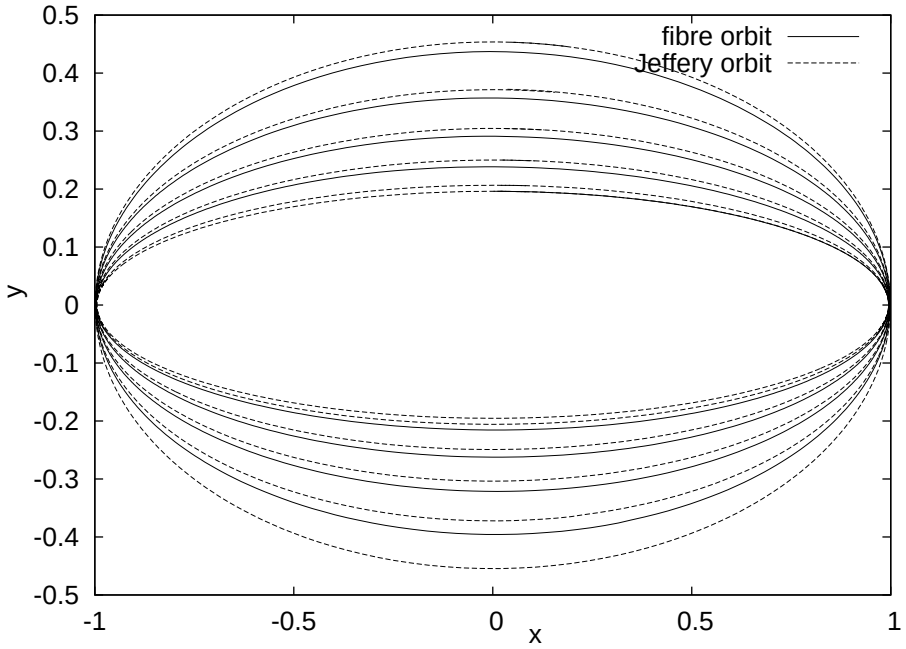

Figure 3.45: Comparison of the trajectory drawn out by the end of the fibre and Jeffery orbits as viewed in the $x-y$ plane.

plane (the end regions in figure 3.45). This is confirmed in figure 3.46 which shows an enlarged view of the end section of figure 3.45, the fibre orbit moves from one Jeffery orbit to the next each time the fibre crosses the flow vorticity plane.

To confirm that the main drift occurs as the fibre crosses the $x-z$ plane we have plotted the drift in orbit constant with time (figure 3.47). Each cross represents the completion of one quarter turn. The small peaks in the graph represent the drift away from and back towards the Jeffery orbit when the fibre is in the compressive and extensional quadrants respectively. Any drift towards $C=\infty$ that occurs in this region is cancelled out by drift back towards $C=0$. The linear increases in the graph occur when the fibre is within $O(\frac{1}{a_r})$ of the $x-z$ plane. This accounts for the main increase in orbit constant. In general using orbit constants to describe flexible fibres is problematic due to the changing geometry of the fibre, however their use here provides a general idea of the changing path of the fibre and is not intended to provide quantative information.

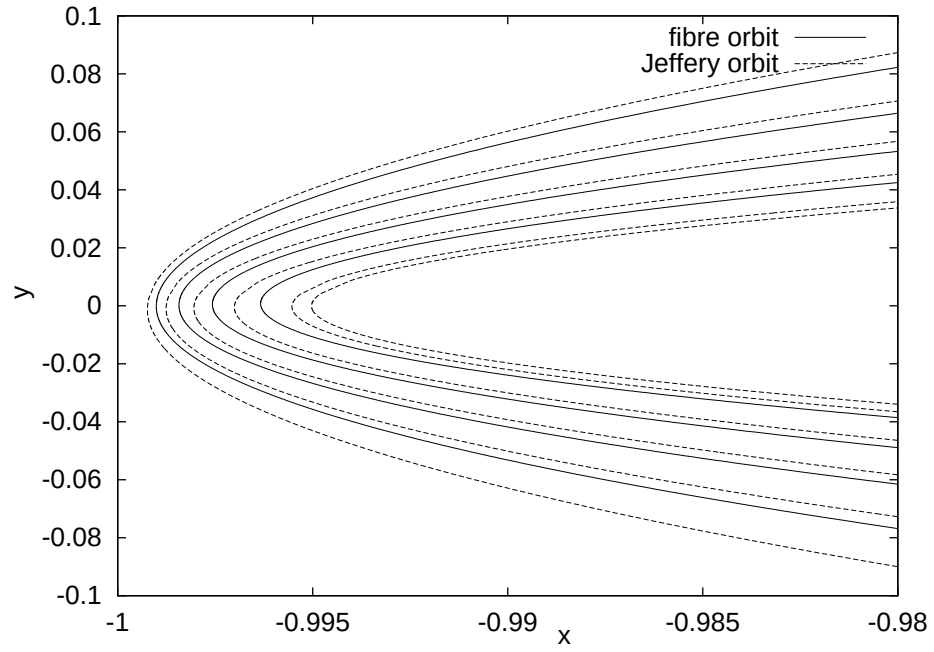

Figure 3.46: Enlarged view of the left end region in figure 3.45.

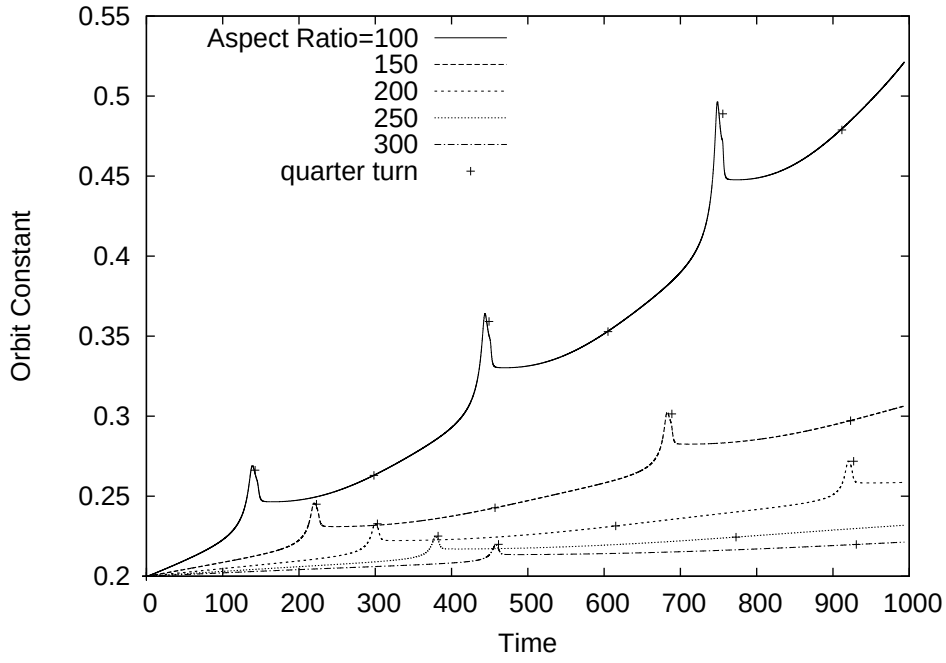

Figure 3.47: Orbit constant vs time for fibres of aspect ratio $a_r = 100, 150..., 300$.

Figure 3.48 shows the drift in orbit constant for fibres with small initial orbit constant drifting towards the flow plane (left) and towards the vorticity axis (right). A fibre rotating close to the vorticity axis is always in the region $O(\frac{1}{a_r})$ from the $x-z$ plane and so the drift is more evenly distributed throughout the entire orbit. As the fibre bends the drift is towards the flow plane and as the fibre straightens the drift is towards the vorticity axis. A fibre with an overall drift towards the flow plane drifts further in the bending phase than it does in the straightening phase and vice-versa. This can also be seen in figure 3.49 and figure 3.50 where the trajectories of the end of the fibre is plotted and compared to a series of Jeffery orbits.

3.4.4 Discussion

The drift in orbit constant for semi-flexible fibres is a consequence of both flexiblity and finite aspect ratio. As with rotation rate, we find that the dominant cause of orbit drift is bending when the fibre is close to the flow vorticity plane. Not only do fibres spend all but a fraction $\frac{1}{a_r}$ of their time in this orientation, but the angle between Jeffery orbits is small so that a small change in angle causes a large change in orbit constant. The drift due to bending in the compressional quadrant is relatively small and is reversed as the fibre straightens.

For a flexible fibre the hydrodynamic forces on a fibre aligned in the $x-z$ plane due to its finite aspect ratio have two effects. First they cause the rotation of the fibre, as in the case of a rigid fibre and second they cause the fibre to bend. As a consequence of bending the hydrodynamic force distribution will be altered causing a change in the rotation angle compared to a straight rigid fibre. This will produce a change in orbit constant as the fibre passes through the $x-z$ plane. The more flexible a fibre is the greater the change in rotation angle and hence the more rapid the drift in orbit constant.

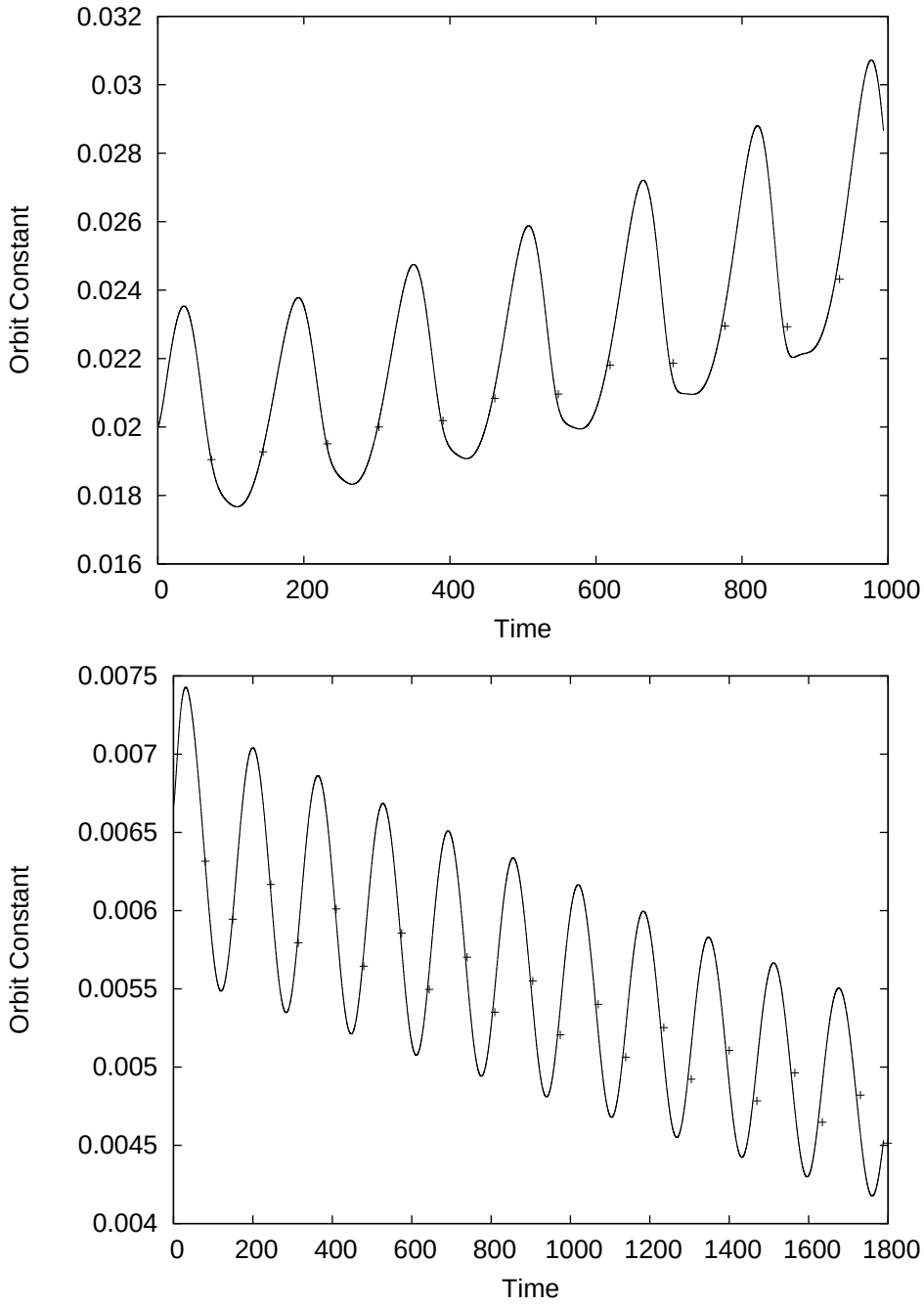

Figure 3.48: Orbit constant vs time for fibre of small initial orbit constant drifting towards flow plane(top). Orbit constant vs time for fibre with small initial orbit constant drifting towards the vorticity axis(bottom).

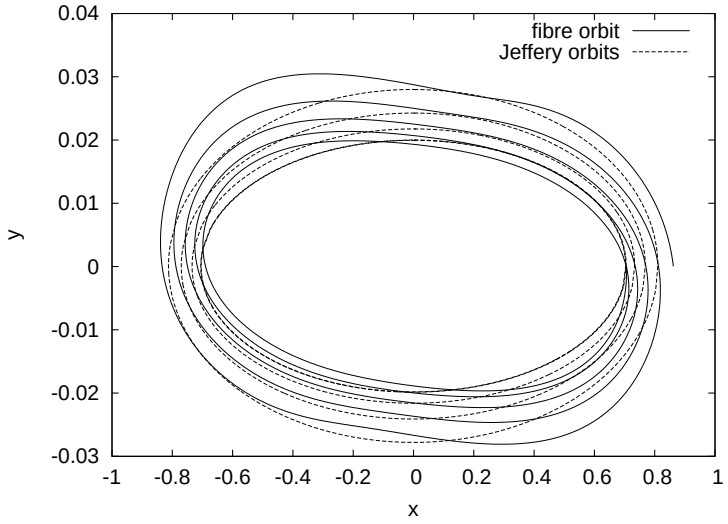

Figure 3.49: Trajectory of the end of a fibre with initial orbit constant $C_0 = 0.02$ and stiffness $k^{(B)} = 2 \times 10^{-4}$drifting towards the flow plane.

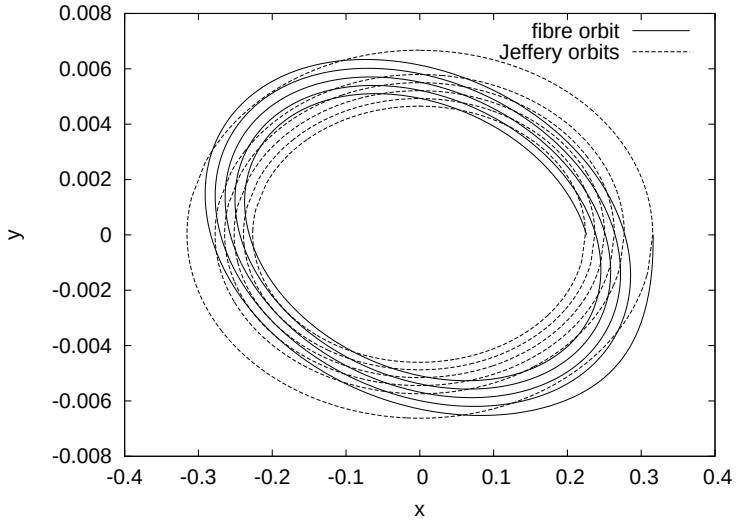

Figure 3.50: Trajectory of the end of a fibre with initial orbit constant $C_0 = 0.00667$ and stiffness $k^{(B)} = 2 \times 10^{-4}$ drifting towards the vorticity axis.

3.5 Stress

In section 3.4 we showed that semi-flexible fibres drift either towards the $x-y$ plane where $C=\infty$ or towards the vorticity axis where $C=0$. Fibres orientated parallel to the vorticity axis make a negligible contribution to the stress so we shall consider only fibres in the $x-y$ plane.

For a high aspect ratio rigid fibre, the leading order non-dimensional fibre stress (or stresslet) is given by

$$\mathbf{S}=\mathbf{p}\cdot\mathbf{E}\cdot\mathbf{ppp}.$$

Hence for a fibre in the $x-y$ plane with orientation

$$\mathbf{p}=\begin{pmatrix}\cos\theta\\ \sin\theta\\ 0\end{pmatrix}$$

where θ is the angle with the x axis, the shear stress is given by
$\sigma_{xy}=\cos^2\theta\sin^2\theta=\frac{1}{4}\sin^2 2\theta$, the first normal stress difference by
$N_1=\sigma_{xx}-\sigma_{yy}=\cos^3\theta\sin\theta-\sin^3\theta\cos\theta=\frac{1}{4}\sin 4\theta$ and the second normal stress difference by $N_2=\sigma_{yy}-\sigma_{zz}=\sin^3\theta\cos\theta$.

The leading order contribution to the shear stress is zero when the fibre is aligned with either the x or y axis as the force from the flow is zero. The shear stress reaches a maximum at angles of $\theta=-\frac{\pi}{4}$ and $\theta=-\frac{3\pi}{4}$ with the x axis as this is where the fibre is under maximum compression and extension respectively. First normal stress difference is zero when the fibre is aligned with either the x or y axis, or when the the fibre is at an angle of $-\frac{\pi}{4}$ or $-\frac{3\pi}{4}$ with the x axis. The latter cases occur as the compressive and extensive forces cancel each other out. N_1 has maxima at $\theta=-\frac{3\pi}{8}$ and $\theta=-\frac{7\pi}{8}$ and

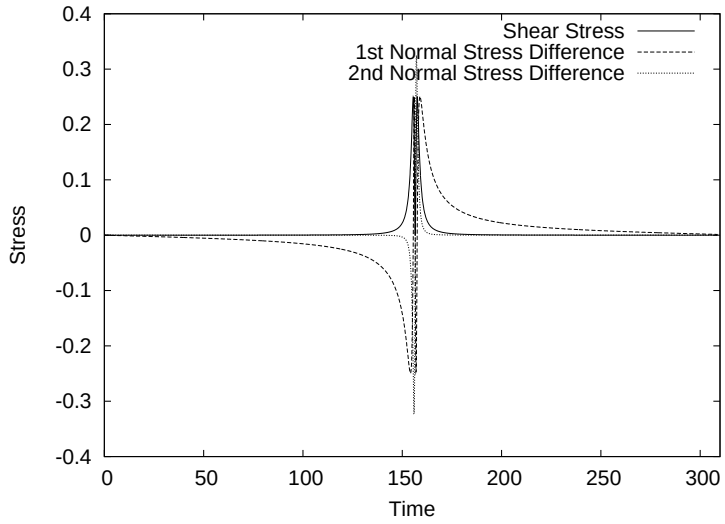

Figure 3.51: Stress contribution for a rigid fibre of aspect ratio 100.

minima at $\theta = -\frac{\pi}{8}$ and $\theta = -\frac{5\pi}{8}$ where a compromise between flow strength and fibre position is reached. The minima and maxima at $-\frac{\pi}{8}$ and $-\frac{7\pi}{8}$ correspond respectively to minima and maxima in σ_{xx} and the others to minima and maxima in σ_{yy} (which in this case is equal to the second normal stress difference).

Integrating σ_{xy}, N_1 and N_2 with respect to θ over a complete orbit gives a contribution of $\frac{\pi}{4}$ to the shear stress and zero contributions to the first and second normal stress difference.

3.5.1 Comparison of Rigid and Semi-Flexible Fibres

Figure 3.51 shows the shear stress σ_{xy}, the first normal stress difference $N_1 = \sigma_{xx} - \sigma_{yy}$ and the second normal stress difference $N_2 = \sigma_{yy} - \sigma_{zz}$ for a stiff finite aspect ratio fibre of $k^{(B)} = 0.05$ and $a_r = 100$ rotating for half an orbit in the x-y plane. The fibre passes through the y axis at a time of 157. Figure 3.52 shows a close up of the middle section of figure 3.51. Comparing this to figure 1.5 in Chapter 1 we can see that the simulation reproduces the expected results for a rigid fibre.

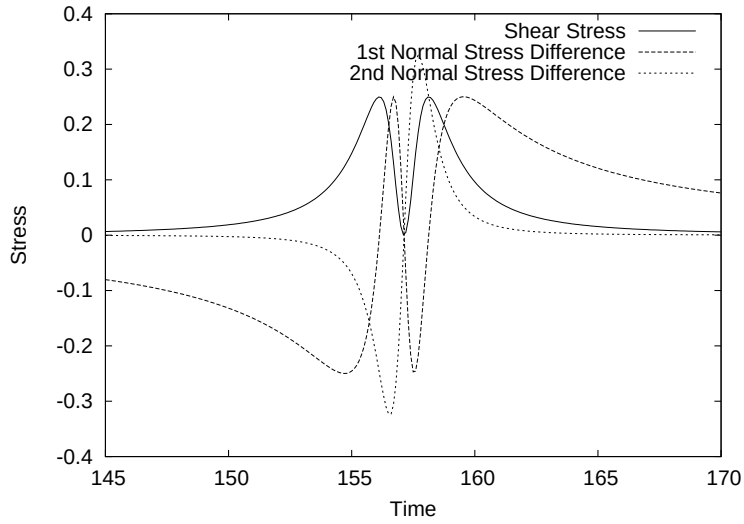

Figure 3.52: Close up of figure 3.51 in the time interval $t = 145$ to 170 when the fibre rotates through the compressional and extensional quadrants.

Figure 3.53 shows the shear stress for semi flexible fibres with stiffnesses in the range of 0.001 to 0.005. The fibre of stiffness 0.005 behaves as a stiff fibre. The fibre of stiffness 0.0025 shows a reduced first maximum at a time of $t \approx 155.5$. This is because the fibre bends slightly and so does not fully resist the compressional forces of the flow. This can be seen in figure 3.54. The second maximum at $t \approx 157$ is not reduced as the fibre fully straightens before reaching $\theta = -\frac{3\pi}{4}$ and so is able to fully resist extension. The minimum value that occurs when the fibre is aligned with the y axis at a time of $t \approx 156.2$ is positive rather than zero as the bend in the fibre produces a small viscous force.

For the more flexible fibre of stiffness 0.0015 the values of both maxima are reduced compared to a rigid fibre as the fibre remains bent through a larger angle of its rotation. The first maximum occurs before the fibre reaches $\theta = -\frac{\pi}{4}$, at a point $t \approx 153$. At $t \approx 154$ there is a point of inflection which corresponds to the fibre reaching its maximum y projection, as shown in figure 3.55. The minimum, which occurs at $t \approx 155$, is negative. We can see from figure 3.55 that, at $t \approx 155$, the fibre is in the extensional quadrant. As the elastic forces also act to straighten the fibre, the fibre is straightening faster than the

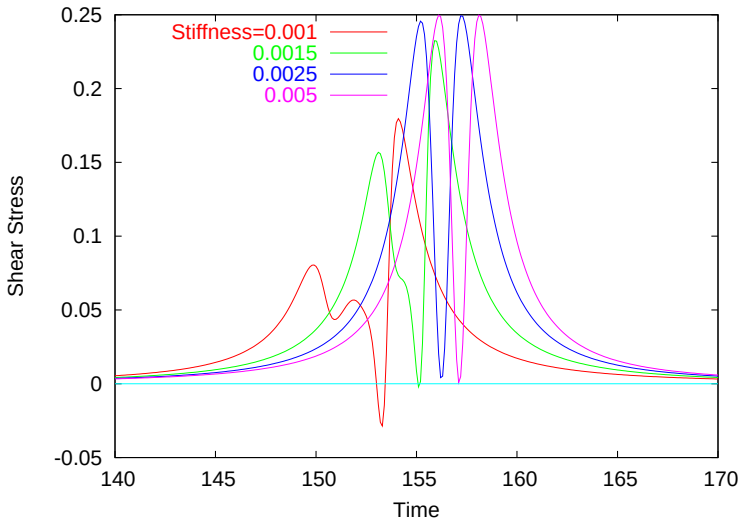

Figure 3.53: Shear stress for semi-flexible fibres of aspect ratio 100.

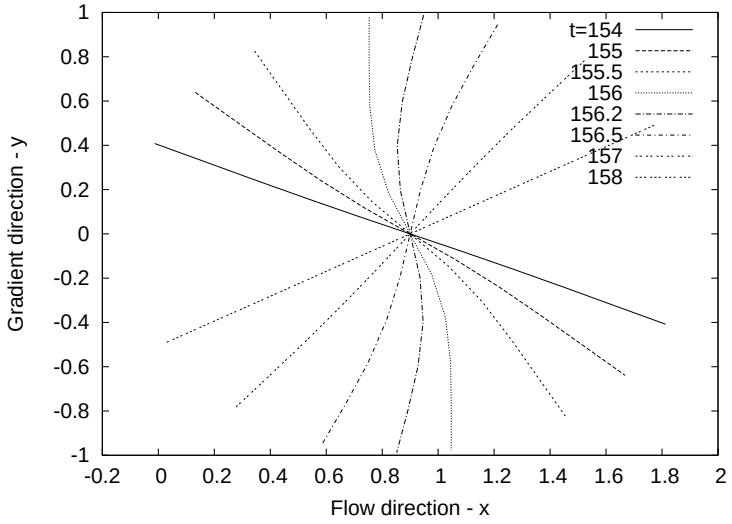

Figure 3.54: Plot showing the fibre shape at various points on figure 3.53 for the fibre of stiffness $k^{(B)} = 0.0025$ and $a_r = 100$.

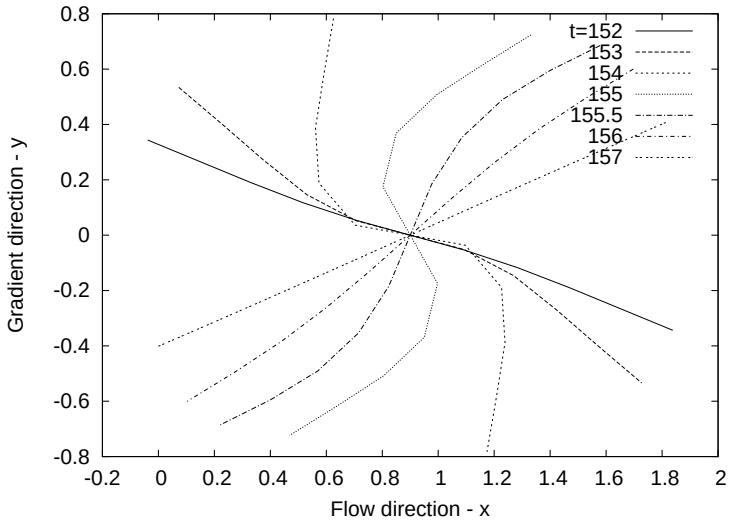

Figure 3.55: Plot showing the fibre shape at various points on figure 3.53 for the fibre of stiffness $k^{(B)} = 0.0015$.

surrounding flow and consequently the force distribution is in the opposite direction to that on a stiff fibre, producing a negative stress component.

For a very flexible fibre ($k^{(B)} = 0.001$) the first maxima occurs at $t \approx 150$ which is again before the end-to-end vector reaches an angle of $-\frac{\pi}{4}$. For the fibre of stiffness 0.0015 a point of inflection occured at the point where the y projection reached a maximum. For the fibre of stiffness 0.001 this inflection point now becomes a minimum ($t \approx 151$). The minimum at $t \approx 153$ occurs when the fibre is in the extensional quadrant and again occurs as the elastic forces of the fibre allow it to straighen faster than the surrounding flow.

Figure 3.57 shows the first normal stress difference given by $\sigma_{xx} - \sigma_{yy}$ for fibres of aspect ratio 100 and $k^{(B)} = 0.001,\ 0.0015,\ 0.0025$ and a stiff fibre of $k^{(B)} = 0.005$. Figures 3.58 and 3.59 show seperate plots for σ_{xx} and σ_{yy} respectively. In the case of a fibre in the $x - y$ plane, σ_{yy} is equal to the second normal stress difference. For all fibre stiffnesses in the range discussed above the maxima in σ_{xx} (second maxima in first normal stress difference) is not reduced as in each case the fibre is straight before reaching $\theta \approx -\frac{7\pi}{8}$. This can be seen in figures 3.56, 3.55 and 3.54 at times of $t \approx 155$, $t \approx 157$ and $t \approx 158$

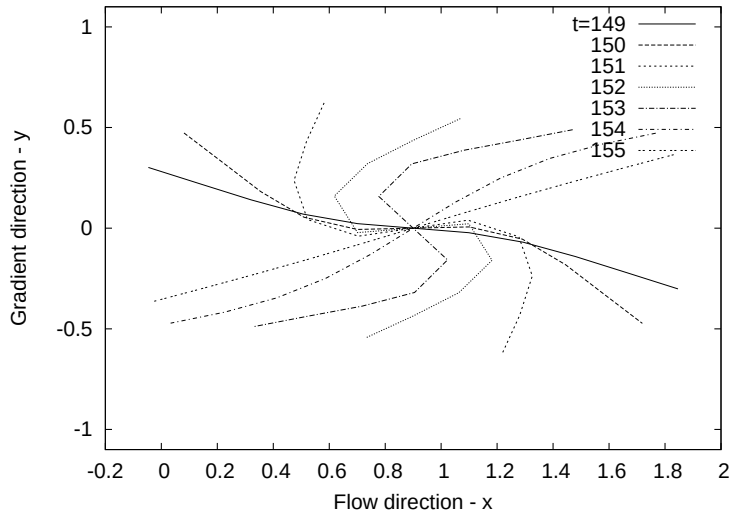

Figure 3.56: Plot showing the fibre shape at various points on figure 3.53 for the fibre of stiffness $k^{(B)} = 0.001$.

respectively.

The minima in σ_{xx} (first minima in first normal stress difference) are only reduced for stiffnesses of $k^{(B)} = 0.001$ and $k^{(B)} = 0.0015$. This is because a fibre of stiffness $k^{(B)} = 0.0025$ is stiff enough to fully resist the small compressive forces that occur at $\theta \approx -\frac{\pi}{8}$. This can be seen in figure 3.54 at a time of 154 which shows that the fibre of stiffness 0.0025 is completely straight at this point and in figures 3.56 and 3.55 at times of 149 and 152 respectively which show that the more flexible fibres are slightly bent at this point.

Unlike the maxima in σ_{xx}, the maxima in σ_{yy} (second minima in the first normal stress difference) are reduced for flexible fibres as at $\theta \approx -\frac{5\pi}{8}$ the fibre is still bent (see figures 3.56, 3.55 and 3.54 at times of 154, 155.5 and 156.5 respectively) and so is not able to fully resist extension.

The minima in σ_{yy} (first maxima in first normal stress difference) are reduced by a greater proportion than the minima in σ_{xx}. This is because the bend in the fibre is greater in the second half of the compressional quadrant than it is in the first.

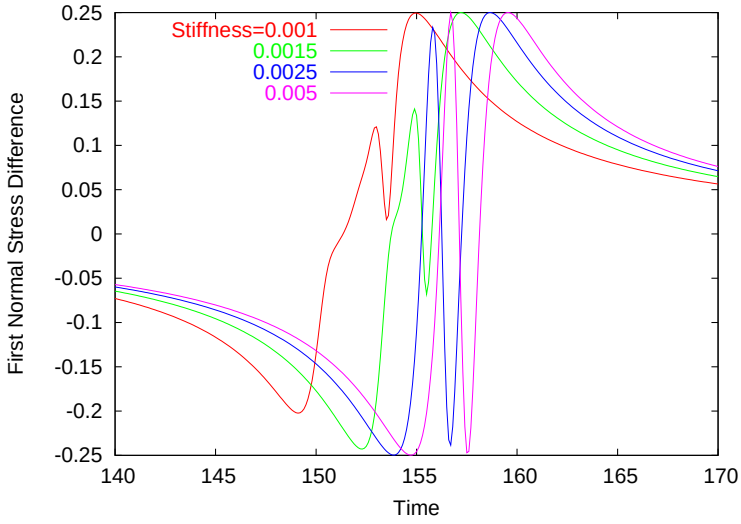

Figure 3.57: First normal stress difference for semi-flexible fibres of aspect ratio $a_r = 100$ and $k^{(B)} = 0.001,\ 0.0015,\ 0.0025,\ 0.005$.

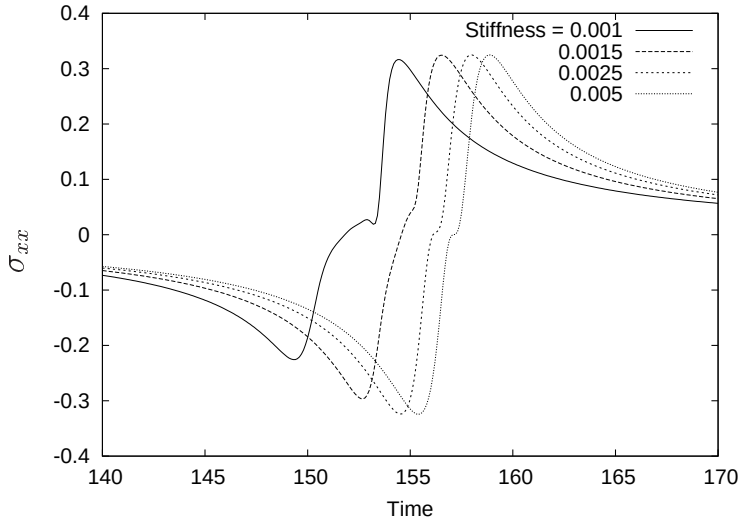

Figure 3.58: σ_{xx} for semi-flexible fibres of aspect ratio $a_r = 100$ and $k^{(B)} = 0.001,\ 0.0015,\ 0.0025,\ 0.005$.

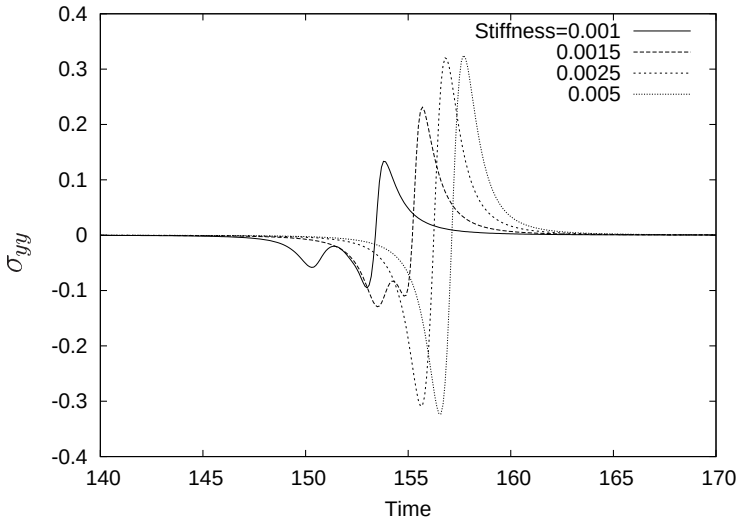

Figure 3.59: σ_{yy} (second normal stress difference) for semi-flexible fibres of aspect ratio $a_r = 100$ and $k^{(B)} = 0.001,\ 0.0015,\ 0.0025,\ 0.005$.

Figures 3.60, 3.61 and 3.62 show the integrals of shear stress, first and second normal stress differences integrated over half an orbit against stiffness for fibres of different aspect ratios. For a rigid fibre the integral of shear stress with respect to time over half an orbit is $\frac{\pi}{2}$ in the limit of infinite aspect ratio. The integrals of first and second normal stress difference are zero. In figure 3.60 the shear stress increases with stiffness until a stiffness is reached at which the fibre is able to resist the compressive forces of the flow. The stiffness required for this to happen is dependent upon aspect ratio. The smaller the aspect ratio, the stiffer the fibre must be before maximum shear stress is reached. The plot shows an aspect ratio dependence that is weaker than $k^{(B)}a_r$, the important parameter with regard to orbit period. This is because orbit period is largely determined by bending in the $x-z$ region where aspect ratio is important, whereas shear stress is influenced by bending in the compressional quadrant which only depends weakly on aspect ratio. In this region the growth rates are independent of aspect ratio, however, the initial amplitude derives from bending when the fibre is aligned in the flow direction. Dividing the integral of shear stress over half an orbit by $\frac{T}{2}$ to obtain an average shear stress shows that this quantity

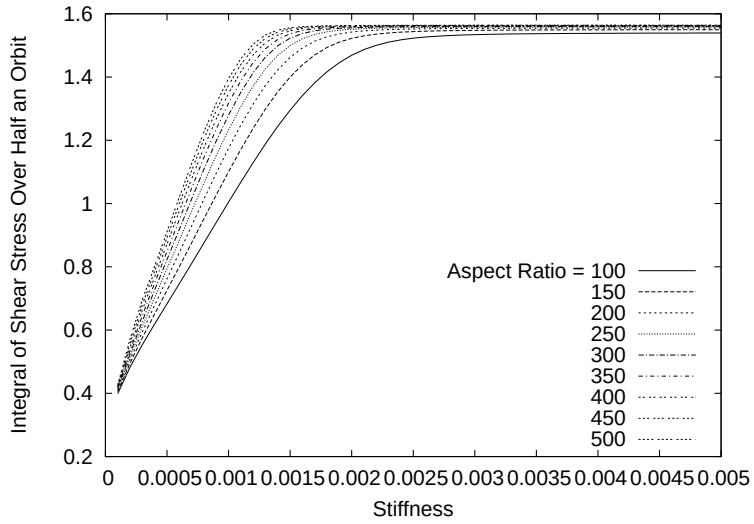

Figure 3.60: Integral of shear stress over half an orbit plotted against stiffness for fibres of aspect ratios 100-500.

decreases with increasing aspect ratio. This is because high aspect ratio fibres spend a greater proportion of their orbit aligned with the flow direction where the shear stress is zero.

In figure 3.61 we see that the integral of the first normal stress difference decreases for increasing stiffness, approaching zero in the limit of infinite stiffness. The rate at which first normal stress difference decreases with stiffness is dependent upon aspect ratio. The larger the aspect ratio the more rapidly the first normal stress difference integral decreases with stiffness. For fibres that bend the first normal stress difference is positive rather than zero, as it is for a rigid fibre, as the magnitude of the minima decrease more than the magnitude of the maxima. In particular the magnitude of the second maximum never reduces however, the magnitude of the first minima gets smaller with increasing flexibility.

The integral of the second normal stress difference (figure 3.62) is negative for very flexible fibres. As stiffness increases the integral becomes zero at $k^{(B)} \approx 0.00125$ (for an aspect ratio of 100) and then increases to a maximum at $k^{(B)} \approx 0.002$. The integral tends to zero in the limit of infinite stiffness. A rigid fibre has a negative second normal stress

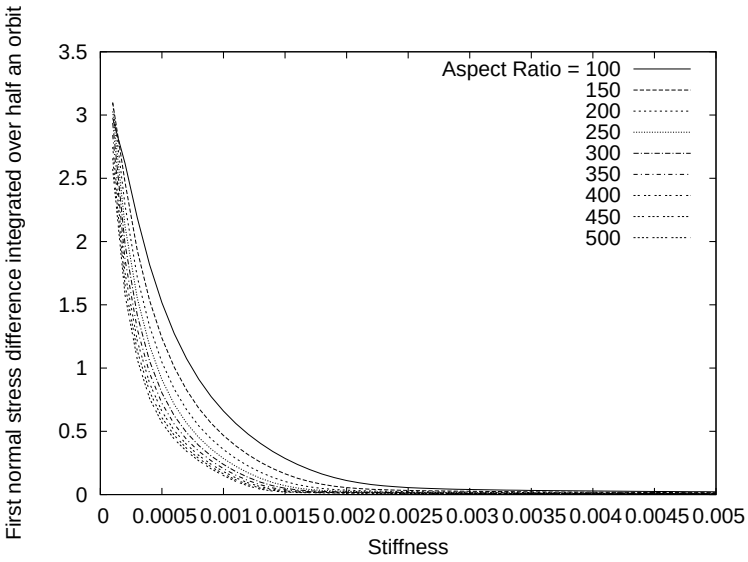

Figure 3.61: Integral of first normal stress difference over half an orbit plotted against stiffness for fibres of aspect ratios 100-500.

difference in the compressional quadrant and a positive second normal stress difference in the extensional quadrant. The integral of second normal stress difference is positive for moderate stiffnesses (eg. $k^{(B)} = 0.0015$ and $k^{(B)} = 0.0025$) as the reduction in the second normal stress difference maximum is smaller than the reduction in the minimum. For very flexible fibres (eg. $k^{(B)} = 0.001$) the integral is negative as the fibre spends a greater proportion of its orbit with a negative second normal stress difference. The second normal stress difference of a fibre of stiffness 0.001 and aspect ratio 100 changes sign at $t \approx 153$ when the fibre is well into the extensional quadrant (as can be seen in figure 3.56), whereas the sign change for a fibre of stiffness 0.0015 occurs at $t \approx 155$, when the end-to-end vector is closer to the y axis (figure 3.55) and hence at an earlier point in the orbit.

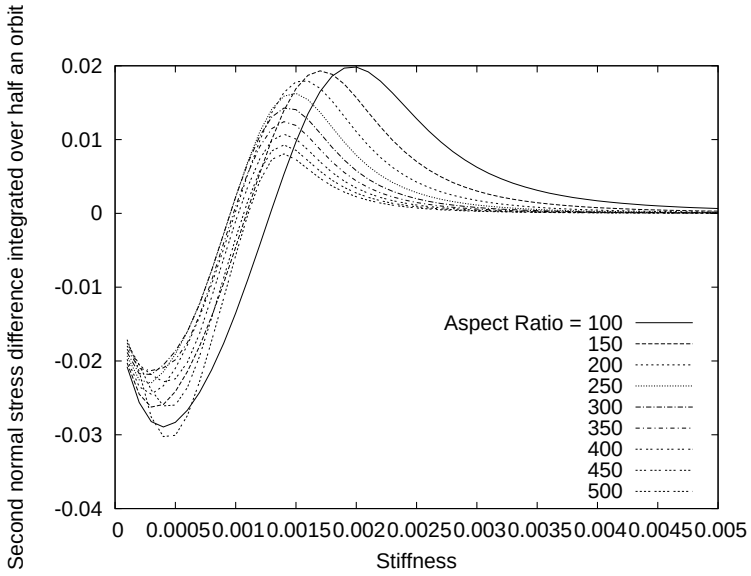

Figure 3.62: Integral of second normal stress difference over half an orbit plotted against stiffness for fibres of aspect ratios 100-500.

3.6 Conclusion

The motivation for this chapter was to determine whether semi-flexible fibres in shear flow performed C turns as predicted by the simulation results of Ross, Klingenberg and Skjetne [31, 34], the linear stability analysis of Becker and Shelley [3] and the experimental observations of Forgacs and Mason [10] or if they perform S turns, as reported in the simulation results of Schmid, Switzer and Klingenberg [33] and as found in our initial simulation results.

Our own linear stability analysis agreed with that of Becker, and found that the C mode is the most unstable in compressional flow. However, by calculating the torque distribution along the fibre when it is aligned in the flow direction, we found that bending in this region seeds an S turn with a bend amplitude of order $\frac{1}{k^{(B)}a_r^2}$ in magnitude. Hence it is odd modes that grow in the compressional quadrant even though even modes are more unstable.

Calculations of bending energy for fibres of different aspect ratios and stiffnesses

highlighted two different regimes; a low stiffness regime in which there was significant bending in the compressional quadrant, where aspect ratio is unimportant, and a high stiffness regime in which perturbations decay in the compressional quadrant but bending still takes place in the region $\frac{1}{a_r}$ from the $x-z$ plane. In this high stiffness regime the energy over one orbit period, E, is proportional to $\frac{1}{k^{(B)^2}a_r^3}$, a result that can also be derived from the bending torque distribution along a fibre when aligned with the flow direction.

As the fibre spends a fraction $\frac{a_r^2}{a_r^2+1}$ of its orbit in the region $\frac{1}{a_r}$ from the $x-z$ plane then it is bending in this region that is important in determining orbit period. Bending of semi-flexible fibres gives a smaller effective aspect ratio and hence faster rotation through the flow-vorticity plane. The function $\frac{T}{T_r}-1$ which gives a measure of the effect of flexibility on the orbit period, in relation to that of an equivalent rigid fibre, is found to be proportional to $\frac{1}{k^{(B)}a_r}$. Hence the effective width of the fibre df is proportional to $\frac{1}{k^{(B)}a_r^2}$, in agreement with our torque distribution calculations.

Bending in the $x-z$ region is also important in determining orbit drift as it is here that the Jeffery orbits are closest together and the fibre spends the most time. Fibres with initial orientations close to the flow-gradient plane drift towards the flow-gradient plane and hence the orbit constant increases, whereas fibres with initial orientations close to the vorticity axis drift towards the vorticity axis and hence the orbit constant decreases.

Stress has a weaker aspect ratio dependence than orbit period and orbit drift, as the leading order contribution to the stress is zero in the flow-vorticity plane where aspect ratio is important. Both shear stress, and first and second normal stress differences are reduced by flexibility as the fibre is unable to resist the compressive and extensional forces of the flow.

To discover why C turns and not S turns were observed in the experimental results of Forgacs and Mason [10], we shall present, in Chapter 4, a modification to the simulation method which allows us to consider the rotation of intrinsically bent and twisted fibres in shear flow.

Chapter 4

Model for an Intrinsically Bent and Twisted Fibre

In the previous simulation, described in chapter 2, we modelled an instrinsically straight semi-flexible fibre as a chain of rigid rods. The straight equilibrium shape was obtained by setting a single bending angle (of π) at each joint. For a high-aspect-ratio particle the resistance co-efficient for rotation about the fibre's axis is sufficiently small that we may neglect the twisting of the rod as any twist relaxes on a very fast timescale. For an intrinsically straight rod the bending energy is only dependent on the angle of bend, so that we only need to consider the angle between tangent vectors of successive rods.

To model an instrinscially bent and twisted fibre this model is not sufficient. Rather than setting only one equilibrium angle it is necessary to set three for a unique equilibrium position to be specified. To model fibres that are bent out of the plane, for example into a helix, it is not only necessary to set more than one equilibrium angle, it is also necessary to consider the dynamics of twisting and writhing. The twist from the fluid relaxes quickly as the rotational friction about the fibre axis is small, however, the initial out of plane bend means we must consider the writhe of the fibre. Writhe means that through bending of the fibre, the fibre will gain an overall twist which can then relax out, on a fast time scale,

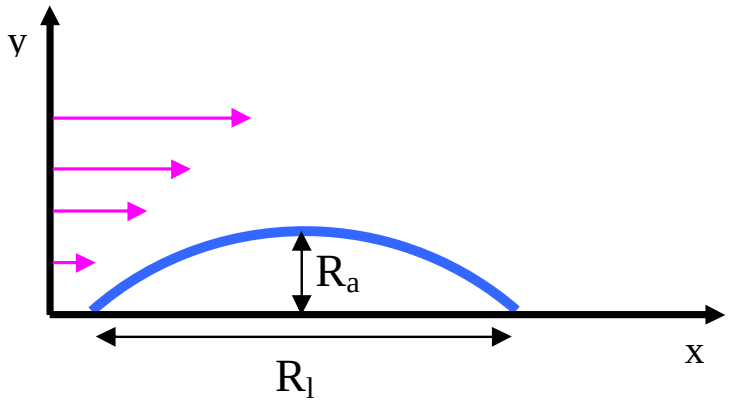

Figure 4.1: Illustration of a bent fibre in the flow-gradient plane in shear flow with amplitude R_a and end to end length R_l.

by untwisting directly about the fibre axis.

4.1 Equilibrium Shapes

There are infinitely many possible fibre equilibrium shapes, but we shall consider just two:

Circular arcs

The first are fibres formed into a circular arc as shown in figure 4.1. The amplitude of the bend is denoted by R_a and the end to end length by R_l as shown in the diagram. We shall also define an end to end vector $\mathbf{R}_l$. For these fibres the shape is confined to a plane.

Helical Fibres

To consider the effects of out of plane bend we shall consider a discretised version of the

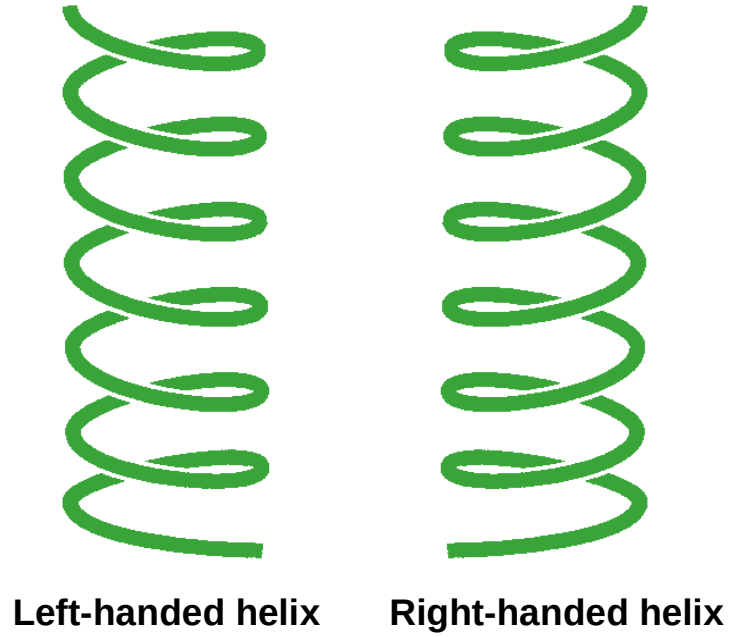

Figure 4.2: Left- and right-handed helices

continuous helix

$$\mathbf{x}(s) = (bs, a\sin(s), a\cos(s)) \tag{4.1.1}$$

where s runs from 0 to $2\pi n_t$. The helix is described by 3 parameters: n_t the number of turns of the helix, a the radius of the helix and $2\pi b$ the pitch of the helix (*i.e.* the length of one complete turn measured along the helix axis). The helix described above is a left-handed helix. To form a right-handed helix it is necessary to negate either the x, y or z component. Illustrations of left- and right-handed helices are shown in figure 4.2.

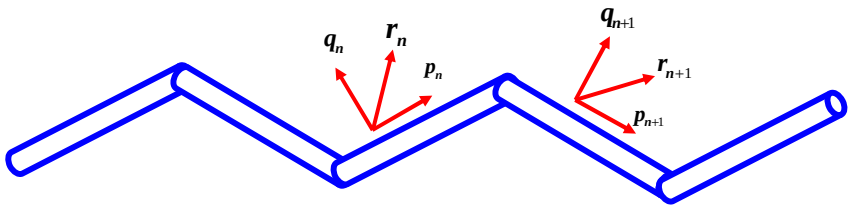

Figure 4.3: Local orthonormal frames of rods n and $n+1$.

4.2 Fibre Configuration

We again model the fibre as a chain of N rigid rods of length $l = \frac{2L}{N}$. The position vector of each rod is given by $\mathbf{x}_n$ and the orientation vector which lies along the axis of each rod by $\mathbf{p}_n$. In order to completely describe the configuration of the fibre it is also necessary to specify orthogonal vectors $\mathbf{q}_n$ and $\mathbf{r}_n$ so that each rod has a local orthonormal frame $\{\mathbf{p}_n, \mathbf{q}_n, \mathbf{r}_n\}$. We can describe the position of rod $n+1$ relative to rod n by

$$\begin{pmatrix} \mathbf{p}_{n+1} \\ \mathbf{q}_{n+1} \\ \mathbf{r}_{n+1} \end{pmatrix} = \mathbf{R}(\Omega_1^n, \Omega_2^n, \Omega_3^n) \begin{pmatrix} \mathbf{p}_n \\ \mathbf{q}_n \\ \mathbf{r}_n \end{pmatrix}$$

where $\mathbf{R}$ is a rotation matrix given by the product of rotations about the three co-ordinate axes, $\mathbf{R} = \mathbf{R}_p\mathbf{R}_q\mathbf{R}_r$ where

$$\mathbf{R}_p(\Omega_3^n) = \begin{pmatrix} 1 & 0 & 0 \\ 0 & \cos\Omega_3^n & -\sin\Omega_3^n \\ 0 & \sin\Omega_3^n & \cos\Omega_3^n \end{pmatrix},$$

$$\mathbf{R}_q(\Omega_2^n) = \begin{pmatrix} \cos\Omega_2^n & 0 & \sin\Omega_2^n \\ 0 & 1 & 0 \\ -\sin\Omega_2^n & 0 & \cos\Omega_2^n \end{pmatrix},$$

$$\mathbf{R}_r(\Omega_1^n) = \begin{pmatrix} \cos\Omega_1^n & -\sin\Omega_1^n & 0 \\ \sin\Omega_1^n & \cos\Omega_1^n & 0 \\ 0 & 0 & 1 \end{pmatrix}.$$

Ω_1^n, Ω_2^n and Ω_3^n are the angles of rotation about $\mathbf{r}_n$, $\mathbf{q}_n$ and $\mathbf{p}_n$ respectively. Hence Ω_3 is the twist about the fibre axis, as shown in figure 4.4 and Ω_1 and Ω_2 are the bend angles about axes perpendicular to the fibre.

Equilibrium Configurations

By specifying non-zero equilibrium angles for Ω_1 or Ω_2 and zero for the other two values we obtain an equilibrium state that is bent in the plane. By specifying non-zero equilibrium values for two or more of the three angles we obtain an equilibrium state which is bent out of the plane. For the circular arc we define $\Omega_1 = 2\sin^{-1}(\frac{L}{NR})$, where R is the radius of curvature and N is the number of rods used in the simulation. This means that the ratio of R_l to R_a is given by

$$\frac{R_l}{R_a} = 2\cot\frac{\Omega_1 N}{4}$$

as shown in figure 4.5.

The discretised helix is formed by dividing a continuous helix (as described by equation 4.1.1) into N segments with a straight rod lying along the chord of each segment (as

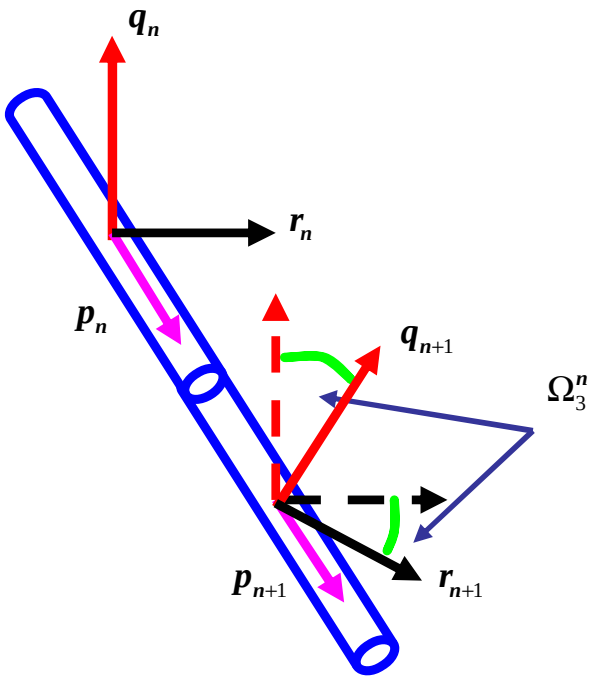

Figure 4.4: Illustration of fibre twist. The orthonormal frame of rod $n+1$ is rotated by Ω_3^n about $\mathbf{p}_n$ from the frame of rod n.

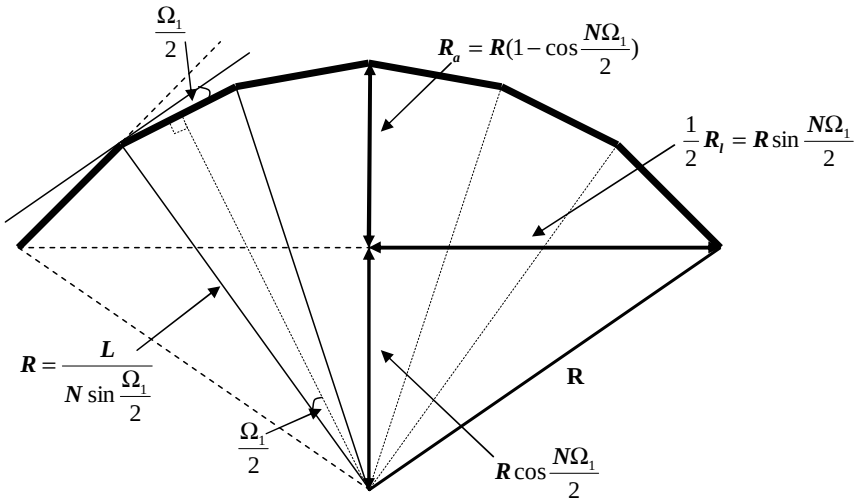

Figure 4.5: Diagram showing a fibre composed of 6 rods bent into a circular arc with radius of curvature $R = \frac{L}{N \sin \frac{\Omega_1}{2}}$.

shown in figure 4.2). The bend angle Ω_1^{eq} is given by

$$\tan \Omega_1^{eq} = -\frac{\tilde{a}\sqrt{(\tilde{a}^2(\cos\Delta + 1) + 2b^2)(1 - \cos\Delta)}}{(\tilde{a}^2 \cos\Delta + b^2)} \tag{4.2.2}$$

and the twist angle Ω_3^{eq} by

$$\tan \Omega_3^{eq} = \frac{2b \sin\Delta\sqrt{\tilde{a}^2 + b^2}}{(\tilde{a}^2(\cos\Delta + 1) + 2b^2 \cos\Delta)} \tag{4.2.3}$$

where $\tilde{a} = \frac{2a \sin\frac{\Delta}{2}}{\Delta}$ and $\Delta = \frac{2\pi n_t}{N}$.

Equations (4.2.2) and (4.2.3) are derived by by calculating the orthonormal frames of neighbouring rods and then calculating the rotation matrix in terms of the helix parameters a and b. This is then compared to the rotation matrix $\mathbf{R}(\Omega_1^{eq}, 0, \Omega_3^{eq})$. A full derivation is given in appendix A.

In our simulation we keep the arc length of the helix constant and vary the radius, pitch

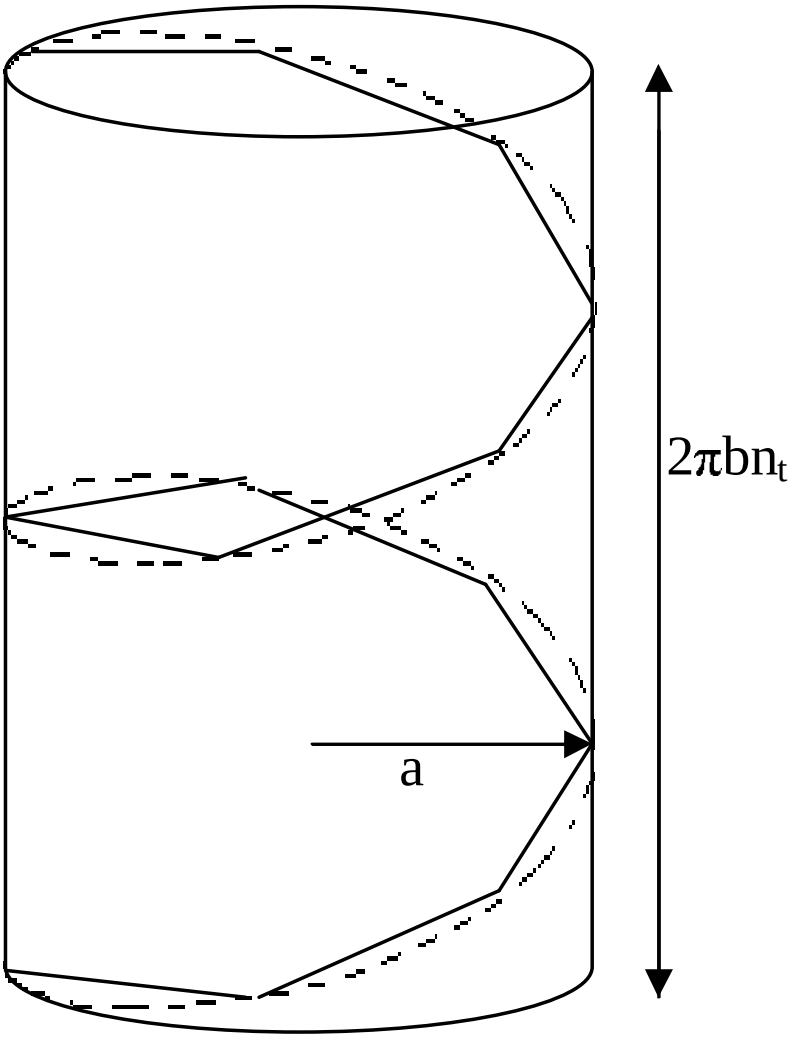

Figure 4.6: A continuous helix of radius a and pitch b discretised in N sections.

and number of turns. Non-dimensionalised with respect to the half length L, the fibre has a non-dimensional length of 2 with rods of length $l = \frac{2}{N}$. The values of a and b are therefore constrained by

$$l = \frac{2}{N} = |\mathbf{x}(\frac{\Delta}{2}) - \mathbf{x}(-\frac{\Delta}{2})| = \sqrt{4a^2 \sin^2 \frac{\Delta}{2} + b^2\Delta^2}$$

where $|\mathbf{x}(\frac{\Delta}{2}) - \mathbf{x}(-\frac{\Delta}{2})|$ is the length of the chord along which the rod lies, as shown in figure 4.7. Rearranging we obtain the value of b in terms of the radius a such that the arc length of the helix is constant.

$$b = \sqrt{\frac{4}{\Delta^2 N^2} - 4\frac{a^2}{\Delta^2} \sin^2 \frac{\Delta}{2}} \tag{4.2.4}$$

Principal axes and moments of inertia

In chapter 5 we consider semi-flexible helices and in order to define axes within a deformed helix we will used the principal axes of the moment of inertia tensor. The moment of inertia tensor is defined as

$$\underline{\tilde{\mathbf{I}}}_{ij} = \int (x_i - X_i)(x_j - X_j) ds$$

where $\mathbf{X}$ is the centre of mass. The principal axes define a set of perpendicular axes with the body, while the ratios of the eigenvalues provide a measure of the aspect ratio.

For the continuous helix given in equation (4.1.1) we find

$$\underline{\tilde{\mathbf{I}}} = \sqrt{a^2 + b^2} \begin{pmatrix} \frac{2}{3}b^2 n_t^3 \pi^3 & -2abn_t\pi & 0 \\ -2abn_t\pi & a^2 n_t \pi & 0 \\ 0 & 0 & a^2 n_t \pi \end{pmatrix}.$$

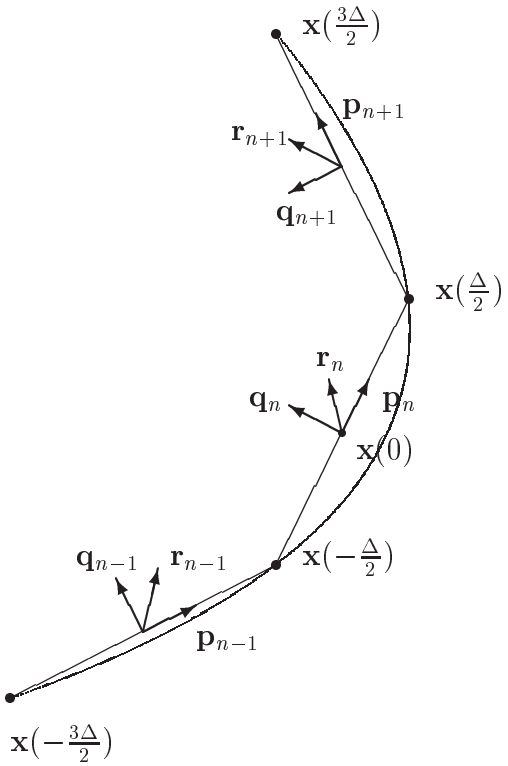

Figure 4.7: The orthonormal frames and position vectors of three neighbouring rods in a discretised helix.

The principal moments of inertia are given by the eigenvalues of the inertia tensor,

$$\lambda_{1,2} = \sqrt{a^2+b^2}\left(\frac{1}{2}a^2 n_t \pi + \frac{1}{3}b^2 n_t^3 \pi^3 \pm \frac{n_t \pi}{6}\sqrt{(3a^2 - 2n_t^2\pi^2 b^2)^2 + (12ab)^2}\right),$$

$$\lambda_3 = a^2 n_t \pi \sqrt{a^2+b^2}.$$

The principal axes are given by the corresponding eigenvectors,

$$\mathbf{E}_{1,2} = \left(\frac{-2abn_t\pi}{\frac{1}{2}a^2 n_t\pi - \frac{1}{3}b^2 n_t^3\pi^3 \pm \frac{n_t\pi}{6}\sqrt{(3a^2 - 2n_t^2\pi^2 b^2)^2 + (12ab)^2}}, 1, 0\right),$$

$$\mathbf{E}_3 = (0,0,1).$$

For a continous helix the path length of the helix $2\pi n_t\sqrt{a^2+b^2}$ must be equal to the non-dimensional fibre length 2 and so

$$\frac{1}{\pi n_t} = \sqrt{a^2+b^2}.$$

Using this we can obtain the helix parameters a and b in terms of the principle moments of inertia and the number of turns of the helix such that

$$a = \sqrt{\lambda_3}$$

and

$$b = \frac{\sqrt{\frac{3}{2}(\lambda_1+\lambda_2-\lambda_3)}}{n_t\pi}.$$

For any configuration of a discretised fibre we can calculate the principal axes and moments of inertia from the position and orientation vectors of the individual rods.

The centre of mass of a fibre composed of N rods is given by $\mathbf{x}_c = \frac{1}{N}\sum_{n=1}^{N}\mathbf{x}_n$ where $\mathbf{x}_n$ is the position vector for the centre of rod n. The inertia tensor for the whole fibre is

given by

$$\tilde{\mathbf{I}} = \sum_{n=1}^{N} \tilde{\mathbf{I}}_n$$

where the contribution $\tilde{\mathbf{I}}_n$ from each rod is given by

$$\tilde{\mathbf{I}}_n = \int_{-\frac{l}{2}}^{\frac{l}{2}} (\mathbf{x}(s) - \mathbf{x}_c)^2 ds.$$

The length of each rod is given by $l = \frac{2L}{N}$ and the position of any point along the rod is given by $\mathbf{x}(s) = \mathbf{x}_n + s\mathbf{p}_n$. The inertia tensor is therefore given by

$$\tilde{\mathbf{I}}_n = \int_{-\frac{L}{N}}^{\frac{L}{N}} (x_i^n + sp_i^n - x_i^c)(x_j^n + sp_j^n - x_j^c) ds$$

$$= \int_{-\frac{L}{N}}^{\frac{L}{N}} (x_i^n - x_i^c)(x_j^n - x_j^c) + s[p_i^n(x_j^n - x_j^c) + p_j^n(x_i^n - x_i^c)] + s^2 p_i^n p_j^n ds$$

$$= \frac{2L}{N}(x_i^n - x_i^c)(x_j^n - x_j^c) + \frac{2L^3}{3N^3} p_i^n p_j^n.$$

As $\tilde{\mathbf{I}}$ is symmetric the eigenvalues and eigenvectors can be calculated numerically using a series of Jacobi transformations [29].

4.3 Numerical Simulation

As in the previous simulation we have a set of $2N$ coupled equations for $\dot{\mathbf{x}}_n$ and $\dot{\mathbf{p}}_n$ describing the evolution of the position and shape of the fibre in time. These are given by

$$\mathbf{A}(\mathbf{p}^n) \cdot (\dot{\mathbf{x}}_n - \mathbf{K}.\mathbf{x}_n) = \mathbf{F}_c^n \tag{4.3.5}$$

and

$$\mathbf{C}(\mathbf{p}^n) \cdot (\dot{\mathbf{p}}_n - \mathbf{K}.\mathbf{p}_n) = \mathbf{T}^n \times \mathbf{p}_n, \tag{4.3.6}$$

where $\mathbf{A}(\mathbf{p}_n) = \frac{2\pi\mu l}{\log 2a_r}(2\mathbf{I} - \mathbf{p}_n\mathbf{p}_n)$ is the component of the grand resistance matrix relating force to translation as derived in subsection 1.2.6 and $\mathbf{C}(\mathbf{p}_n) = \frac{\pi\mu l^3}{3\log 2a_r}(\mathbf{I} - \mathbf{p}_n\mathbf{p}_n)$ is the component of the grand resistance matrix relating torque to rotation. $\mathbf{F}_c^n$ and $\mathbf{T}^n$ are the forces and torques acting on each individual rod.

Equations for $\dot{\mathbf{x}}_n$ and $\dot{\mathbf{p}}_n$ are coupled through the non-dimensionalised connectivity constraint

$$\dot{\mathbf{x}}_{n+1} - \dot{\mathbf{x}}_n = \frac{1}{N}(\dot{\mathbf{p}}_{n+1} + \dot{\mathbf{p}}_n) \tag{4.3.7}$$

as derived in chapter 2.

In addition we need a third set of equations to describe the spin of each rod about its axis. We shall define a twist angle ϕ_n for each rod given by

$$\phi_1 = 0$$

$$\phi_n = \phi_{n-1} + \Omega_3^{n-1} \text{ for } n = 2, .., N.$$

Thus $\dot{\phi}_n$ gives the relative angular velocity of rod n, compared to $n-1$ and is given by

$$\xi_a \dot{\phi}_n = \boldsymbol{\tau}^n \cdot \mathbf{p}_n \tag{4.3.8}$$

where $\xi_a = 4\pi\mu b^2 l$ is the hydrodynamic resistance to spin and $\boldsymbol{\tau}^n \cdot \mathbf{p}_n$ is the component of torque acting along the fibre axis.

For rods of high aspect ratio, $l >> b$ the resistance to axial spin ξ_a is negligible in comparison to the resistance to rotation $\xi_t = \frac{\pi\mu l^3}{3\log 2a_r}$ about axes perpendicular to $\mathbf{p}_n$

so that the rods will rapidly rotate to a configuration for which

$$\xi_a \dot{\phi}_n = \boldsymbol{\tau}^n \cdot \mathbf{p}_n \approx 0. \tag{4.3.9}$$

As the timescale for relaxation of spin is fast in comparison to the slow rotation timescale equation (4.3.9) may be decoupled from the solution of equations (4.3.5) and (4.3.6).

4.4 Balance of Forces and Torques

We now consider the forces and torques acting on each individual rod. The forces acting on each rod arise entirely from the connectivity constraint and have been derived in chapter 2. They are given by

$$\mathbf{F}_c^n = \frac{1}{l}(\mathbf{F}_n - \mathbf{F}_{n-1})$$

where the same non-dimensionalisation has been used as given in chapter 2.

The torques acting on each rod arise from both the connectivity constraint and from the elastic torques resulting from the bending and twisting stiffness at the joints. The torque on each rod as a result of the connectivity constraint was derived in chapter 2 and is given by

$$\mathbf{T}_c^n = \frac{l}{2}\mathbf{p}_n \times (\underline{\mathbf{I}} - \mathbf{p}_n\mathbf{p}_n) \cdot (\mathbf{F}_n + \mathbf{F}_{n-1}).$$

Again this has been non-dimensionalised as described in chapter 2.

In order to ensure that there is no net torque on the fibre the torques at each joint are calculated with respect to intermediate axes between rods n and $n+1$ (figure 4.8)

$$\mathbf{p}_n^* = \frac{\mathbf{p}_n + \mathbf{p}_{n+1}}{|\mathbf{p}_n + \mathbf{p}_{n+1}|},$$
$$\mathbf{q}_n^* = \frac{\mathbf{q}_n + \mathbf{q}_{n+1}}{|\mathbf{q}_n + \mathbf{q}_{n+1}|},$$
$$\mathbf{r}_n^* = \frac{\mathbf{r}_n + \mathbf{r}_{n+1}}{|\mathbf{r}_n + \mathbf{r}_{n+1}|}.$$

The elastic torques on each rod are then given by

$$\begin{aligned}
\boldsymbol{\tau}_1^n &= -k^B(\bar{\Omega}_1^n - \bar{\Omega}_1^{eq})\mathbf{r}_n^* + k^B(\bar{\Omega}_1^{n-1} - \bar{\Omega}_1^{eq})\mathbf{r}_{n-1}^*, \\
\boldsymbol{\tau}_2^n &= -k^B(\bar{\Omega}_2^n - \bar{\Omega}_2^{eq})\mathbf{q}_n^* + k^B(\bar{\Omega}_2^{n-1} - \bar{\Omega}_2^{eq})\mathbf{q}_{n-1}^*, \\
\boldsymbol{\tau}_3^n &= -k^T(\bar{\Omega}_3^n - \bar{\Omega}_3^{eq})\mathbf{p}_n^* + k^T(\bar{\Omega}_3^{n-1} - \bar{\Omega}_3^{eq})\mathbf{p}_{n-1}^*.
\end{aligned} \tag{4.4.10}$$

where the angles $\bar{\Omega}_i^n$ are formed from the transformations with respect to axes $\mathbf{p}_n^*$, $\mathbf{q}_n^*$, $\mathbf{r}_n^*$.

There will be $n-1$ sets of intermediate axes corresponding to the $n-1$ joints.

$\bar{\Omega_i^n}$ is given by

$$\bar{\Omega_i^n} = \Omega_i^{n^-} + \Omega_i^{n^+}$$

where $\Omega_i^{n^+}$ for $i = 3, ..1$ are the angles of rotation from $\{\mathbf{p}_n^*, \mathbf{q}_n^*, \mathbf{r}_n^*\}$ to $\{\mathbf{p}_{n+1}, \mathbf{q}_{n+1}, \mathbf{r}_{n+1}\}$ and $-\Omega_i^{n^-}$ for $i = 3, .., 1$ are the angles of rotation from $\{\mathbf{p}_n^*, \mathbf{q}_n^*, \mathbf{r}_n^*\}$ to $\{\mathbf{p}_n, \mathbf{q}_n, \mathbf{r}_n\}$ such that

$$\begin{pmatrix} \mathbf{p}_{n+1} \\ \mathbf{q}_{n+1} \\ \mathbf{r}_{n+1} \end{pmatrix} = \mathbf{R}^+ \begin{pmatrix} \mathbf{p}_n^* \\ \mathbf{q}_n^* \\ \mathbf{r}_n^* \end{pmatrix}, \tag{4.4.11}$$

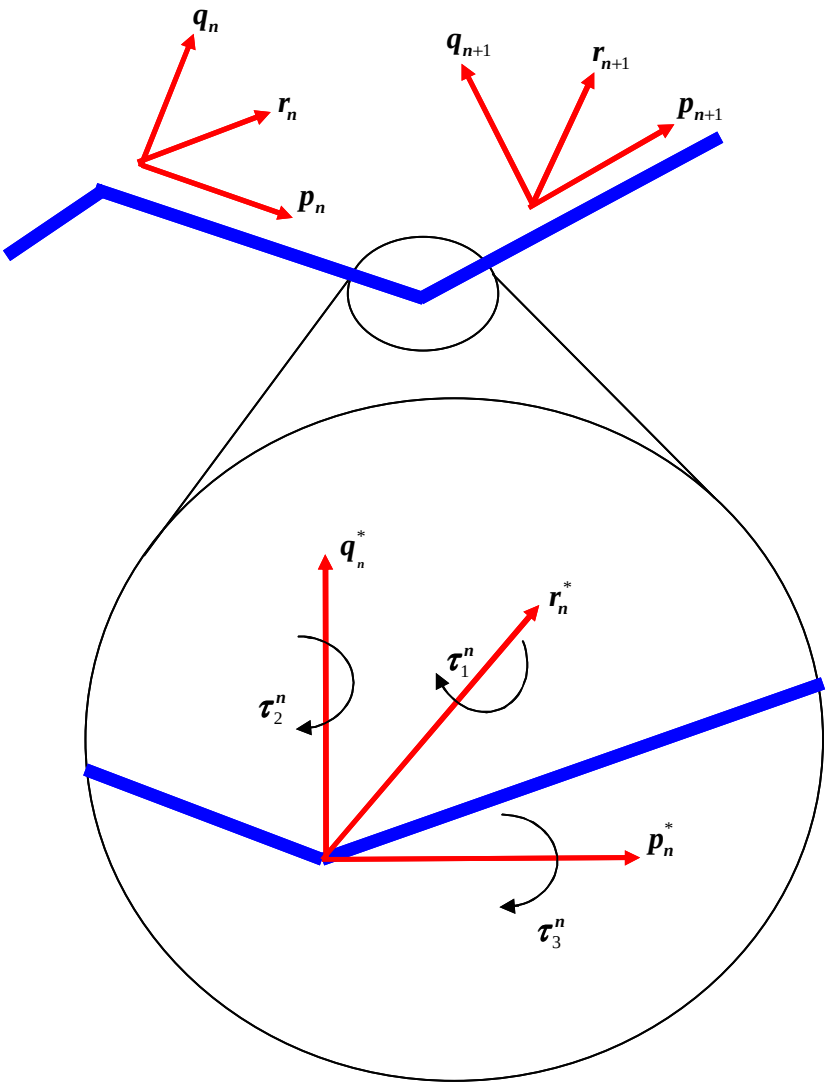

Figure 4.8: Torques $\boldsymbol{\tau}_1^n$, $\boldsymbol{\tau}_2^n$ and $\boldsymbol{\tau}_3^n$ at the junction between rods n and $n+1$ defined with respect to the mean of the local frames of rods n and $n+1$.

and

$$\begin{pmatrix} \mathbf{p}_n \\ \\ \mathbf{q}_n \\ \\ \mathbf{r}_n \end{pmatrix} = \mathbf{R}^- \begin{pmatrix} \mathbf{p}_n^* \\ \\ \mathbf{q}_n^* \\ \\ \mathbf{r}_n^* \end{pmatrix} \tag{4.4.12}$$

where $\mathbf{R}^+ = \mathbf{R}(\Omega_1^{n^+}, \Omega_2^{n^+}, \Omega_3^{n^+})$ and $\mathbf{R}^- = \mathbf{R}(-\Omega_1^{n^-}, -\Omega_2^{n^-}, -\Omega_3^{n^-})$.

The angles may be calculated from the local frames as follows

$$\begin{aligned} \Omega_1^{n^+} &= -\tan^{-1}\left(\frac{\mathbf{q}_n^* \cdot \mathbf{p}_{n+1}}{\mathbf{p}_n^* \cdot \mathbf{p}_{n+1}}\right), \\ \Omega_2^{n^+} &= \sin^{-1}(\mathbf{r}_n^* \cdot \mathbf{p}_{n+1}), \\ \Omega_3^{n^+} &= -\tan^{-1}\left(\frac{\mathbf{r}_n^* \cdot \mathbf{q}_{n+1}}{\mathbf{r}_n^* \cdot \mathbf{r}_{n+1}}\right) \end{aligned}$$

and

$$\begin{aligned} \Omega_1^{n^-} &= -\tan^{-1}\left(-\frac{\mathbf{q}_n^* \cdot \mathbf{p}_n}{\mathbf{p}_n^* \cdot \mathbf{p}_n}\right), \\ \Omega_2^{n^-} &= \sin^{-1}(-\mathbf{r}_n^* \cdot \mathbf{p}_n), \\ \Omega_3^{n^-} &= -\tan^{-1}\left(-\frac{\mathbf{r}_n^* \cdot \mathbf{q}_n}{\mathbf{r}_n^* \cdot \mathbf{r}_n}\right). \end{aligned}$$

The torques acting on each rod are then resolved into those acting perpendicular to the rod,

$$(\mathbf{I} - \mathbf{p}_n\mathbf{p}_n) \cdot \boldsymbol{\tau}^n$$

and parallel to the rod,

$$\mathbf{p}_n \cdot \boldsymbol{\tau}^n$$

where $\boldsymbol{\tau}^n = \boldsymbol{\tau}_1^n + \boldsymbol{\tau}_2^n + \boldsymbol{\tau}_3^n$.

The term $\mathbf{T}^n$ in equation (4.3.6) is composed from the constraint torques together with elastic torques perpendicular to $\mathbf{p}_n$, and is given by

$$\mathbf{T}^n = \mathbf{T}_c^n + (\mathbf{I} - \mathbf{p}_n\mathbf{p}_n) \cdot \boldsymbol{\tau}^n.$$

Substituting the expressions for force and torque into equations (4.3.5), (4.3.6) and (4.3.9) together with equation (4.3.7) make up the full system of equations. Written in full, non-dimensionalised form they are

$$\dot{\mathbf{x}}_n = \mathbf{K}.\mathbf{x}_n + (\mathbf{I} + \mathbf{p}_n\mathbf{p}_n).(\mathbf{F}_n - \mathbf{F}_{n-1}), \tag{4.4.13}$$

$$\dot{\mathbf{p}}_n = \mathbf{K}.\mathbf{p}_n - \mathbf{p}_n.\mathbf{K}.\mathbf{p}_n\mathbf{p}_n + 3N(\mathbf{I} - \mathbf{p}_n\mathbf{p}_n).(\mathbf{F}_n + \mathbf{F}_{n-1}) + (\mathbf{I} - \mathbf{p}_n\mathbf{p}_n).(\boldsymbol{\tau}_1^n + \boldsymbol{\tau}_2^n + \boldsymbol{\tau}_3^n) \times \mathbf{p}_n, \tag{4.4.14}$$

$$\mathbf{p}_n.(\boldsymbol{\tau}_1^n + \boldsymbol{\tau}_2^n + \boldsymbol{\tau}_3^n) = 0, \tag{4.4.15}$$

$$\dot{\mathbf{x}}_{n+1} - \dot{\mathbf{x}}_n = \frac{1}{N}(\dot{\mathbf{p}}_{n+1} + \dot{\mathbf{p}}_n). \tag{4.4.16}$$

Figure 4.9 gives a flow diagram for the simulation algorithm. To start with we choose values of Ω_1, Ω_2 and Ω_3. We then generate an initial configuration of rods by using the rotation matrix $\mathbf{R}$ to calculate the local orthonormal frames. The orthonormal frames can

then be used to calculate the symmetric equilibrium and initial values $\bar{\Omega}_1^{eq}$, $\bar{\Omega}_2^{eq}$, $\bar{\Omega}_3^{eq}$ and Ω_1^{eq}, Ω_2^{eq}, Ω_3^{eq} respectively.

At each timestep we first solve equation (4.4.15), using a multi-dimensional Newton Raphson scheme[29], to find the change in ϕ and therefore the change in Ω_3. We then update the values of $\mathbf{q}_n$ and $\mathbf{r}_n$ accordingly. We then solve equations (4.4.13) and (4.4.14) by using the constraint equation (4.4.16) to set up a system of tridiagonal equations that can be solved to give the constraint forces, as described in chapter 2. We then integrate equations (4.4.13) and (4.4.14), using a 4th order Runge Kutta scheme [29], to give new values of $\mathbf{x}_n$ and $\mathbf{p}_n$. The axes $\mathbf{q}_n$ and $\mathbf{r}_n$ are then parallel transported using

$$\mathbf{q}_n(t+h) = -(\mathbf{q}_n(t) \cdot \mathbf{p}_n(t+h))\mathbf{p}_n(t) + \mathbf{q}_n(t)$$

and

$$\mathbf{r}_n(t+h) = -(\mathbf{r}_n(t) \cdot \mathbf{p}_n(t+h))\mathbf{p}_n(t) + \mathbf{r}_n(t).$$

The resulting vectors are not perfectly orthogonal and hence the Gram-Schmidt process is used at the end of each time step to re-orthogonalize the vectors. The values of $\bar{\Omega}_1$, $\bar{\Omega}_2$, $\bar{\Omega}_3$ are then updated before proceeding to the next time-step.

4.5 Rigid Helix Simulation

In order to validate our code in the limit of high stiffness and to provide a comparison for our flexible helix simulations, we developed a separate numerical simulation for a rigid helix. The motion of a rigid particle in a linear flow can be found from its grand resistance matrix (see section 1.2.6).

The grand resistance matrix relates the hydrodynamic force, torque and stress exerted by the fluid on the particle to the fluid and particle velocities

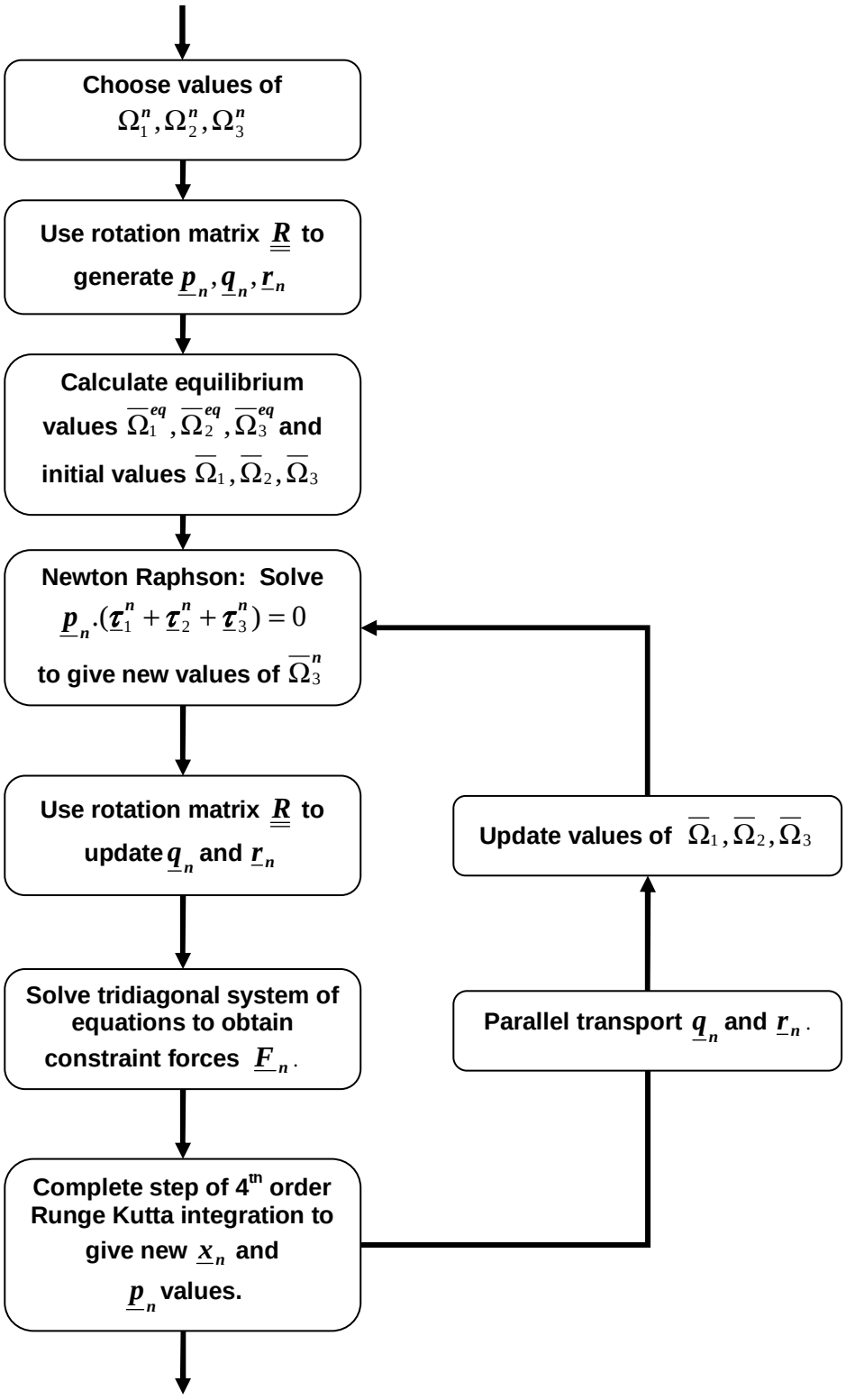

Figure 4.9: Flow diagram for the simulation algorithm.

$\mathbf{u}^{\infty} = \mathbf{U}_0 + \mathbf{K}\cdot\mathbf{x}_c + \frac{1}{2}\boldsymbol{\omega}^{\infty}\times(\mathbf{x}-\mathbf{x}_c) + \underline{\mathbf{E}}\cdot(\mathbf{x}-\mathbf{x}_c)$ and $\mathbf{u}^{h} = \mathbf{U}+\boldsymbol{\omega}\times(\mathbf{x}-\mathbf{x}_c)$ such that

$$\begin{pmatrix} \mathbf{F} \\ \mathbf{T} \\ \mathbf{S} \end{pmatrix} = \begin{pmatrix} \mathbf{A} & \tilde{\mathbf{B}} & \tilde{\mathbf{G}} \\ \mathbf{B} & \mathbf{C} & \tilde{\mathbf{H}} \\ \mathbf{G} & \mathbf{H} & \mathbf{M} \end{pmatrix} \begin{pmatrix} \mathbf{U_0} + \mathbf{K}\cdot\mathbf{x_c} - \mathbf{U} \\ \boldsymbol{\omega}^{\infty} - \boldsymbol{\omega} \\ \mathbf{E}^{\infty} \end{pmatrix}. \tag{4.5.17}$$

The tensor resistivities $\mathbf{A}$, $\tilde{\mathbf{B}}$, $\tilde{\mathbf{G}}$, $\mathbf{B}$, $\mathbf{C}$, $\tilde{\mathbf{H}}$, $\mathbf{G}$, $\mathbf{H}$ and $\mathbf{M}$ are fixed with respect to the axes fixed with the rigid body. Consequently to calculate the motion with respect to fixed axes it is necessary to either rotate the resistivity tensors to take account of the rotation of the body. Alternatively, since the flow is at zero Reynolds number, we can perform the calculation with respect to the body axes by rotating the external flow.

For a helix of radius a and pitch b we define body axes $\{\mathbf{p},\ \mathbf{q},\ \mathbf{r}\}$ so that position vector along the helix is given by

$$\mathbf{x}'(s) = bs\mathbf{p} + a\sin(s)\mathbf{q} + a\cos(s)\mathbf{r}. \tag{4.5.18}$$

The axes $\{\mathbf{p},\mathbf{q},\mathbf{r}\}$ are related to $\{\mathbf{e}_1,\mathbf{e}_2,\mathbf{e}_3\}$, the standard basis in $\mathcal{R}^3$, by

$$\begin{pmatrix} \mathbf{p} \\ \mathbf{q} \\ \mathbf{r} \end{pmatrix} = \mathbf{R}\begin{pmatrix} \mathbf{e}_1 \\ \mathbf{e}_2 \\ \mathbf{e}_3 \end{pmatrix} \tag{4.5.19}$$

where $\mathbf{R}$ is given by

$$\mathbf{R} = \begin{pmatrix} \cos\theta_1\cos\theta_2 & -\cos\theta_2\sin\theta_1 & \sin\theta_2 \\ \sin\theta_1\cos\theta_3 + \cos\theta_1\sin\theta_2\sin\theta_3 & \cos\theta_1\cos\theta_3 - \sin\theta_1\sin\theta_2\sin\theta_3 & -\cos\theta_2\sin\theta_3 \\ \sin\theta_1\sin\theta_3 - \cos\theta_1\sin\theta_2\cos\theta_3 & \cos\theta_1\sin\theta_3 + \sin\theta_1\sin\theta_2\cos\theta_3 & \cos\theta_2\cos\theta_3 \end{pmatrix}.$$

θ_1, θ_2 and θ_3 are the angles of rotation from the cartesian axes to the local axes about $\mathbf{e}_3$, $\mathbf{e}_2$ and $\mathbf{e}_1$ respectively .

Using this transformation we can transform the velocity gradient

$$\mathbf{K} = \begin{pmatrix} 0 & \dot{\gamma} & 0 \\ 0 & 0 & 0 \\ 0 & 0 & 0 \end{pmatrix}$$

for a shear flow into $\{\mathbf{p}, \mathbf{q}, \mathbf{r}\}$ co-ordinates using $\mathbf{K}' = \mathbf{R}(\mathbf{K}\mathbf{R}^T)$.

In the following we shall use prime to denote quantities with respect to $\{\mathbf{p}, \mathbf{q}, \mathbf{r}\}$ and unprimed for those measured with respect to $\{\mathbf{e}_1, \mathbf{e}_2, \mathbf{e}_3\}$.

4.5.1 Numerical Simulation for a Rigid Helix

The initial orientation of the helix is choosen by selecting values of θ_1, θ_2 and θ_3 and hence $\mathbf{R}(t=0)$. The velocity, $\mathbf{u}'$, and angular velocity, $\boldsymbol{\omega}'$, are then calculated at time t, in body co-ordinates. The change to the local axes are given by solving

$$\begin{aligned} \dot{\mathbf{p}} &= \boldsymbol{\omega}'(t) \times \mathbf{p} = \omega_r'\mathbf{q} - \omega_q'\mathbf{r} \\ \dot{\mathbf{q}} &= \boldsymbol{\omega}'(t) \times \mathbf{q} = \omega_p'\mathbf{r} - \omega_r'\mathbf{p} \\ \dot{\mathbf{r}} &= \boldsymbol{\omega}'(t) \times \mathbf{r} = \omega_q'\mathbf{p} - \omega_p'\mathbf{q}. \end{aligned}$$

To obtain the rotation matrix $\mathbf{R}$ for the helix in Cartesian co-ordinates we calculate the new values of θ_1, θ_2 and θ_3 using $\{\mathbf{p}, \mathbf{q}, \mathbf{r}\}$ such that

$$\begin{aligned} \theta_1 &= -\tan^{-1}(\tfrac{p_2}{p_1}) \\ \theta_2 &= \sin^{-1}(p_3) \\ \theta_3 &= -\tan^{-1}(\tfrac{q_3}{r_3}) \end{aligned}$$

where $-\pi \leq \theta_1 \leq \pi$, $-\frac{\pi}{2} \leq \theta_2 \leq \frac{\pi}{2}$ and $-\pi \leq \theta_3 \leq \pi$.

The velocity of the helix with respect to Cartesian axes can then be found from $\mathbf{u} = \mathbf{R}^{-1}(t)\mathbf{u}'$ and hence the position vector updated from $\frac{d\mathbf{x}}{dt} = \mathbf{u}$.

4.5.2 Grand Resistance Matrix for a Helix

The contributions to the grand resistance matrix are calculated using slender body theory. Here we shall assume that both the radius a and pitch $2\pi b$ are large compared to the thickness of the fibre so that hydrodynamic interactions betweeen different parts of the helix may be neglected. Note this is the same approximation made in the flexible fibre simulation.

The helix is given by

$$\mathbf{x} = (bs, a\sin(s), a\cos(s))$$

where $0 \leq s \leq 2\pi n_t$ and n_t is the number of turns of the helix. The path length $2L$ of the helix is

$$2L = 2\pi n_t \sqrt{a^2 + b^2}.$$

The unit tangent vector at a point s along the helix is given by

$$\mathbf{p} = \frac{d\mathbf{x}}{ds} = \frac{1}{\sqrt{a^2 + b^2}}(b, a\cos(s), -a\sin(s)).$$

We consider a small section ds of a helix moving with velocity $\mathbf{u}^h$ in a flow with velocity $\mathbf{u}^\infty$. At leading order in slender body theory the resistance of the fluid to the motion of this section of helix is given by $\mathbf{f}ds$ where

$$\mathbf{f} = \frac{2\pi\mu}{\log 2a_r}(\mathbf{I} - \mathbf{pp}) \cdot (\mathbf{u}^\infty - \mathbf{u}^h).$$

Here we have assumed that a and b are of order L. We non-dimensionalise length with respect to L and force density with repect to $\mu L\dot{\gamma}$, so that $a^* = \frac{a}{L}$, $b^* = \frac{b}{L}$ and $\mathbf{f}^* = \frac{\mathbf{f}}{\mu L\dot{\gamma}}$. The force, torque and stress acting on the entire helix are given by

$$\mathbf{F} = \int_0^{2\pi n_t} \mathbf{f}(s)ds,$$

$$\mathbf{T} = \int_0^{2\pi n_t} (\mathbf{x} - \mathbf{x}_c) \times \mathbf{f}ds,$$

$$\mathbf{S} = \frac{1}{2}\int_0^{2\pi n_t} (\mathbf{x} - \mathbf{x}_c)\mathbf{f} + \mathbf{f}(\mathbf{x} - \mathbf{x}_c)ds.$$

Where $\mathbf{x}_c$ is the centre of resistance of the helix, which must be determined as part of the calculation.

To calculate the first column of the grand resistance matrix we consider the translation of a helix at a steady velocity $\mathbf{U}$ in a stationary fluid such that $\mathbf{u}^h = \mathbf{U}$ and $\mathbf{u}^\infty = 0$. This gives us the following expressions for the force, torque and stress on the helix in terms of the elements of the grand resistance matrix

$$F_i = -A_{ij}U_j,$$

$$T_i^* = \int \epsilon_{ikl}x_k f_l ds = -B_{ij}U_j + \epsilon_{ikl}x_{c_k}F_l = -(B_{ij} + \epsilon_{ikl}x_{c_k}A_{lj})U_j,$$

$$S_{ij}^* = \frac{1}{2}\int x_i f_j + f_i x_j ds = -(G_{ijk} + \frac{1}{2}x_{c_i}A_{jk} + \frac{1}{2}A_{ik}x_{c_j})U_k.$$

Calculating the force for the cases $\mathbf{U} = -\mathbf{e}_j$ for $j = 1..3$ gives the j^{th} column of A_{ij}, similarly calculating $\mathbf{T}^*$ gives the j^{th} column of $(B_{ij} + \epsilon_{ikl} x_{c_k} A_{lj})$. Calculating S^*_{ij} for the cases $\mathbf{U} = -\mathbf{e}_k$ for $k = 1..3$ gives the k^{th} components of $(G_{ijk} + \frac{1}{2} x_{c_i} A_{jk} + \frac{1}{2} A_{ik} x_{c_j})$. The resulting values for the tensors $\mathbf{A}$ and $\mathbf{B} + \mathbf{x}_c \times \mathbf{A}$ are given by

$$\mathbf{A} = 2\pi n_t \begin{pmatrix} \frac{2a^2+b^2}{\sqrt{a^2+b^2}} & 0 & 0 \\ 0 & \frac{3a^2+4b^2}{2\sqrt{a^2+b^2}} & 0 \\ 0 & 0 & \frac{3a^2+4b^2}{2\sqrt{a^2+b^2}} \end{pmatrix} \tag{4.5.20}$$

$$\mathbf{B} + \mathbf{x}_c \times \mathbf{A} = 2\pi n_t \begin{pmatrix} \frac{a^2 b}{\sqrt{a^2+b^2}} & 0 & 0 \\ \frac{ab^2}{\sqrt{a^2+b^2}} & -\frac{a^2 b}{4\sqrt{a^2+b^2}} & -\frac{b\pi n_t (3a^2+4b^2)}{2\sqrt{a^2+b^2}} \\ 0 & \frac{b\pi n_t (3a^2+4b^2)}{2\sqrt{a^2+b^2}} & -\frac{3a^2 b}{4\sqrt{a^2+b^2}} \end{pmatrix}. \tag{4.5.21}$$

We omit the calculation of $\mathbf{G}$ as this is not needed for our simulation.

The principle directions, given by the eigenvectors of matrix $\mathbf{A}$ give the natural co-ordinate system of the helix. As we can see matrix $\mathbf{A}$ has only diagonal elements so that the principle directions are given by the standard Cartesian axes. Translation along either of these axes will produce a force along that axis only.

To find $\mathbf{B}$ and $\mathbf{x}_c$ we note that $\mathbf{B}$ is symmetric when calculated with respect to the centre of resistance.

To calculate the centre of resistance we follow the derivation of Kim and Karrila [20]. We let $\mathbf{T}(\mathbf{x}_c)$ be the torque calculated with respect to the centre of resistance, for a helix

undergoing translation and $\mathbf{T}(0)$ be the torque calculated with respect to the origin.

$$\begin{aligned}\mathbf{T}(\mathbf{x}_c) - \mathbf{T}(0) &= \int_S (\mathbf{x} - \mathbf{x}_c) \times (\sigma \cdot \hat{\mathbf{n}}) ds - \int_S \mathbf{x} \times (\sigma \cdot \hat{\mathbf{n}}) ds \\ &= \int_S -\mathbf{x}_c \times (\sigma \cdot \hat{\mathbf{n}}) dS \\ &= -\mathbf{x}_c \times \mathbf{F}\end{aligned} \tag{4.5.22}$$

This can be written in term of the elements of the grand resistance matrix as

$$B_{ij}^{(c)} = B_{ij}^{(0)} - \epsilon_{ikl}(\mathbf{x}_c)_k A_{lj} \tag{4.5.23}$$

where the superscripts denote the centres used in the calculations.

The coupling tensor calculated with respect to the centre of resistance is symmetric therefore the antisymmetric part of equation (4.5.23) is given by

$$B_{ij}^{(0)} - B_{ji}^{(0)} = \epsilon_{ikl}(\mathbf{x}_c)_k A_{lj} - \epsilon_{jkl}(\mathbf{x}_c)_k A_{li}.$$

Mulitplying through by ϵ_{mij} gives

$$\begin{aligned}\epsilon_{mij}[B_{ij}^{(0)} - B_{ji}^{(0)}] &= \epsilon_{mij}\epsilon_{ikl}(\mathbf{x}_c)_k A_{lj} - \epsilon_{mij}\epsilon_{jkl}(\mathbf{x}_c)_k A_{li} \\ &= (\delta_{jk}\delta_{lm} - \delta_{jl}\delta_{km})(\mathbf{x}_c)_k A_{lj} - (\delta_{km}\delta_{il} - \delta_{lm}\delta_{ik})(\mathbf{x}_c)_k A_{li} \\ &= (A_{mj}(\mathbf{x}_c)_j - (\mathbf{x}_c)_m A_{jj}) - ((\mathbf{x}_c)_m A_{ii} - A_{mi}(\mathbf{x}_c)_i) \\ &= 2[(\mathbf{A} - (tr\mathbf{A})\mathbf{I}) \cdot \mathbf{x}_c]_m\end{aligned} \tag{4.5.24}$$

As our matrix $\mathbf{A}$ has only diagonal elements the matrix $(\mathbf{A} - (tr\mathbf{A})\mathbf{I})$ and its inverse are easily calculated. Since $\mathbf{A}$ is symmetric it can always be diagonalised by using its principal directions as a basis. We therefore obtain the following expression for the centre

of resistance of the helix,

$$\mathbf{x}_c = \frac{B^{(0)}_{32} - B^{(0)}_{23}}{A_{22} + A_{33}}\mathbf{e}_1 + \frac{B^{(0)}_{13} - B^{(0)}_{31}}{A_{33} + A_{11}}\mathbf{e}_2 + \frac{B^{(0)}_{21} - B^{(0)}_{12}}{A_{11} + A_{22}}\mathbf{e}_3,$$

where $\mathbf{e}_i$ for $i = 1..3$ are the cartesian axes and A_{ii} are the diagonal elements and in this case the principle values of $\mathbf{A}$.

Calculating the centre of rotation for the helix described gives

$$\mathbf{x}_c = \begin{pmatrix} b\pi n_t \\ \\ 0 \\ \\ \frac{2ab^2}{7a^2+6b^2} \end{pmatrix}.$$

Calculating $\mathbf{B}$ from equation (4.5.21) gives

$$\mathbf{B} = 2\pi n_t \begin{pmatrix} \frac{a^2 b}{\sqrt{a^2+b^2}} & \frac{ab^2(3a^2+4b^2)}{(7a^2+6b^2)\sqrt{a^2+b^2}} & 0 \\ \\ \frac{ab^2(3a^2+4b^2)}{(7a^2+6b^2)\sqrt{a^2+b^2}} & -\frac{a^2 b}{4\sqrt{a^2+b^2}} & 0 \\ \\ 0 & 0 & -\frac{3a^2 b}{4\sqrt{a^2+b^2}} \end{pmatrix}.$$

To calculate the second column of entries in grand resistance matrix we consider the rotation of a helix at an angular velocity $\boldsymbol{\omega}$ in a stationary fluid such that $\mathbf{u}^h = \boldsymbol{\omega} \times (\mathbf{x} - \mathbf{x}_c)$ and $\mathbf{u}^\infty = 0$. In this case expressions for force, torque and stress are given by

$$F_i = -\tilde{B}_{ij}\omega_j,$$

$$T_i = -C_{ij}\omega_j,$$

$$S_{ij} = -H_{ijk}\omega_k.$$

As $\tilde{\mathbf{B}}$ is given by the transpose of $\mathbf{B}$ and $\mathbf{H}$ is not required in this simulation then we need only calculate $\mathbf{C}$, which is obtained by calculating the torque for the cases $\boldsymbol{\omega} = -\mathbf{e}_j$ for $j = 1..3$ to give the j^{th} column of $\mathbf{C}$. From this we obtain $\mathbf{C}$ as

$$\mathbf{C} = \begin{pmatrix} \frac{2a^2\pi n_t(80b^6+210a^2b^4+49a^6+182a^4b^2)}{\sqrt{a^2+b^2}(7a^2+6b^2)^2} & \frac{ab\pi n_t(35b^2a^2+24b^4+14a^4)}{(7a^2+6b^2)\sqrt{a^2+b^2}} & 0 \\ \frac{ab\pi n_t(35b^2a^2+24b^4+14a^4)}{(7a^2+6b^2)\sqrt{a^2+b^2}} & \frac{C*}{6\sqrt{a^2+b^2}(7a^2+6b^2)^2} & 0 \\ 0 & 0 & \frac{\pi n_t(-3b^2a^2+12a^4+\pi^2n_t^2(6a^2b^2+8b^4))}{6\sqrt{a^2+b^2}} \end{pmatrix}$$

where

$$C^* = \pi n_t(588a^8+1743a^6b^2+1452a^4b^4+300a^2b^6+\pi^2n_t^2(294a^6b^2+896a^4b^4+888a^2b^6+288b^8)).$$

Finally to calculate the 3rd row of entries in the grand resistance matrix we consider a stationary helix in a rate of strain field such that $\mathbf{u}^h = 0$ and $\mathbf{u}^\infty = \mathbf{E}\cdot\mathbf{x}$. In this case the expressions for force, torque and stress are given by

$$F_i = -\tilde{G}_{ijk}E^\infty_{jk},$$

$$T_i = -\tilde{H}_{ijk}E^\infty_{jk},$$

$$S_{il} = -M_{iljk}E^\infty_{jk}.$$

By calculating the force, torque and stress for the 9 cases $E^\infty_{ik} = 1$ and all other entries zero for $j = 1..3$, $k = 1..3$ we obtain $\tilde{G}_{ijk}$, $\tilde{H}_{ijk}$ and M_{iljk} respectively. Values of $\tilde{\mathbf{G}}$ and $\tilde{\mathbf{H}}$ are given in appendix B. $\mathbf{M}$ is not needed for the simulation.

Using the grand resistance matrix we can now obtain expressions for the force and torque

on a helix in terms of the velocity and angular velocity. By setting the force and torque to zero and solving for the velocity and angular velocity we obtain the values required in our simulation.

4.5.3 Mobility Tensor and Axis of Rotation

The mobility tensor relates the velocity, angular velocity and stress of the particle to the force, torque and strain on the particle such that

$$\begin{pmatrix} \mathbf{U_0} + \mathbf{K} \cdot \mathbf{x_c} - \mathbf{U} \\ \boldsymbol{\omega}^{\infty} - \boldsymbol{\omega} \\ \mathbf{S} \end{pmatrix} = \begin{pmatrix} \mathbf{a} & \tilde{\mathbf{b}} & \tilde{\mathbf{g}} \\ \mathbf{b} & \mathbf{c} & \tilde{\mathbf{h}} \\ \mathbf{g} & \mathbf{h} & \mathbf{m} \end{pmatrix} \begin{pmatrix} \mathbf{F} \\ \mathbf{T} \\ \mathbf{E}^{\infty} \end{pmatrix}. \tag{4.5.25}$$

In chapter 6 in order to get a uniform swimming direction it is necessary to calculate the axis about which a helix rotates. This can be achieved by calculating the principle axes of $\mathbf{c}$. The matrix $\mathbf{c}$ can be obtained directly from the values of the grand resistance matrix [20] and is given by

$$\mathbf{c} = (\mathbf{C} - \mathbf{B}\mathbf{A}^{-1}\mathbf{B}^{T})^{-1}.$$

By calculating the eigenvectors $\mathbf{c}_1$, $\mathbf{c}_2$ and $\mathbf{c}_3$ of $\mathbf{c}$ we obtain the axes of rotation of the helix. The eigenvectors are given in local co-ordinates by

$$\mathbf{c}_1 = \begin{pmatrix} \frac{-2c_{12}}{-c_{22}+c_{11}-\sqrt{c_{22}^2-2c_{22}c_{11}+c_{11}^2+4c_{12}^2}} \\ 1 \\ 0 \end{pmatrix},$$

$$\mathbf{c}_2 = \begin{pmatrix} \frac{-2c_{12}}{-c_{22}+c_{11}+\sqrt{c_{22}^2-2c_{22}c_{11}+c_{11}^2+4c_{12}^2}} \\ 1 \\ 0 \end{pmatrix},$$

$$\mathbf{c}_3 = \begin{pmatrix} 0 \\ 0 \\ 1 \end{pmatrix},$$

where c_{ij} are the entries of $\mathbf{c}$ given in appendix C.

Numerically we find that $\mathbf{c}_1$ lies close to $\mathbf{p}$, $\mathbf{c}_2$ lies close to $\mathbf{q}$ and $\mathbf{c}_3$ is equal to $\mathbf{r}$.

Chapter 5

Simulation Results for Intrinsically Bent Fibres

In this chapter we study the motion of infinite aspect ratio fibres with non-straight equilibrium shapes using the numerical simulation described in chapter 4. In particular we shall compare the effect of the effective aspect ratio due to the intrinsic bend of the fibre with the behaviour of intrinsically straight fibres of infinite and finite aspect ratio described in chapter 3.

We consider two types of intrinsic bend. The first section deals with fibres that are bent into circular arcs so that the bend is confined to the plane. These equilibrium shapes are given by $\Omega_2^{eq} = \Omega_3^{eq} = 0$ with a non zero value for Ω_1^{eq} so that the fibres are bent into a circular arc. The second section deals with fibres with an intrinsic helical shape. As discussed in chapter 4, the equilibrium shape for a helix requires Ω_1^{eq} and Ω_3^{eq} to be non-zero and calculated from the values of radius and pitch.

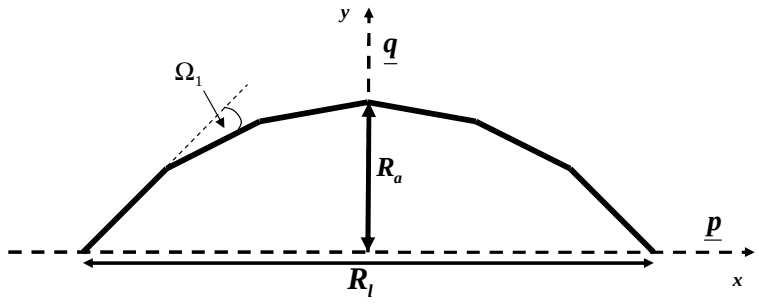

Figure 5.1: Illustration of a bent fibre with end-to-end vector $\mathbf{p}$, end-to-end length R_l, normal vector in the plane of the fibre $\mathbf{q}$ and amplitude R_a. The bend angle is Ω_1.

5.1 Fibre with in-plane bend

We begin by considering the rotation of a fibre whose intrinsic shape is a circular arc with its end-to-end vector, $\mathbf{R}$, aligned along the x axis and its bend in the flow-gradient, $x-y$ plane. Recall that for a fibre whose intrinsic bend is confined to a plane we can define local axes with $\mathbf{p}$ in the direction of the end-to-end vector and $\mathbf{q}$, the normal direction to $\mathbf{p}$ in the plane of the fibre. For fibres bent in circular arcs the degree of bend can be measured by the bend amplitude R_a as illustrated in figure 5.1. The fibre rotates forming C turns as shown in figure 5.2 for a fibre with bend amplitude $R_a = 2.5 \times 10^{-2}$ and bending angle $\Omega_1 = 0.01$. The fibre performs C turns rather than S turns as it does not have the symmetry of an instrinsically straight finite aspect ratio fibre. As the fibre has no component in the $x-z$ plane it does not drift across Jeffery orbits nor spin about its major axis. Consequently the twisting stiffness has no effect upon the fibre dynamics for a fibre in the flow gradient plane as the fibre is not subject to any twisting torques.

5.1.1 Orbit Period

We now consider the effect of bend amplitude R_a and bending stiffness $k^{(B)}$ upon the orbit period of a fibre aligned along the x axis with bend in the flow gradient plane. As

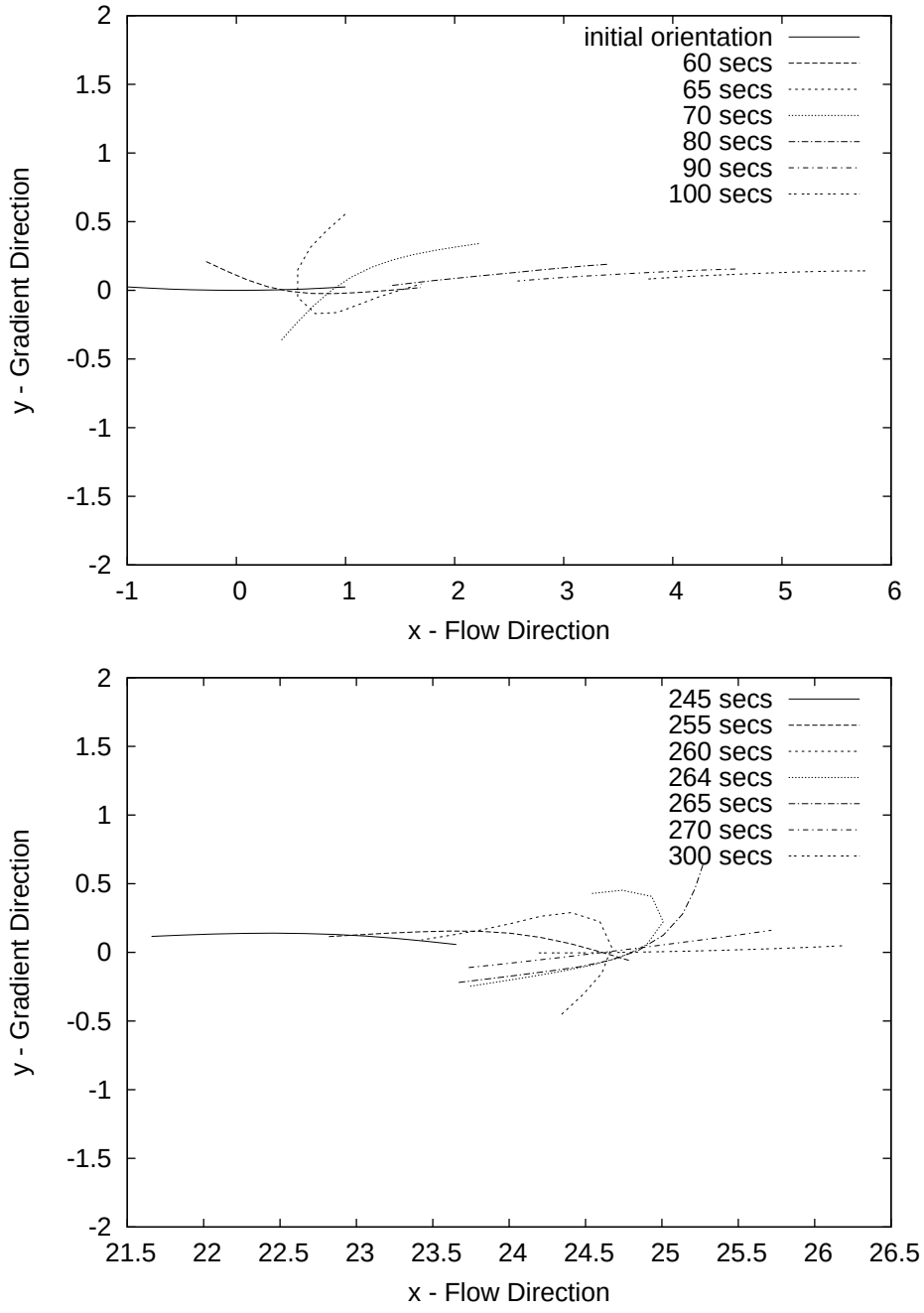

Figure 5.2: Intrinisically bent fibre performing a C turn in shear flow (top). Fibre continues to rotate performing another C turn after passing throught the flow direction (bottom). The stiffness of the fibre is $k^{(B)} = k^{(T)} = 2.5 \times 10^{-3}$, the bend amplitude is $R_a = 2.5 \times 10^{-2}$ and the bending angle is $\Omega_1 = 0.01$.

noted above the intrinsic bend allows a fibre of infinite aspect ratio to perform periodic rotations because the bend always gives the fibre a finite projection in the direction of the velocity gradient.

Bend Amplitude and Effective Aspect Ratio

For an intrinsically bent fibre of large length to thickness ratio the actual value of the aspect ratio is relatively unimportant compared to the effective aspect ratio due to its bend. To obtain a suitable measure of the effective aspect ratio of a bent fibre we compare the effective aspect ratio calculated from the orbit period

$$a_{r_{eff}} = \frac{T\dot{\gamma}}{4\pi} + \sqrt{\frac{T^2\dot{\gamma}^2}{16\pi^2} - 1} \tag{5.1.1}$$

for a very stiff fibre which does not change shape, with three possible measures of aspect ratio, which we shall call maximum aspect ratio, average aspect ratio and the square root of the eigenvalue ratio.

- Maximum aspect ratio is given by

  $$\frac{R_l}{R_a} = \frac{2\cot N\Omega_1}{4}$$

  where R_a and R_l are illustrated in figure 5.1.

- Average aspect ratio for a fibre aligned along the x-axis with its bend in the direction of the y-axis the is given by

  $$a_{r_{ave}} = \frac{R_l \int R_l(y)dy}{R_a \int R_a(x)dx}$$

  where $R_l(y)$ is horizontal distance between two sections of the fibre at a height y from the end of the fibre and $R_a(x)$ is the amplitude of the bend at a point x from the end of the fibre.

- The square root of the eigenvalue ratio is given by

$$a_{r_{eig}} = \sqrt{\frac{\lambda_l}{\lambda_m}}$$

  where λ_l is the largest principle moment of the moment of inertia tensor and λ_m is the middle principle moment as defined in section 4.2. The third principle moment is zero for a circular arc.

Figure 5.3 shows each of these three measures plotted against effective aspect ratio. All three show a linear correlation with effective aspect ratio. However, as the average aspect ratio shows an almost 1:1 correspondence we shall choose this as our measure of aspect ratio for the fibre.

Orbit period of a semi-flexible fibre

In the remainder of this section we shall consider semi-flexible fibres. We expect the orbit period to increase roughly in proportion to aspect ratio so in figure 5.4 we show the orbit period divided by aspect ratio plotted against average aspect ratio for fibres of various stiffnesses. For a very stiff fibre the relationship is linear just as it is for stiff finite aspect ratio fibres. For more flexible fibres the orbits of small aspect ratio fibres are longer than those of a stiff fibre of the same intrinsic shape. For larger aspect ratios the orbits are shorter than those of stiff fibres. The point at which the change occurs is dependent on the fibre stiffness.

Flexibility causes the aspect ratio of the fibre to change due to the bending moments exerted by the hydrodynamic forces from the external flow. For an intrinsically straight fibre (chapter 3) flexibility can only lead to a reduction in effective aspect ratio and hence a decrease in orbit period. However, the hydrodynamic forces on an intrinsically bent fibre aligned in the extensional quadrant of a shear flow will cause it to straighten, thereby increasing the effective aspect ratio. Thus there is a competition between the effect of this

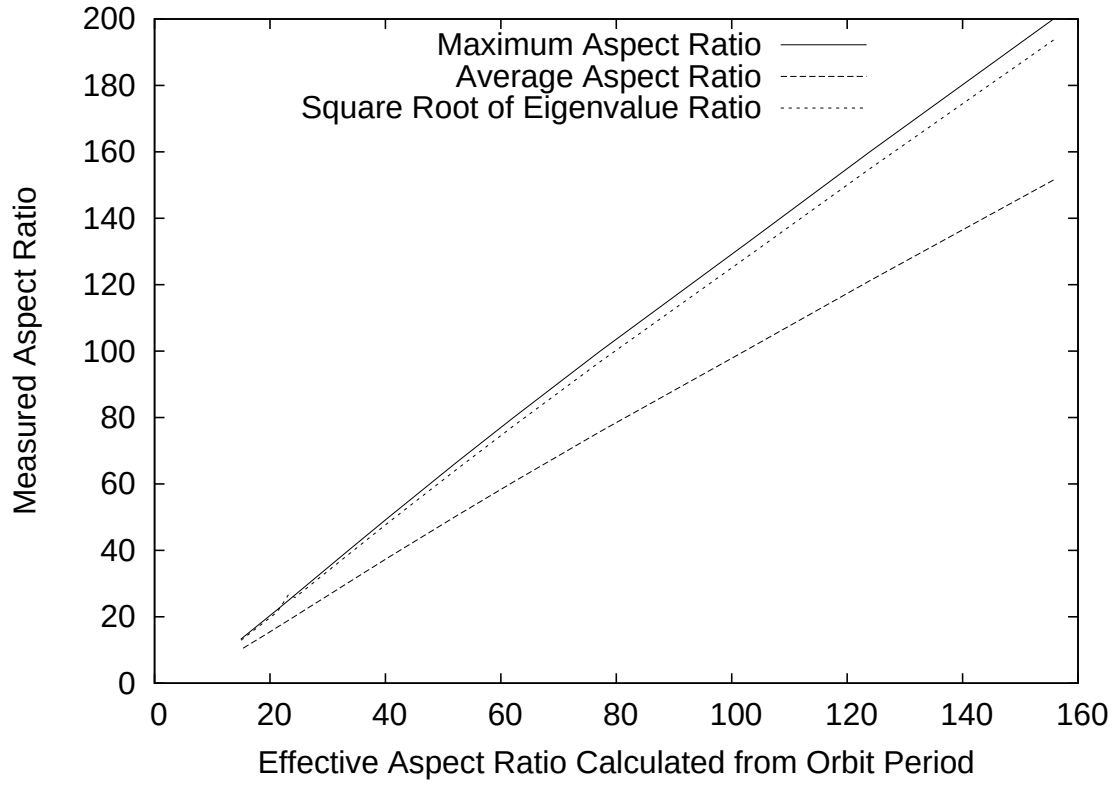

Figure 5.3: Ratio of principle moments of inertia, average aspect ratio and maximum aspect ratio plotted against effective aspect ratio for a stiff fibre of bending stiffness $k^{(B)} = 0.05$.

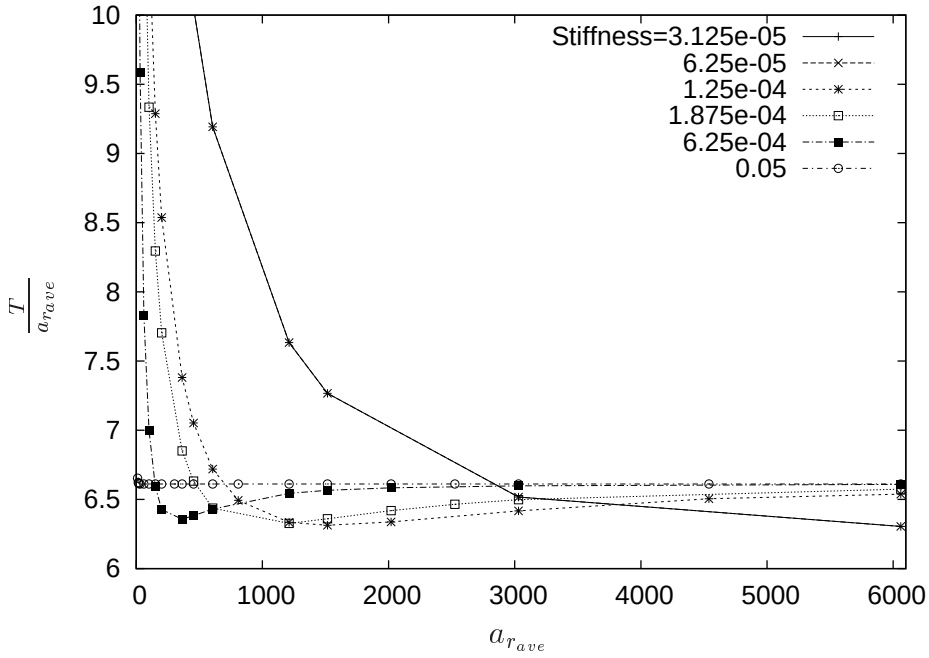

Figure 5.4: Orbit period divided by average aspect ratio $\frac{T}{a_{r_{ave}}}$ vs average aspect ratio, $a_{r_{ave}}$ for fibres of stiffness 3.125×10^{-5} to 0.05.

straightening and the bending that occurs in the compressional quadrant (and that due to finite thickness in the flow gradient plane).

The degree to which a semi-flexible fibre changes aspect ratio is approximately inversely proportional to its stiffness. However, since a fibre cannot straighten beyond being perfectly aligned; the balance between the effects of straightening and further bending depends upon the bend amplitude (or aspect ratio). For small aspect ratio fibres with $k^{(B)}a_r \leq 0.085$ the orbit period is longer than for a rigid fibre, because the decreased rotation speed caused by straightening is dominant. However, for fibres above this critical value $k^{(B)}a_r \geq 0.085$ the orbit period is shorter than for a rigid fibre as the effects of bending become dominant. For $k^{(B)}a_r \geq 0.189$ the effects of bending and straightening reduce and the orbit period tends towards that of a rigid fibre. In figure 5.5 we show that by plotting the orbit period divided by aspect ratio against $k^{(B)}a_r$ we obtain an almost universal curve for different fibre stiffnesses.

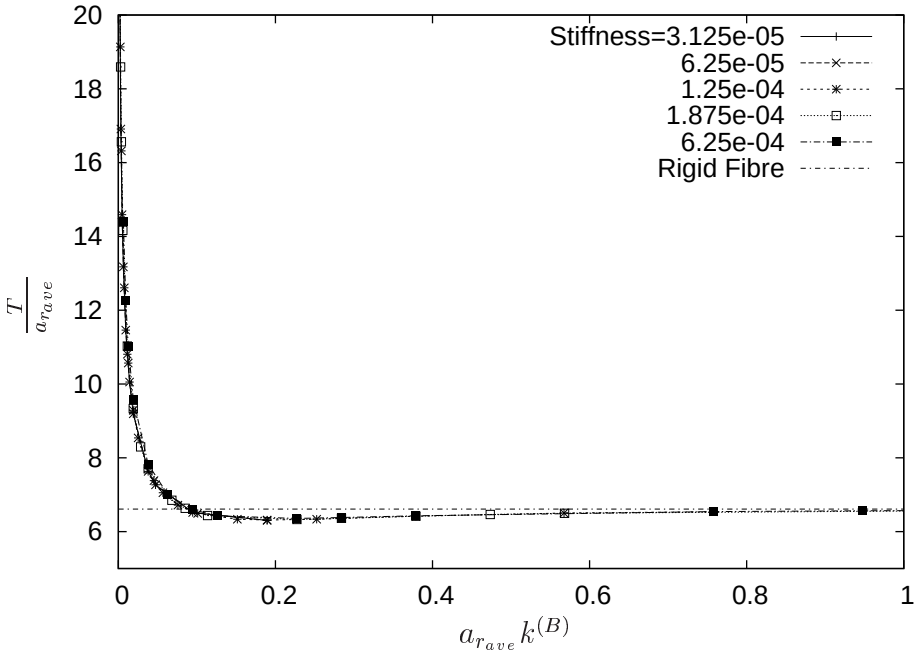

Figure 5.5: Orbit period divided by average aspect ratio, $\frac{T}{a_{r_{ave}}}$ vs the product of average aspect ratio and stiffness, $a_{r_{ave}} k^{(B)}$ for fibres of stiffness 3.125×10^{-5} to 0.05.

Variation from equilibrium shape

To demonstrate the differences for small and large $k^{(B)}a_r$ figures 5.6 and 5.7 show the measure of the deviation from the equilibrium, given by

$$\sum_{n=0}^{N}(\Omega_1^n - \Omega_1^{eq}),$$

for fibres of average aspect ratio $a_{r_{ave}} = 30$ with $k^{(B)}a_{r_{ave}} = 0.06$ and $k^{(B)}a_{r_{ave}} = 0.6$ respectively. Positive values of this quantity correspond to an increase in the average bend angle while negative values indicate that the fibre is being straightened. The horizontal line at zero represents no divergence from equilibrium and crosses mark every quarter of a semi-flexible fibre orbit.

As expected the fibre bends considerably as it passes through the compressional quadrant with the divergence from equilibrium increasing the more flexible the fibre. In the extensional quadrant the fibre straightens beyond its equilibrium shape. The fibre with $k^{(B)}a_{r_{ave}} = 0.06$ is straighter than its equilbrium shape as it enters the compressional quadrant. The fibre with $k^{(B)}a_{r_{ave}} = 0.6$ has returned back to its equilibrium shape by the time it crosses the $x - z$ plane.

Time spent in the compressional and extensional quadrants

Figure 5.8 shows time spent in the compressional quadrant and time spent in the extensional quadrant plotted against the fibre stiffness for fibres with an average aspect ratio of $a_{r_{ave}} = 30$. In general an increase in stiffness causes an increase in time spent in the compressional quadrant and a decrease in time spent in the extensional quadrant. This is because the fibre bends more than its equilibrium shape, decreasing its effective aspect ratio in the compressional quadrant and straightens beyond its equilibrium shape, increasing its effective aspect ratio in the extensional quadrant. However very flexible fibres spend longer in the compressional quadrant than slightly stiffer fibres. This is because a very flexible fibre will be almost completely straightened out when it passes

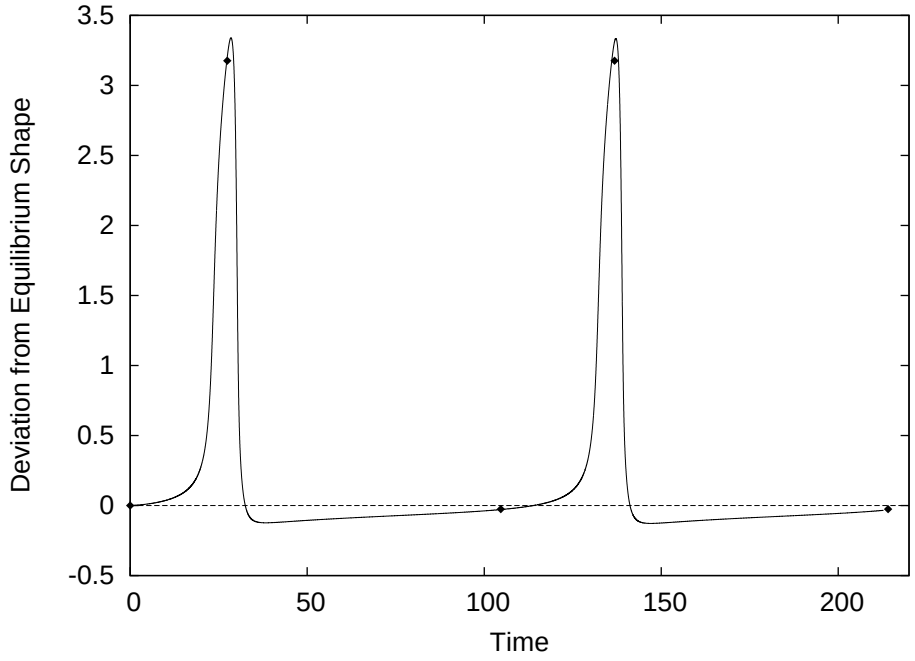

Figure 5.6: Deviation from equilbrium shape for a fibre of $k^{(B)}a_{r_{ave}} = 0.06$ rotating for one orbit in the $x - y$. Crosses mark each quarter orbit.

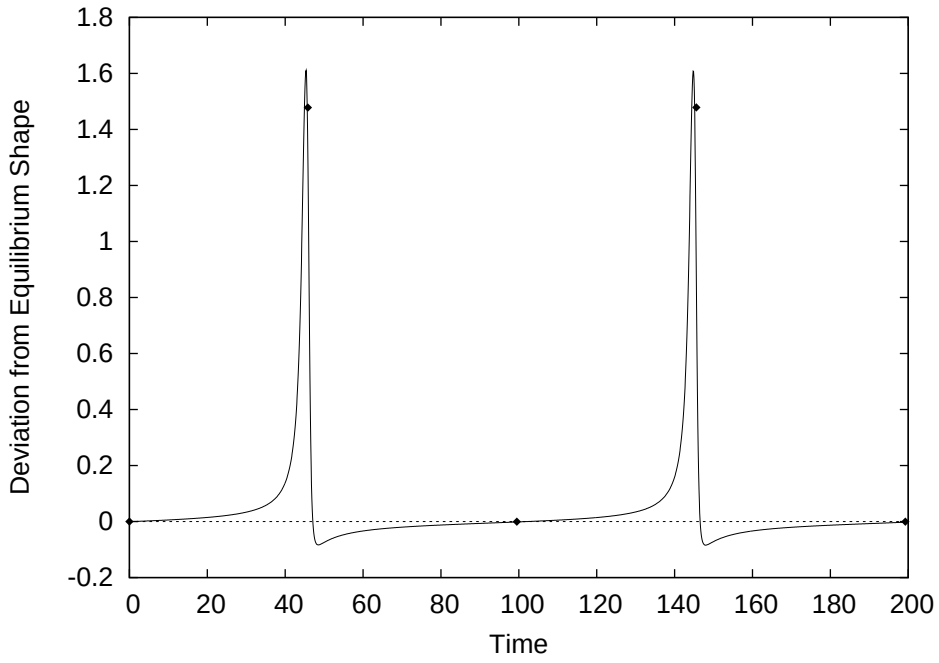

Figure 5.7: Deviation from equilbrium shape for a fibre of $k^{(B)}a_{r_{ave}} = 0.6$ rotating for one orbit in the $x - y$. Crosses mark each quarter orbit.

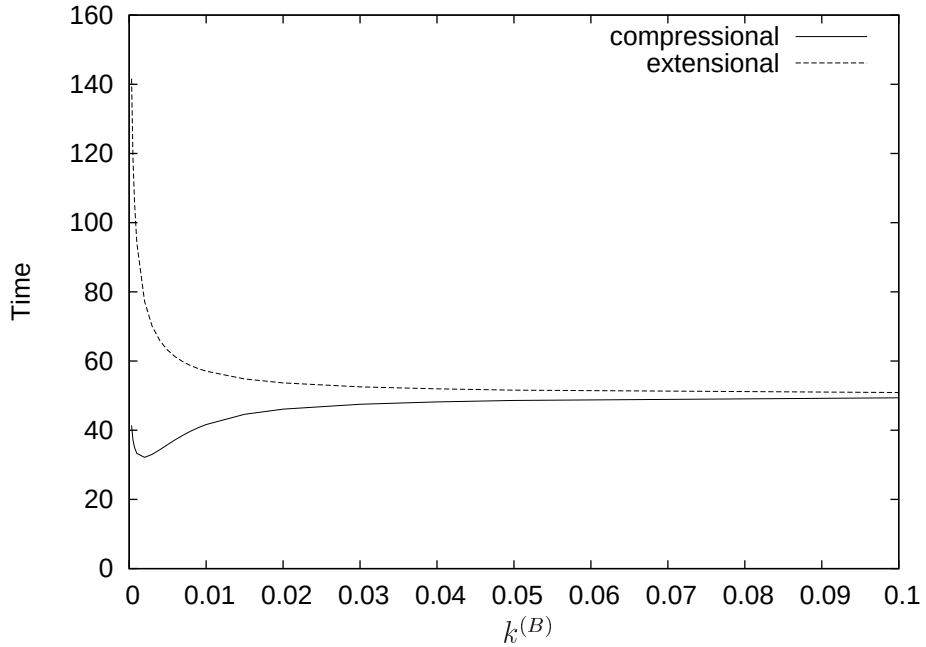

Figure 5.8: Time spent in the compressional quadrant and time spent in the extensional quadrant plotted against fibre stiffness $(k^{(B)})$ for a fibre with $a_{r_{ave}} = 30$.

through the flow direction and so will take longer to leave the flow-vorticity plane at the beginning of the compressional quadrant. The minimum for time spent in the compressional quadrant occurs at approximately $k^{(B)} = 0.0028$ or $k^{(B)}a_{r_{ave}} = 0.085$, this corresponds to the point at which the the orbit period changes from being greater than that of a rigid fibre to less than that of a rigid fibre.

A fibre of average aspect ratio $a_{r_{ave}} = 30$ has a minimum orbit period at a stiffness of approximately $k^{(B)} = 0.0063$ and hence $k^{(B)}a_{r_{ave}} = 0.189$. The sharp initial decrease in time spend in the extensional quadrant corresponds with the sharp initial decrease in orbit period. As this decrease in time spent in the extensional quadrant starts to level off as $k^{(B)}$ approaches 0.0063 the increase in time spent in the compressional quadrant becomes more significant and hence causes an overall increase in orbit period.

5.2 Initial Orientation and Spin

In the previous section we considered the case of a fibre with initial orientation such that the end-to-end vector $\mathbf{p}$ was aligned with the x-axis and the normal vector $\mathbf{q}$ was aligned with the y-axis. Symmetry then ensures that the fibre continues to remain in the $x-y$ plane. However, this orientation is unstable. In this section we consider the case of a fibre with initial orientation such that the normal vector $\mathbf{q}$ is initially in the y direction but the end-to-end vector $\mathbf{p}$ is at an angle λ_{xz} to the x-axis in the $x-z$ plane. For an intrinscially straight fibre with initial orientation in the $x-z$ plane the fibre would experience orbit drift (see section 3.4), in which the end-to-end vector $\mathbf{p}$ changes its orbit. For an intrinsically bent fibre we do not get a chance to observe orbit drift as the fibre spins about its axis and, within a few orbits of $\mathbf{p}$, ceases to rotate. We define spin as rotation of the normal vector $\mathbf{q}$ about an axis parallel to the end-to-end vector $\mathbf{p}$. The fibre ceases to rotate or spin once the normal vector $\mathbf{q}$ lies in the $x-z$ plane as the fibre no longer has an effective aspect ratio. While the fibre is still able to rotate it rotates in the $p-q$ plane rather than the $x-y$ plane. Figure 5.9 shows the rotation and spin of a fibre with intial orientation such that the normal vector q is in the y-direction and end-to-end vector $\mathbf{p}$ is at an angle $\lambda_{xz} = 0.0175$ with the x axis. The top figure shows the $y-z$ view of the fibre in which the spin of the fibre can clearly be seen and the bottom figure shows the $x-z$ view of the fibre in which the changing plane of rotation of the fibre can be seen.

Changing the stiffness or the bend amplitude of the fibre has no effect on the spin rate of the fibre. The only factor affecting the rate of spin is the initial angle λ_{xz} of the fibre in the flow-vorticity plane. Decreasing the angle so that the fibre starts closer to the vorticity axis increases the rate of spin. This is shown in figure 5.10 which shows the angle of spin of the fibre plotted against time. The angle of spin is measured as the angle between the plane of the fibre's bend and the y axis. All fibres start with their bend in the y direction so this angle starts at zero. Spin rate is initially rapid and linear, dropping quickly as the

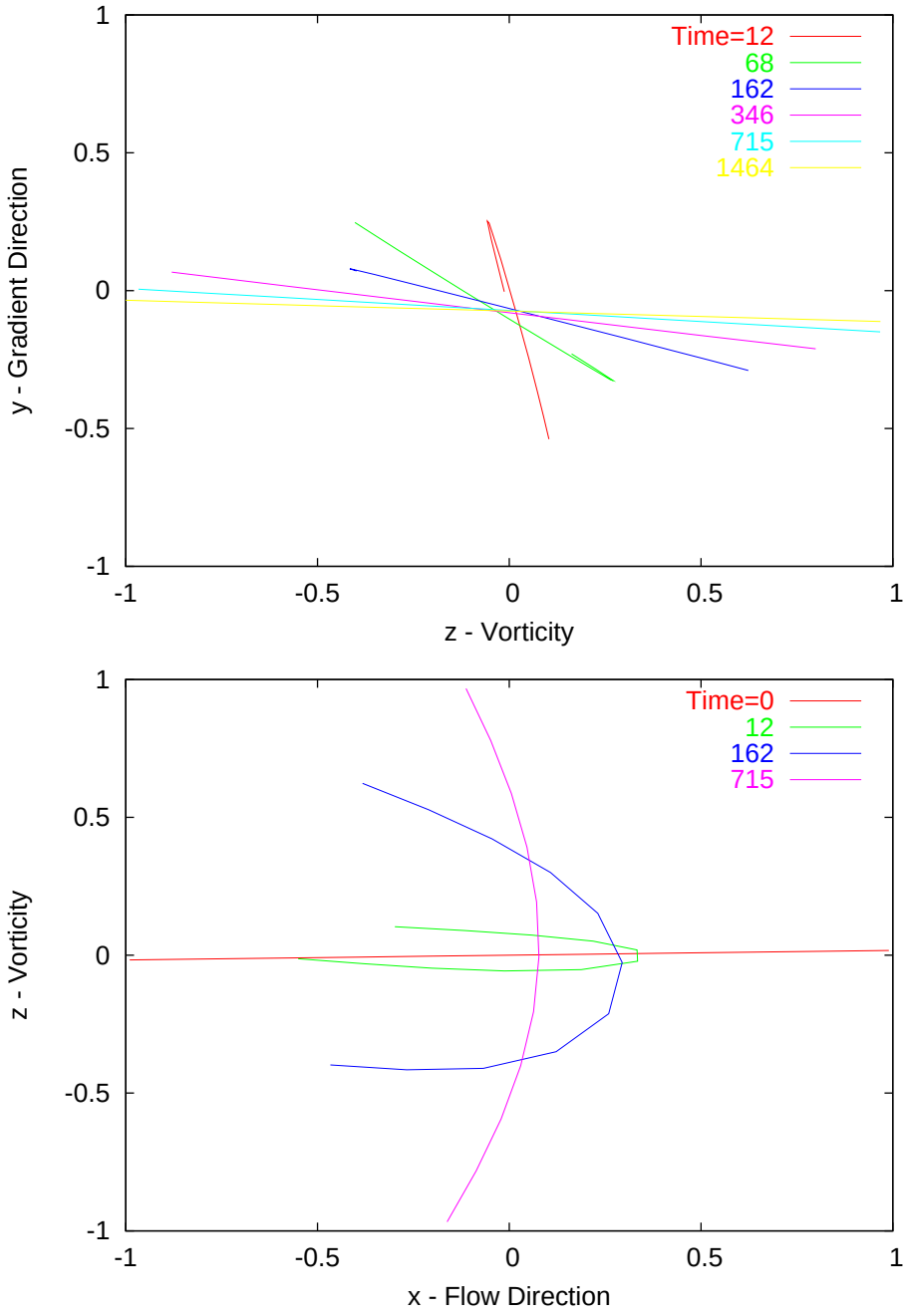

Figure 5.9: Views in the $y-z$ plane (top) and $x-z$ plane (bottom) of a bent fibre with initial orientation $\lambda_{xz} = 0.0175$, average aspect ratio 12 and stiffness $k^{(B)} = 0.005$ rotating and spinning about its axis.

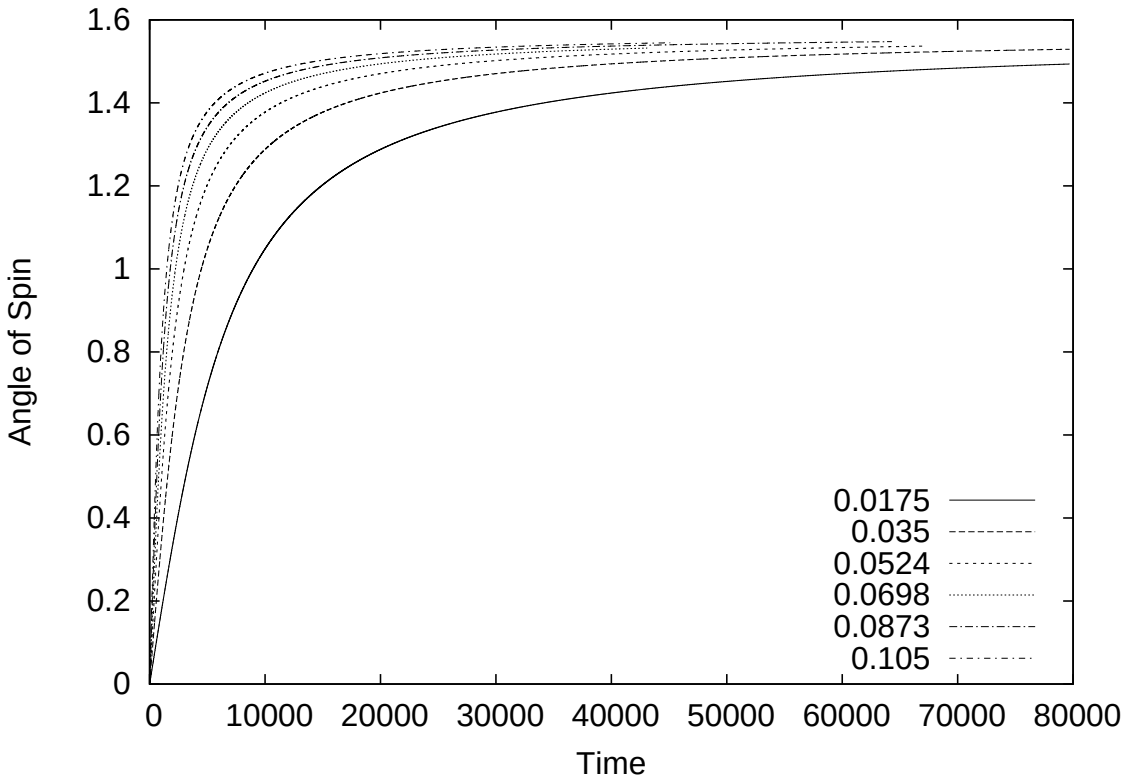

Figure 5.10: Angle of spin measured in the $y-z$ plane for a fibre of average aspect ratio 12.5 and stiffness $k^{(B)} = k^{(T)} = 0.005$ starting at angles $\lambda_{xz} = 0.0175,\ 0.035,\ 0.0524,\ 0.0698,\ 0.0873,\ 0.105$ with the x-axis.

plane of bend approaches the flow-vorticity plane.

5.3 Helical Fibres

In this section we consider the dynamics of rigid and semi-flexible helical fibres in shear flow. First we consider rigid helices using the rigid helix simulation derived in section 4.5. We consider helical fibres of non-dimensional arc-length 2 with radius a, pitch $2\pi b$ and number of turns n_t as shown in figure 5.3. We shall only consider helices with a whole number of turns. The arc length of the helix expressed in terms of a and b, which must be

equal to the the length of the fibre, is given by

$$2\pi n_t\sqrt{a^2+b^2}=2.$$

From this we obtain the value of b that must be used for chosen values of a and n_t,

$$b=\sqrt{\frac{1}{\pi^2 n_t^2}-a^2}.$$

We shall define the aspect ratio of the helix as the axial length divided by its diameter, given by

$$a_r^h=\frac{\pi n_t b}{a}=\sqrt{\frac{1}{a^2}-\pi^2 n_t^2}.$$

To assess the effects of flexibility on the dynamics of the helix we use the semi-flexible fibre simulation derived in chapter 4. Unlike the rigid helix simulation, which is for a continuous helix, the semi-flexible fibre simulation simulates a discretised helix composed of N straight rods. Using equation (4.2.4) given for b in section 4.1 we can express the aspect ratio of a discretised helix as

$$a_r^h=\sqrt{\frac{1}{a^2}-N^2\sin^2\frac{\Delta}{2}},$$

where $\Delta=\frac{2\pi b n_t}{N}$. In order to have a good approximation of the continuous helix it is necessary for $\frac{n_t}{N}$ to be small. In this chapter we use $N=12$ as we shall only consider flexible helices with one turn.

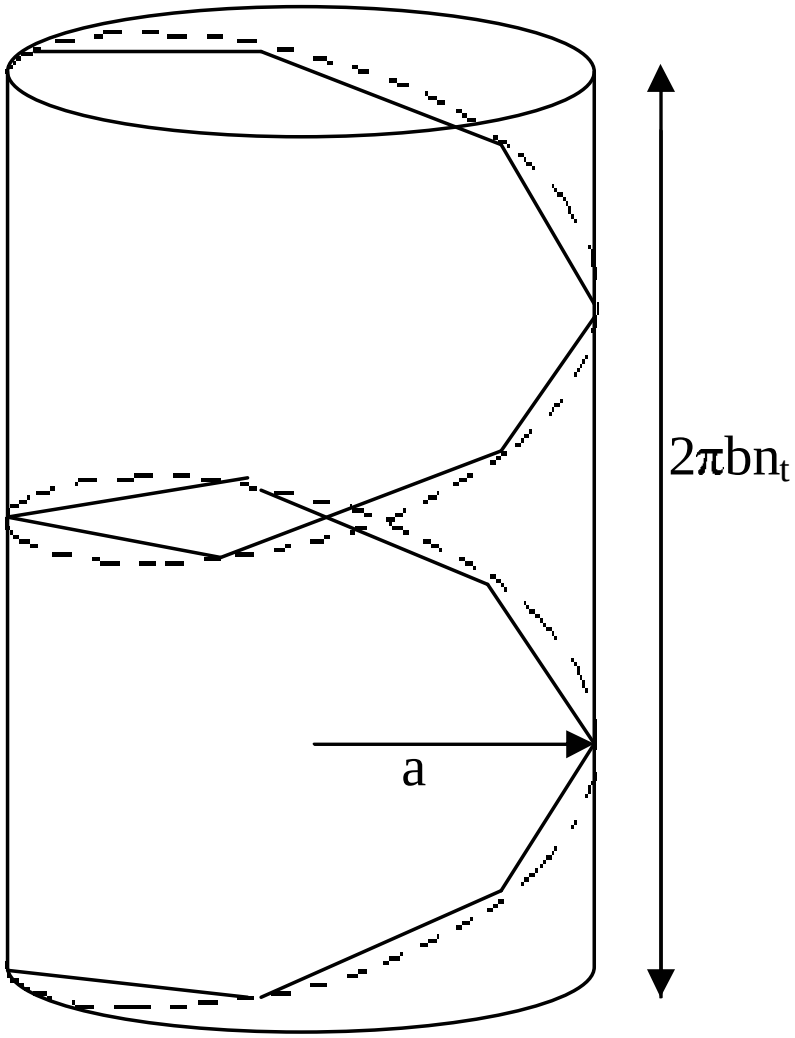

Figure 5.11: A continuous helix of radius a and pitch b discretised in N sections.

5.3.1 Orbit Period

Rigid Helices

Figure 5.12 shows orbit period plotted against aspect ratio for rigid helices with different numbers of turns. Helices with a high number of turns rotate faster than those with fewer turns. For small n_t we find that the relationship between aspect ratio and orbit period is linear. For large n_t this linear relationship holds only at large aspect ratios. For $n_t \geq 2$ an approximately universal linear plot can be obtained by plotting orbit period against aspect ratio and scaling both quantites by n_t, the number of turns. This is shown in figure 5.13. A high turn helix of small aspect ratio will approach the shape of a hollow cylinder, thus we can compare the results for large n_t with the result obtained by Burgers that a cylinder with aspect ratio a_r rotates like an ellipsoid with aspect ratio $0.74a_r$ [5]. For helices with a large number of turns there appears to be a transistion between having the properties of a cylinder when the aspect ratio (and pitch angle) is small and having the properties of an open helix once the aspect ratio (and pitch angle) gets larger. This is further supported by figure 5.14 which shows orbit period versus number of turns for a helix of constant aspect ratio $a_r^h = 10$. The horizontal line shows the orbit period of a cylinder of aspect ratio 10. As number of turns increases and hence pitch angle increases the orbit period approaches that of a cylinder of the same aspect ratio. It should be noted however that as our model excludes hydrodynamic interactions it is only valid for $\frac{2\pi b}{d} \gg 1$, where d is the fibre thickness and $\frac{2\pi b}{d}$ is the slenderness ratio described by Higdon [16]. In figure 5.15 we plot the orbit period scaled with number of turns against pitch angle for helices with different values of n_t. The plot shows a universal curve confirming that it is pitch angle that determines whether the fibre will rotate as a helix or as a cylinder.

Figure 5.16 shows the orbit period plotted against number of turns for a helix with constant pitch angle. Unlike figure 5.14 where the orbit period decreases with number of turns due to the increases in pitch angle, figure 5.16 shows a linear increase in orbit

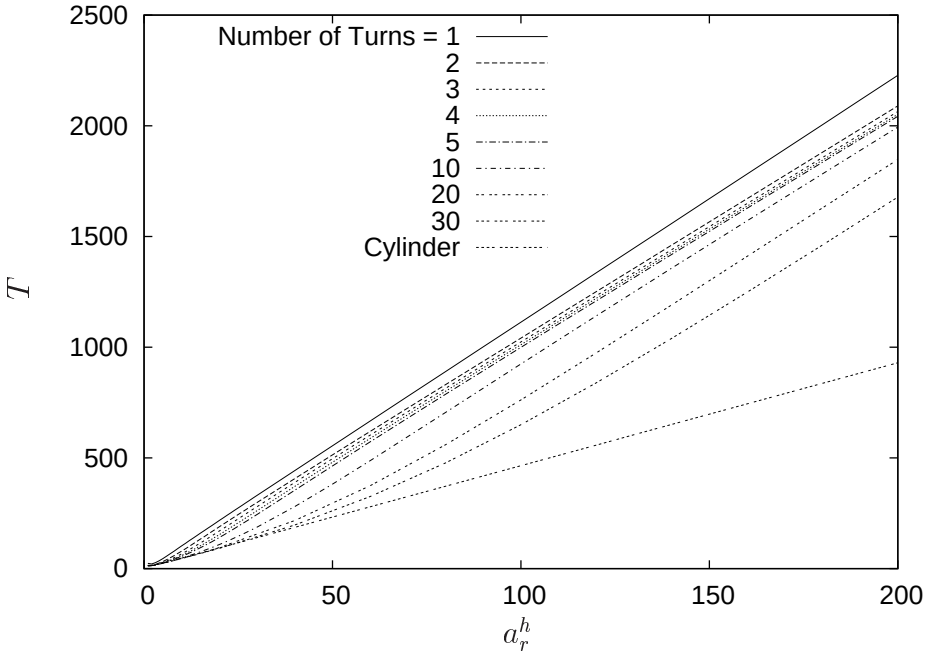

Figure 5.12: Plot of orbit period, T, vs helix aspect ratio , $a_r^h = \frac{\pi n_t b}{a}$, for different values of n_t.

period. This is because an increase in number of turns results in an increase in aspect ratio and as expected, orbit period increases linearly with aspect ratio.

Semi-flexible helices

We now use the flexible fibre simulation to assess the effect of flexibility on the orbit period of the helix. However, first we must verify that the flexible helix simulation reproduces the results for a rigid helix in the limit of large $k^{(B)}$. Figure 5.17 shows that the orbit period calculated for a 1 turn helix plotted using the rigid helix simulation is in excellent agreement with the flexible fibre simulation when the stiffness is set to $k^{(B)} = 0.048$ and $k^{(B)} = 0.096$.

For semi-flexible helices with stiffnesses in the range 2.41×10^{-4} to 9.65×10^{-3} we find that an almost universal curve is obtained by plotting the orbit period scaled with the orbit period of a rigid helix against $a_r^h {k^{(B)}}^{\frac{1}{2}}$, as shown in figure 5.18. For

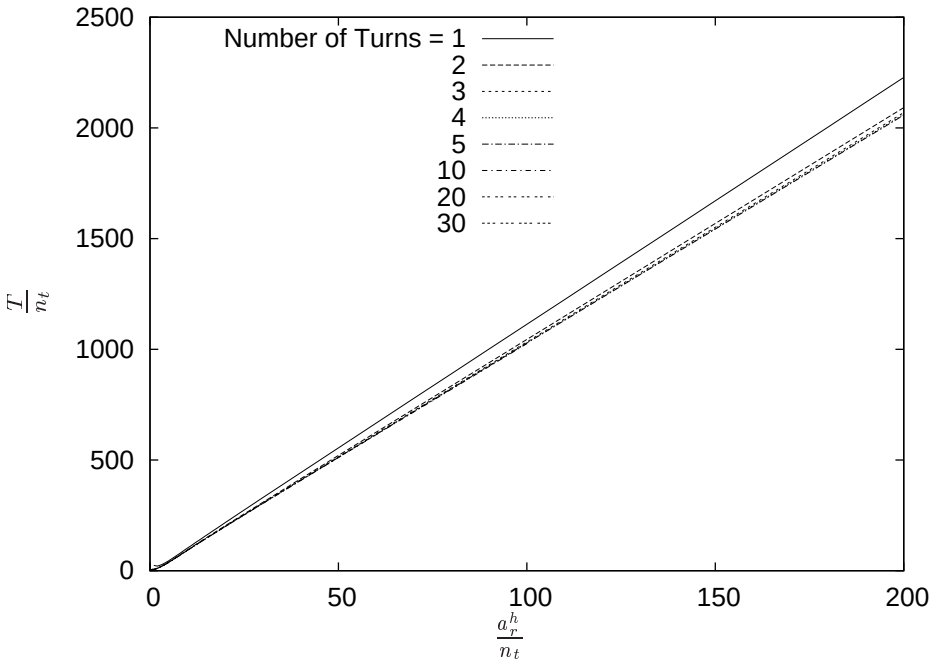

Figure 5.13: Plot of orbit period divided by number of turns, $\frac{T}{n_t}$, against helix aspect ratio divided by number of turns , $\frac{a_r^h}{n_t} = \frac{\pi b}{a}$, for different values of n_t.

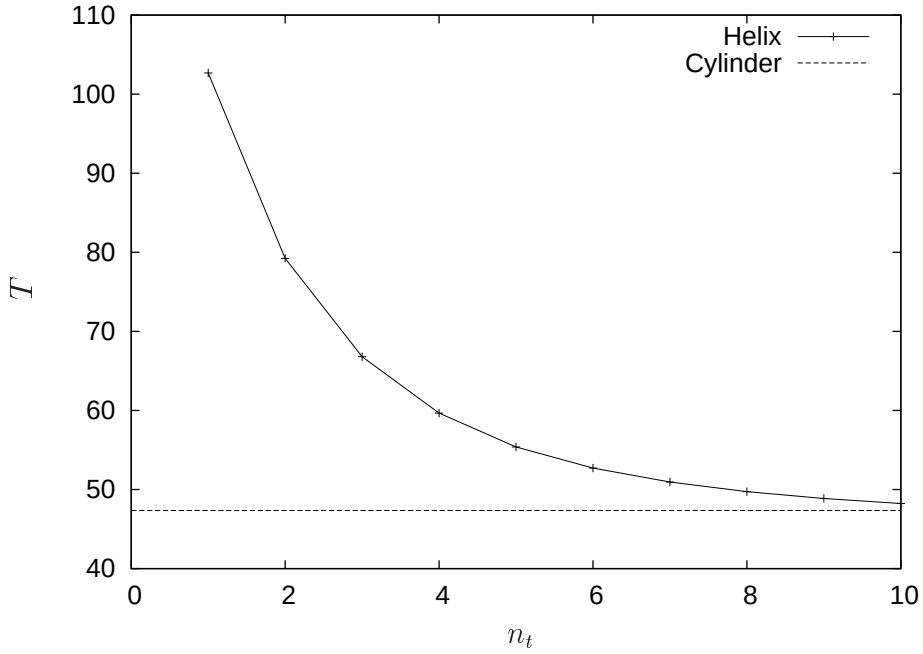

Figure 5.14: Plot of orbit period, T, vs number of turns, n_t, for a helix of aspect ratio $a_r^h = 10$. Horizontal line shows the orbit period of a helix with the same aspect ratio.

$a_r^h k^{(B)^{\frac{1}{2}}} < 0.2$ the orbit period for a flexible helix is greater that that of the equivalent rigid helix. As in the case of a curved fibre, flexibility causes the helix to increase in aspect ratio in the extensional quadrant and so rotates more slowly through the $x-z$ plane. For $a_r^h k^{(B)^{\frac{1}{2}}} > 0.2$ the orbit period of a flexible helix is shorter than that of an equivalent rigid helix as the increase in aspect ratio in the compressional quadrant dominates over the decrease in aspect ratio in the extensional quadrant. The orbit period reaches a minimum at approximately $a_r^h k^{(B)^{\frac{1}{2}}} = 0.4$ and further increases in $a_r^h k^{(B)^{\frac{1}{2}}}$ result in the orbit period tending to that of a rigid helix as bending decreases.

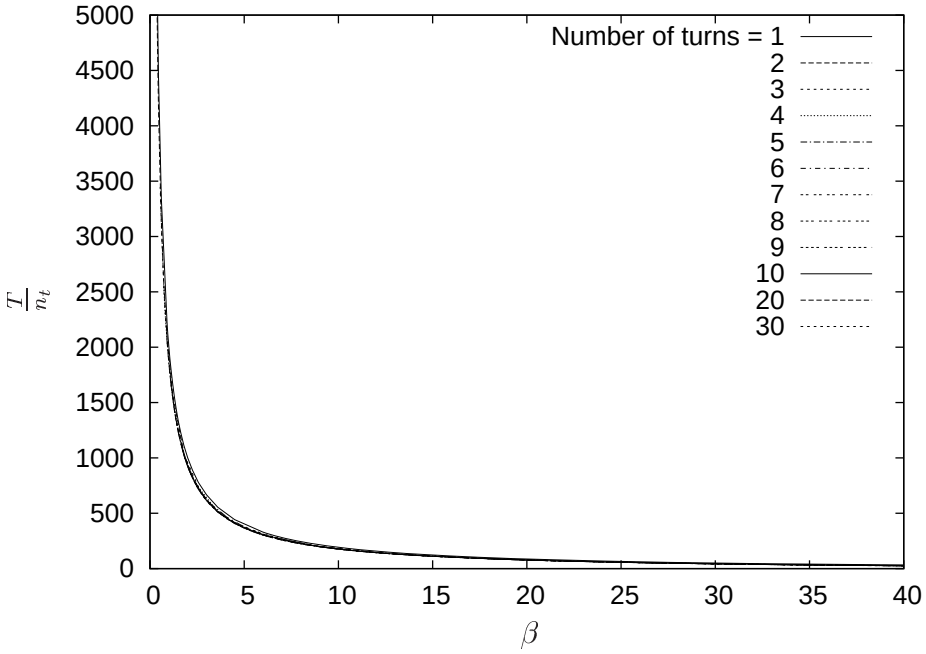

Figure 5.15: Plot of orbit period divided by number of turns, $\frac{T}{n_t}$, against pitch angle, β, for helices with different values of n_t.

5.3.2 Drift of Centre of Mass in the Vorticity Direction

The rotation of a helix in the $x-y$ plane results in translation in the vorticity direction. Figure 5.19 shows translation in the z direction plotted against time for rigid single turn left and right-handed helices of aspect ratio 10. The crosses mark each quarter of the orbit as determined by the central axis of the helix. In figure 5.20 which shows the velocity in the x direction for each helix, the changes in direction of translation occur close to but not exactly at the points where the central axis crosses the x and y axes. Instead the change in the direction of translation corresponds to the positions where a second axis, fixed in the frame of the helix, crosses the x and y axes, which we shall refer to as the translation axis.

For a left-handed helix, translation is in the positive z direction as the helix rotates through the compressional quadrant. As it enters the extensional quadrant the direction

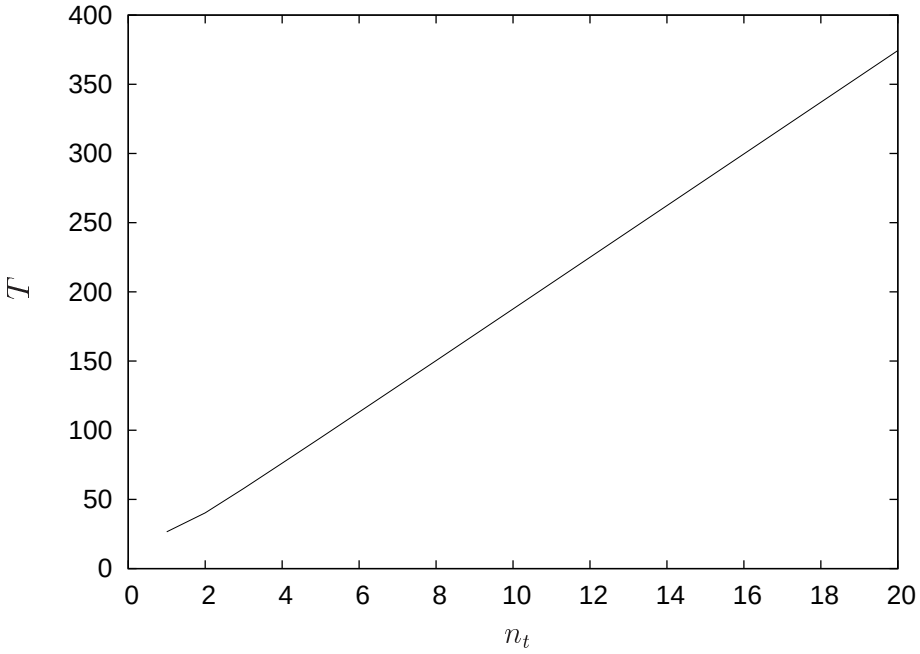

Figure 5.16: Plot of orbit period against number of turns for a helix of constant pitch angle of 46.32.

of translation changes sign. It switches back to positive as it passes through the flow direction. For a right-handed helix the directions are reversed and translation is predominantly in the negative z direction as shown in the lower plot in figure 5.19, which is a mirror of the upper plot. The dotted lines in figure 5.19 show the translation for the same helices after they have been rotated about their central axis by an angle of π. Maximum velocity occurs when the helix is under maximum compression or maximum extension. Zero velocity occurs when the translation axis is aligned with the x or the y axis.

We can explain the direction of drift by considering the $x-y$ and $x-z$ projections of a left-handed helix aligned so that its central axis is initially in the x direction, at key points during the orbit. In section (a) of figure 5.21 the central axis of the helix is aligned with the x-axis, the first half of the helix (solid line) is above the x-axis and the second half of the helix (dashed line) is below the x-axis. The block arrows indicate the flow directon

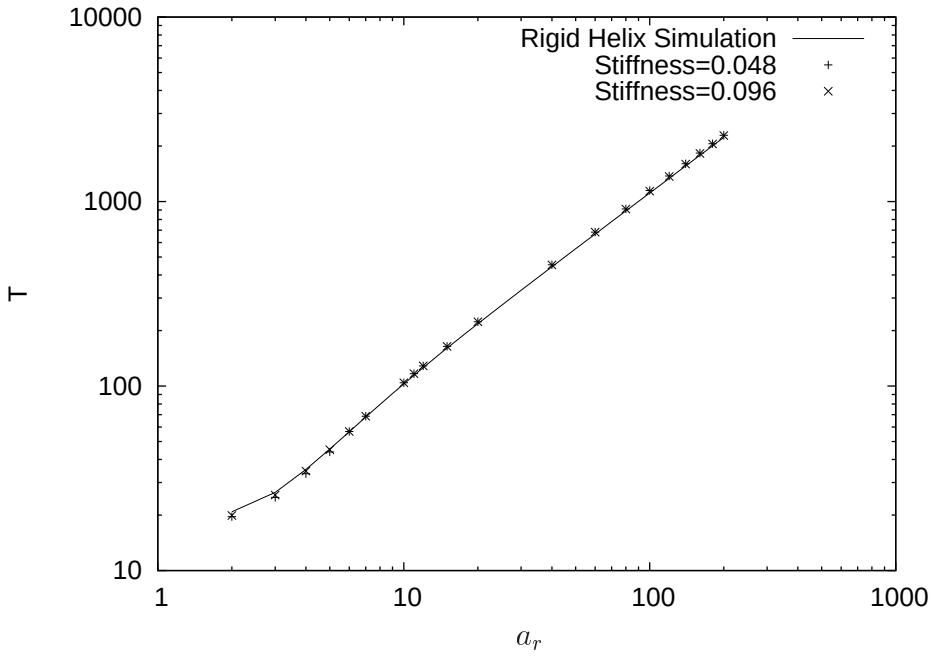

Figure 5.17: Plot of orbit period against aspect ratio for a 1 turn helix. Plot shows the rigid helix simulation, and the semi-flexible fibre simulation for stiffnesses of $k^{(B)} = 0.048$ and $k^{(B)} = 0.096$.

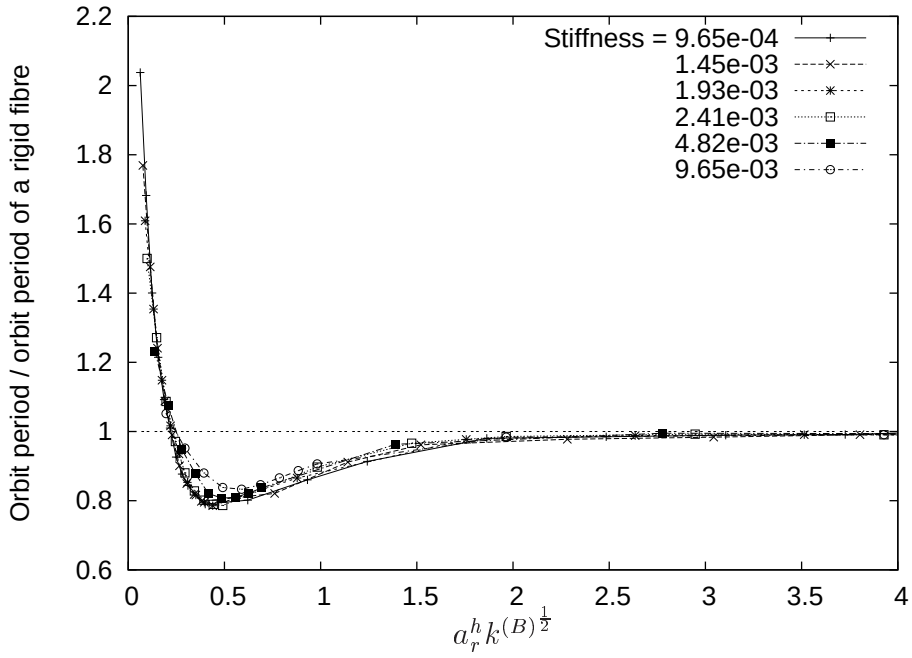

Figure 5.18: Plot of orbit period scaled with rigid orbit period against $a_r^h k^{(B)\frac{1}{2}}$ for semi-flexible helices of stiffness $k^{(B)} = 2.41 \times 10^{-4}, .., 9.65 \times 10^{-3}$.

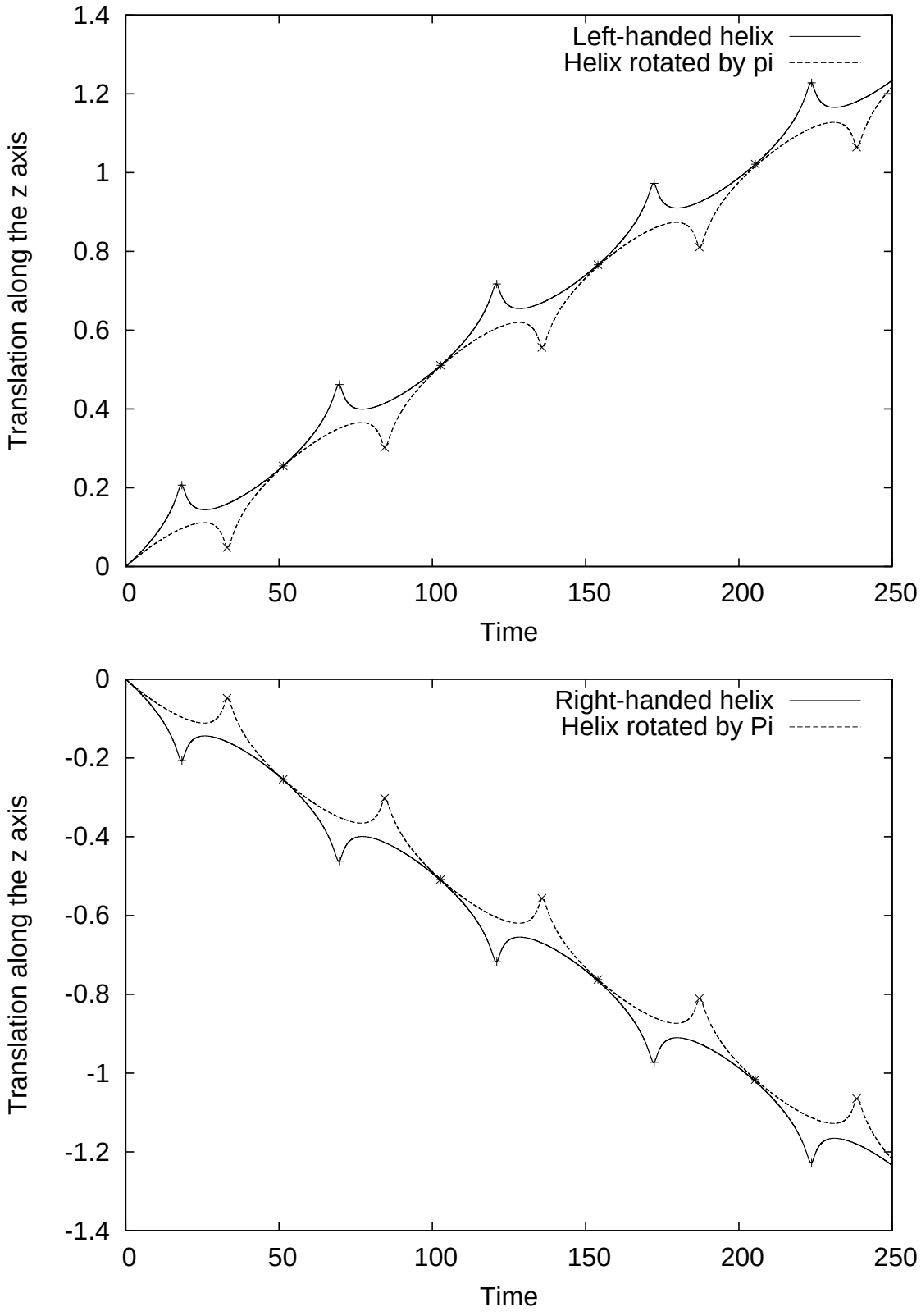

Figure 5.19: Plots of translation along the z axis against time for left (top) and right-handed (bottom) helices of aspect ratio $a_r^h = 10$ and number of turns $n_t = 1$.

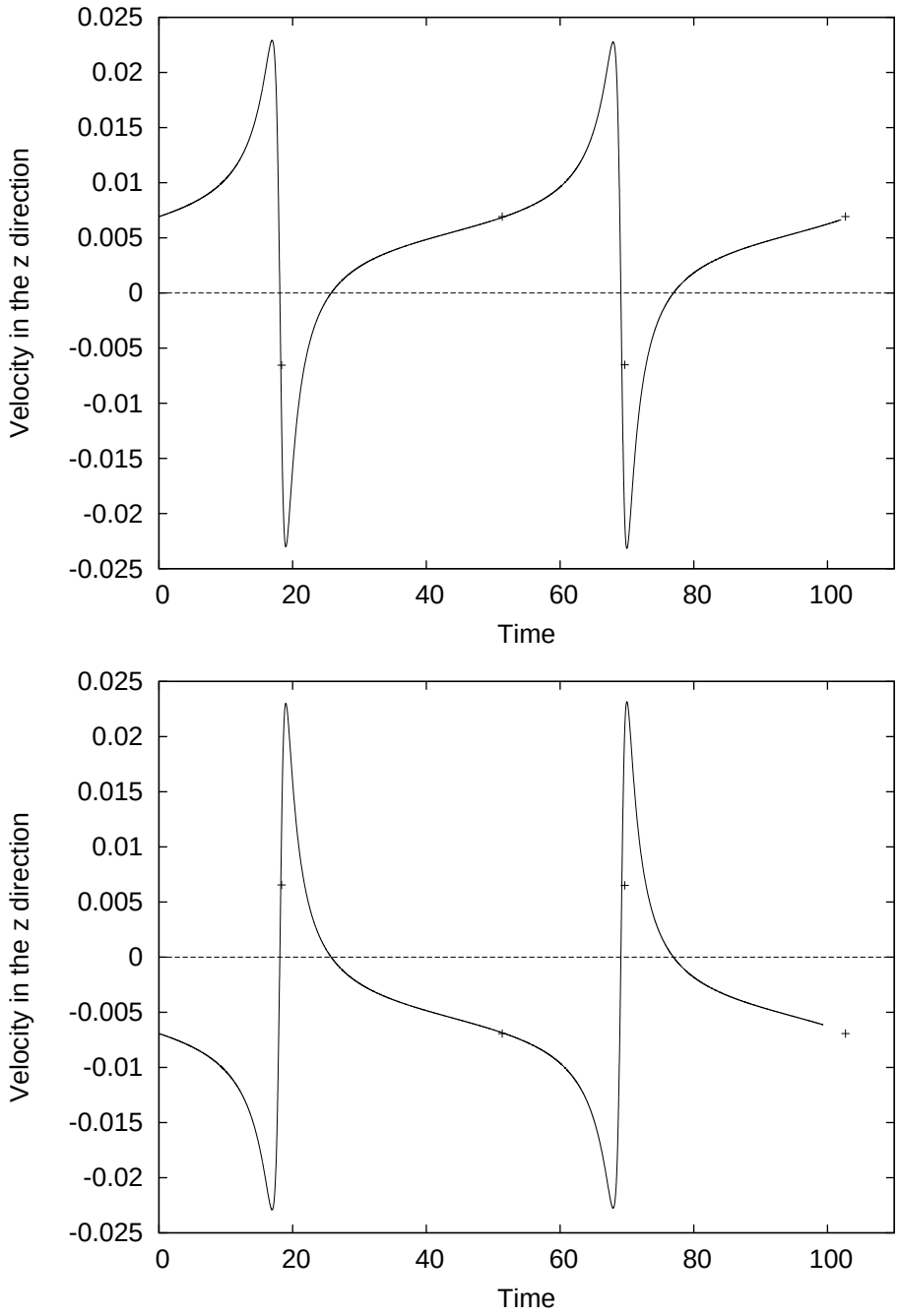

Figure 5.20: Plots of velocity in the z direction against time for left (top) and right-handed (bottom) helices of aspect ratio $a_r^h = 10$ and number of turns $n_t = 1$.

and the line arrows the direction of translation. Translation in this direction occurs due to the 2:1 ratio of the resistance co-efficients for motion perpendicular and parallel to the fibre. This is illustrated in figure 5.22 which shows the motion of the helix relative to the fluid. Rather than moving in the x direction, motion is at an angle closer to the tangent to the helix and hence has a component in the z direction.

As the helix rotates through the compressional quadrant ((a) and (b) figure 5.21) it translates in the positive z direction. Once in the extensional quadrant ((c) figure 5.21) the helix translates in the negative z direction due to the two halves of the helix, as viewed in the $x-z$ plane, crossing over. As the helix approaches the flow direction ((d) figure 5.21), translation changes back to the positive z direction, this is due to the dashed half of the helix moving above the x-axis and the solid half of the helix moving below the x-axis. This change means the flow acting on each section is now in the opposite direction.

The rate of rotation of the helix is determined by the orientation of the central axis, whereas the direction of drift is determined by the translation axis. As a consequence when the central axis is aligned in the flow direction there is tranlation in the positive z direction. When the central axis is aligned with y axis there is translation in the negative z direction. The time taken for the central axis to cross the flow direction is significantly longer than the time taken to cross the y-axis and hence translation in the positive z direction is greater (see figure 5.20). The smaller the angle between the translation axis and the central axis the smaller the net displacement. Hence the net displacement tends to zero in the limit of infinite helix aspect ratio or infinite number of turns.

We now consider the effect of aspect ratio, number of turns and stiffness on the net displacement of the helix over one orbit. We begin by considering the effect of aspect ratio and number of turns on a rigid helix. Figure 5.23 shows the net displacement in the z direction per orbit against aspect ratio divided by number of turns for left-handed helices with n_t=1,..,10. Maximum translation occurs at $\frac{a_r^h}{n_t} = 7$ regardless of number of turns, however, for small n_t the size of the maximum is smaller. This is because for small

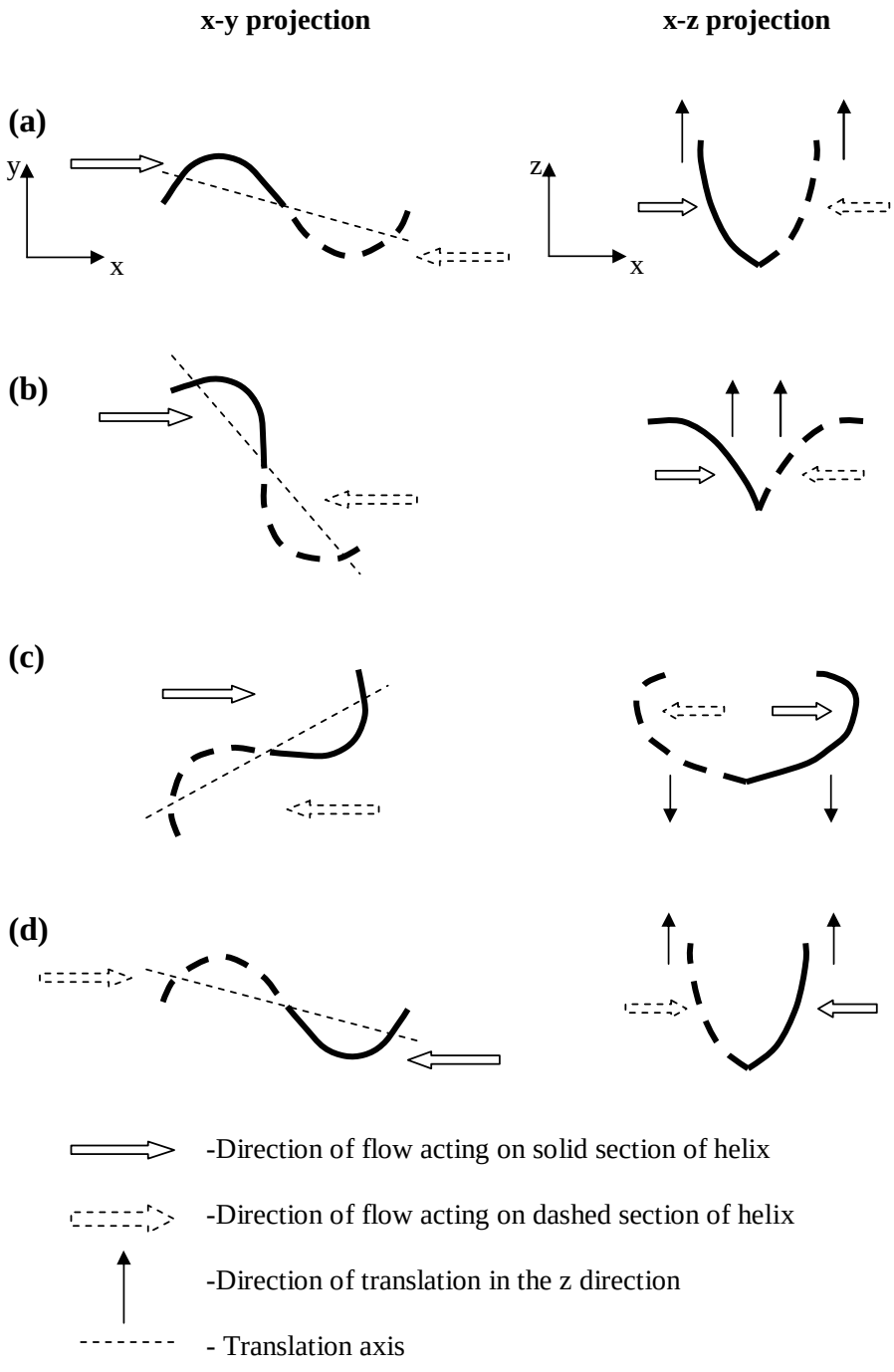

Figure 5.21: Diagram showing the direction of translation for a rigid handed helix at a sequence of positions during a half rotation.

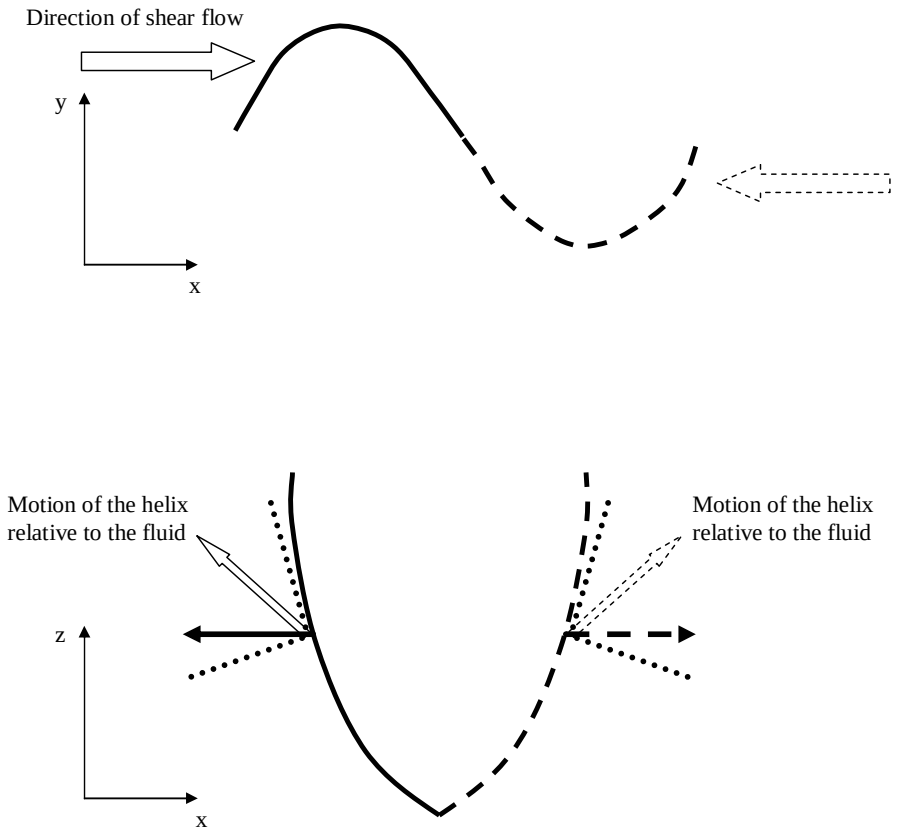

Figure 5.22: Diagram showing the motion of the helix relative to the fluid.

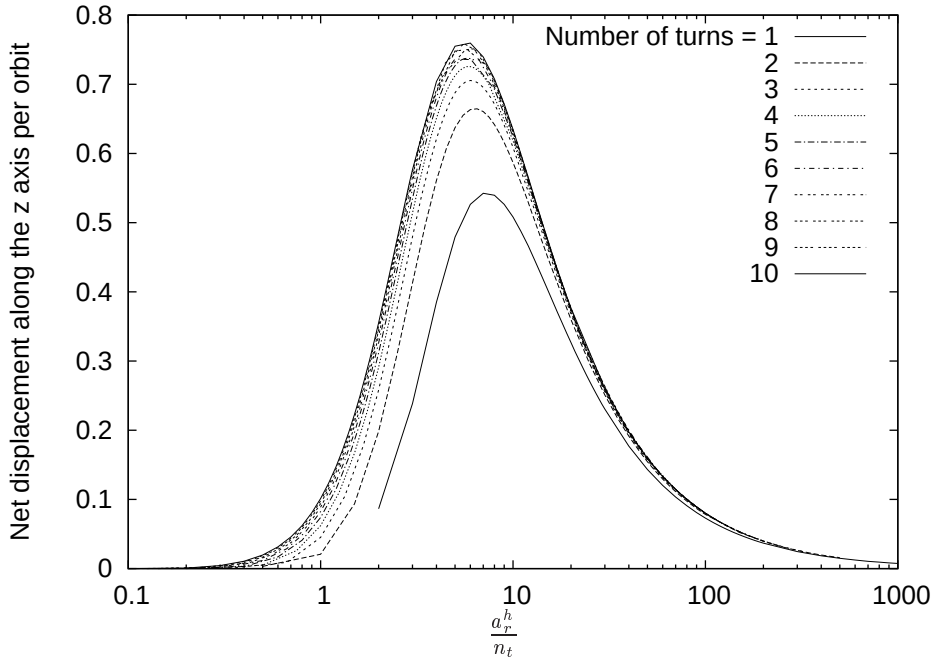

Figure 5.23: Net displacement along the z axis per orbit plotted against aspect ratio divided by number of turns for helices of 1 to 10 turns.

n_t the aspect ratio is also smaller meaning the helix spends a smaller fraction of its orbit close to the $x-z$ plane and a greater fraction in the extensional quadrant where translation in the negative z direction occurs. In figure 5.24 we plot the total distance travelled in the z direction over an orbit, T, given by

$$\Delta = \int_0^T |u_z| dt$$

as opposed to the net displacement. Here u_z is the velocity in the z direction. It can be seen that maximum total distance travelled is independent of the number of turns.

Figure 5.25 shows maximum translation speed (which occurs when the helix is under maximum compression or extension) against aspect ratio, and translation speed when the central axis of the helix aligned in the $x-z$ plane against aspect ratio, for a 1 turn helix. The aspect ratios for which these translation speeds are greatest are 4 ($\beta = 46.3°$) and 3

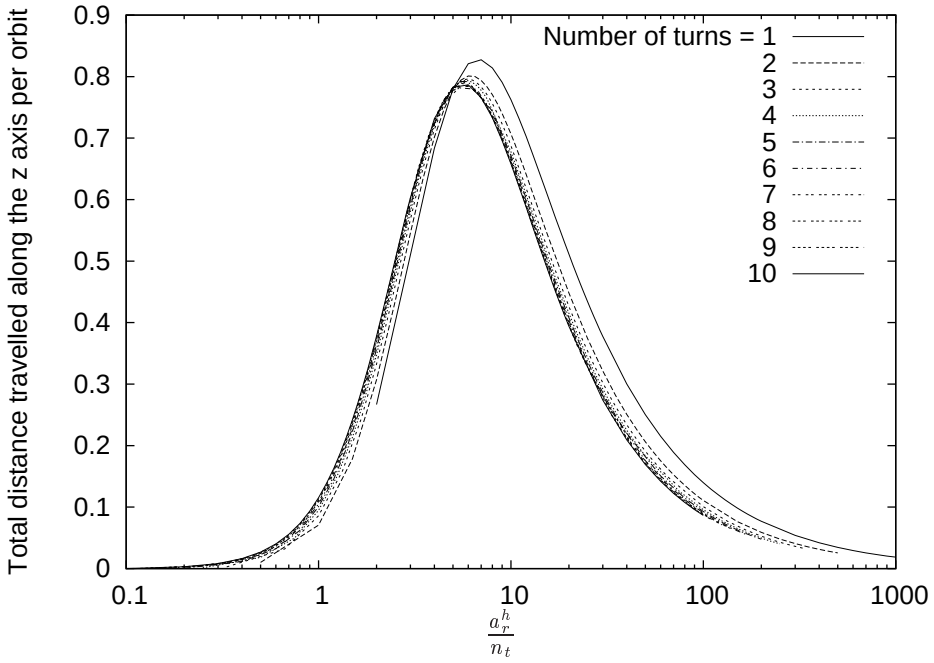

Figure 5.24: Total distance travelled along the z axis per orbit plotted against aspect ratio divided by number of turns for helices of 1 to 10 turns.

($\beta = 38.1°$) respectively. Note that both values are smaller than the optimum aspect ratio of $\frac{a_r^h}{n_t} = 7$ at which a rotating helix will translate the greatest distance per orbit. This is because for aspect ratios in the range $3 \leq \frac{a_r^h}{n_t} \leq 7$ the decrease in translation speed is more than offset by the increase in the orbit period and hence both the net displacement and total distance increases. For $\frac{a_r^h}{n_t} \geq 7$ the reduction in speed outweighs the increase in orbit period.

Semi-flexible fibres

To assess the effects of flexibility on the translation rate of a flexible helix we use the flexible fibre simulation. Again we first verify that the semi-flexible fibre simulation agrees at large stiffnesses. Figure 5.26 shows that the average translation speed over one orbit for the rigid helix simulation and for the flexible fibre simulation with helices of stiffnesses 0.048 and 0.096 are in good agreement.

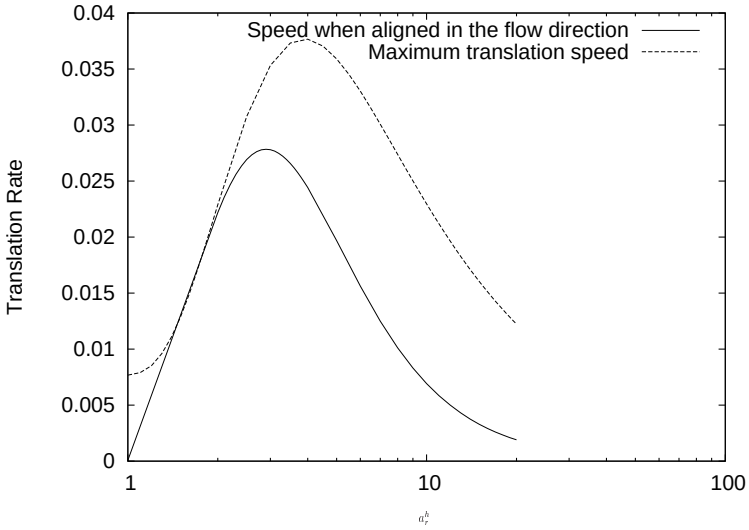

Figure 5.25: Translation rate of a 1 turn helix aligned along the x-axis plotted against aspect ratio. Plot is calculated from the grand resistance matrix for a rigid helix of arc-length 2.

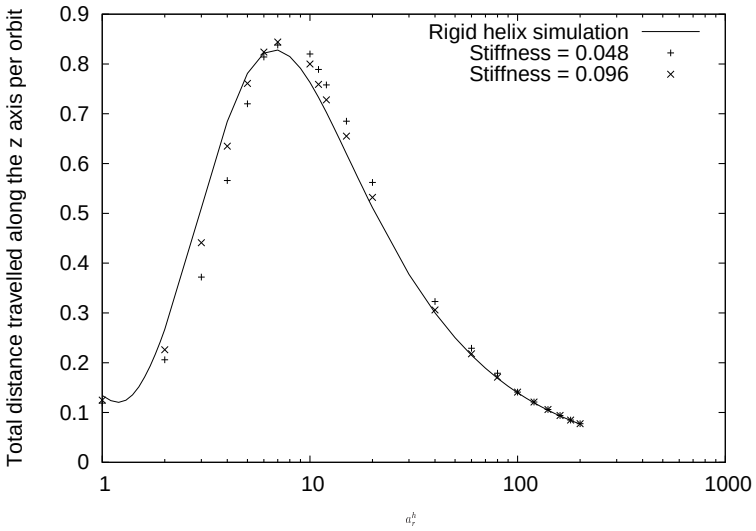

Figure 5.26: Comparison of rigid helix and flexible fibre simulations for total distance travelled along the z axis per orbit against helix aspect ratio. For the flexible fibre simulation stiffnesses of $k^{(B)} = 0.048$ and $k^{(B)} = 0.096$ were used.

Figure 5.27 shows the net displacement per orbit for helices with stiffnesses in the range 9.65×10^{-4} to 9.65×10^{-3} plotted against aspect ratio. For very low aspect ratio helices the net displacement of a very flexible helix is less than that of the equivalent rigid helix, however, in figure 5.28 which plots total distance travelled against aspect ratio we see that the total distance travelled is greater for more flexible helices. This is because straightening of the helix in the extensional quadrant increases the orbit period, and hence increases the total distance travelled, however, the increased time in the extensional quadrant means that the helix spends a greater proportion of its time travelling in the negative z direction. Figure 5.29 shows the velocity of the helix in the z direction against time for one complete orbit. The velocity is zero just prior to the central axis being aligned with the flow direction and the y axis. Maximum translation occurs in the compressional and extensional quadrants (for rigid helices both maxima are equal in magnitude). Increasing flexibility reduces the size of the maxima as the resistance of the helix to the shear flow is reduced. The maximum in the compressional quadrant is reduced by a greater amount, despite the increase in effective aspect ratio, as the helix is better able to resist straightening than bending.

For moderate aspect ratios, both the net displacement and total distance travelled for a very flexible helix is less than that of a stiff helix as flexibility reduces both the translation rate and the length of the orbit period. For high aspect ratios both the net displacement and total distance travelled for a flexible helix are greater than that of a stiff helix despite maximum translation rate being reduced (see figure 5.30). This is because the proportion of time spent away from the $x - z$ plane, where translation rate is fastest, is greater the more flexible the helix (see figure 5.30). There is less of a difference between net displacement for helices of different stiffnesses than in total distance travelled because of the cancellation between positive and negative translation. For high aspect ratios the effect of stiffness on orbit period is small as in all cases $k^{(B)^{\frac{1}{2}}} a_r^h$ is large and hence orbit period is close to that of a rigid helix.

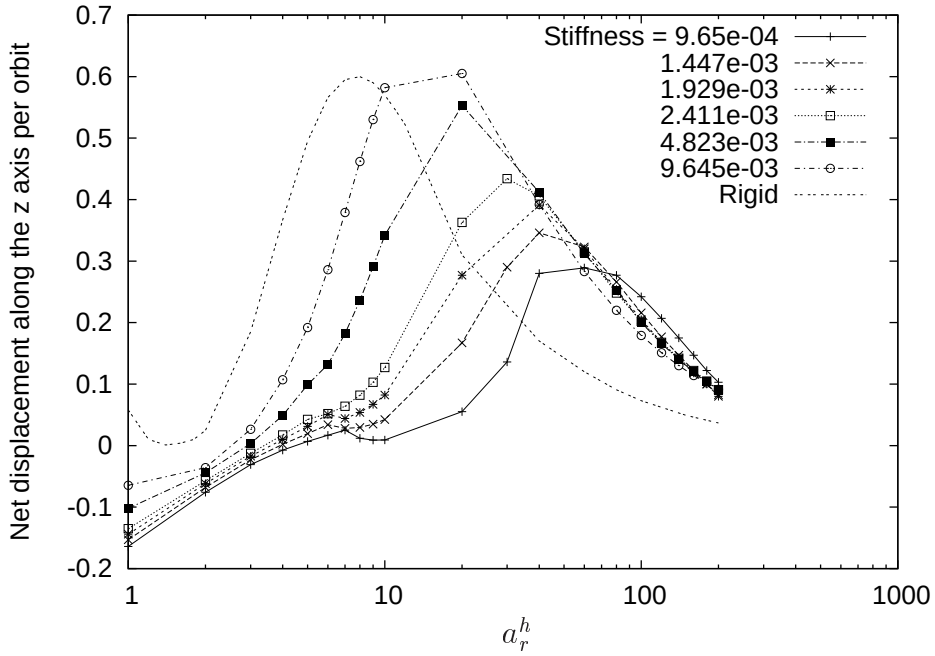

Figure 5.27: Net displacement along the z axis per orbit plotted against aspect ratio for semi-flexible helices.

For a one turn rigid helix the maximum translation occurs at an aspect ratio of $a_r^h = 7$, as this aspect ratio is large enough to give a large orbit period but not too large that the translation rate is small. For helices with the same stiffness, the aspect ratio at which maximum net displacement per orbit and maximum total distance per orbit occurs, increases with flexiblity. This is because the orbit period of flexible helices at moderate aspect ratios (ie. aspect ratios close to $a_r^h = 7$) are smaller than those of rigid helices. However, the orbit periods of flexible, high aspect ratio helices are very close to those of rigid helices. For this reason, by plotting net displacement (figure 5.31) and total distance travelled (figure 5.32) against $a_r^h k^{(B)\frac{1}{2}}$, the same scaling that was used for plotting orbit period, we see that maximum net displacement and total distance occur at $a_r^h k^{(B)\frac{1}{2}} \approx 1.5$ for all stiffness.

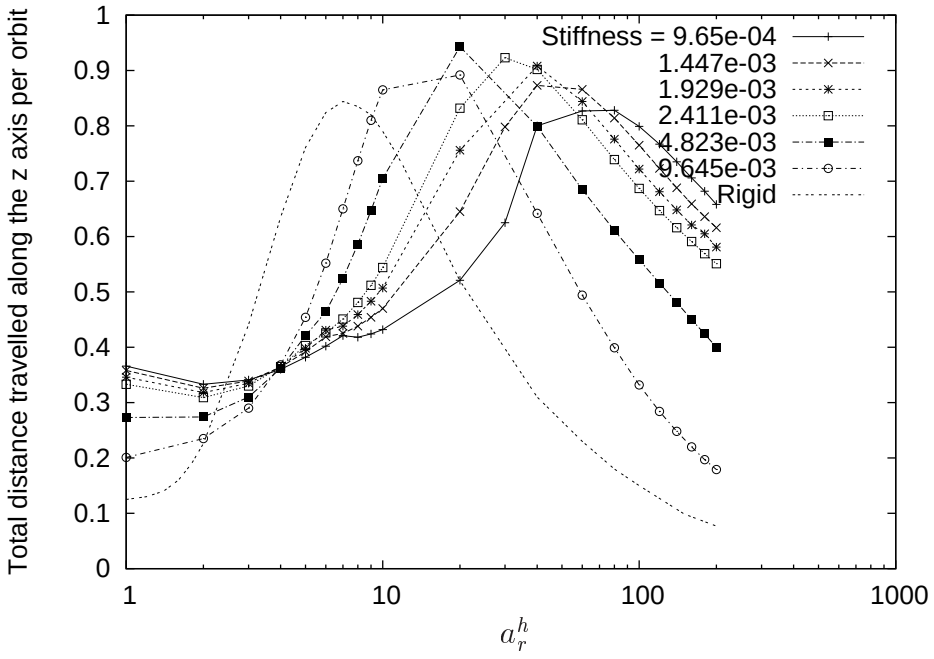

Figure 5.28: Total distance travelled along the z axis per orbit plotted against aspect ratio for semi-flexible helices.

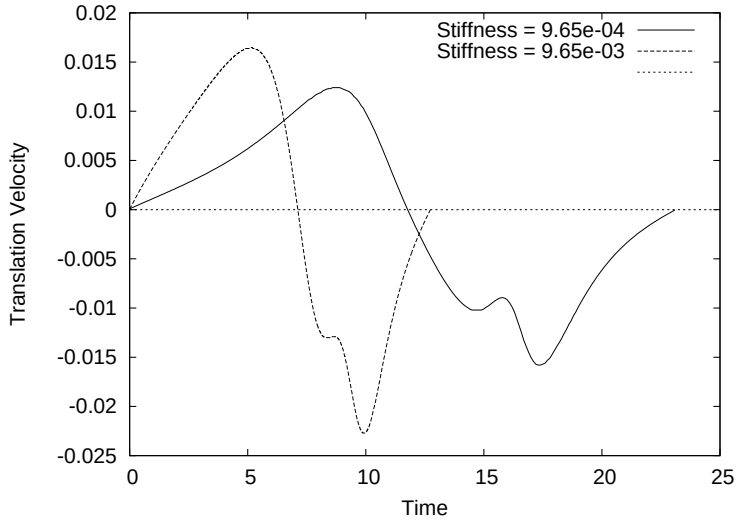

Figure 5.29: Plot of translation velocity against time for helices of aspect ratio $a_r^h = 3$ and stiffnesses $k^{(B)} = 9.65 \times 10^{-3}$ and $k^{(B)} = 9.65 \times 10^{-4}$.

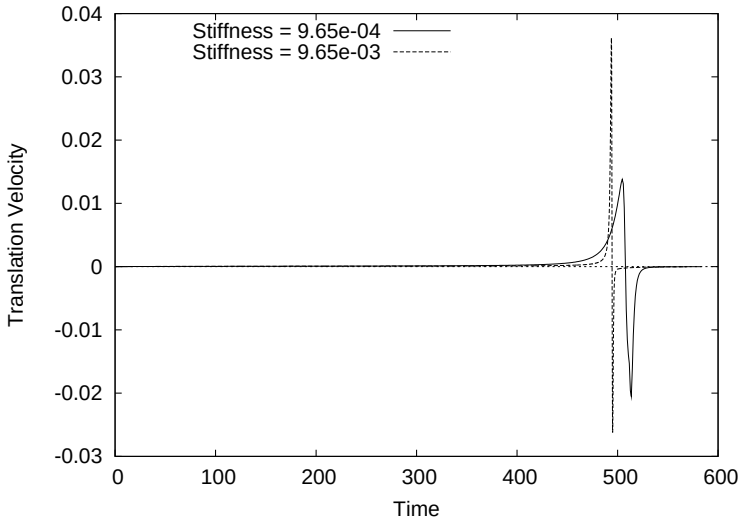

Figure 5.30: Plot of translation velocity against time for helices of aspect ratio $a_r^h = 100$ and stiffnesses $k^{(B)} = 9.65 \times 10^{-3}$ and $k^{(B)} = 9.65 \times 10^{-4}$.

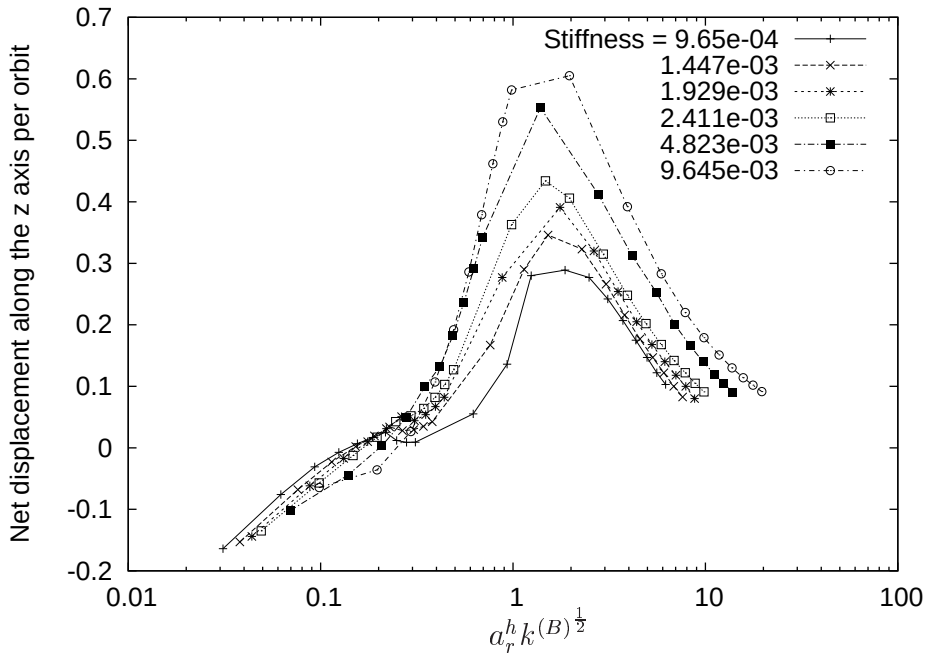

Figure 5.31: Net displacement along the z axis per orbit plotted against $a_r^h k^{(B)\frac{1}{2}}$ for semi-flexible helices.

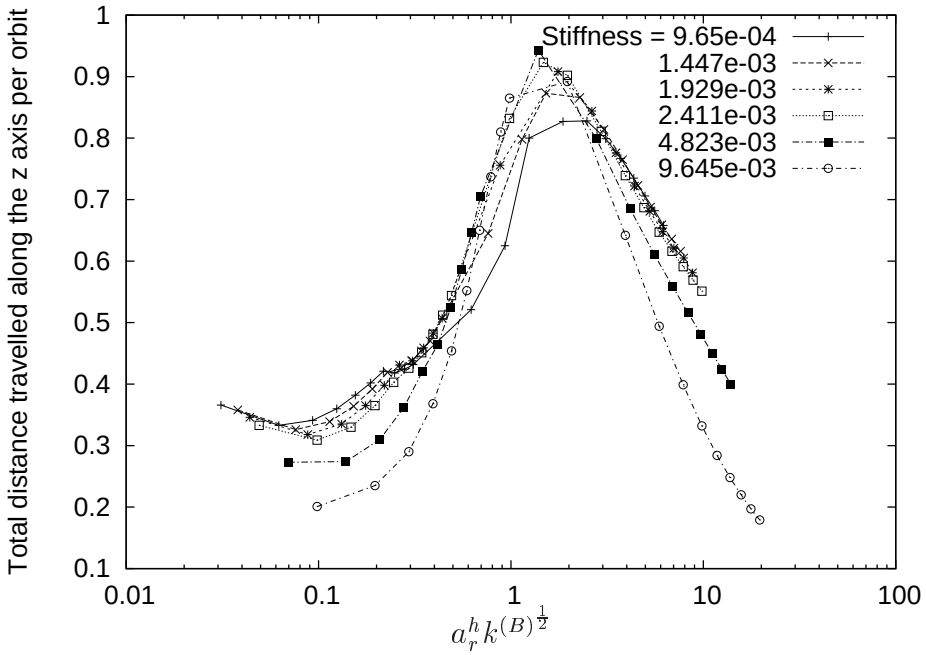

Figure 5.32: Total distance travelled along the z axis per orbit plotted against $a_r^h k^{(B)\frac{1}{2}}$ for semi-flexible helices.

5.3.3 Deformation of semi-flexible helices

In chapter 3 we found that intrinsically straight fibres perform S turns, whereas bent fibres perform C turns. In shear flow the spine of a semi-flexible helix can bend in a similar way to a flexible fibre. Figure 5.34 shows a 2 turn semi-flexible helix of aspect ratio 20 with its central axis and mobility axis $\mathbf{c}_1$ aligned in the flow-gradient plane, rotating in shear flow. The helix forms an S turn as it bends in the compressional quadrant. If we now spin this helix about its axis so that its mobility axis $\mathbf{c}_1$ has a component in the vorticity direction it forms a C turn as seen in figure 5.35, as the fibre is now asymmetric in the $x-y$ plane, as shown in figure 5.33. As the helix spins about its axis, C turns will be more common, however, S turns will occassionally be seen.

For semi-flexible helices with stiffnesses $k^{(B)}$ greater than 0.0015, initially in the $x-y$ plane, the principal axis of the moment of inertia tensor rotates in the $x-y$ plane. As

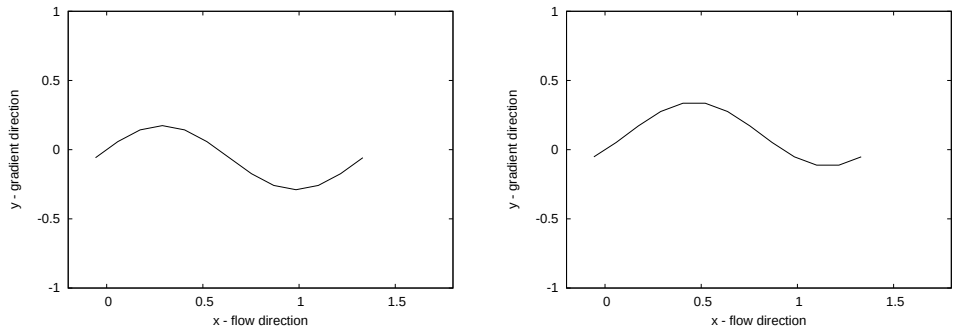

Figure 5.33: $x-y$ view of a helix with its mobility axis $\mathbf{c}_1$ in the $x-y$ plane (left) and $x-y$ view of the same helix rotated through an angle of $\frac{\pi}{4}$ about its central axis so that its mobility axis $\mathbf{c}_1$ has a component in the vorticity direction.

it rotates through the compressional quadrant the associated eigenvalue decreases as the helix compresses slightly, like a spring. However, the principal axes of more flexible helices such as that shown in figures 5.34 and 5.35 do not rotate, but rock back and forth, even though the ends of the fibre change side every half-turn. These helices deform sufficiently during their rotation that the principal axis always remains close to the $x-z$ plane.

5.3.4 Orbit Drift for Helical Fibres

As we have seen in previous chapters axisymmetric rigid particles rotate in closed periodic Jeffery orbits and orbit drift is only seen for semi-flexible fibres. However, in a shear flow even rigid helices do not rotate in closed orbits but exhibit orbit drift. For most initial orientations direction of orbit drift is towards the $x-y$ plane however, some helices settle in orbits close to the $x-y$ plane.

For example in figure 5.36 we consider 1 turn helices placed at an angle of $\frac{\pi}{32}$ with the x axis in the $x-z$ plane so that they are close to but not in the $x-y$ plane and orbit drift is towards the $x-y$ plane. The orbit drift of helices with aspect ratio 20, 40 and 100 with $n_t = 1$ are illustrated in figure 5.36 by plotting the trajectory of the central mobility axis

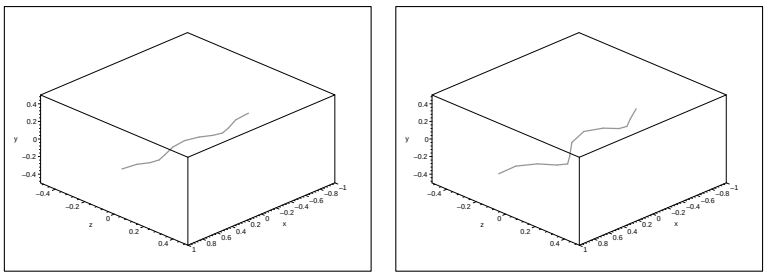

(a) (b)

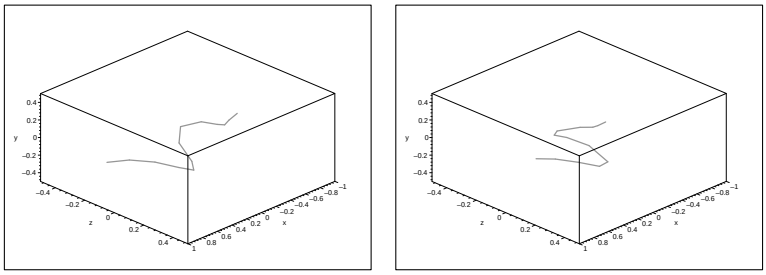

(c) (d)

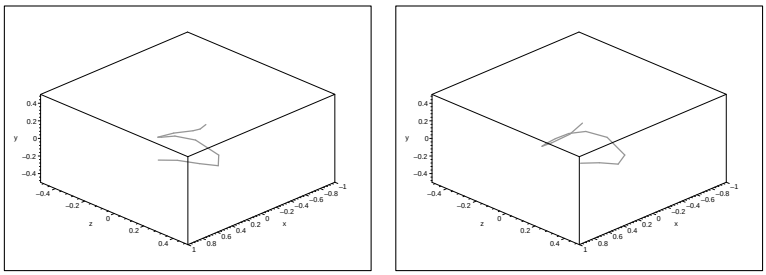

(e) (f)

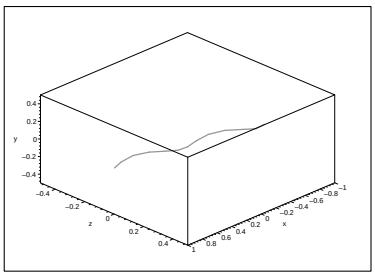

(g)

Figure 5.34: A semi-flexible helix of aspect ratio, $a_r^h = 20$, number of turns, $n_t = 2$ and stiffness $k^{(B)} = k^{(T)} = 6.25 \times 10^{-4}$ performing a S turn in shear flow.

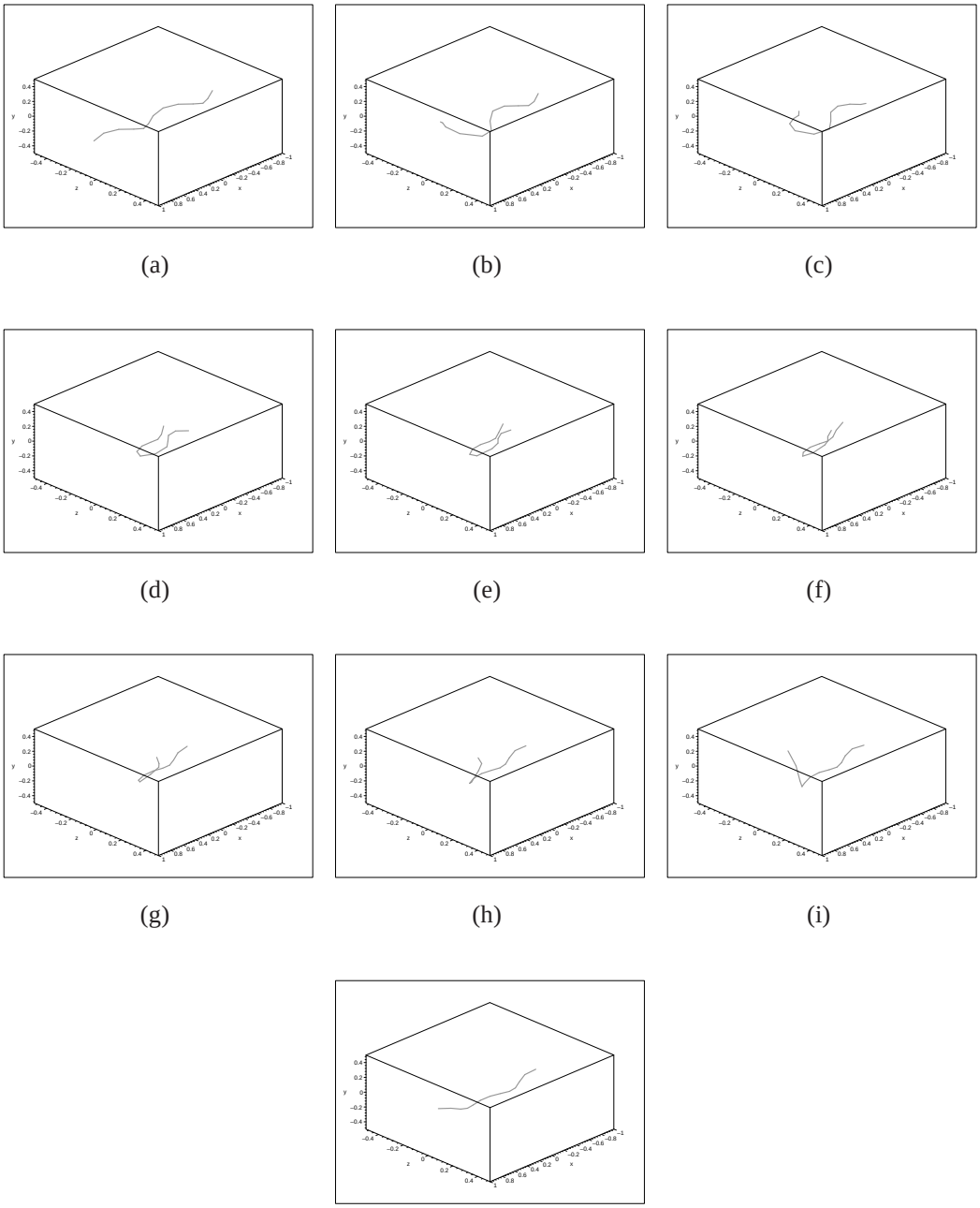

(a) (b) (c)

(d) (e) (f)

(g) (h) (i)

(j)

Figure 5.35: The same semi-flexible helix as in figure 5.34, performing a C turn.

$\mathbf{c}_1$, as defined in section 4.5.3. The drift rate is faster the smaller the aspect ratio.

For helices with 2 or more turns the drift direction is variable, after the first half orbit drift may be towards the $x-y$ plane and then after the second half orbit, towards the vorticity axis, and drift continues long after the 1-turn helices have settled in the $x-y$ plane. Some helices found intermediate orbits as shown in figures 5.37 and 5.38. We have not been able to predict the direction of drift, how long it will take for the helix to reach a stable orbit and where that orbit will be, or if the helix will eventually reach a stable orbit. For a larger number of turns eg. $n_t \geq 20$ there is no noticeable orbit drift and hence we conclude that orbit drift is a property of helices with small numbers of turns. For a helix with a finite number of turns the rotation and spin of the helix are coupled in a non-trivial manner and this could potentially give chaotic motion.

Helices placed at angles greater than $\frac{\pi}{32}$ to the x axis in the $x-z$ plane still drifted towards the $x-y$ plane. A one turn helix of aspect ratio 10 placed at an angle of $\frac{15\pi}{32}$ with the x axis took approximately 100 orbits to reach the $x-y$ plane. Helices with more than one turn did drift in the direction of the $x-y$ plane however, after 10^9 orbits they had still not reached a steady orbit.

Semi-flexible helices also drift towards the $x-y$ plane. Just as with rigid helices, 1 turn helices drift faster than helices with a greater number of turns.

5.4 Conclusion

In this chapter we have considered instrinsically bent fibres (with in-plane bends) and helical fibres (out-of-plane bends). Unlike the intrinsically straight fibres studied in chapter 3 which perform S turns and only exhibit orbit drift when flexible, bent fibres perform C turns and a helical fibre can perform both C and S turns depending upon its angle of spin. Bent fibres do not exhibit orbit drift as the axial spin of the fibres quickly

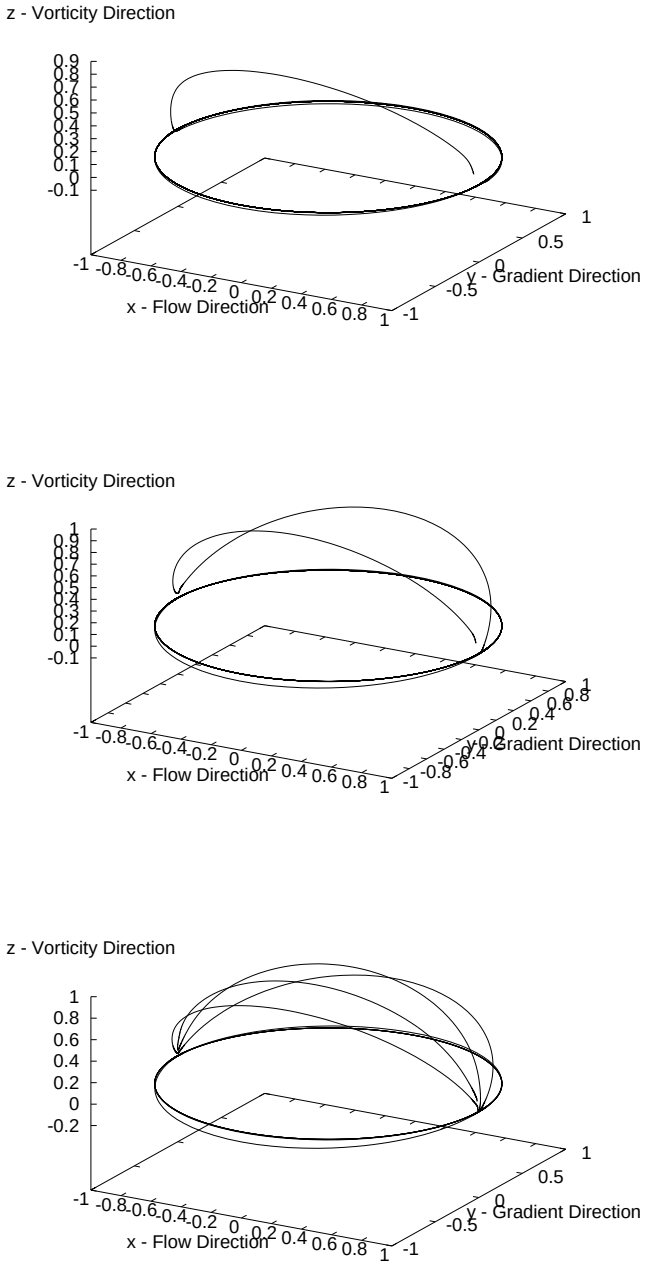

Figure 5.36: From top to bottom plots of $\mathbf{c}_1$ for helices of aspect ratios of 20, 40 and 100 drifting towards the $x-y$ plane.

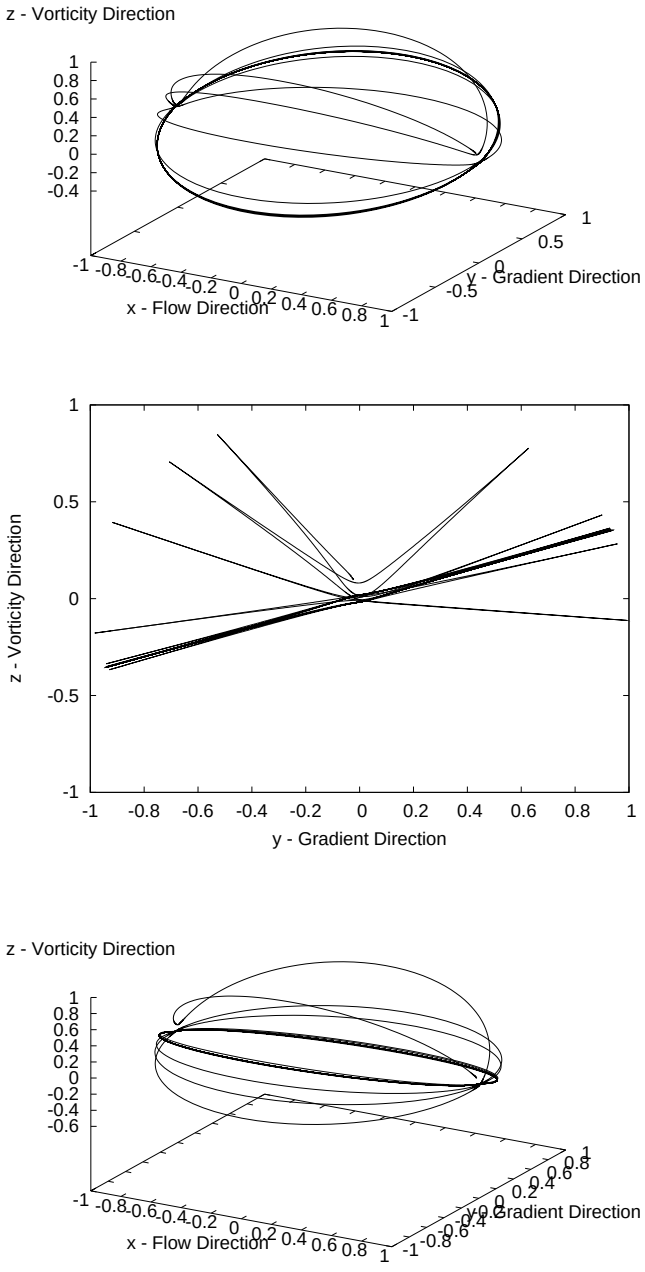

Figure 5.37: Helix with 2 turns and aspect ratio 20 drifting in random directions before settling to orbit in a plane at and angle about z with the $x-y$ plane (top, view in the $y-z$ plane (middle). Helix with 2 turns and aspect ratio 30 (bottom).

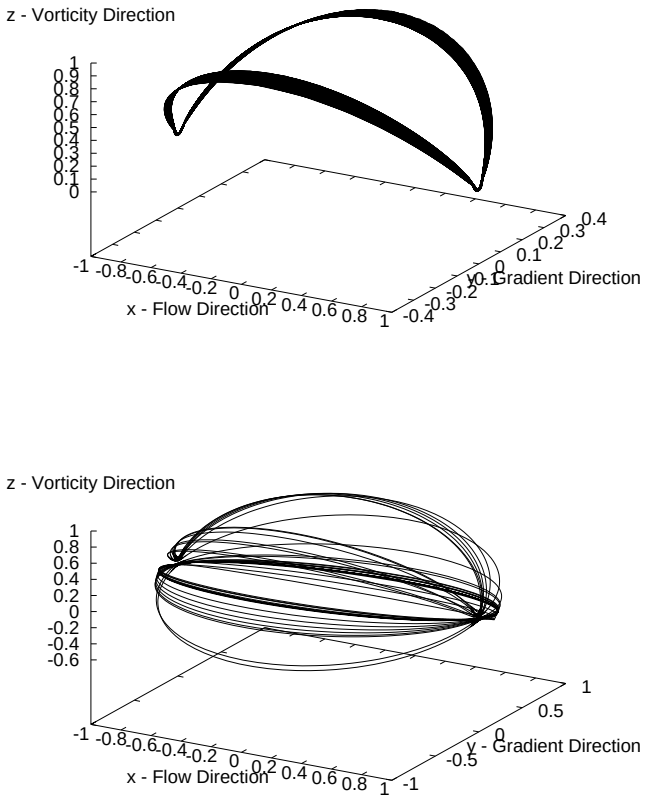

Figure 5.38: Helix with 2 turns and aspect ratio 40 drifting very slowly from its initial orbit (top), helix with 3 turns and aspect ratio 30 settling into an intermediate orbit.

rotates them into the $x-z$ plane where they are no longer able to rotate through the flow plane. Rigid and semi-flexible helices exhibit a complex pattern of orbit drift due to the coupling between spin and rotation.

For moderate stiffnesses the orbit period of semi-flexible bent and helical fibres is reduced due to the bending of the fibre causing a decrease in effective aspect ratio, just as it does for intrinsically straight fibres, however, for very low stiffnesses the orbit period is increased as the fibre not only bends under compression but straightens in the extensional quadrant resulting in a increase in effective aspect ratio just prior to the fibre crossing the flow plane. Just as with intrinsically straight fibres the parameter determining how much the orbit period of a bent fibre differs from that of an equivalent rigid fibre is given by $a_{r_{eff}}k^{(B)}$. For helical fibres the parameter is $a_r^h k^{(B)\frac{1}{2}}$ suggesting that aspect ratio has a greater effect on bending than it does with bent and straight fibres.

As well as exhibiting orbit drift, helical fibres also translate along the z axis, as their handedness provides a coupling between rotation about the vorticity axis due to the shear flow and translation along that axis. This effect is greatest at points of maximum compression and extension and hence greater for helices in the flow-gradient plane. Semi-flexible helices translate more slowly as they are unable to fully resist the compressive and extensional forces of the flow.

Chapter 6

Swimming of Helical Fibres

In this chapter we use the flexible fibre simulation method described in chapter 4 to study the swimming motion of a semi-flexible helical fibre at zero Reynolds number. In Stokes flow inertial forces are negligible and fluid motion is linearly dependent on the applied forces. This makes any time reversal symmetric swimming motion impossible as any motion induced on the forward stroke is reversed on the return [30]. For micro-organisms, with length scales of order 10^{-4}m swimming in water at speeds of order 10^{-4}ms^{-1} the Reynolds number is of order 10^{-2}, and hence they cannot swim using a reciprocal motion and therefore must find an alternative method of propulsion. One solution is rotation of a helical flagellum. A helical fibre subjected to a torque will translate through the fluid due to the handedness of the helix providing a coupling between torque and translation.

Let us recall the grand resistance matrix, derived in section 4.5. In a stationary flow the strain-rate is zero and hence we need only consider the following part of the matrix:

$$\begin{pmatrix} \mathbf{F} \\ \\ \mathbf{T} \end{pmatrix} = \begin{pmatrix} \mathbf{A} & \tilde{\mathbf{B}} \\ \\ \mathbf{B} & \mathbf{C} \end{pmatrix} \begin{pmatrix} \mathbf{U} \\ \\ \boldsymbol{\omega} \end{pmatrix}. \tag{6.0.1}$$

Imposing a torque $\boldsymbol{\tau}$ on the helix with force $\mathbf{F} = 0$ produces a velocity given by

$$\mathbf{U} = (\mathbf{B} - \mathbf{C}\tilde{\mathbf{B}}^{-1}\mathbf{A})^{-1}\boldsymbol{\tau},$$

and angular velocity of

$$\boldsymbol{\omega} = (\mathbf{C} - \mathbf{B}\mathbf{A}^{-1}\tilde{\mathbf{B}})^{-1}\boldsymbol{\tau} = \mathbf{c}\boldsymbol{\tau}$$

where $\mathbf{c}$ is an entry in the grand mobility tensor (see section 4.5.3).

For an axisymmetric body the coupling tensor $\mathbf{B}$ vanishes at the centre of resistance and hence imposing a torque on the object results in a rotation only. However, for a helix, the tensor is non-zero and so imposing a torque produces both rotation and translation. The tensor $(\mathbf{B} - \mathbf{C}\tilde{\mathbf{B}}^{-1}\mathbf{A})^{-1}$ is dependent on the helix parameters a, b, and n_t, as defined in section 4.1, and therefore each of these parameters affects the swimming speed $|\mathbf{U}|$. A semi-flexible helix will deform as it rotates and the swimming speed is affected by the whole fibre stiffness $k^{(B)}$.

Before considering the effects of flexiblity on swimming motion we first use the grand resistance matrix to investigate the swimming motion of a rigid helix. In order to produce steady swimming we impose a torque of unit magnitude in the direction of the principle axis, $\mathbf{c}_1$, of the mobility tensor $\mathbf{c}$ (derived in section 4.5.3). This produces uniform swimming in the direction of $\mathbf{c}_1$ at speed $V = \mathbf{U} \cdot \mathbf{c}_1$ as shown in figure 6.5.

For fibres in shear flow we have non-dimensionalised time with respect to the inverse shear-rate of the fluid $\frac{1}{\dot{\gamma}}$. In this chapter the shear rate is zero and so we must choose a different timescale. As swimming occurs by imposing a torque $\boldsymbol{\tau}$ we may use $\frac{\xi_t}{|\boldsymbol{\tau}|}$ as a timescale where ξ_t is the rotational resistance coefficient for a fibre of length $2L$ derived in section 1.2.6. This enables a direct comparison of the swimming efficiency for different helices by comparing swimming speeds for fixed torque. The non-dimensionalised

swimming speed and stiffness are then given by

$$V_\tau^* = \frac{\xi_t V}{L|\boldsymbol{\tau}|}$$

and

$$k_\tau^{(B)} = \frac{EI}{l|\boldsymbol{\tau}|}$$

respectively. However, this situation where an external torque is applied to an isolated filament is rather different to models such as those of Takano and others [35, 36] where the filament is attached to a head that receives a torque in the opposite direction so that there is no net torque on the body as a whole. In these studies the swimming speed is calculated at a fixed angular velocity. Thus an alternative timescale is the inverse angular velocity, $\frac{1}{|\boldsymbol{\omega}|}$, giving non-dimensional swimming speed and stiffness as

$$V_\omega^* = \frac{V}{L|\boldsymbol{\omega}|}$$

and

$$k_\omega^{(B)} = \frac{EI}{l|\boldsymbol{\omega}|\xi_t}.$$

We first present our results for rigid helices in which we consider the effect of number of turns, n_t and pitch angle, $\beta = \tan^{-1}\frac{a}{b}$ on the swimming speed of the helix.

6.1 Swimming of Rigid Helices

Figure 6.1 shows the swimming speed at constant torque, V_τ, plotted against the aspect ratio per turn for helices of 1, 2, 3 and 4 turns. For small $\frac{a_r^h}{n_t}$, where a_r^h is the helix aspect ratio as defined in section 5.3, increasing the aspect ratio results in an increase in swimming speed. The increase in aspect ratio reduces the radius resulting in an increase in the angular velocity which in turn gives a larger forward velocity.

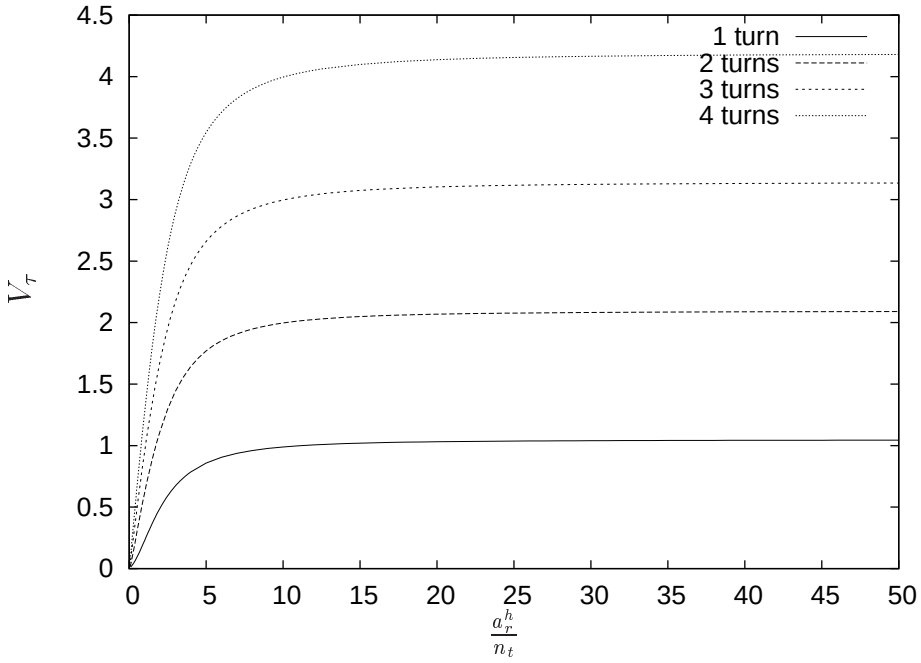

Figure 6.1: Swimming speed V_τ plotted against $\frac{a_r^h}{n_t}$ for rigid helices of 1, 2, 3 and 4 turns.

Figure 6.2 shows the swimming speed for constant angular velocity, V_ω plotted against aspect ratio per turn for helices of 1, 2 3 and 4 turns. Plotted this way we observe that maximum swimming speed occurs at a value of $\frac{a_r^h}{n_t} = 2.8$. For small aspect ratios, an increase in aspect ratio results in an increase in swimming speed. However, above an aspect ratio of $\frac{a_r^h}{n_t} = 2.8$, which corresponds to a pitch value of $\beta = 48°$, the swimming speed decreases with further increases in aspect ratio, as the decrease in pitch angle results in a decreased propulsive thrust. There are two limits at which the swimming speed of the helix tends to zero, the limit of a circular a ring ($\beta = 90°$) and that of a straight rod ($\beta = 0°$). Both shapes are symmetrical and therefore do not provide forward thrust. The swimming speed therefore reaches a maximum at a pitch angle that falls between these two limits.

Figures 6.3 and 6.4 show the swimming speeds V_τ and V_ω respectively plotted against number of turns for helices with a constant pitch angle ($\frac{a_r^h}{n_t}$ =constant). V_τ increases

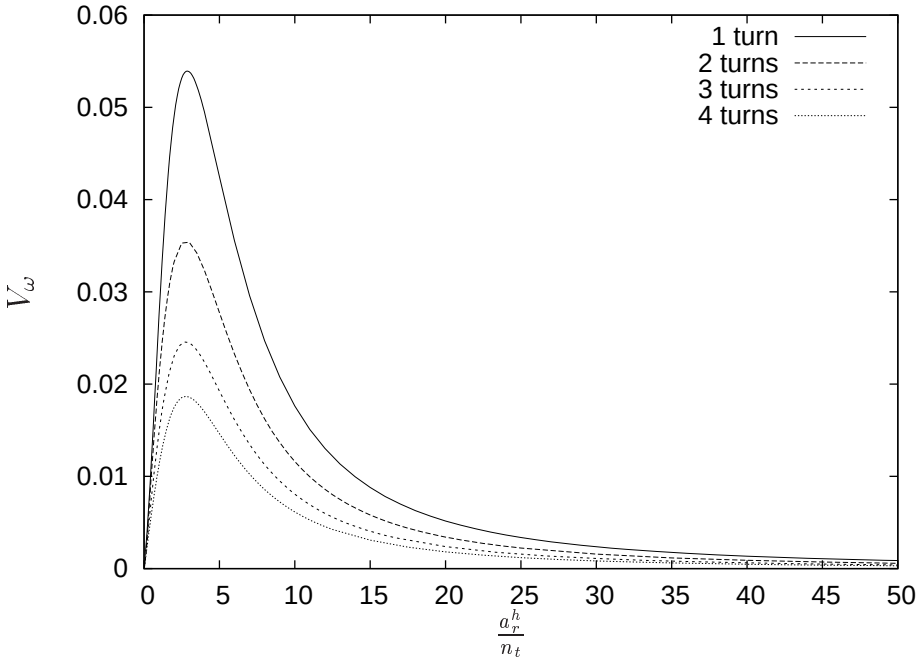

Figure 6.2: Swimming speed V_ω plotted against $\frac{a_r^h}{n_t}$ for rigid helices of 1, 2, 3 and 4 turns.

linearly with increasing number of turns. In order to maintain a constant pitch angle and length both the radius a and the pitch parameter b must both decrease with increasing number of turns. The decrease in radius results in an increase in angular velocity and hence an increase in V_τ. However, in figure 6.4 we find that V_ω decreases with increasing number of turns as the decrease in pitch means the helix approaches the geometry of a hollow cylinder, therefore losing the asymmetry that allows it to swim.

Comparing our results to those of Goto, Inaoka and Takano [12], who used the method described by Higdon [16] to produce results for a rigid helical tail and a spherical cell body, we obtain a similar optimum pitch angle of 48° compared to the 44° obtain by Goto *et. al.*, despite the absence of a cell head in our simulations. Goto *et. al.* obtain an optimal number of turns of $n_t = 1.5$. The increase for small n_t was due to the reduced torque and hence reduced counter rotation of the cell head. For larger n_t, the swimming speed decreased due to the increase in slenderness ratio, $\frac{2\pi b}{d}$ where d is the fibre diameter.

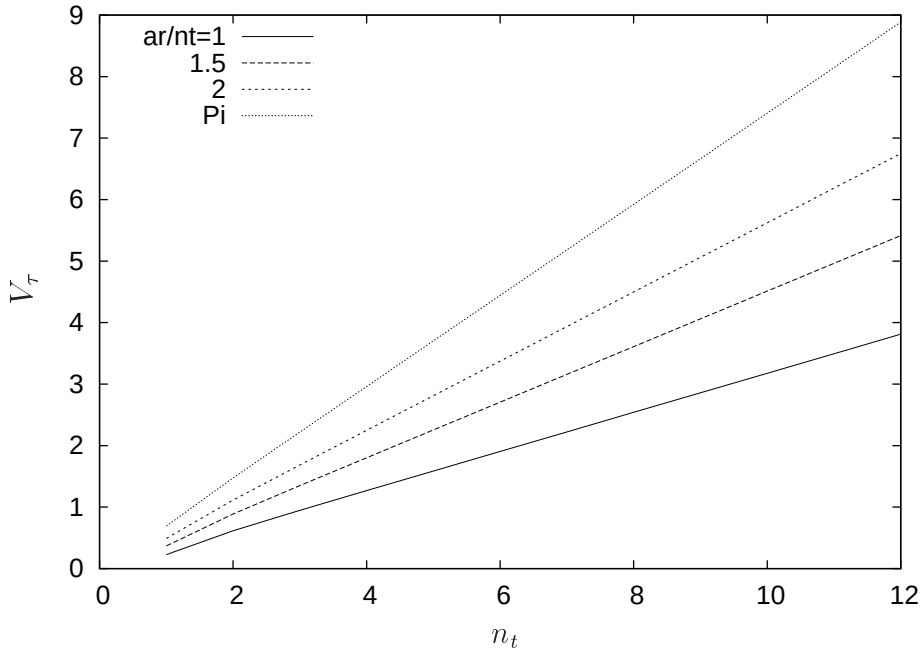

Figure 6.3: Swimming speed V_τ plotted against number of turns n_t for rigid helices of constant pitch.

The slenderness ratio is important as it is the 2:1 ratio of tangential to normal motion of a slender fibre that allows the helix to swim (described in section 5.3.2). In our results we see neither of these effects as our simulation does not include a cell head and we include only the first order terms in slender body theory, hence making our fibre of infinite aspect ratio. Despite this we obtain an optimum pitch angle very close to that of Goto *et. al.* as the optimum value must occur between the limits of a ring and a straight rod.

6.2 Swimming of Semi-Flexible Helices

We now use our flexible fibre simulation to calculate the swimming speeds of semi-flexible helices. In order to obtain a uniform swimming direction parallel to the x-axis we align the mobility axis $\mathbf{c}_1$ (derived in subsection 4.5.3) with the x-axis and then apply a torque of magnitude 1 and direction $\mathbf{c}_1$ to the first rod. Forwards swimming is in the

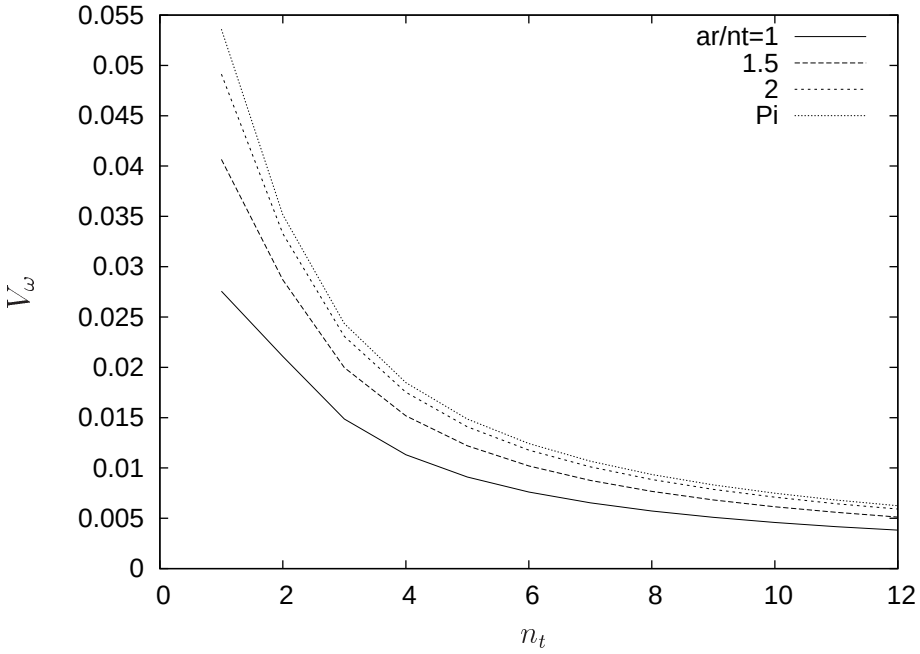

Figure 6.4: Swimming speed V_ω plotted against number of turns n_t for rigid helices of constant pitch.

direction of the first rod and backwards swimming is in the direction of the last rod as shown in figure 6.5. For a left-handed helix forward swimming requires a negative torque and the rotation is anti-clockwise. Backwards swimming requires a positive torque and the rotation is clockwise. To verify the results of our numerical simulation we compare the swimming speeds of rigid helices obtained from the grand resistance matrix with those of our flexible fibre simulation for a fibre composed of 24 rods with a whole fibre stiffness of $k^{(B)} = 9.65$. This is sufficiently large that the forwards and backwards swimming speeds of the helix are the same. Figure 6.6 shows the results obtained for the swimming speed, V_ω, against $\frac{a_r^h}{n_t}$ for both the simulation and the grand resistance matrix. Our simulation is in good agreement with the results of the grand resistance matrix, although the accuracy decreases with increasing number of turns, as the number of rods per turn is reduced. To compare forwards and backwards swimming speeds of semi-flexible fibres we use a 2 turn helix in order to reduce discretisation errors.

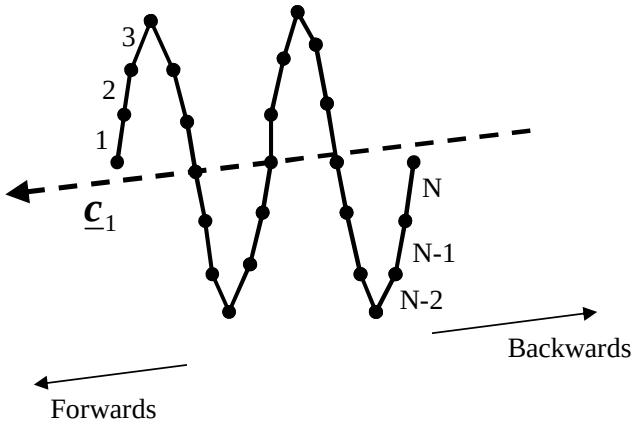

Figure 6.5: Illustration of a 24 rod helix with forwards swimming in the direction of the first rod and backwards swimming in the direction of the last.

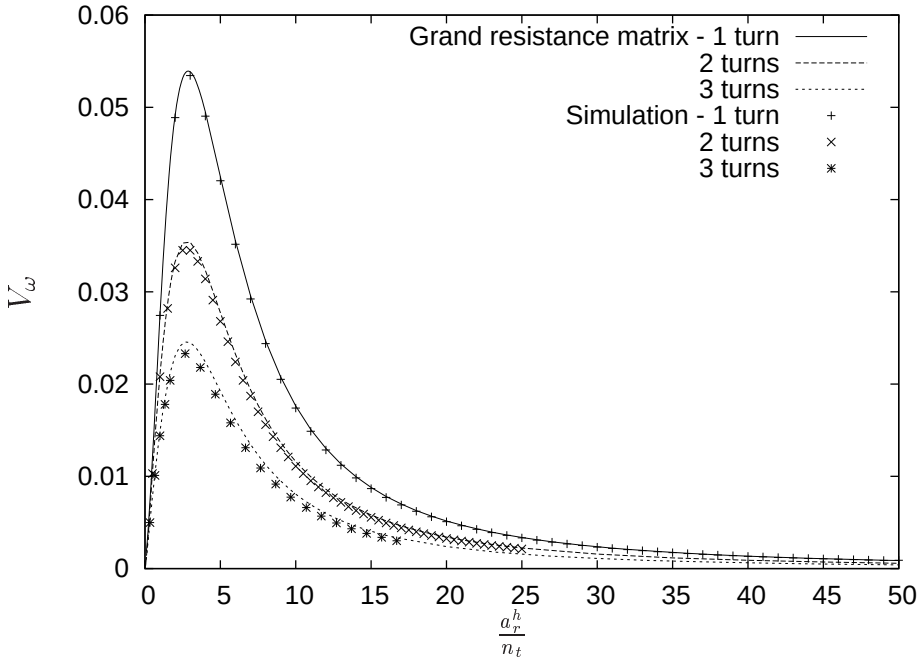

Figure 6.6: Plot of non-dimensional swimming speed V_ω against $\frac{a_r^h}{n_t}$, showing results from the grand resistance matrix for a rigid helix and the flexible fibre simulation set at a stiffness of $k^{(B)} = 9.65$.

We shall now consider the effect of flexibility on the forwards and backwards swimming speeds of semi-flexible fibres. To do this we measure the swimming speed and angular velocity of the helix once the angular velocities for the rods become equal and the swimming speed has reached equilibrium. We also consider the shape changes that occur with forwards and backwards swimming. In order to measure shape changes we require a measure of radius and pitch that can be used for distorted helices.

For a regular continuous helix we can obtain the radius and pitch of the helix from the principle moments of the moment of inertia tensor as derived in section 4.2. The radius is given by

$$a = \sqrt{\lambda_3} \tag{6.2.2}$$

and the pitch parameter b (where $2\pi b$ is the pitch of the helix) by

$$b = \sqrt{\frac{6(\lambda_1 + \lambda_2 - \lambda_3)}{n_t}}. \tag{6.2.3}$$

We verified these formulae by calculating the principle moments for a discretised helix and comparing the actual values of a and b to those calculated using equations (6.2.2) and (6.2.3).

In figures 6.7 and 6.8 we consider 2 turn helices with aspect ratios of 2, 3, 4 and 6, which correspond to pitch angles of $72.3°$, $64.5°$, $57.5°$ and $46.3°$ respectively. Figure 6.7 shows the swimming speed for a constant torque, V_τ, against the stiffness measure $k_\tau^{(B)}$, while figure 6.8 shows the swimming speed for constant angular velocity V_ω against stiffness $k_\omega^{(B)}$. The solid lines show forwards swimming speeds and the dashed lines the backwards swimming speed. In the case of constant torque forwards swimming speed is faster than backwards swimming speed for a semi-flexible fibre, however, in the case of constant angular velocity, backwards swimming is faster. The backwards swimming speed increases as the stiffness decreases, however, forwards swimming speed

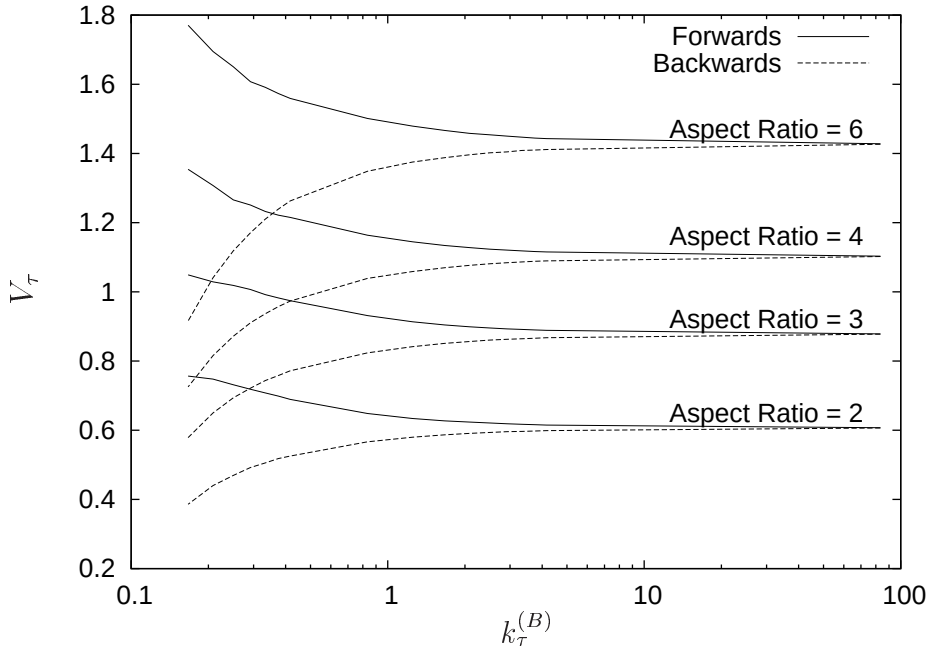

Figure 6.7: Swimming speed V_τ plotted against stiffness $k_\tau^{(B)}$ for semi-flexible helices of aspect ratios 2, 3, 4 and 6.

decreases as stiffness decreases. For very small stiffnesses the backwards swimming speed drops significantly, eventually becoming lower than the forwards swimming speed. The difference between forwards and backwards swimming speed therefore varies greatly depending upon the exact stiffness of the fibre. To assess the reasons for the changes in swimming speeds as the fibre becomes more flexible we consider how the shape of the fibre changes.

Figure 6.9 shows that for forwards swimming, the average radius of semi-flexible fibres decreases, while for backwards swimming the radius increases. Figure 6.10 shows that for forwards swimming the pitch parameter b decreases while for backwards swimming it increases. Figure 6.11 shows that forwards swimming causes an increase in the number of turns while backwards swimming results in a decrease in number of turns. In summary, the effect of flexibility, means that for forwards swimming the helix winds up and for backwards swimming the helix unwinds.

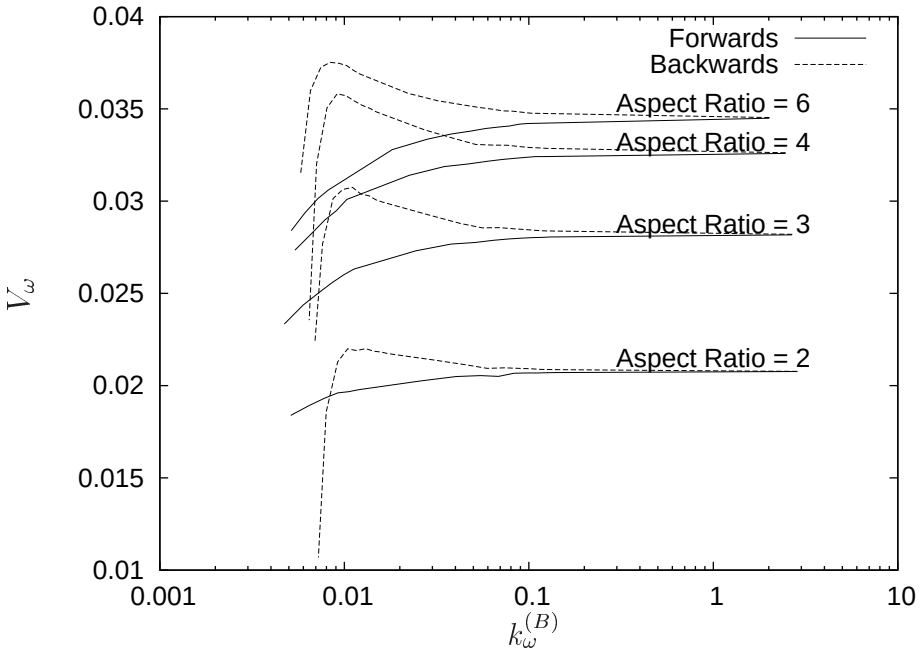

Figure 6.8: Swimming speed V_ω plotted against stiffness $k_\omega^{(B)}$ for semi-flexible helices of aspect ratios 2, 3, 4 and 6.

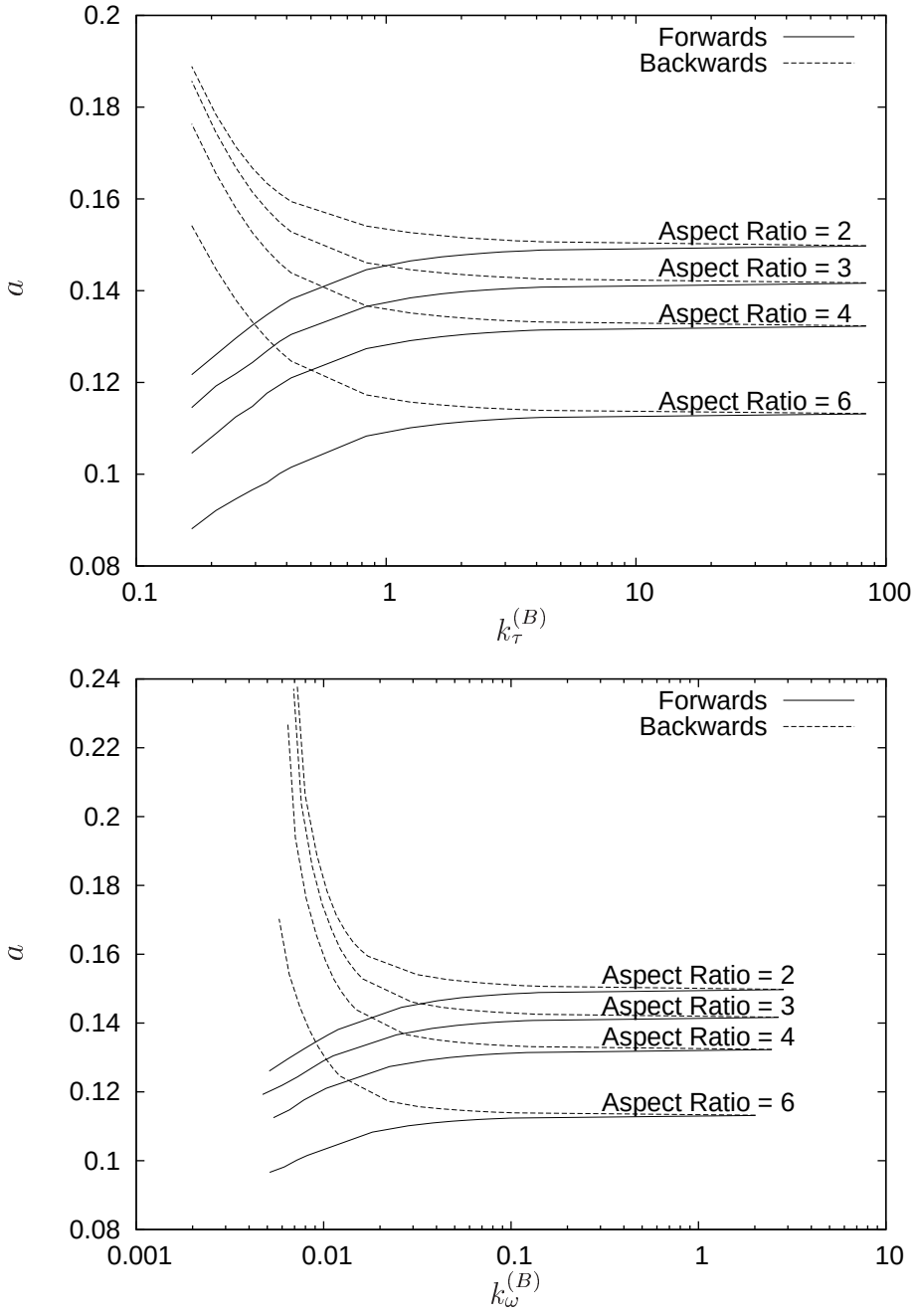

Figure 6.9: Radius plotted against stiffness $k_\tau^{(B)}$ (top) and radius plotted against stiffness $k_\omega^{(B)}$ (bottom) for semi-flexible helices of aspect ratios 2, 3, 4 and 6.

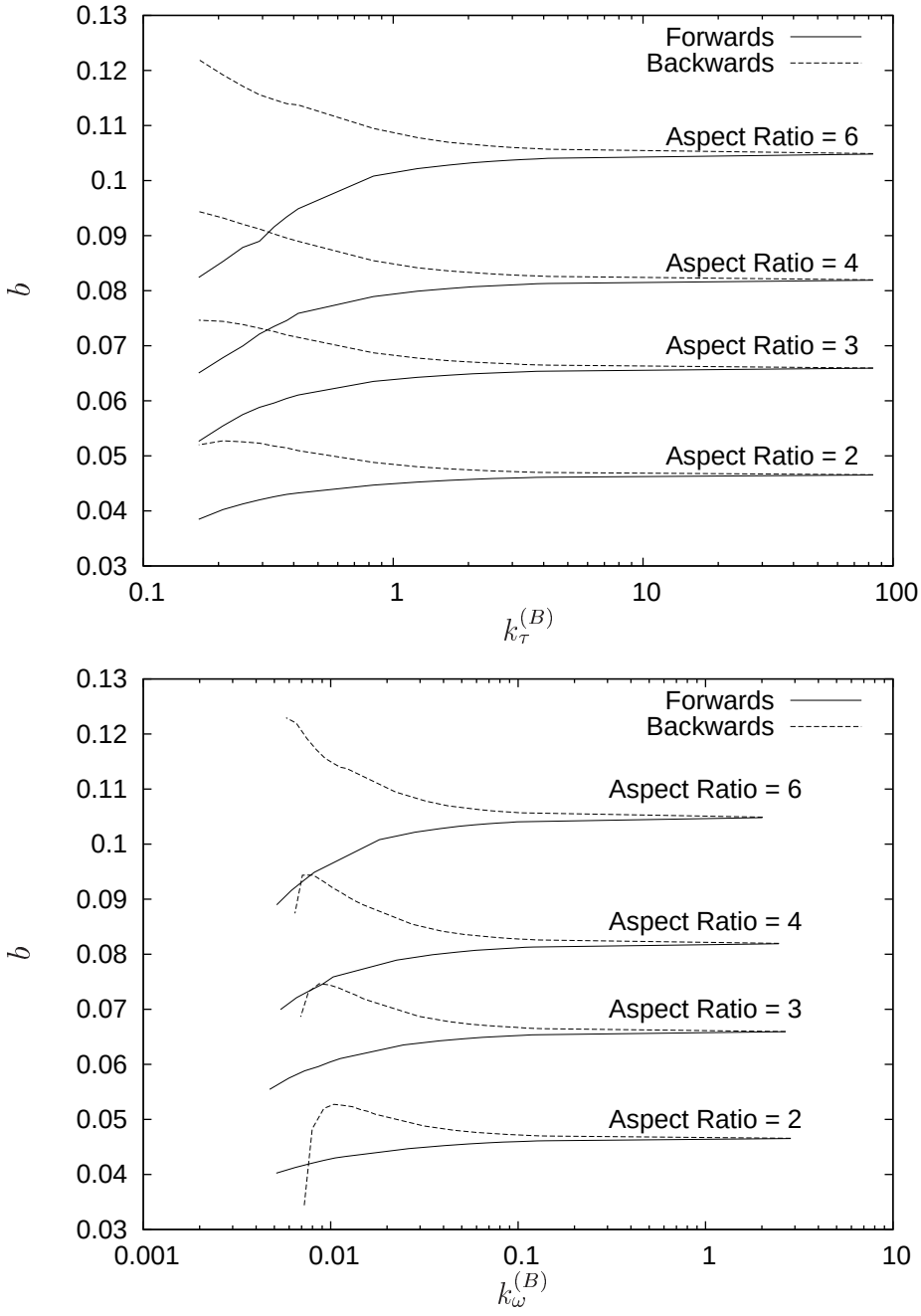

Figure 6.10: Pitch parameter, b, plotted against stiffness $k_\tau^{(B)}$ (top) and pitch plotted against stiffness $k_\omega^{(B)}$ (bottom) for semi-flexible helices of aspect ratios 2, 3, 4 and 6.

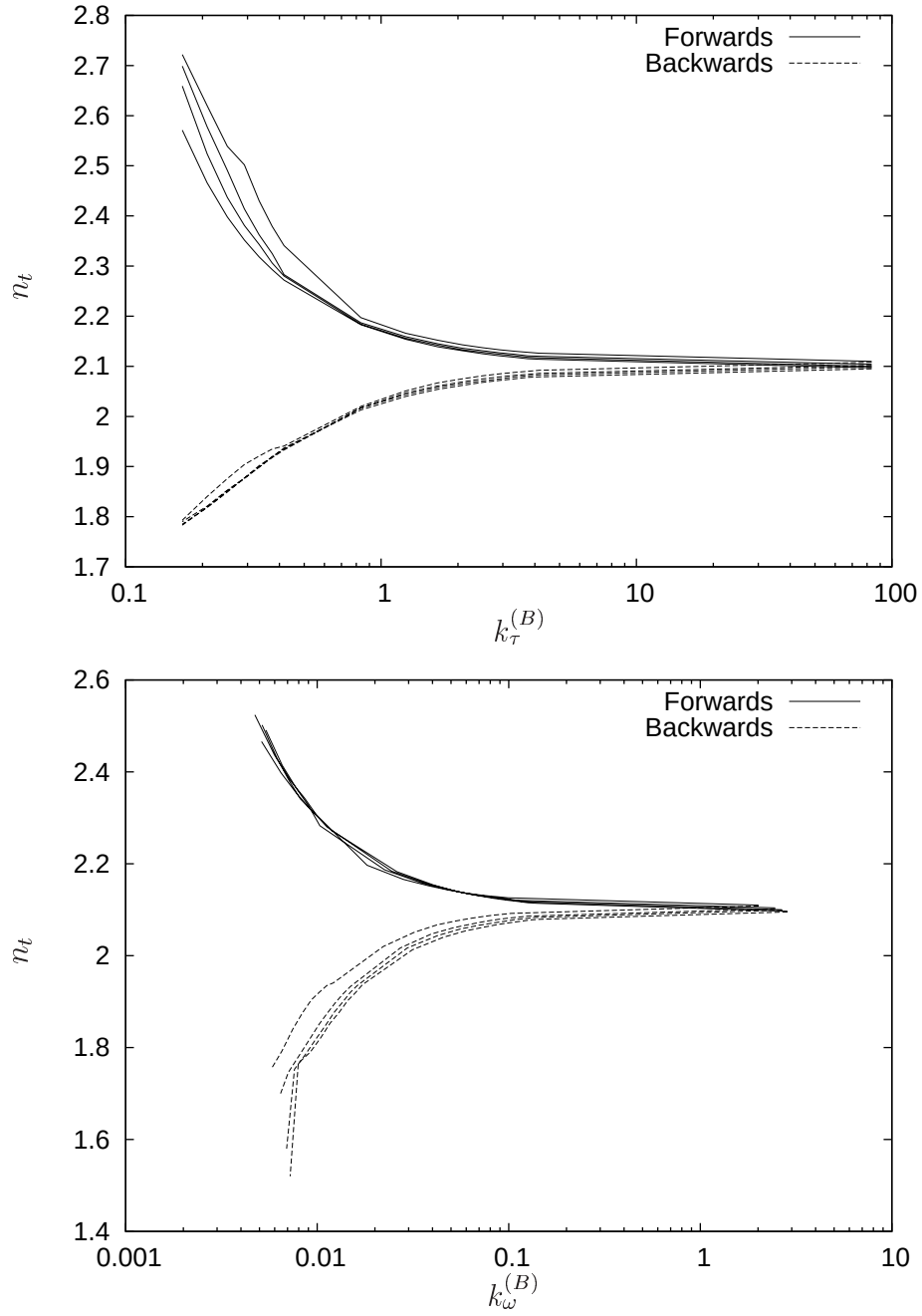

Figure 6.11: Number of turns plotted against stiffness $k_\tau^{(B)}$ (top) and number of turns plotted against stiffness $k_\omega^{(B)}$ (bottom) for semi-flexible helices of aspect ratios 2, 3, 4 and 6.

For forwards swimming, both radius, a and pitch, b decrease such that the pitch angle $\beta = \tan^{-1}\frac{a}{b}$ remains relatively constant. The increase in n_t with the decrease in b means that the axial length also remains relatively constant. However, in swimming backwards there is a slight increase in pitch angle and a slight decrease in axial length for very flexible fibres.

These shape changes are the cause of the apparently contradictary results for swimming speeds V_τ and V_ω in figures 6.7 and 6.8. For small stiffnesses the swimming speed for constant torque V_τ increases for forwards swimming as the stiffness decreases due to the decrease in radius and hence the increase in angular velocity. However, the swimming speed at constant angular velocity V_ω decreases for forwards swimming with decreasing stiffness due to the decrease in pitch and increase in number of turns resulting in the helix approaching the limit of a hollow cylinder. The backwards swimming speed increases with decreasing stiffness as the decrease in the number of turns increases the asymmetry of the helix. The reliability of the results for very low stiffnesses is compromised due to the long time taken to reach equilibrium and the certainty as to whether equilibrium has been reached. The sudden drop in swimming speed for backwards swimming at low stiffnesses may occur due to the loss of a true helical shape and consequent increase in motion perpendicular to the swimming direction (this motion is still periodic and so does not change the net swimming direction).

Takano and Goto [35] calculated the swimming speed at constant angular velocity, V_ω, for a flagella of stiffness $k_\omega^{(B)} \approx 0.0075$, pitch angle 48° and approximately 3 turns. They obtained a backwards swimming speed that was approximately 4% faster than the forward swimming speed. In our results we obtain a backwards swimming speed that is approximately 23% faster than the forwards swimming speed for a flagella of stiffness $k_\omega^{(B)} \approx 0.0075$, pitch angle 46% and 2 turns. This is much closer to, though still smaller than the 50% difference observed on average by Magariyama *et. al.* [23] in experiments in which video recordings were taken of the bacterium *Vibrio alginolyticus*, using high-

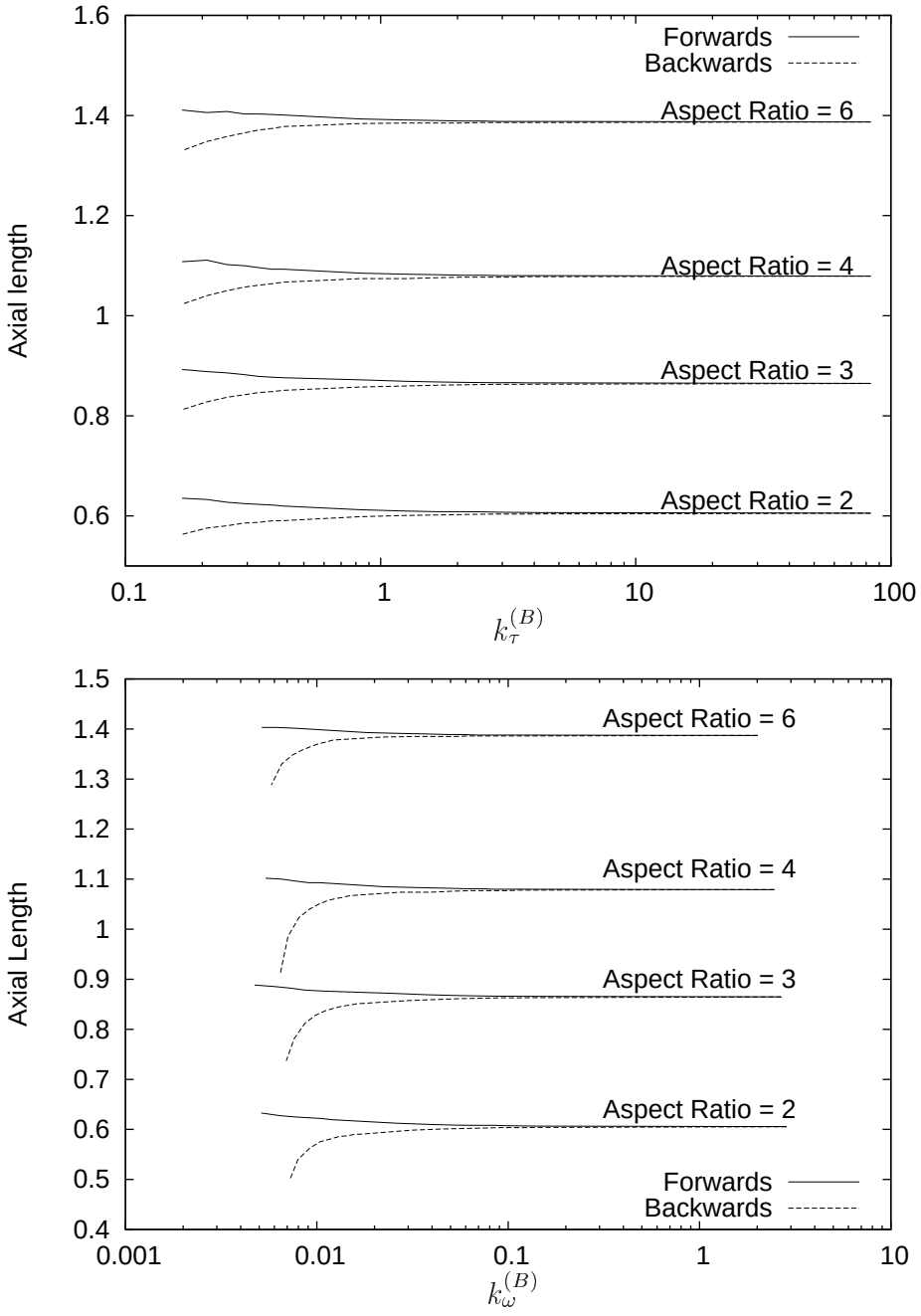

Figure 6.12: Axial length plotted against stiffness $k_\tau^{(B)}$ (top) and axial length plotted against stiffness $k_\omega^{(B)}$ (bottom) for semi-flexible helices of aspect ratios 2, 3, 4 and 6.

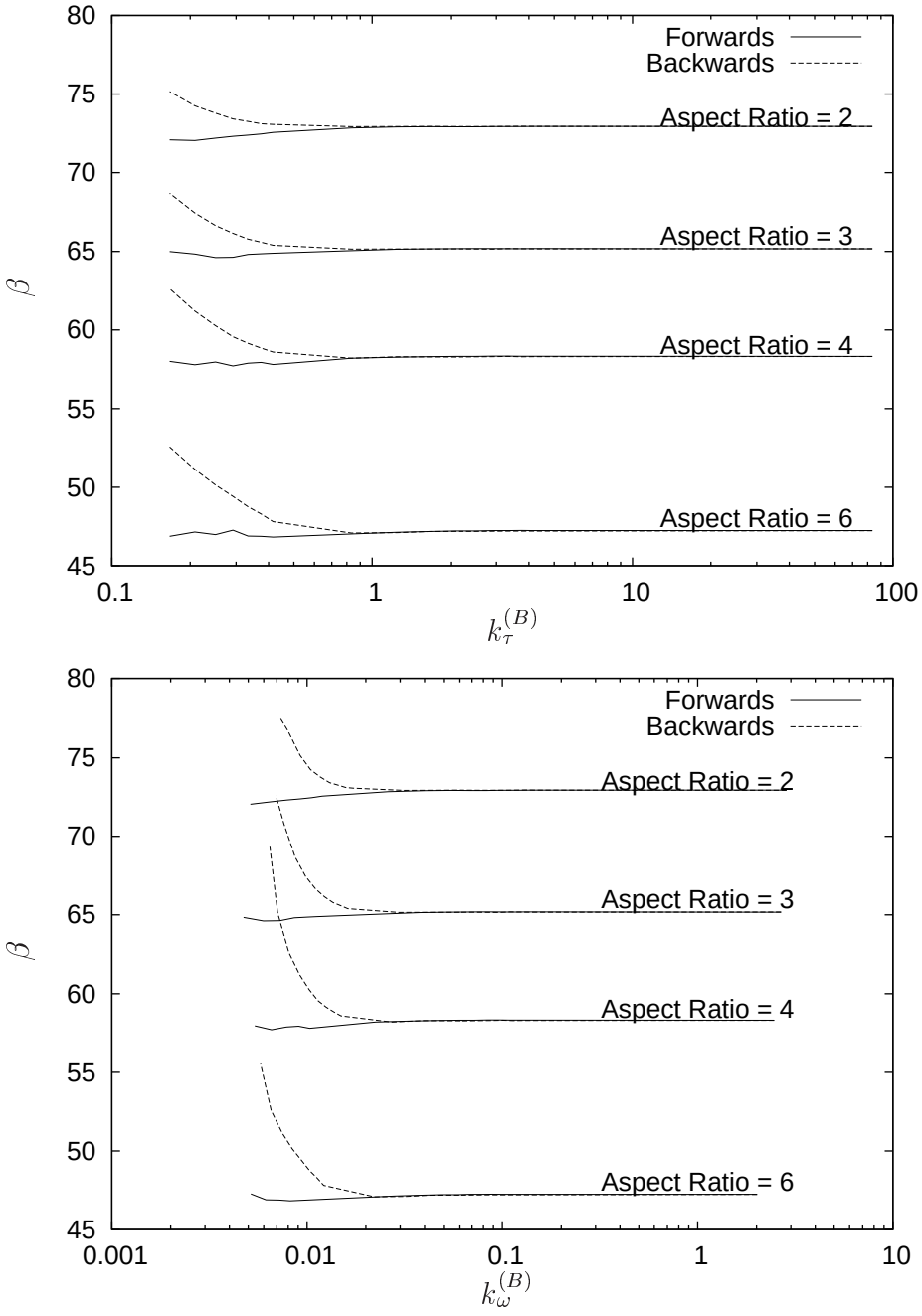

Figure 6.13: Pitch angle plotted against stiffness $k_\tau^{(B)}$ (top) and pitch angle plotted against stiffness $k_\omega^{(B)}$ (bottom) for semi-flexible helices of aspect ratios 2, 3, 4 and 6.

intensity dark-field microscopy, and then analysed to obtain the forwards and backwards swimming speeds. In our simulations small differences in forwards and backwards swimming, similar to those calculated by Takano and Goto [35], are only seen for much larger or much smaller stiffnesses than those used in the work of Takano and Goto. The discrepancy between our work and that of Takano and Goto may be explained by the differences in the models. In particular we do not include a cell head in our simulations but apply an external torque to the flagella. Also our simulation uses a helix of uniform radius with smaller number of turns whereas the flagella in the work of Takano and Goto [35] has an exponentially increasing radius at the junction between the flagella and the cell head.

Takano and Goto [35] and Takano *et. al.* [36] both report the same shape changes that we have found. Takano and Goto [35] report an increased radius and pitch and decreased number of turns for backwards swimming and Takano *et. al.* [36] report a constant length and pitch angle. Takano *et. al.* found that the number of turns for a flagella of stiffness $k_\omega^{(B)} = 0.016$ and pitch angle 41° increases from 2.84 to 2.92 for forwards swimming and decrease from 2.84 to 2.77 for backwards swimming. In comparison our results for a fibre of stiffness $k_\omega^{(B)} = 0.016$, and pitch angle 46° show an increase from 2.1 to 2.2 for forwards swimming and decrease from 2.1 to 2.0 for backwards swimming.

In conclusion, our results support the findings of Takano and Goto [35] and Takano *et. al.* [36] that flexibility does result in a difference between forwards and backwards swimming speed. We find a much larger difference in speeds in those found by Takano and Goto [35] however, this is still not as large as the 50% difference observed in the experiments of Magariyama [23]. Takano and Goto provide results for a flagellum whose dimensions and stiffness are chosen to match those of *Vibrio alginolyticus*. However, rather than focussing on matching a particular biological organism with the added complications of the interaction between the head and flagellum, we have studied the simpler problem of the swimming dynamics of isolated helical flagella over a range of stiffnesses and

pitch angles. Our results show that the exact stiffness of the flagellum is very important in determining how much the forwards and backwards speeds differ. We show results ranging from a zero difference for rigid fibres to a maximum of $\approx 23\%$ difference at stiffnesses between $k^{(B)} \approx 0.007$ and $k^{(B)} \approx 0.0085$. This demonstrates that the changes in shape due to flagella flexibility can produce the significant differences in forwards and backwards swimming speeds observed in *Vibrio alginolyticus*. However, our model is not intended to be an accurate representation of the dynamics of this creature, and so cannot provide a quantitative comparison.

Chapter 7

Discussions and Conclusions

In this thesis we have presented a semi-flexible fibre model in which chains of slender rods are connected via constraint forces and bending and twisting is resisted by torques at the joints. In chapter 2 we presented details of our model and simulation method for intrinsically straight fibres. This considers only bending. In chapter 3 we used this model to study semi-flexible fibres in shear flow and provided results for the orbit period, orbit drift, bending dynamics and stress. To model non-straight equilibrium shapes such as circular arcs and helices we developed a second simulation model that includes an equilibrium twist angle in addition to the equilibrium bend angle at the joints. This model together with a rigid helix simulation based on the grand resistance matrix are presented in chapter 4. In chapter 5 we presented results for the orbit period, shape changes and spin rate of intrinsically bent, semi-flexible fibres in shear flow plus details of the orbit period, translation and orbit drift of rigid and semi-flexible helices in shear flow. Finally in chapter 6 we use our simulation to determine the effect of flexibility on the forwards and backwards swimming speeds of intrinsic helices in a stationary flow.

7.1 Intrinsically Straight Fibres

In chapter 3 we considered the question of whether semi-flexible fibres in shear flow performed C turns or S turns. Simulation results of Klingenburg, Ross and Skjetne [31, 34] and linear stability analysis results of Becker and Shelley [3] suggested that the C turn was the most unstable mode and hence only very flexible fibres would perform S turns. Our own linear stability analysis also confirmed that the C mode was the most unstable. However, in our simulation results we found that intrinsically straight fibres almost always perfomed S turns except in a few cases in which very flexible fibres would perform mode 4 turns. C turns were only observed for fibres with initial shape deformations. Schmid, Switzer and Klingenberg, also used chains of rigid rods in their simulation and found that instrinsically straight fibres performed S turns.

There are two regions of a fibre orbit in which bending is important; in the compressional quadrant, close to an angle of -45° with the flow direction, where compressive forces are greatest and the largest degree of bending occurs; and within $\frac{1}{a_r}$ of the $x-z$ plane where, although the compressional forces are weaker by a factor of $\frac{1}{a_r}$, the fibre spends almost its entire orbit. In the compressional quadrant our linear stability results show that the C mode is the most unstable, however, simulation results in extensional flow show that a C mode can only grow if the initial perturbation is even. When the initial perturbation is odd the S mode is seen for flow rates where it is unstable.

By calculating the bending torque distribution along a fibre aligned in the flow direction we showed that the torque distribution is anti-symmetric and hence the bending of the fibre in the $x-z$ plane seeds an initial S shape (an odd mode) with bend amplitude proportional to $\frac{1}{k^{(B)}a_r^2}$. This then means that only odd modes grow in the compressional quadrant.

As high aspect ratio fibres spend a fraction $\frac{a_r^2}{a_r^2+1}$ of their orbit within $\frac{1}{a_r}$ of the $x-z$ plane it is bending in this region which most affects orbit period. The relative difference between

the orbit period of the rigid fibre T_r and the semi-flexible fibre T is given by the function $f = \frac{T_r}{T} - 1$ and measures the effect of flexiblity on orbit period compared to that of an equivalent rigid fibre. In chapter 3 we found that f was proportional to $\frac{1}{k^{(B)}a_r}$. Thus the effect of flexibility is to give the fibre an effective thickness, df, which is proportional to $\frac{1}{k^{(B)}a_r^2}$ in agreement with the results of the bending torque analysis. Flexible fibres rotate faster than rigid fibres as the bend in the fibre decreases its aspect ratio.

We also calculated how the integral of the bending energy, E, over a period depends upon the stiffness and aspect ratio of the particle. At high fibre stiffnesses we find that E is proportional to $\frac{1}{k^{(B)^2}a_r^3}$. This scaling can be predicted using the bending torque analysis for a fibre close to the $x-z$ plane as the orbits of high aspect ratio fibres are dominated by time spent here. At lower stiffnesses a different regime exists in which the bending energy over one orbit is dominated by bending in the compressional quadrant, which is significantly greater than the bending that occurs in the $x-z$ region. The stiffness values marking the transistion between these 2 regimes correspond to the values obtained in the linear stability analysis at which the S mode becomes unstable, hence at high stiffnesses bending in the compressional quadrant is no longer important as small distortions created in the $x-z$ plane decay during rotation through the compressional quadrant.

Graphs of shear stress and first and second normal stress differences show scalings similar to those obtained for the low stiffness regime. This is because stress is greatest in the compressional and extensional quadrants and zero when the fibre is in the $x-z$ plane. At high stiffnesses where bending only occurs in the $x-z$ plane and the bend decays in the compressional quadrant, the stress of a semi-flexible fibre is no different from that of a completely rigid fibre.

Semi-flexible fibres with initial orientation that are not in the $x-y$ plane do not rotate in closed Jeffery orbits but drift towards one of two attracting orbits: rotation in the $x-y$ plane or alignment in the vorticity direction. Orbit drift occurs mainly in the $x-z$ region where orbit paths are closest together and hence only a small bend is required to

significantly alter the path of the fibre. Although the fibre does drift away from its initial Jeffery orbit in the compressional quadrant it drifts back again in the extensional quadrant.

7.2 Non-straight Equilibrium Shapes

In chapter 5 we considered fibres with non-straight equilibrium shapes. We limited our attention to fibres bent into circular arcs and fibres with intrinsically helical shapes. In constrast to intrinsically straight semi-flexible fibres, where orbit period always decreases with increasing fibre flexibility, very flexible circular arcs have longer orbit periods than rigid fibres because the flexibility allows the fibre to straighten in the extensional quadrant, hence increasing its effective aspect ratio so that it takes longer to pass through the flow direction. For stiffer fibres we find the opposite behaviour, the effect of bending is dominant and orbit periods are shorter than those of rigid fibres.

Straight flexible fibres drift across Jeffery orbits. Intrinsically bent fibres have an alternative mechanism for changing their orientation by spinning about their end-to-end axis. Fibres with in-plane bend projected out of the $x-y$ plane, spin about an axis parallel to the end-to-end vector $\mathbf{p}$. Once the plane of bend reaches the $x-z$ plane, the fibre ceases to rotate or spin. Consequently only fibres with an out-of-plane bend rotate indefinitely. We have therefore presented results for helical fibres in shear flow.

Results from our rigid helix simulation show that in addition to rotation in the flow gradient plane, rigid helices translate along the vorticity axis and exhibit orbit drift. Neither of these properties were present for intrinsically straight fibres and both are a direct result of the assymmetry of the fibre. These effects disappear in either the limit of infinite effective aspect ratio (when the helix becomes straight) or the limit of an infinite number of turns as all major axes of the helix become aligned with the central axis. Just as with circular arcs the orbit period of a flexible helix is longer than an equivalent rigid helix but at higher stiffnesses the flexible helix has a shorter period. Translation along the

vorticity axis, which is at its greatest when under maximum compression or extension is reduced in semi-flexible fibres as the fibre is unable to resist the forces of the flow. Orbit drift is quicker for semi-flexible fibres but like rigid helices is chaotic due to the non-linear relationship between the period of rotation and period of spin.

7.3 Swimming of Helical Fibres

Finally, in chapter 6 we considered the effect of flexibility on the forwards and backwards swimming speeds of helical flagella. We find that backwards swimming speed is faster than forwards swimming speed in semi-flexible helices of constant angular velocity as forwards swimming causes the helix to wind up so that the average radius is reduced, the pitch decreases and the number of turns increases. For backwards swimming the average radius increases, the pitch increases and the number of turns decreases. Experimental observations by Magariyama [23] showed a 50% difference between forwards and backwards swimming speeds of *Vibrio alginolyticus*. Simulation results of Takano and Goto [12] however, showed only a 4% difference for a flagella of similar stiffness and dimensions. Our results, although not taken for the same dimensions as Magariyama [23] and Takano and Goto [12] show that over a range of stiffnesses the range of differences between forwards and backwards swimming speed range from $0-23\%$ with the maximum swimming speed occuring at $k_\omega^{(B)} = 0.0075$, the same stiffness used in both studies. Our results show that swimming speeds are very sensitive to stiffness, and that predicting the difference between forwards and backwards swimming speed for *Vibrio alginolyticus* is reliant upon determining the exact stiffness of the flagella.

Extensions to the work on swimming speed would be to include a cell body and an exponentially increasing flagella radius in the portion close to the cell body. The cell body could be included by using a higher order slender body approach similar to that of Higdon [16]. This would also allow for the inclusion of long range hydrodynamic interactions

between different parts of the fibre. The effect of hydrodynamic interactions would be to replace the tridiagonal matrix for the constraint forces with a full matrix, which would increase the computational cost. Including long range hydrodynamic interactions would also allow interactions between several fibres to be considered, which is necessary for the study of the swimming of organisms with multiple flagella.

Appendix A

Equilibrium Configuration

To calculate the values of Ω_1^{eq} and Ω_3^{eq} in terms of the continuous helix parameters a and b we calculate the rotation matrix in terms of a and b and compare to $\mathbf{R}(\Omega_1^{eq}, 0, \Omega_3^{eq})$. To do this we need to calculate the orthonormal frames of neighbouring rods $n-1$, n and $n+1$.

The position of any point on a helix is given by

$$\mathbf{x}(s) = \begin{pmatrix} bs \\ a\sin(s) \\ a\cos(s) \end{pmatrix}$$

for s running through an angle of $2\pi n_t$. When divided into N segments, s runs through an angle of $\Delta = \frac{2\pi n_t}{N}$ for each segment. If we let the centre of rod n lie at $\mathbf{x}(0)$ as illustrated in figure A.1 then the orientation vectors for rods $n+1$, n and $n-1$ are given by

$$\mathbf{p}_{n+1} = \frac{\mathbf{x}(\frac{3\Delta}{2}) - \mathbf{x}(\frac{\Delta}{2})}{\Delta} = \kappa_p^{-\frac{1}{2}} \begin{pmatrix} b \\ \tilde{a}\cos\Delta \\ -\tilde{a}\sin\Delta \end{pmatrix},$$

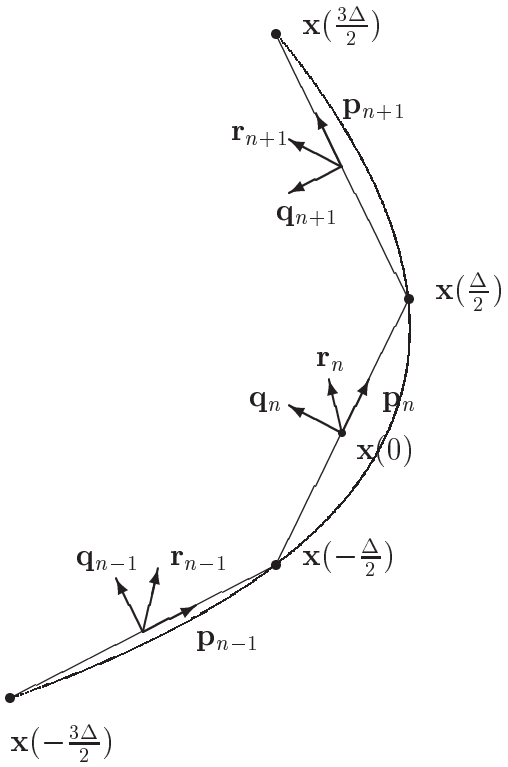

Figure A.1: The orthonormal frames and position vectors of three neighbouring rods in a discretised helix.

$$\mathbf{p}_n = \frac{\mathbf{x}(\frac{\Delta}{2}) - \mathbf{x}(-\frac{\Delta}{2})}{\Delta} = \kappa_p^{-\frac{1}{2}} \begin{pmatrix} b \\ \tilde{a} \\ 0 \end{pmatrix}$$

and

$$\mathbf{p}_{n-1} = \frac{\mathbf{x}(-\frac{\Delta}{2}) - \mathbf{x}(-\frac{3\Delta}{2})}{\Delta} = \kappa_p^{-\frac{1}{2}} \begin{pmatrix} b \\ \tilde{a}\cos\Delta \\ \tilde{a}\sin\Delta \end{pmatrix}$$

where $\tilde{a} = \frac{2a\sin\frac{\Delta}{2}}{\Delta}$ and $\kappa_p = \tilde{a}^2 + b^2$.

Vectors $\mathbf{r}_{n-1}$, $\mathbf{r}_n$, $\mathbf{q}_{n-1}$ and $\mathbf{q}_n$ are given by

$$\mathbf{r}_{n-1} = -\mathbf{p}_{n-1} \wedge \mathbf{p}_n = \kappa_r^{-\frac{1}{2}} \begin{pmatrix} -\tilde{a}^2\sin\Delta \\ \tilde{a}b\sin\Delta \\ \tilde{a}b(1-\cos\Delta) \end{pmatrix},$$

$$\mathbf{r}_n = -\mathbf{p}_n \wedge \mathbf{p}_{n+1} = \kappa_r^{-\frac{1}{2}} \begin{pmatrix} -\tilde{a}^2\sin\Delta \\ \tilde{a}b\sin\Delta \\ -\tilde{a}b(1-\cos\Delta) \end{pmatrix},$$

$$\mathbf{q}_{n-1} = \mathbf{p}_{n-1} \wedge \mathbf{r}_{n-1} = (\kappa_p\kappa_r)^{-\frac{1}{2}} \begin{pmatrix} \tilde{a}^2 b(1-\cos\Delta) \\ \tilde{a}^3\sin^2\Delta + \tilde{a}b^2(1-\cos\Delta) \\ -(\tilde{a}^3\cos\Delta + \tilde{a}b^2)\sin\Delta \end{pmatrix},$$

$$\mathbf{q}_n = \mathbf{p}_n \wedge \mathbf{r}_n = (\kappa_p\kappa_r)^{-\frac{1}{2}} \begin{pmatrix} \tilde{a}^2 b(1-\cos\Delta) \\ -\tilde{a}b^2(1-\cos\Delta) \\ -(\tilde{a}^3 + \tilde{a}b^2)\sin\Delta \end{pmatrix},$$

where $\kappa_r = 2\tilde{a}^2 b^2(1-\cos\Delta) + \tilde{a}^4\sin^2\Delta$.

Neighbouring orthonormal frames are related by

$$\begin{pmatrix} \mathbf{p}_n \\ \mathbf{q}_n \\ \mathbf{r}_n \end{pmatrix} = \begin{pmatrix} \tilde{r}_{11} & \tilde{r}_{12} & \tilde{r}_{13} \\ \tilde{r}_{21} & \tilde{r}_{22} & \tilde{r}_{23} \\ \tilde{r}_{31} & \tilde{r}_{32} & \tilde{r}_{33} \end{pmatrix} \begin{pmatrix} \mathbf{p}_{n-1} \\ \mathbf{q}_{n-1} \\ \mathbf{r}_{n-1} \end{pmatrix},$$

hence the components of the rotation matrix are given by

$$\tilde{r}_{11} = \mathbf{p}_{n-1} \cdot \mathbf{p}_n = (\tilde{a}^2 \cos\Delta + b^2)\kappa_p^{-1},$$

$$\tilde{r}_{12} = \mathbf{q}_{n-1} \cdot \mathbf{p}_n = \tilde{a}\sqrt{\kappa_*(1-\cos\Delta)}\kappa_p^{-1}$$

$$\tilde{r}_{13} = \mathbf{r}_{n-1} \cdot \mathbf{p}_n = 0,$$

$$\tilde{r}_{21} = \mathbf{p}_{n-1} \cdot \mathbf{q}_n = -\tilde{a}\sqrt{\kappa_*(1-\cos\Delta)}\kappa_p^{-1}(\tilde{a}^2(\cos\Delta+1) + 2b^2\cos\Delta)\kappa_*^{-1},$$

$$\tilde{r}_{22} = \mathbf{q}_{n-1} \cdot \mathbf{q}_n = (\tilde{a}^2 \cos\Delta + b^2)\kappa_p^{-1}(\tilde{a}^2(\cos\Delta+1) + 2b^2\cos\Delta)\kappa_*^{-1},$$

$$\tilde{r}_{23} = \mathbf{r}_{n-1} \cdot \mathbf{q}_n = -2b\sin\Delta\kappa_p^{\frac{1}{2}}\kappa_*^{-1},$$

$$\tilde{r}_{31} = \mathbf{p}_{n-1} \cdot \mathbf{r}_n = -\tilde{a}\sqrt{\kappa_*(1-\cos\Delta)}\kappa_p^{-1}2b\sin\Delta\kappa_p^{\frac{1}{2}}\kappa_*^{-1},$$

$$\tilde{r}_{32} = \mathbf{q}_{n-1} \cdot \mathbf{r}_n = (\tilde{a}^2 \cos\Delta + b^2)\kappa_p^{-1}2b\sin\Delta\kappa_p^{\frac{1}{2}}\kappa_*^{-1},$$

$$\tilde{r}_{33} = \mathbf{r}_{n-1} \cdot \mathbf{r}_n = (\tilde{a}^2(\cos\Delta + 1) + 2b^2\cos\Delta)\kappa_*^{-1},$$

where $\kappa_* = \tilde{a}^2(\cos\Delta + 1) + 2b^2$.

By comparison with the rotation matrix

$$\mathbf{R}(\Omega_1^{eq}, 0, \Omega_3^{eq}) = \begin{pmatrix} \cos\Omega_1^{eq} & -\sin\Omega_1^{eq} & 0 \\ \sin\Omega_1^{eq}\cos\Omega_3^{eq} & \cos\Omega_1^{eq}\cos\Omega_3^{eq} & -\sin\Omega_3^{eq} \\ \sin\Omega_1^{eq}\sin\Omega_3^{eq} & \cos\Omega_1^{eq}\sin\Omega_3^{eq} & \cos\Omega_3^{eq} \end{pmatrix}$$

as derived in section 4.2 with $\Omega_2^{eq} = 0$, we can see that

$$\sin\Omega_1^{eq} = -\tilde{a}\sqrt{\kappa_*(1-\cos\Delta)}\kappa_p^{-1},$$

$$\cos\Omega_1^{eq} = (\tilde{a}^2\cos\Delta + b^2)\kappa_p^{-1},$$

$$\sin\Omega_3^{eq} = 2b\sin\Delta\kappa_p^{\frac{1}{2}}\kappa_*^{-1},$$

and

$$\cos\Omega_3^{eq} = (\tilde{a}^2(\cos\Delta + 1) + 2b^2\cos\Delta)\kappa_*^{-1}.$$

We therefore obtain the following expressions for Ω_1^{eq} and Ω_3^{eq}.

$$\tan\Omega_1^{eq} = -\frac{\tilde{a}\sqrt{(\tilde{a}^2(\cos\Delta+1)+2b^2)(1-\cos\Delta)}}{(\tilde{a}^2\cos\Delta + b^2)}$$

$$\tan\Omega_3^{eq} = \frac{2b\sin\Delta\sqrt{\tilde{a}^2+b^2}}{(\tilde{a}^2(\cos\Delta+1)+2b^2\cos\Delta)}$$

Appendix B

Grand Resistance Matrix

The non-zero entries of $\tilde{\mathbf{G}}$ and $\tilde{\mathbf{H}}$ are given by

$$\tilde{G}_{113} = -\frac{4ab^2\pi n_t(2a^2+b^2)\sqrt{a^2+b^2}}{7a^4+13b^2a^2+6b^4},$$

$$\tilde{G}_{123} = -\frac{a^2bn_t\pi}{\sqrt{a^2+b^2}} = -\tilde{G}_{132} = \tilde{G}_{213} = \frac{1}{2}\tilde{G}_{231} = -\tilde{G}_{312} = \frac{1}{2}\tilde{G}_{321},$$

$$\tilde{G}_{131} = \tilde{G}_{311} = -\frac{(2ab^2\pi n_t}{\sqrt{a^2+b^2}},$$

$$\tilde{G}_{223} = \tilde{G}_{333} = -\frac{2(3a^2+4b^2)ab^2n_t\pi\sqrt{a^2+b^2}}{7a^4+13b^2a^2+6b^4},$$

and

$$\tilde{H}_{113} = -\frac{6a^3b^3\pi n_t\sqrt{a^2+b^2}}{7a^4+13b^2a^2+6b^4},$$

$$\tilde{H}_{123} = -\frac{a^2\pi n_t(49a^6+88b^6+216a^2b^4+182a^4b^2)\sqrt{a^2+b^2}}{49a^6+133a^4b^2+120a^2b^4+36b^6},$$

$$\tilde{H}_{131} = -\frac{(24b^4 + 41b^2a^2 + 14a^4)\pi n_t ba}{(7a^2 + 6b^2)\sqrt{a^2 + b^2}},$$

$$\tilde{H}_{132} = \frac{(a^2 + 2b^2)\pi n_t a^2}{\sqrt{a^2 + b^2}},$$

$$\tilde{H}_{213} = \frac{(196a^6 + 483a^4b^2 + 372a^2b^4 + 76b^6)a^2\pi n_t\sqrt{a^2 + b^2}}{2(49a^6 + 133a^4b^2 + 120a^2b^4 + 36b^6)},$$

$$\tilde{H}_{223} = \frac{7a^3b\pi n_t(2a^2 + 3b^2)\sqrt{a^2 + b^2}}{3(7a^4 + 13b^2a^2 + 6b^4)},$$

$$\tilde{H}_{231} = -\frac{\pi n_t b^2(21a^4 + 6b^2a^2 + 46b^2n_t^2\pi^2a^2 + 24b^4\pi^2n_t^2 + 21a^4\pi^2n_t^2)\sqrt{a^2 + b^2}}{3(7a^4 + 13b^2a^2 + 6b^4)},$$

$$\tilde{H}_{232} = \frac{2(28a^4 + 63b^2a^2 + 36b^4)ab\pi n_t\sqrt{a^2 + b^2}}{3(7a^4 + 13b^2a^2 + 6b^4)},$$

$$\tilde{H}_{311} = \frac{2ba\pi n_t(2a^2 - b^2)}{\sqrt{a^2 + b^2}},$$

$$\tilde{H}_{312} = -\frac{\pi n_t a^2(b^2 + 4a^2)}{2\sqrt{a^2 + b^2}},$$

$$\tilde{H}_{321} = \frac{\pi n_t b^2(-3a^2 + 3a^2\pi^2n_t^2 + 4b^2\pi^2n_t^2)}{3\sqrt{a^2 + b^2}},$$

$$\tilde{H}_{322} = -\frac{2ab\pi(5a^2 + 6b^2)}{3\sqrt{a^2 + b^2}},$$

$$\tilde{H}_{333} = -\frac{ba^3\pi n_t(14a^2+3b^2)\sqrt{a^2+b^2}}{3(7a^4+13b^2a^2+6b^4)},$$

respectively.

Appendix C

Mobility Matrix

The non-zero components of matrix **c** are given by

$$c_{11} = \frac{144a^8 + 72b^2a^6\pi^2n_t^2 + 438a^6b^2 + 351a^4b^4 + 228b^4\pi^2n_t^2a^4 + 224b^6a^2\pi^2n_t^2 + 24a^2b^6 + 64b^8\pi^2n_t^2}{4((a^2+b^2)^{\frac{3}{2}}(72a^6 + 36b^2\pi^2n_t^2a^4 + 111a^4b^2 + 96a^2b^4\pi^2n_t^2 - 120a^2b^4 - 192b^6 + 64b^6\pi^2n_t^2)\pi n_t a^2)},$$

$$c_{12} = -\frac{12(3a^2+4b^2)(a^2+b^2)^{\frac{3}{2}}b}{\pi n_t a(72a^8 + 183a^6b^2 - 9a^4b^4 - 312a^2b^6 - 192b^8 + 4\pi^2n_t^2(9b^2a^6 + 33b^4a^4 + 40b^6a^2 + 16b^8))},$$

$$c_{21} = c_{12},$$

$$c_{22} = \frac{12\sqrt{a^2+b^2}(3a^2+4b^2)}{(72a^6 + 36b^2\pi^2n_t^2a^4 + 111a^4b^2 + 96a^2b^4\pi^2n_t^2 - 120a^2b^4 - 192b^6 + 64b^6\pi^2n_t^2)\pi n_t},$$

$$c_{33} = \frac{12\sqrt{a^2+b^2}(3a^2+4b^2)}{\pi n_t(51a^4b^2 - 24a^2b^4 + 96a^2b^4\pi^2n_t^2 + 64b^6\pi^2n_t^2 + 72a^6 + 36b^2\pi^2n_t^2a^4)}.$$

Bibliography

[1] G. K. Batchelor. Slender-body theory for particles of arbitrary cross-section in Stokes flow. *J. Fluid Mech.*, 44:419, 1970.

[2] G. K. Batchelor. Stress system in a suspension of force-free particles. *J. Fluid Mech.*, 41:545, 1970.

[3] L. E. Becker and M. J. Shelley. Instability of elastic filaments in shear flow yields first-normal-stress differences. *Phys. Rev. Lett.*, 87:19, 2001.

[4] F.P. Bretherton. The motion of rigid particles in a shear flow at low Reynolds number. *J. Fluid Mech.*, 14:294, 1962.

[5] J. M. Burgers. On the motion of small particles of elongated form suspended in a viscous liquid. Second report on viscosity and plasticity, Chap. III. *Kon. Ned. Akad. Wet.*, 16:113, 1938.

[6] S. Camalet, F. Julicher, and J. Prost. Self-organised beating and swimming of internally driven filaments. *Phys. Rev. Lett.*, 82:1590, 1999.

[7] A. T. Chwang and T. Y. Wu. A note on the helical movement of micro-organisms. *Proc. Roy. Soc. Lond. B*, 178:327, 1971.

[8] R. G. Cox. The motion of long slender bodies in a vicous fluid. Part 1. General theory. *J Fluid Mech.*, 44:791, 1970.

[9] R. Dreyfus, J. Baudry, M. L. Roper, M. Fermigier, H. A. Stone, and J. Bibette. Microscopic artificial swimmers. *Nature*, 437:862, 2005.

[10] O. L. Forgacs and S. G. Mason. Orbits of flexible threadlike particles. *J.Colloid Sci.*, 14:473, 1959.

[11] O. L. Forgacs and S. G. Mason. Spin and Deformation of Threadlike Particles. *J. Colloid Sci.*, 14:457, 1959.

[12] T. Goto, R. Inaoka, and Y. Takano. Numerical analyis of bacterium motion based on the slender body theory. *JSME International Journal*, 43:875, 2000.

[13] J. Gray and G. J. Hancock. The propulsion of sea-urchin spermatozoa. *J. Exp. Biol.*, 32:802, 1955.

[14] G. J. Hancock. The self propulsion of microscopic organisms through liquid. *Proc. R. Soc. Lond. A*, 217:96, 1953.

[15] J. J. L. Higdon. A hydrodynamic analysis of flagellar propulsion. *J. Fluid Mech.*, 90:685, 1979.

[16] J. J. L. Higdon. The hydrodynamics of flagellar propulsion: helical waves. *J. Fluid Mech.*, 94:331, 1979.

[17] E.J. Hinch. The distortion of a flexible inextensible thread in a shearing flow. *J. Fluid Mech.*, 74:317, 1976.

[18] J. Howard. *Mechanics of motor proteins and the cytoskeleton*. Sinauer Associates, Inc., 2001.

[19] G.B. Jeffery. Ellipsoidal paricles immersed in a viscous fluid. *Proc. R. London, Ser.A*, 102:161, 1922.

[20] S. Kim and S. J. Karrila. *Microhydrodynamics: Principles and selected applications*. Butterworth-Heinemann, 1991.

[21] J.G. Kirkwood and J. Riseman. The Intrinsic Viscosities and Diffusion Constants of Flexible Macromolecules in Solution. *J. Chem. Phys.*, 16:565, 1948.

[22] L. G. Leal. *Laminar flow and convective transport processes*. Butterworth-Heinemann, 1992.

[23] Y Magariyama, S. Masuda, Y. Takano, T. Ohtani, and S. Kudo. Difference between forward and backward swimming speeds of the single-polar-flagellated bacterium. *FEMS Microbiology Letters*, 205:343, 2001.

[24] A. C. Maggs. Writhing geometry at finite temperature: Random walks and geometric phases for stiff polymers. *J. Chem. Phys.*, 114:5888, 2001.

[25] M. Manghi, X. Schlagberger, and R. R. Netz. Propulsion with a rotating elastic nanorod. *Phys. Rev. Lett.*, 96:068101, 2006.

[26] Queensland College of Art Design. "Computer Animation QCA 7008, Basic Modelling", May 2007. http://kali.qca.gu.edu.au/ ani/week2.html .

[27] N. Phan-Thien, T. Tran-Cong, and M. Ramia. A boundary-element analysis of flagellar propulsion. *J. Fluid Mech.*, 184:533, 1987.

[28] C. Pozrikidis. *Boundary integral and singularity methods for linearised viscous flow*. Cambridge University Press, 1992.

[29] W. H. Press, S. A. Teukolsky, W. T. Vetterling, and B. P. Flannery. *Numerical recipes in Fortran: The art of scientific computing*. Cambridge University Press, 1992.

[30] E. M. Purcell. Life at low Reynolds number. *Am. J. Phys*, 45:3, 1977.

[31] R. F. Ross and D. J. Klingenberg. Dynamic simulation of flexible fibers composed of linked rigid bodies. *J. Chem. Phys.*, 106(7):2949, 1997.

[32] B. Scharf. Real-time imaging of fluorescent flagellar filaments of *Rhizobium lupini* H13-3: Flagellar rotation and pH-induced polymorphic transitions. *J.Bacteriol.*, 184:5979, 2002.

[33] C. F. Schmid, L. H. Switzer, and D. J. Klingenberg. Simulations of fiber flocculation: Effects of fiber properties and interfiber friction. *J.Rheol.*, 44:781, 2000.

[34] Skjetne, P. and Ross, R. F. and Klingenberg, D. J. Simulation of single fiber dynamics. *J. Chem. Phys.*, 107(6):2108, 1997.

[35] Y. Takano and T. Goto. Numerical analysis of small deformation of flexible helical flagellum of swimming bacteria. *JSME International Journal*, 46:1234, 2003.

[36] Y. Takano, K. Yoshida, S. Kudo, M. Nishitoba, and Y. Magariyama. Analysis of small deformation of helical flagellum of swimming *Vibrio alginolyticus*. *JSME International Journal*, 46:1241, 2003.

[37] G. I. Taylor. Analysis of the swimming of microscopic organisms. *Proc. R. Soc. Lond. A*, 209:447, 1951.

[38] G. I. Taylor. The action of waving cylindrical tails in propelling microscopic organisms. *Proc. R. Soc. Lond. A*, 211:225, 1952.

[39] J. P. K. Tillett. Axial and transverse Stokes flow past slender axisymmetric bodies. *J. Fluid Mech.*, 44:401, 1970.

[40] B.J. Trevelyan and S.G. Mason. Particle motions in sheared suspensions. *J. Colloid Sci.*, 6:354, 1951.

[41] G. Williams. www.topometrix.com, December 2006.